Development of injection moulded, ultrasonically welded immiscible phase filtration devices

Kistrup, Kasper

Publication date:
2015

Document Version
Publisher's PDF, also known as Version of record

Development of injection moulded, ultrasonically welded immiscible phase filtration devices

Kasper Kistrup
PhD Thesis, June 2015

DTU Nanotech
Department of Micro- and Nanotechnology

Development of injection moulded, ultrasonically welded immiscible phase filtration devices

Kasper Kistrup, M. Sc.

Submitted in partial fulfilment of the requirements for the
degree of Philosophiae Doctor, Technical University of Denmark,
June 2015

Department of Micro- and Nanotechnology
Technical University of Denmark
Kgs. Lyngby, Denmark

Preface

This PhD thesis entitled "*Development of injection moulded, ultrasonically welded immiscible phase filtration devices*" was submitted in partial fulfilment of the requirements for obtaining the degree of Philosophiae Doctor (PhD) at the Technical University of Denmark. The work has been carried out at the Department of Micro- and Nanotechnology (DTU Nanotech) from February 2012 to June 2015 within the Magnetic Systems group. The work was supported by the Danish Council for Strategic Research through the Strategic Research Centre PolyNano (grant no. 10-092322/DSF). The PhD project was supervised by Associate professor Mikkel Fougt Hansen (DTU Nanotech) and co-supervised by Associate professor Anders Wolff (DTU Nanotech).

First, I would like to thank my supervisor Mikkel Fougt Hansen for introducing me to microfluidics and for his exceptional support and counselling during these last three years. I would also like to thank my co-supervisor Anders Wolff for his advice, ideas, and for encouraging me to take up ultrasonic welding.

I would further like to thank both past and present colleagues at DTU Nanotech for good company and fruitful scientific discussions, especially: Carl Esben Poulsen for being a good colleague, friend, debater, and for all the hours in the lab. Karen Skotte Jørgensen for not letting me get lost in physics and good company at the office. The rest of the Magnetic systems group. All the people from the TransForm Project and PolyNano.

I extend my gratitude to: Karsten Brandt Andersen (DTU Nanotech) and Julia Skov (DELTA) for getting me started with MRSA. Kenneth Brian Haugshøj (Centre for Microtechnology and Surface analysis, Danish Technological Institute) for helping with MVD coating of chips. Jørgen Garnæs (Danish National Metrology Institute (DFM)) and Morten Hannibal Madsen (DFM) for helping with surface metrology. Peter Friis Østergaard (Centre for Microtechnology and Surface analysis, Danish Technological Institute) and Marco Matteucci (DTU Nanotech) for their injection moulding expertise. Nis Korsgaard Andersen and Rafael Taboryski for advice on materials and assistance with contact angle measurements. Lars Peter Nielsen (Statens Seruminstitut) for providing me with biological samples and assay knowledge.

Last, but not least, I wish to thank my friends and family for being supportive throughout the last three years, my girlfriend Karen for her loving endless patience and understanding, and finally, my son Bertram for allowing his dad to *go to work* continuously for the last weeks up to the final deadline.

Kasper Kistrup
Kgs. Lyngby, Denmark
June 30, 2015

Abstract

Having advanced tremendously over the past two decades, microfluidics is today a well-established scientific field. The governing physics are under control and the teething troubles of preliminary device fabrication have been overcome. The applications of microfluidics are wide ranging from components in inkjet printing, to disposable chips for point-of-care diagnostics, to advanced chemical analysis systems. Nevertheless, the original prophesied commercial success as a whole has been limited.

The modest existence of microfluidic devices as products is due in part to a manufacturing schism that has befallen the field. In academia, microfluidic devices have historically been fabricated using materials and technologies that while efficient at rapid prototyping, are near incompatible with industrial mass production. The research conducted has generated immense knowledge of such techniques and materials, however, technology transfer to the industry is challenging.

This PhD project has focused on applying industry-compliable technologies for rapid prototyping of microfluidic devices. In specific, a thermoplastic disposable microfluidic chip system for sample preparation has been realised. The device applies magnetic bead-based solid-phase extraction for nucleic acid extraction from biological samples, using the immiscible phase filtration (IPF) approach. Device development has employed injection moulding for part fabrication and ultrasonic welding for bonding. Rapid prototyping was accomplished by micromilling and laser micromachining of mould inserts, allowing for design-to-production of chips within a day. The rapid overall fabrication cycle of a few minutes per chip allowed for conducting research in a single-use disposable fashion.

Chip development has centred on manufacturing of an IPF chip, by generating a microfluidic channel system capable of fluid handling using capillary forces. A key aspect of IPF is to replace the required washing steps of the magnetic beads with passage through capillary microvalves. Furthermore, much development has gone into creating energy directors for ultrasonic welding, suitable for microfluidic systems. A methodology has been established where energy directors can be quickly added to existing mould inserts, using laser micromachining. The produced device was performance tested by isolating methicillin-resistant *Staphylococcus aureus* from bovine whole blood, followed by off-chip quantification using real time quantitative polymerase chain reaction.

Resumé

Efter stor fremgang i løbet af de sidste to årtier er mikrofluidik i dag et veletableret videnskabeligt felt. Den underliggende fysik er under kontrol og børnesygdommene i forbindelse med chipfabrikation er overkommet. Anvendelserne for mikrofluidik er bredt omfattende, fra delelementer i inkjet printning, til engangschips til patientnær diagnostik, til avancerede kemiske analysesystemer. Ikke desto mindre er den oprindeligt profeterede kommercielle succes stadig begrænset.

Den beskedne eksistens af mikrofluidchips som produkter er delvist grundet et fremstillingsskisme der er overgået feltet. I den akademiske verden er mikrofluidchipsystemer historisk blevet fabrikeret ved at bruge materialer og teknologi, der ganske vidst er hurtig til prototypefremstilling, men nærmest inkompatibel med industriel masseproduktion. Forskning har genereret enorm viden om disse teknikker og materialer, men teknologioverførsel af disse til industrien er udfordrende.

Dette ph.d.-projekt har fokuseret på at anvende industrikompatible teknologier til hurtig prototypefremstilling af mikrofluidchips. Specifikt er et engangsmikrofluidsystem i termoplastik til prøveoprensning blevet realiseret. Chippen anvender magnetisk kugle-baseret fast-legeme-udvinding ved hjælp af ikke-blandbar fasefiltrering (IFF), til isolering af nukleinsyrer fra biologiske prøver. Chipudviklingen har benyttet sprøjtestøbning til chipfabrikation og ultralydssvejsning til sammenføjning. Hurtig prototypeudvikling blev opnået ved at mikrofræse og lasermaskinbearbejde formindsatser, hvilket tillod at gå fra design til produktion af chips i løbet af en dag. Den overordnede fabrikationstid var få minutter per chip, hvilket tillod engangsanvendelse af chipsne til forskning.

Chipudvikling har fokuseret på fremstilling af en IFF chip, ved at generere et mikrofluidkanalsystem, der er i stand til at håndtere væsker ved hjælp af kapillarkrafter. Et nøglepunkt for IFF er at erstatte de ellers krævede vasketrin af de magnetiske kugler, med passage gennem kapillære mikroventiler. Ydermere er der udviklet omfattende på at skabe svejseledere til ultralydssvejsning, der er velegnede til mikrofluidsystemer. En fremgangsmåde er blevet etableret, hvor svejseledere nemt kan blive tilføjet til eksisterende fromindsatser, ved brug af laser maskinbearbejdning. Det producerede chipdesign blev præstationstestet ved at isolere methicillin-resistent *Staphylococcus aureus* fra ko fuldblod, efterfulgt af kvantificering via konventionel realtid kvantitativ polymerasekædereaktion.

Table of contents

List of abbreviations

ABS	Acrylonitrile butadiene styrene
CAD	Computer-aided design
CFU	Colony forming unit
CLP	Cone-like-protrusion
CNC	Computer numerical control
COC	Cyclic olefin copolymer
EDM	Electric discharge machining
FDTS	1H,1H,2H,2H-perfluorodecyltrichlorosilane
IPF	Immiscible phase filtration
LoC	Lab-on-a-chip
MB	Magnetic bead
MRSA	Methicillin-resistant *Staphylococcus aureus*
µTAS	Miniaturised total chemical analysis system
PC	Polycarbonate
PDMS	Poly(dimethylsiloxane)
PE	Polyethylene
PMMA	Poly(methyl methacrylate)
PoC	Point-of-care
PP	Polypropylene
PS	Polystyrene
PTFE	Polytetrafluoroethylene
qPCR	Real-time quantitative polymerase chain reaction
SPE	Solid-phase extraction
UW	Ultrasonic welding

Chapter 1 Introduction

Throughout this thesis references to different parts of microfluidic devices will be applied extensively. To avoid confusion, here follows clear definitions of what is meant by different terms:

- A *chip part* refers to the (often) injection moulded component containing the majority of the structures or channels *e.g.* the channel layout of a microfluidic system.
- A *sheet part* refers to the thin polymer piece that is fused with the chip part to complete the chip. The sheet part can be either a piece of extruded polymer, or an injection moulded part.
- A *chip* refers to the fused product of all the parts needed to complete a microfluidic system, but does not take into account any other back-end processing, such as surface coating.

1.1 List of publications

For the sake of clarity, the list of published work with short descriptions are found below, in order to provide a brief overview of the conducted work. It also serves as lookup table. Own published work will be referenced as *Paper X* throughout the thesis and the actual papers are included as appendices.

Peer-reviewed publications:

Paper 1

K. Kistrup, C.E. Poulsen, P.F. Østergaard, K.B. Haugshøj, R. Taboryski, A. Wolff, M. F. Hansen, Fabrication and modelling of injection moulded all-polymer capillary microvalves for passive microfluidic control, *J. Micromechanics Microengineering.* **24** (2014) 125007. doi:10.1088/0960-1317/24/12/125007.

Paper 1 presents the fabrication of a microfluidic system featuring an array of capillary microvalves. The objective was to determine the performance of the microvalves in an injection moulded system bonded using ultrasonic welding. Furthermore, a numerical model able to predict burst pressures of capillary microvalves was developed for microvalves having geometries that does not have a complete analytical solution.

Paper 2

K. Kistrup, K. Skotte Sørensen, A. Wolff, M. Fougt Hansen, Liquid carry-over in an injection moulded all-polymer chip system for immiscible phase magnetic bead-based solid-phase extraction, *J. Magn. Magn. Mater.* **100** (2014) 1–6. doi:10.1016/j.jmmm.2014.10.020.

Paper 2 presents a microfluidic chip system featuring capillary microvalves for nucleic acid extraction using the immiscible phase filtration approach. The chip was characterised in relation to surfactant compatibility and liquid carry-over, two important performance parameters.

Paper 3

K. Kistrup, C.E. Poulsen, M. Hansen, A. Wolff, Ultrasonic welding for fast bonding of self-aligned structures in lab-on-a-chip systems, *Lab Chip*. **15** (2015) 1998-2001. doi:10.1039/C5LC00174A.

Paper 3 further explored the usage of ultrasonic welding for bonding of microfluidic systems. An ultrasonic welding joint design that allowed for alignment of two parts prior to bonding, and for minimising of the bond gap introduced by the welding, were presented. Ultrasonic welding allows for bonding of large area, low-aspect ratio chambers, which was also demonstrated.

Paper 4

C.E. Poulsen, **K. Kistrup**, N. K. Andersen, M. F. Hansen, R. Taboryski, A. Wolff, Laser induced micropillar energy directors for ultrasonic welding of microfluidic systems. *Submitted manuscript.*

Paper 4 presents the continued work on ultrasonic welding. In this paper, a new type of "micropillar" energy directors were introduced, and tested, in a microfluidic system having freestanding high-aspect ratio channel walls. The micropillar energy directors were added to existing moulds as a fast back-end process. Ultrasonic welding preserved the structural integrity of the channel system and the fused chip showed high bonding strength.

Conference contributions:

K. Kistrup, K.S. Sørensen, P.F. Østergaard, R.J. Taboryski, A. Wolff, M.F. Hansen, All-polymer chip system for magnetic bead-based solid phase extraction, EMBL Conference: Microfluidics 2014, Heidelberg, Germany, 2014, Poster presentation.

K. Kistrup, K.S. Sørensen, P.F. Østergaard, A. Wolff, R.J. Taboryski, M.F. Hansen, Liquid carry-over in an all-polymer chip system for Magnetic bead-based mobile solid phase extraction, 10th International Conference on the Scientific and Clinical Applications of Magnetic Carriers, Dresden, Germany, 2014, Poster presentation.

C.E. Poulsen, K. Kistrup, N.K. Andersen, R.J. Taboryski, M.F. Hansen, A. Wolff, TransForm: Injection moulded 3D superhydrophobic surfaces, DTU Sustain Conference, 2014, Poster presentation.

Patents:

Two patent applications have been filed to the European Patent Office on 2014-12-05.

C.E. Poulsen, N. K. Andersen, K. Kistrup, A. Wolff, R. Taboryski, Micro-scale energy directors for ultrasonic welding, EP14196586, 2014.

C.E. Poulsen, N. K. Andersen, K. Kistrup, A. Wolff, R. Taboryski, Method of producing an item with enhanced wetting properties by fast replication and replication tool used in the method, EP14196584, 2014.

1.2 Microfluidic devices

In the recent report: *Microfluidics Market by Material (Polymer, Glass, Silicon) Application (Pharmaceutical (Genomics, Proteomics, Capillary Electrophoresis) Diagnostic (POC, Clinical, Environmental, Industrial) Drug Delivery (Inhaler, Micropump)) - Global Forecast to 2020* by MarketsandMarkets (www.marketsandmarkets.com/Market-Reports/microfluidics-market-1305.html, accessed 2015-06-24), the world microfluidics market, in the areas indicated in the title, is expected to

grow from $3 billion in 2015 to $7.5 billion in 2020. The report underlines that the field of microfluidics has reached an important milestone, where the technology is mature enough to support a multi billion dollar market.

Microfluidics is quite simple by definition, put elegantly by Whitesides:

> What is microfluidics? It is the science and technology of systems that process or manipulate small (10^{-9} to 10^{-18} litres) amounts of fluids, using channels with dimensions of tens to hundreds of micrometres.
>
> - *George M. Whitesides, 2006*[1].

Utilisation of the physical conditions that dominate small volumes (laminar flow and surface tension) allows microfluidics to cover a broad field of disciplines; from design and fabrication of devices, to applications like chemical analysis, cell biology, and diagnostics[1,2].

Applications of microfluidics most often take the form of *lab-on-a-chip* (LoC) systems that are microfluidic channel systems realised in a solid material, for some application. Figure 1.1 shows two important examples of microfluidic systems. To the left is the first presented LoC system from 1979, where a gas chromatograph was presented. To the right is one of the early poly(dimethylsiloxane) (PDMS) systems that revolutionised the way LoCs could be fabricated.

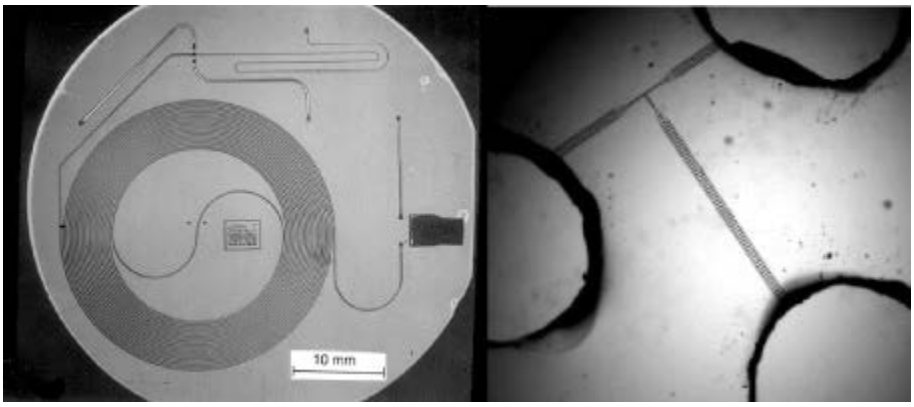

Figure 1.1 Examples of LoC systems. **Left** The *gas chromatographic air analyzer* presented by Terry *et al.* in 1979. The device was etched in a silicon wafer using photolithography, and then anodically bonded to pyrex glass, to seal it. It was capable of separating a mixture of nitrogen, pentane, and hexane. The device featured 200 µm wide and a 30 µm deep channels[3]. **Right** The *microfabricated fluorescence-activated cell sorter* presented by Fu *et al.* in 1999. The device was a disposable PDMS chip created using soft lithography and bonded to glass. It was able to sort Green Fluorescent Protein-expressing *Escherichia coli* from wild-type *E. coli*. The device featured 100 µm wide (3 µm sorting junctions) and 4 µm deep channels[4]. The device was later applied for capillary electrophoresis of DNA[5].

Much effort has been directed towards biomedical research, where microfluidics offer many appealing traits. Following the report mentioned above, the main growth of the microfluidics market is expected to stem from the increasing demand for point-of-care (PoC) LoC devices. The recent review by Sackman *et al.*[2] eloquently describes the current status of the biomedical branch of microfluidics. LoC devices

have up to now mostly been iterative improvements to existing solutions, that have quite simply not provided enough benefit, to be directly taken up by the clinicians and biologists. Sackman points to lack of cooperation as one of the main causes for the slow uptake of LoC technology into the biomedical field. The key challenge is to identify problems where microfluidics provide a solution that cannot be accommodated by conventional technology – and then solve that problem in collaboration, so the technological expertise of the engineers and assay knowledge of the clinicians can be put to good use. One of the few good examples are the lateral flow test systems, such as the home pregnancy test. The convenience of the easy sample introduction, rapid analysis time, and colorimetric detection, that can be performed at the PoC by an inexperienced user is unparalleled.

1.3 Sample preparation in microfluidics

The core elements of microfluidics like transport, analysis, and detection of targets in miniscule volumes are well underway. However, sample preparation remains a central challenge for the microfluidics community[1,6]. In academia, the major focus point for microfluidics is within biological assays, and diagnostics in particular[2], yet, most real-life samples for diagnostics are large volume, complex matrices, like blood, saliva or faeces. These types of samples cannot be readily introduced to a microfluidic device, but require “world-to-chip” interfacing – an issue already highlighted in 1999 by J.M. Ramsey[7]. Large sample volumes are sometimes also a requirement because the target concentration can be so low that it reaches the Poisson statistical limit for small volume samples[6].

1.3.1 The immiscible phase filtration approach to sample preparation

Immiscible phase filtration (IPF) is a re-thinking of the classic magnetic bead(MB)-based solid-phase extraction (SPE) kits that today are a standard for cell separation, protein/nucleic acid isolation, and immunoassays[8,9]. Solutions are available from various suppliers *e.g.* Life Technologies (www.lifetechnologies.com, accessed 2015-06-12) and Miltenyi Biotec (www.miltenyibiotec.com, accessed 2015-06-12), going from manual separation kits for small scale research use, up to fully automated systems for routine use.

Immiscible phase filtration (coined by the Kelso group[10]), *immiscible filtration assisted by surface tension* (coined by the Beebe group[11]), *Magneto-capillary valve* (coined by the Prins group[12]), or *centrifugal gas-phase transition magnetophoresis* (coined by the Zengerle group[13]) (the devil is known by many names) all share the same approach to facilitating the separation process, be it for sample preparation or immunoassays. The principles of the original MB-based SPE approach and IPF approach are outlined in Figure 1.2.

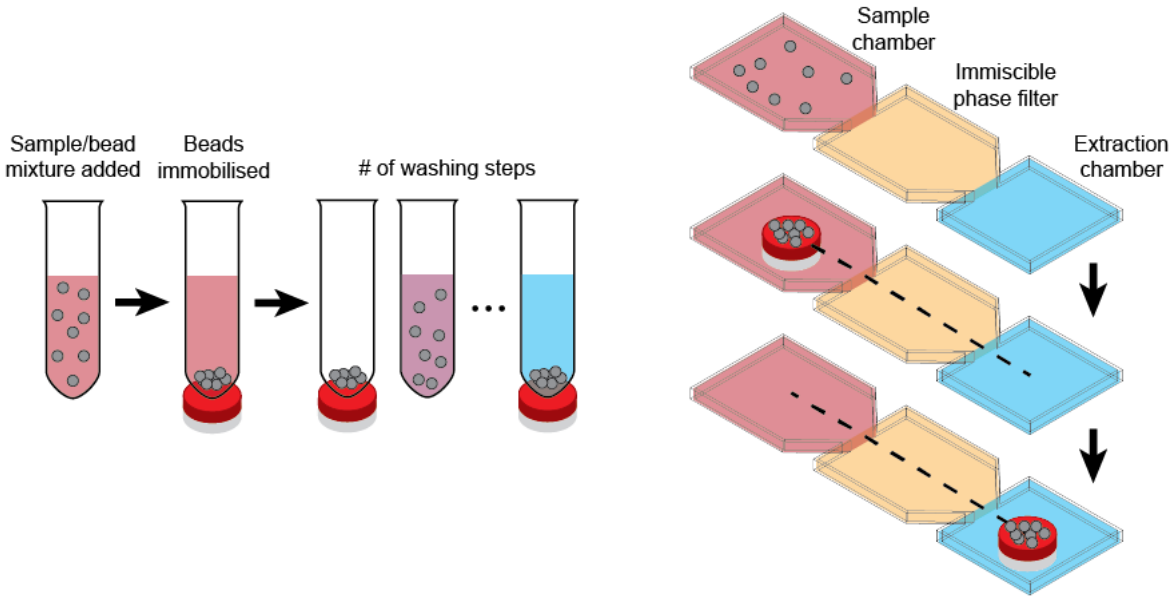

Figure 1.2 The principle of traditional MB-based solid phase extraction (left) *vs.* IPF (right). The classic approach involves mixing MBs with the sample in a tube. The MBs are incubated to capture the target, and immobilised in the tube using an external magnet. The target-MB complex is then washed by removing the sample volume, resuspending the beads in a washing buffer, re-immobilising the beads, and then removing the washing buffer. This process is repeated until contaminants from the original sample volume have been eliminated. The IPF approach is based on passage of the MB cluster through stable immiscible fluid interfaces, rather than washing. An array of chambers connected by capillary microvalves are first filled with aqueous solutions including the sample/MB mixture, followed by filling of the intermediate chamber(s) with an immiscible liquid (usually oil). The MBs are then gathered by an external magnet and pulled through the immiscible phase(s).

MB-based SPE relies on functionalised MBs to capture a given target (proteins, cells or nucleic acids) in a sample matrix. The first step is to incubate the magnetic beads with the sample matrix in a tube and allow them to mix. The MBs are then separated from the sample, either to enrich (reduce the sample volume) or to purify (remove contaminants from the target that will inhibit down-stream analysis). This is typically done by fixating the MBs with an external magnet and emptying the tube. Because biological material is not magnetic, only the target specifically bound to the MBs will be retained, in theory. In praxis, a small amount of the original sample volume will be retained along with the MBs, demanding the need to add washing steps to successfully eliminate contaminants. The drawback of the original MB-based SPE is this need for washing steps, requiring manual pipetting or robotics to move the beads around. This is costly and the open chambers are unfeasible outside the lab setting. Furthermore, washing is time consuming and integration of wash steps into microfluidic systems is difficult, requiring pumps, valves, *etc*.

The IPF approach circumvents the need of washing steps by creating a system where sample and an extraction buffer are loaded into the same microfluidic channel system, separated by an immiscible phase. The system is kept stable by controlling the surface tensions associated with the fluid interfaces and the chip substrate, typically by use of capillary microvalves. The governing physics are explained in chapter 2. The MBs can be moved directly from the sample volume to the extraction buffer by actuation with an external magnet. IPF does not completely eliminate the carry-over of liquid (the *carry-over liquid*) from the sample volume to the extraction buffer. However, depending on a given system it

can either be minimised by optimising the parameters of the system, or by transporting the MBs through a number of washing solutions, as we shall see below. IPF is a flexible method and thus the many types of systems differ in almost all aspects; substrate materials, immiscible phase type, magnetic bead type, physical design, fabrication method, *etc.* A selection of IPF systems from the literature are presented in Figure 1.3.

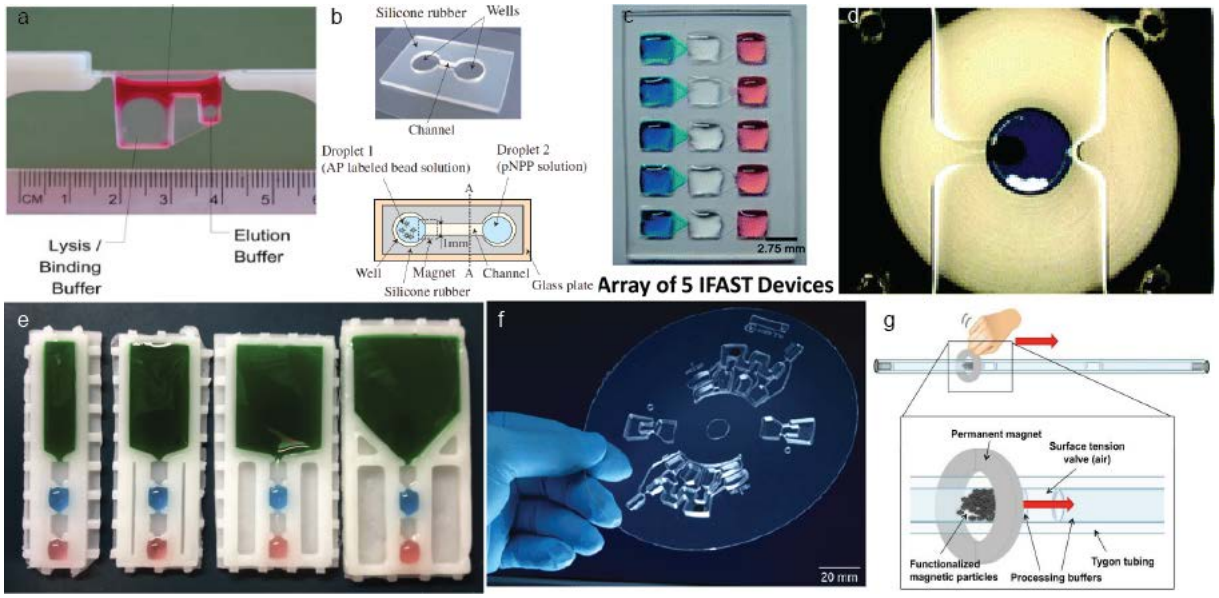

Figure 1.3 Examples of immiscible phase filtration systems in the literature. (a) injection moulded polypropylene system for wax based extraction of nucleic acids presented by Sur *et al.*[10]. (b) Parylene coated silicone-glass plate system for silicone oil based enzymatic immunoassays presented by Shikida *et al.*[14]. (c) PDMS cast on glass system for olive oil based nucleic acid extraction presented by Strotman *et al.*[15]. (d) Fluorosilane-patterned glass plate system with adhesive tape spacer for air/paraffin based extraction of nucleic acids and proteins presented by den Dulk *et al.*[12]. (e) Wax embossed system for FC-40 oil based nucleic acid extraction presented by Berry *et al.*[16]. (f) Polyolefin blow moulded adhesive bonded system for air based nucleic acid extraction presented by Strohmeier *et al.*[13]. (g) Tygon tubing based system for air based nucleic acid extraction presented by Bordelon and Adams *et al.*[17]. Figures are adapted from their quoted sources.

Not counting electrowetting-on-dielectric or digital microfluidic systems, the (to my knowledge) first presentation of a system employing IPF was the one presented by Shikida *et al.*[14,18] in 2006 (see Figure 1.3b). It consisted of a simple open PDMS on glass system that had been coated with parylene to increase the contact angle. A simple enzymatic immunoassay was performed using droplets submerged in silicone oil. Pipper *et al.*[19] also presented a droplet based system in 2007, where RNA was isolated from a throat swab sample. The system consisted of a perfluorinated glass surface, where the droplets were placed and immersed in mineral oil. Sur *et al.*[10] presented a system for nucleic acid purification in 2010 (see Figure 1.3a). It consisted of an open system that was injection moulded in polypropylene. The system distinguishes itself by being a vertical system, relying in part on gravity to assist with stabilising the interfaces. The Beebe group have had many activities within IPF, starting with an open PDMS cast on glass system seen in Figure 1.3c. Variations of the system has been used for cell isolation, nucleic acid extraction, co-immunoprecipitation, and fluorescent immunoassays[11,15,20–23]. The next device was an upright version of the previous, this time computer-numerical control (CNC) milled in PS and solvent bonded together. Cell isolation and nucleic acid extraction was

performed on this device[24,25]. The Beebe group also did a paper using a glass capillary tube, similar to the system by Bordelon and Adams *et al.* (Figure 1.3g). By capillary action, nucleic acids were extracted by first allowing the sample to enter the tube, then fixating the MBs using an external magnet, and finally allowing for an oil to displace the original sample by capillary action[26]. A variant of their first system fabricated by wax embossing has also been presented demonstrating nucleic acid extraction, where the sample was first pulled through a washing buffer (see Figure 1.3e)[16,27]. The last system shown here by the Beebe group was based on a wax covered glass slide, on which fluid droplets were placed. A sliding lid containing magnets could then be moved across the droplets, moving the beads from drop to drop. This system was applied for cell isolation, cell staining, nucleic acid extraction, immunoprecipitation, and virus particle isolation[28]. Apart from the last system, all the Beebe group systems apply oils as the immiscible phase. den Dulk *et al.* presented a system based on two glass plates kept together by a transfer adhesive spacer (see Figure 1.3d). The enclosed fluidic system was based on virtual walls generated by patterning the glass surfaces with fluorosilane. Nucleic acid extraction and protein isolation was presented using air and paraffin as the immiscible phase[12]. Strohmeier *et al.* have presented a polyolefin blow moulded disk system enclosed by a transfer adhesive sheet (see Figure 1.3f). By using centrifugal force, preloaded reagents and MBs could be mixed with a sample, and IPF was carried out by an external magnet, combined with rotary movement, using air as the immiscible phase. Nucleic acid extraction was demonstrated on the system[13]. Bordelon and Adams *et al.* presented a very simple system based on Tygon tubing, where sample and extraction reagents were loaded into the tube, separated by air plugs (see Figure 1.3g). A toroid shaped magnet was then pulled along the tube to actuate the magnetic beads. The system was used to extract nucleic acids[17].

The above research activities portrait IPF as a good example of a LoC system. Different fabrication approaches have been made use of, from the simple open PDMS system, to industrial methods like blow moulding and injection moulding. IPF has been demonstrated for a number of different applications, fitting well with its role as an alternative to the traditional MB-based SPE. It also opens up for opportunities, since the IPF system can much easier be automated or semi-automated, enabling faster, repeatable experiments. Sample preparation is a critical part of microfluidics that is still lagging behind other parts of microfluidic research, so efforts towards developing universal sample preparation devices are welcomed[6].

This PhD project has utilised the IPF approach to sample extraction to serve as a case, and aimed at developing such a device. Sample preparation provides a challenge that is directly dependent on the fabrication quality of the chip and addresses an issue that still does not have a standard solution in microfluidics.

1.4 Current challenges of LoC development for commercial use

The big microfluidic hype started sometime in the early 1990's, where the realisation that miniaturisation of conventional analysis systems could potentially follow the explosive development microelectronics had experienced[29]. This spawned the concept of the so-called μTAS or miniaturised total chemical analysis system, proposed in the seminal paper by Manz *et al.*[30]. The potential was

clear: analysis of compounds of interest in complex matrices was a growing industrial interest within several markets, such as analytical sciences and life sciences – and the theories of microfluidics dictated that better and faster analyses could be achieved, if one could successfully miniaturise sensors and laboratory analytical procedures[30].

Since then, the field of microfluidics has had a bumpy ride that was evaluated around 2010[31–33]. In particular, Holger Becker from the company microfluidic ChipShop (www.microfluidic-chipshop.com, accessed 2015-05-24) wrote a series of focus articles about commercialisation of microfluidics, which are a recommended read[32,34–44] and forms the basis of this section. The consensus was that the commercial aspects of microfluidics, or more fitting; LoC systems have followed a development that can be described using the Gartner Hype Cycle model, see Figure 1.4[45]. The model describes the life cycle of a technology by relating its public visibility (and success) to the maturity of the technology.

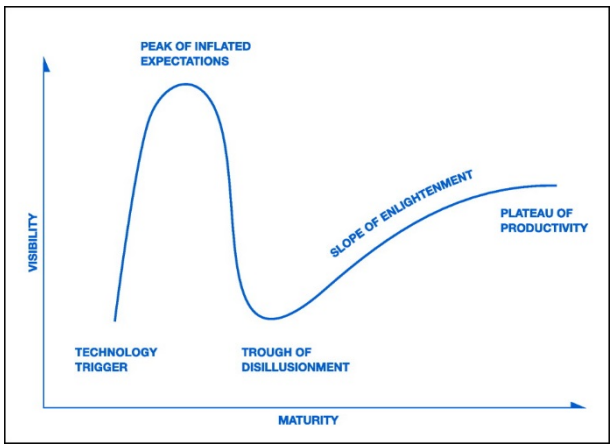

Figure 1.4 The Gartner Hype Cycle Model (www.gartner.com/technology/research/methodologies/hype-cycle.jsp, accessed 2015-05-23) explains a technology's life cycle by dividing it into five phases. It begins with a *technology trigger* that leads to a *peak of inflated expectations*, which then crumbles into a *trough of disillusionment* when there is no immediate 'killer app' to carry the technology to market. Slowly, the technology will then mature on the *slope of enlightenment* until a *plateau of productivity* is reached, either as a niche product, or leading product (figure adapted from Mukhopadhyay, R[31]).

Hopes and expectations fueled by a *technology trigger e.g.*, papers such as Manz *et al.* (although to be fair, Manz himself did speculate an immediate success[29]) formed a quest for the *killer application*; a product that in itself generates extensive revenues. This spawned an initial wave of research, public awareness and the founding of a few companies (*e.g.* Caliper, Aclara, Nanogen, Fluidigm) that attracted a lot of funding, culminating in a *peak of inflated expectations* around the year 2000. What then happened was the technology failed to deliver a killer application – the few commercial products that existed did not create sufficient revenue. Faith in microfluidics dropped and consequently its ability to attract funding, forcing the field down into the *trough of disillusionment* that could have easily killed microfluidics in a commercial sense. This did not happen. Instead, microfluidics started to steadily climb again. This was due to several factors, first of all because microfluidics is a technology that genuinely solves problems that cannot be solved otherwise[1]. Also, a maturation of the field had occurred which gave a more nuanced view of the capabilities of microfluidics, both in regard to the technology itself, but also in regard to industry[31–33,44]. This puts microfluidics on the *slope of enlightenment*, which

is where it is today. This phase is characterised by a sound understanding of the underlying physical principles, manufacturing processes that stretch into the industry, companies who can supply components for microfluidics, and a slow, but steady implementation of microfluidics in products[45]. The FluidicMEMS blog keeps a list of microfluidic companies worldwide, which has now grown to above 250 (www.fluidicmems.com, accessed 2015-05-24).

The realisation is that microfluidics is an enabling technology – a tool that can be used in products, rather than be a product by itself. This is also something experts agree on that has come out of the last 30 years of development; all the modules of microfluidics, such as pumps, valves, mixers, filters, separaters, *etc.* are now under control[39]. This does not mean that there is no killer application for lab on a chip systems – they still show a great deal of promise in many different areas[1], the issue is that the technology is still not mature enough to reach it.

One of the central challenges that microfluidics has faced – and still is facing – is the schism between the manufacturing of microfluidic devices in the academic setting, and in the industry. The reason behind this has much to do with the origins of microfluidics, especially those within microelectromechanical systems and cell biology. As Whitesides mentioned in his review, *The origins and the future of microfluidics*[1], the first microfluidic systems were based on the same fabrication methods of microelectronics *i.e.* photolithography in silicon (see Figure 1.1(left) for an example). The hope was that microfluidics largely could adapt the same fabrication techniques. However, it was quickly realised that silicon was not ideal for many of the biological applications that called for features like permeability to gases and optical transparency. Furthermore, such fabrication methods are quite expensive and requires a cleanroom.

The big breakthrough was made by Whitesides' group in the early 1990's, where they (re)discovered[46] the elastomer PDMS. Back then, they were studying self-assembled monolayers and used PDMS as a stamp, but they quickly realised that if the stamps were fused to surfaces, they produced microfluidic systems[47]. The microfluidics community welcomed PDMS fabrication for several reasons; PDMS has great material properties for working with biological samples, such as the ones mentioned above; it is elastic allowing for easy fabrication of pumps and valves, it is non-toxic, and it can be bonded without the use of adhesives, to name just a few. Soft lithography used to create PDMS systems is cheap, easy, and does not necessarily require a cleanroom. Even if a cleanroom is utilised, it is only to apply and develop the resist[48–50]. However, PDMS also had shortcomings that were largely overlooked by the community or thought to be manageable through engineering[50,51]: 1) Poor organic solvent compatibility that cause swelling of the PDMS and dissolution of PDMS into the solvent[52]. 2) Evaporation of solvent, changing its osmolality, which affected cell viability[53]. 3) Absorption of small molecules into PDMS, such as drugs or cellular signalling agents, which is critical if you are using microfluidics to analyse the same[54]. Even so, to this day PDMS is still the material of choice for the majority of all published systems[44,55].

Coming back to commercialisation, PDMS faces a big problem: It is very attractive for rapid prototyping, but elastomer casting is unfavourable for mass production, because of the need for curing

(that takes about an hour), and the need for surface activation (often done by plasma treatment) for bonding of the channel system[49,56]. This does not mean that PDMS systems cannot be commercialised, evident from the success of Fluidigm (www.fluidigm.com, accessed 2015-05-25) and Cellectricon (www.cellectricon.com, accessed 2015-05-25). However, for commercialisation within a field with the potential of microfluidics, a few good success stories are hardly convincing. Another issue is that PDMS is such an established technique *"that people are so strapped to PDMS that they are trying to make it work for applications when there are much better choices"* in the words of Steve Soper (Louisiana State University, Louisiana)[50].

What has been lacking from the start is better synchronisation between the devices manufactured in academia and devices that are suited for mass production[31,41]. You could rightfully claim that this does not apply to basic research, but in engineering, the end-goal of the research is often a product, and for that endeavour to be successful, you need to be able to compete with existing commercial solutions. To do so, one must think carefully about the materials and tools to use. Holger Becker notes in his focus article about manufacturing from 2009 that *"[…](for any conceivable microfluidic device there is in principle a fabrication method available, which can generate the device in high volumes), one of the most important stumbling blocks on the road to commercialise microfluidic devices has always been and still is the manufacturing cost."*[36]. Very briefly, what you want to take advantage of is what is known as economy-of-scale, which relates production volume to cost, and this is where elastomer casting falls short of other mass production techniques, such as hot embossing and injection moulding (see Figure 1.5).

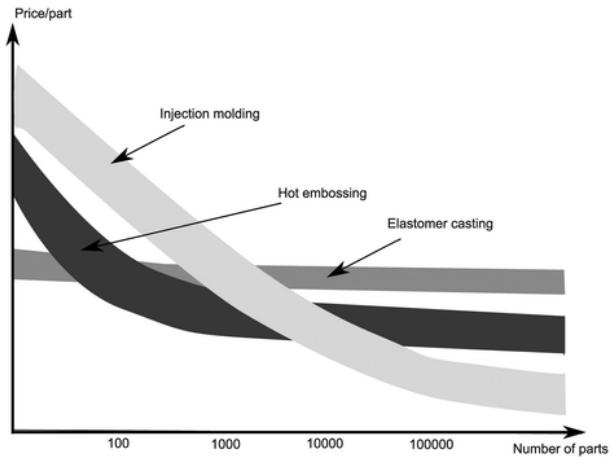

Figure 1.5 Economy-of-scale comparison for polymer replication processes. It illustrates that cost per part is reduced when scaling up production. For small-scale production, the main cost is associated with acquiring the production machinery and costs of the design and replication master, whereas for large-scale production, the costs are mainly associated with the materials cost. Figure adapted from Becker, H[36].

The key point here is the process time for elastomer casting, which does not provide economy of scale – the price of parts remain the same regardless of production number. Obviously, the price associated with acquiring an injection moulding tool is not insignificant, but other tools exist that are able to process materials, such as thermoplastics that are more suited for mass production. If more efforts are put into

making university developed devices more transferable to the industrial setting, it should spawn more commercial products[41].

One such effort is the strategic research centre PolyNano (www.polynano.org, accessed 2015-05-25), which this PhD project is also a part of.

Aim of PolyNano

The strategic research centre PolyNano aims at becoming the Danish competence centre for production-ready fabrication of polymer, nano-scale lab-on-a-chip (LoC) devices. PolyNano will provide a competitive edge for Danish biotech companies launching LoC products, by removal of the technology barrier between lab-scale proof-of-principle and high-volume low-cost production of LoCs, and further enable new research by easy access to LoC technology.

The centre will exploit a unique combination of

- technologies for polymer nanofabrication being micro-injection molding and nano imprint lithography.
- cutting edge biotech research within polymer single use LoCs for next generation sequencing of genomes, high throughput screening, point of care diagnostics, and cell-culturing.
- innovation and new product development from Danish biotech SMEs with large growth potential.

The facilities available at DTU Danchip and the Department of Micro- and Nanotechnology, Technical University of Denmark provides a range of tools that allows PolyNano to accomplish its aims. In practise, these tools also define the framework of the manufacturing processes available for use. The next sub-sections cover the elements essential for microfluidic systems and how these set demands for the development of such systems.

1.5 Process steps to consider when manufacturing a microfluidic system

There are many conceptions of what constitutes a microfluidic system, where perhaps the most comprehensive is the µTAS that incorporates all elements, going from sampling to conveying the analysis result. This section is more focused and will only describe process steps one has to go through when setting out to design and fabricate the core microfluidic parts:

- Choice of substrate material
- Part microfabrication methods
- Back-end processing
    - Bonding
    - Surface coating and integration with other components

Before going into the individual process steps it is important to state that no microfluidic systems are alike, and one should think carefully about what is required of a given system. Quantity,

chemical/mechanical/electrical/optical properties, open or closed channels, need for integration, *etc*. These factors limit the choice of material. In addition, the many fabrication technologies available should be taken into account. On one hand, it is a luxury to have so many means at your disposal, on the other, this diversity also makes it challenging to make the optimal choices. Thankfully, there are a few reviews published that compare materials and fabrication methods to assist in this effort[51,55,57–61].

Choice of substrate material

There are copious amounts of materials available to create microfluidic systems, so the challenge is really to select the material that fits your application best[55,57,59,60]. Figure 1.6 gives insight into the diversity, strengths, and weaknesses of some of the materials available, and clearly indicates that there is no perfect material. There is always a trade-off somewhere.

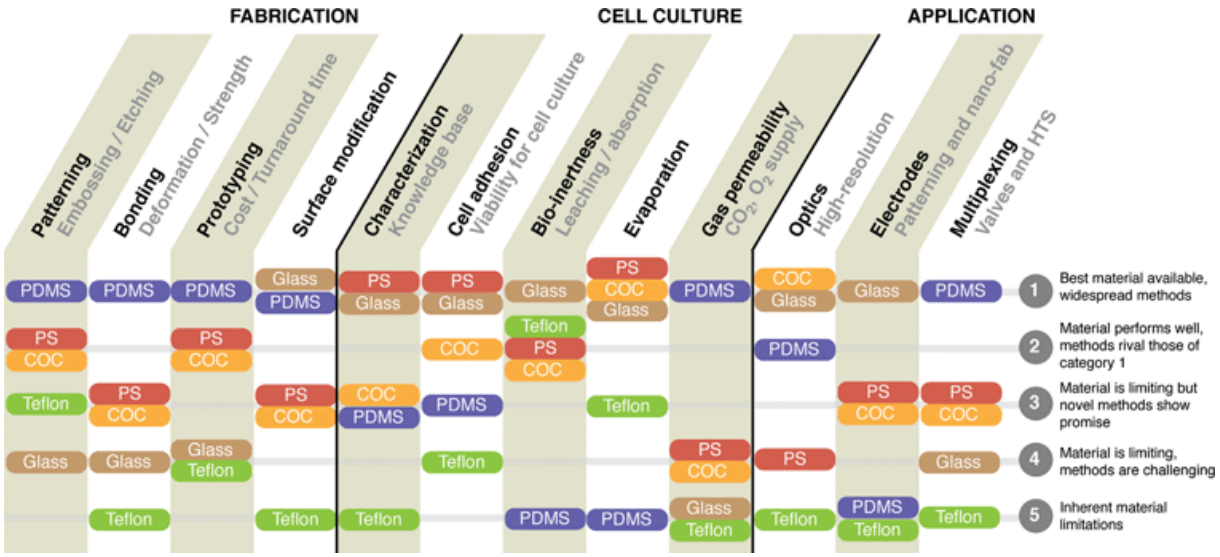

Figure 1.6 Comparison of different materials that can be used to fabricate microfluidic systems for cell-based applications. The figure shows the strengths and weaknesses of these materials for fabrication, (bio)sample compatibility, and integration. Figure adapted from Berthier, E[51].

Generally speaking there are four types of materials that can be used for microfluidic systems:

- Glass and silicon
- Polymers
    - Thermosets
    - Thermoplastics
    - Elastomers
- Metals
- Paper

For the sake of brevity, and due to the scope of this dissertation, details of metal and paper microfluidics will not be covered. Also because metals are rarely used for the chip itself, but more often for electrodes or moulds. Paper microfluidics is a relatively novel technology, so the commerciality of this method is still unclear, and most of the research has focused on simple devices that can be used in developing

countries. However, it is an interesting approach to microfluidics and a review can be found here for those inclined[62]. Also, paper microfluidics is incompatible with magnetic beads, which are an essential component of IPF systems.

Silicon and glass were the first materials applied back when microfluidics started within the field of analytical chemistry, with the groundbreaking paper by Terry *et al.* in 1979[3]. Enabled by technologies from the microelectronics industry, namely photolithography and etching, μTAS systems were able to perform sub-microlitre sample transport and manipulation steps[63]. There are a multitude of parameters to compare for silicon/glass vs. polymers, and both types have benefits and limitations. Most of these are nicely summed up in tables found here[55,57,60]. It would not be productive to go over all of them here, so a few key points will be mentioned instead.

Production complexity and cost First, silicon/glass is more expensive than polymers, as well as the manufacturing process, since it requires both photolithography (that requires a cleanroom) and wet/dry etching, which is a complicated process. Moreover, cost is increased by the fact that each device has to be etched individually, which also significantly reduces the throughput. For microelectronics this is not too big of an issue, because you can fit in a lot of chips on a single wafer. Microfluidics, however, cannot be scaled down due to rheology, and thus requires a relatively large area per chip, significantly increasing cost. On the other hand, it allows for very well defined structures of nano resolution.

Material properties Generally, silicon/glass is more restricted, since the properties of polymers can be tweaked quite a bit and are already commercially available due to the ubiquitous presence of polymers in commodity products. Glass in particular does, however, hold some advantages, such as a much higher operational temperature and excellent optical features (transparency down to the UV range and extremely low auto fluorescence)[60,63]. For *e.g.* microreactors, high temperature and chemical resistance is critical, which is something only glass (and metals) can support. Additionally, the semiconductive nature of silicon makes this material ideal for applications where microelectromechanical system components are needed[57].

Polymers are by far the most important material for fabrication of microfluidic systems, because they are easier to fabricate, scale better with mass production, and have a number of properties that are beneficial when working with biological samples. Another very important factor is the low cost of polymer chips (both material and manufacturing method), allowing for production of disposable single-use chips[64]. As stated above, polymers can be divided into three groups:

- Thermosets are defined by the need for curing, during which the polymer undergoes irreversible chemical reactions, effectively locking it in a state that cannot be reverted. Popular thermosets include the photocurable epoxy SU-8 that is more often used as resist for photolithography, or as a master for soft lithography, than for creating actual microfluidic systems.
- Thermoplastics are defined by softening substantially once they pass their glass transition temperature (T_g), allowing them to be easily moulded into arbitrary 3D shapes. Thermoplastics do not cure, which allows them to be re-shaped. Since most of the plastic parts there exists in the world are made from thermoplastics, it is of no surprise that a plethora of types exists, such

as poly(methyl methacrylate) (PMMA), polystyrene (PS), polycarbonate (PC), polyethylene (PE), polypropylene (PP), cyclic olefin copolymer (COC), Polytetrafluoroethylene (PTFE), and acrylonitrile butadiene styrene (ABS) – all with different physical/chemical properties[57].

- Elastomers are simply polymers characterised by a very low Young's modulus[58], meaning they are elastic. PDMS is the most popular elastomer for microfluidic systems for reasons mentioned above. It is liquid at room temperature making it easy to manage, but becomes a heat curable thermoset when mixed with a curing agent. Alternatives to PDMS also exist, some of which are reviewed in[58].

Given the scope of PolyNano, the focus of this project was on polymer microfluidic chips and hence the following sections will deal with fabrication methods of such systems.

Part microfabrication methods

With a given design there are basically two ways to manufacture a polymer microfluidic chip, styled *one-step* and *two-step* manufacturing processes by Waldbaur *et al.*[57]. One-step manufacturing processes cover all fabrication methods where the microfluidic chip is directly generated from the design, whether by removing or adding material (be it glass, metal, plastic, *etc.*). Examples are electric discharge machining (EDM), micromilling, laser micromachining, etching, photolithography, stereolithography, layer-to-layer manufacturing, and 3D printing. Two-step manufacturing processes are the classic replication techniques, where you first create a master (using one of the one-step manufacturing processes) and then produce the actual part from the master using embossing, casting, injection moulding, or thermoforming. Providing details on all of these processes would require too much space and is hence omitted, but detailed descriptions can be found in[55,57]. Chapter 3 covers all materials and manufacturing processes utilised in this project as well as the arguments for choosing them.

Back-end processing

Manufacturing of a microfluidic chip system consists of a collection of processes or a process chain. The number and complexity of processes needed vary greatly from design to design. Back-end processes are all process steps required to yield a functional device, not pertaining to design and fabrication of the replication master, and/or microfabrication of the chip parts themselves. Figure 1.7 shows a generic example of process chains for a range of microfluidic devices. Note that some of the elements, like master fabrication may itself be a process chain.

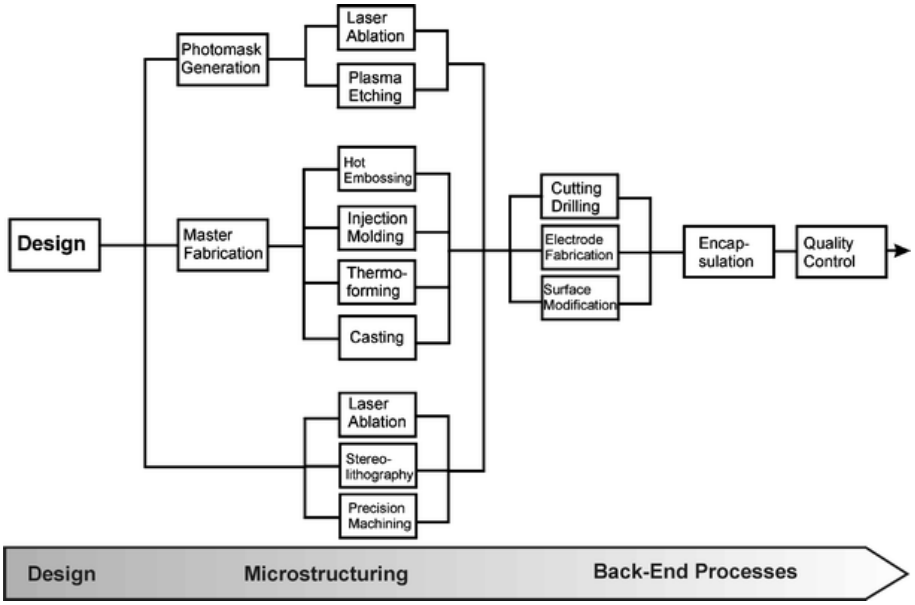

Figure 1.7 Example of a process chain for the production of a glass-based or polymer-based device. The first step is designing the device, followed by microfabrication of the replication master/actual device. The last steps are all additional modifications that need to be applied to the device, before it is ready to be used, known as back-end processing. Back-end processing also includes quality control of the device. Figure adapted from Becker, H [55].

An example of a simple system in terms of materials (only PDMS mounted to glass), yet a complex design with a lot of fluidic connections can be seen in Figure 1.8, for which the process (in brief) is as follows: First, master moulds for the two microfluidic channel systems were fabricated by spin-coating photoresist on silicon wafers, which was then developed after being exposed to light via a mask that defines the structures. Next, PDMS was cast from the moulds by pouring in the PDMS and allowing it to cure. Then, interconnect holes are punched through the PDMS to allow for integration with fluids. The two PDMS parts are then bonded together by another curing process and mounted onto glass slides by yet another curing process. After this, all the fluid connections with pumping systems have to be mounted *etc.*[65]. In this case, only the initial replication master fabrication and actual casting are processes not part of back-end processing. Chips employing *e.g.* electrochemical sensors require the addition of electrodes, and other systems might require surface coatings of the chip parts. Other common back-end processes include drilling of holes for connections, dicing in the case of silicon wafers, and bonding.

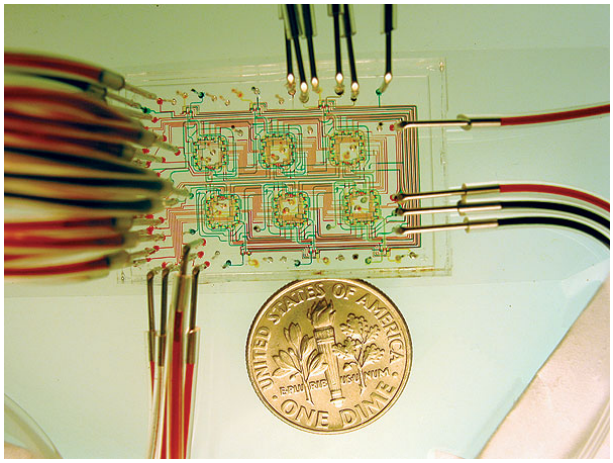

Figure 1.8 A photograph of the microchemostat presented by Stephen R. Quake's group in 2005[65].

What is important to note is that back-end processes can often be time consuming and take up the majority of the entire manufacturing process[55]. In production, back-end processes are an issue because they complicate production and significantly add to costs.

Bonding

An often critical back-end process is that of bonding. Due to the fabrication processes available, most microfluidic devices are *open* post-microfabrication, in the sense that the channels are actually trenches. Since most applications of microfluidic systems are either sensitive to contamination or require pressurised flow, a lid is fused to the chip part to form enclosed channels.

Tsao and DeVoe have made an excellent review on bonding of thermoplastic microfluidic systems in which they classify bonding into indirect and direct types[66]. Due to the scope of this dissertation, specific bonding methods for silicon/glass and metal based chips, such as anodic bonding will not be covered here, but descriptions of these methods can be found in[67]. Indirect bonding covers all fusion processes where an adhesive layer is added in-between the two parts to-be-fused, resulting in integration of the intermediate adhesive into the device. This means that the physical and chemical properties of the adhesive are imposed on the channel system, which may influence optical properties, or flow patterns. Direct bonding, on the other hand, relies on the bulk material of the parts to provide the adhesion. Both types have benefits and limitations depending on what is required of the microfluidic system. Indirect bonding methods often have poor solvent compatibility, however they are simple to utilise and are therefore widely used. Direct bonding methods offer stronger binding strength, but might require high temperatures or pressures to accomplish quality fusion. Both types of bonding may require surface cleaning or activation (*e.g.* by plasma) to create strong fusions.

Indirect fusion is the simplest approach to bonding requiring only a liquid adhesive *i.e.* glue or a lamination film *e.g.* tape.

The challenge of using glue and tape is to avoid clogging up the microchannels in the process. Various approaches have been attempted to avoid blocking of channels by *e.g.* contact printing[68], or by forming a capillary between the two parts to guide the glue[69]. Depending on the glue type, the bonding

is achieved by simple solvent evaporation, curing using UV light (*e.g.* PDMS[70]), or by elevated temperature. The chemical composition of the glue type also limits applicability depending on the chip part materials.

Pressure sensitive adhesives are a promising choice, since they are very easy to apply, however, it changes the ceiling of the channel to the material of the adhesive. Alternatively you cut out the channel system in the lamination film, which adds the thickness of the film to the height of your channels, and yields uneven sidewalls, both chemically and physically[55,64,66]. Indirect fusion processes have the benefit of being very cross-material compatible.

Direct bonding is more exotic and includes (pressure/UV assisted) thermal bonding, solvent bonding, and welding processes.

Thermal bonding is another very common bonding technique, especially for thermoplastics, because of the typical large temperature difference between the glass transition temperature and the decomposition temperature of the plastic. This allows for the polymer chains of the two parts to entangle and form tight seals, which in principle can reach the bulk strength of the material. The drawback of thermal bonding is the high pressures and temperatures that need to be exerted on the chip parts. This limits the compatibility with pre-loaded reagents for biological applications[71]. Also, care has to be taken to avoid collapse or deformation of the microchannels by precisely controlling pressure, temperature, and time during bonding[66]. Construction of special bonding masks has also been attempted to alleviate some of the pressure on the channels[72].

Solvent assisted bonding is achieved by applying a thin film of solvent to one of the parts, bringing the two parts together, and then waiting for the solvent to dry. By selecting a solvent with solubility parameters that match both parts, the interface melts and re-solidifies, fusing the two parts. The challenge of solvent bonding resembles that of thermal bonding in that care has to be taken to avoid melting of the chip structures. This is done by controlling the solvent composition, exposure time, temperature, and phase (liquid or vapour) of the solvent[55,66].

The last type of direct bonding is ultrasonic and laser welding. Ultrasonic welding (UW) requires energy directors (small protrusions, usually apex shaped) to be present on either parts to-be-fused, see Paper 1. The parts are clamped together and vibrational friction heating is locally applied to the interface between the energy director and other chip part. The result is melting and fusion of the interface. Laser welding functions by taking advantage of material properties. Chip part materials are selected so that the laser emission will be transmitted through one of the parts and absorbed close to the interface in the other. This causes the interface to melt and the parts to fuse[55,66]. The local energy deposition of the welding processes (resulting in better compatibility with biological samples) – and the relatively short processing times when comparing with the other direct bonding methods – should promote the use of these fusion processes. Peculiarly, they have been largely overlooked in the microfluidic literature[55,66,73–78].

Direct bonding methods are also cross-material compatible to some extent, depending on the T_g or solubility parameters of the materials. Fusion of fluoropolymers has been presented using thermal bonding[79].

Surface coating and integration with other components

Although a range of materials exists, it is sometimes needed to change the surface characteristics of a microfluidic chip. This might be done in order to introduce a conductive layer for implementation of electrodes, changing the wetting properties to guide fluids, add a layer to attach proteins or DNA, block the surface with a passivation agent to avoid binding of cells, *etc.*[55,66].

Depending on the microfabrication process used to generate the chip parts, most often some modification of the parts must be made to be able to connect pumps, tubing, or electrical connections to the channel system. Commonly this is done by either drilling a hole in the chip and then fixating whatever needs to be connected *e.g.* with glue, or by fixating some adapter part with connectors that readily fits with tubings *etc.*

1.6 Demands of LoC systems for commercial use

Most lab-on-a-chip systems are novel approaches to, or offer improvements to existing technological solutions, meaning they have to compete with the other solutions for a market share. Assuming the LoC system is part of a turnkey solution on par with the existing offers, you are reduced to competing on commodities. The rule of thumb for commodities is that unless you are offering a massive improvement (an order of magnitude or more), you are competing on cost[36]. This is the reality for many LoC systems for diagnostics or other types of analyses, and for that reason what is known as *design for manufacturability* becomes important[80]. There are entire books written on this topic that covers the entire life cycle of a product, but in essence, the goal is to create a manufacturing process that is as easy and low-cost as possible, without compromising product function or quality beyond tolerances. This reality has repercussions for microfluidic chip design in academia, where taking up some of the basic principles can help move the field forward.

Here follows some of the key points that are easy to take into account when developing microfluidic systems[36,80].

- *Simplicity*. Keeping the design simple and the parts few helps to achieve a short manufacturing process chain resulting in lower cost. A simple system without fragile design features also promotes reliable performance. Parts must be unambiguously assembled.
- *Standardisation*. Designing products with standard dimensions and connectors allows for easy implementation with other devices, which is beneficial during the development phase. In addition, using materials often applied by the industry allows you to draw on industry experience. Also, they are often the most processible.
- *Tolerances*. Carefully specify the needs of the microfluidic system. Processes for reducing error *e.g.* surface roughness are time consuming and expensive. Make sure that the tolerances of your prototype resemble those of a final product.

1.7 Project goals

The goal of this PhD project was:

- To explore the potential of using production-ready techniques for rapid prototyping, by;
- Creating an all-polymer device for sample extraction using MB-based SPE, taking advantage of the IPF approach.

This meant keeping the design of the system simple *i.e.* using minimum amount of parts and few assembly steps. Part of the project was also to define and characterise materials and structures for fluid handling. The overall fabrication process should aim at producing disposable proof-of-principle prototypes that are ready for pilot production. By only applying machinery that is already relevant to mass fabrication of thermoplastic parts, more commercially appealing prototypes can be manufactured. The facilities at DTU Nanotech allowed for utilising injection moulding and ultrasonic welding, two broadly applied methods of manufacturing. The result of these efforts was to demonstrate that it is possible to conduct academic research in a fashion that bridges the gap between academia and industry.

1.8 Thesis outline

This thesis describes the design, manufacturing, characterisation, and application of an injection moulded, ultrasonically welded single-use microfluidic chip system. The device was used for extraction of Methicillin-resistant *Staphylococcus aureus* (MRSA) bacteria from whole blood. Validation of the extraction processes was done by conventional (off-chip) real-time quantitative polymerase chain reaction (qPCR).

Chapter 2 provides the necessary theory to understand the physics governing microfluidics systems and in particular how the capillary microvalve works. A brief description of the forces acting on magnetic beads is also provided.

Chapter 3 gives a description of the fabrication processes and materials applied to manufacture the microfluidic chip systems, and where applicable, they have been compared to alternative processes/materials, stating the reasoning for not choosing those.

Chapter 4 describes how the prototypes have been manufactured, any experimental apparatus constructed, and covers the methodology for characterising the prototypes. The details of the sample extraction experiments are also described, as well as an overview of some of the produced prototypes.

Chapter 5 presents the most important results obtained over the course of the project. This chapter has been divided into three. First, a structural characterisation of the chip system is presented. Next, the physical performance of the IPF is reported, and finally, application of the microfluidic system to isolate MRSA is presented.

Chapter 6 concludes the thesis by evaluating the project goals and making perspective comments on the feasibility of using the developed methodology for rapid prototyping.

Chapter 2 Theory

It is not within the scope of this thesis to do a thorough analysis of the physical theory pertaining to the subjects. Instead, this chapter presents the needed theoretical knowledge to proper interpret the results.

2.1 Liquid flow in microfluidic systems

The equation of motion for an incompressible liquid flow is governed by the Navier-Stokes equation,

$$\rho[\partial_t \mathbf{v} + (\mathbf{v}\cdot\boldsymbol{\nabla})\mathbf{v}] = \sum_j \mathbf{f}_j, \tag{2.1}$$

where ρ is the density, $\mathbf{v}$ is the velocity and $\mathbf{f}_j$ are the force densities comprised of pressure, viscosity and other body forces.

In most microfluidic systems, the main body forces are pressure gradients and viscosity. Equation (2.1) then becomes

$$\rho[\partial_t \mathbf{v} + (\mathbf{v}\cdot\boldsymbol{\nabla})\mathbf{v}] = -\boldsymbol{\nabla} p + \eta\nabla^2\mathbf{v}, \tag{2.2}$$

where $-\boldsymbol{\nabla} p$ is the pressure gradient term and $\eta\nabla^2\mathbf{v}$ is the viscosity term.

To identify the dominating terms for microfluidic systems, we normalise all physical variables to characteristic scales *e.g.* L_0 for length and U_0 for velocity. Equation (2.2) thus becomes:

$$Re[\widetilde{\partial}_t \tilde{\mathbf{v}} + (\tilde{\mathbf{v}}\cdot\widetilde{\boldsymbol{\nabla}})\tilde{\mathbf{v}}] = -\widetilde{\boldsymbol{\nabla}}\tilde{p} + \widetilde{\nabla}^2\tilde{\mathbf{v}}, \tag{2.3}$$

where ~ denotes dimensionless physical variables and

$$Re \equiv \frac{\rho U_0 L_0}{\eta}, \tag{2.4}$$

where ρ is the density, U_0 is the velocity of the fluid, L_0 is the characteristic length scale, and η is the viscosity. The Reynolds number (Re) describes the ratio between inertial and viscous forces. In systems having a Reynold's number $\ll 1$, the Navier-Stokes equation is reduced to the linear Stokes equation,

$$\mathbf{0} = -\boldsymbol{\nabla} p + \eta\nabla^2\mathbf{v}. \tag{2.5}$$

In microfluidic systems where equation (2.5) is true, turbulence is absent and the flow becomes laminar. The linear Stokes equation can be solved analytically for many simple microfluidic systems, such as the Poiseuille flow that is present in most microfluidic channels and characterised by a parabolic flow profile.

2.2 Surface energy and contact angles

Consider a molecule of a liquid at the liquid-gas interface shown in Figure 2.1.

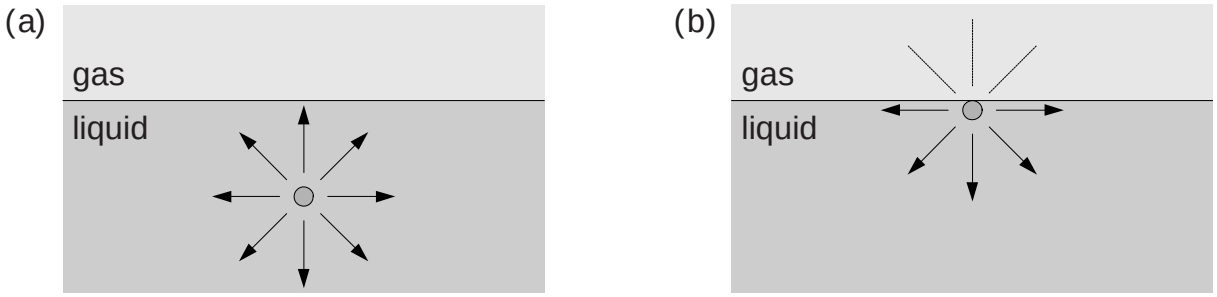

Figure 2.1 shows schematics of the interactions of a molecule inside the bulk (a) and at the interface (b) of a liquid. When the molecule is situated inside the bulk of the liquid, transient interactions with neighbouring molecules are constantly happening. At the interface, the lack of molecules to interact with puts the molecule in a higher energetic state. Figure adapted from Bruus, H[81].

In the liquid, the molecule has many transient interactions with like molecules (indicated by arrows in Figure 2.1a), whereas at the interface (Figure 2.1b), such interactions are limited due to lower accessibility to molecules in the gas. The lack of bonding partners cause the energy of the surface molecules to be higher than those of the bulk, and consequently the formed interface gives rise to what is known as surface tension (γ) defined by the Gibbs free energy (G) per area (A) for fixed pressure (p) and temperature (T):

$$\gamma \equiv \left(\frac{\partial G}{\partial A}\right)_{p,T}. \tag{2.6}$$

The system will always strive to minimise its total free energy and consequently try to minimise the area of the interface[81].

Consider a droplet lying on a surface (Figure 2.2). Due to the existence of surface tension, the droplet will shape itself according to the surface tensions associated with the different interfaces to achieve minimum energy.

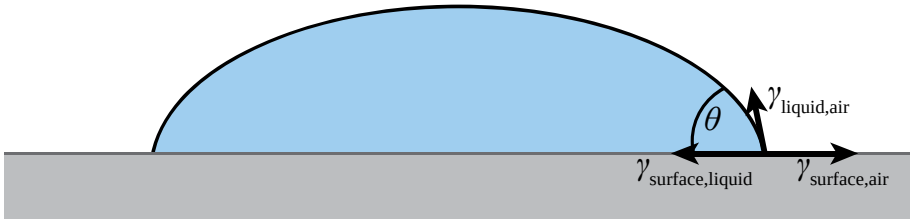

Figure 2.2 A sketch of a liquid drop lying on a smooth surface. Due to the interfacial tensions between the liquid, solid, and air ($\gamma_{\text{liquid,air}}$, $\gamma_{\text{surface,liquid}}$, and $\gamma_{\text{surface,air}}$), the droplet will minimise its energy and take up a given shape, depending on the balance of the energies. The ratio between the interfacial tensions can be described by the contact angle, θ.

Depending on the nature of the phases of the system (in this case liquid, air, and solid), the droplet will shape itself accordingly. Surface tension can also be interpreted as a force per unit length and by doing so, the Young equation can be written for the balance of forces[81,82]:

$$\gamma_{\text{surface,air}} = \gamma_{\text{surface,liquid}} + \gamma_{\text{liquid,air}} \cos\theta, \tag{2.7}$$

where $\gamma_{\text{surface,air}}$, $\gamma_{\text{surface,liquid}}$, and $\gamma_{\text{liquid,air}}$ are the surface tensions between the different phases and θ is the *contact angle* formed between the surface and liquid phase.

The contact angle is an important parameter because it can be quantified easily with a goniometer, and reveals the ratio between the surface tensions of a system. For example, systems where $\theta < 90°$ are considered hydrophilic and are expected to (partially) wet the surface of the solid. Contrary, if $\theta > 90°$ the surface is considered hydrophobic.

Equation (2.7) is based on a smooth surface, but in reality, physical and chemical imperfections are scattered across the surface of the solid, affecting θ. Depending on the nature of the imperfections, the change in contact angle can be described by the Wenzel law or Cassie-Baxter law[82].

Wenzel's law states that the contact angle on a rough surface is modified by the roughness (r) defined as the ratio between the actual area of the surface and the projected area:

$$\cos\theta_{\mathrm{W}} = r\cos\theta. \tag{2.8}$$

Note that $r \geq 1$, which implies that $|\cos\theta_{\mathrm{W}}| \geq |\cos\theta|$ *i.e.* the roughness will always increase the theoretical contact angle[82].

The Cassie-Baxter law assumes that the solid surface is heterogeneous and thus constituted by *e.g.* two materials with different surface tensions, θ_1 and θ_2, where f_1 and f_2 correspond to the fractions of the surface they cover, respectively:

$$\cos\theta_{\mathrm{C}} = f_1\cos\theta_1 + f_2\cos\theta_2, \tag{2.9}$$

It is important to keep in mind the effect of roughness and chemical impurities on surface tension, when developing microfluidic devices, since they will likely carry both[82].

2.3 Capillary microvalves and burst pressure

The IPF approach relies on capillary microvalves to pin the aqueous liquids and form stable interfaces with the immiscible phases. Capillary microvalves rely on the capillary forces dominant in microfluidics systems, which will now be briefly introduced.

An interface between two fluids with a non-zero surface tension will curve if a pressure difference exists across the interface. This pressure difference is termed the Laplace pressure and can be described by the Young-Laplace equation:

$$\Delta P = \gamma\left(\frac{1}{R_1} + \frac{1}{R_2}\right), \tag{2.10}$$

where γ is the surface tension between the two fluids and R_1 and R_2 are the radii of curvature of the interface.

In a rectangular microfluidic channel with width, w, and height, h, where a liquid-air interface exists, equation (2.10) can be re-written as done by Cho *et al.*[83]:

$$\Delta p = -\gamma\left(\frac{2\cos\theta_{\mathrm{wall}}}{w} + \frac{\cos\theta_{\mathrm{floor/ceiling}}}{h}\right), \tag{2.11}$$

where θ_{wall} and $\theta_{\text{floor/ceiling}}$ are the contact angles between the liquid and side-walls and floor or ceiling of the channel, respectively. If $\Delta p > 0$, the fluid will spontaneously propagate through the channel.

A geometric capillary microvalve consists of an abrupt expansion of a microfluidic channel with expansion angle (α), see Figure 2.3. From geometric considerations, it is evident that when the interface reaches the edge of the expanded region, the interfacial contact angle to the expanded region (ϕ) is smaller than the expanded region advancing contact angle (θ) and the interface is thus pinned as long as $\phi \leq \theta + \alpha$[Paper 1].

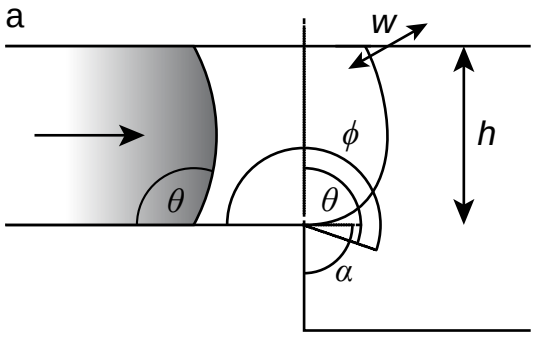

Figure 2.3 Sketch of a geometric capillary microvalve, where pinning is achieved through a sudden change in geometry. θ, α, and ϕ denote the liquid contact angle with air, expansion angle, and effective contact angle, respectively. w and h denote width and height of the channel. Figure adapted from [Paper 1].

We can now write the Young-Laplace equation for the interface at the geometric expansion (the capillary microvalve), and determine the minimum pressure drop required to advance the interface beyond the expansion with regard to ϕ, which yields:

$$p_{\text{burst}} = -\gamma\left(\frac{2\cos\theta}{w} + \frac{\cos(\min\{\theta+\alpha; 180°\})}{h} + \frac{\cos\theta}{h}\right), \qquad (2.12)$$

where p_{burst} is the bursting pressure of the microvalve.

p_{burst} is an important factor when designing capillary microvalves, since it can be used to predict if a given liquid will be retained or not. p_{burst} can also be estimated by means of finite element analysis, as we shall see later.

2.4 Forces affecting magnetic bead clusters in IPF systems

Consider a system where a bead cluster is situated on the floor of a microfluidic channel with a capillary microvalve, such as the one shown in Figure 2.4.

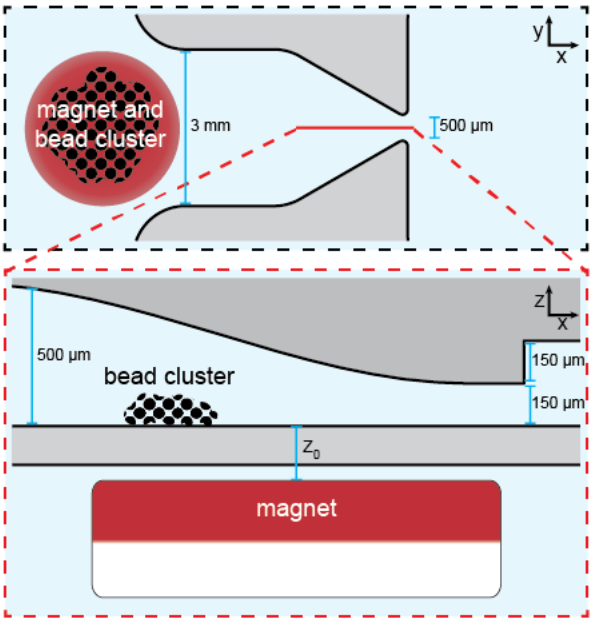

Figure 2.4 A schematic of a microfluidic channel system with a capillary microvalve. A bead cluster is situated in the channel on top of an external permanent magnet, placed z_0 distance below the bead cluster.

By moving the magnet in the x-direction with a constant low velocity (< 1mm/s), the bead cluster can be assumed to be in quasi-static equilibrium, and the equation of motion of the bead cluster thus becomes

$$F_{\text{magnetic},x} + F_{\text{capillary}} + F_{\text{friction}} = 0, \tag{2.13}$$

where $F_{\text{magnetic},x}$ is the x-component of the force exerted by the magnet on the bead cluster, $F_{\text{capillary}}$ is the interfacial capillary force the beads have to overcome to pass through the capillary microvalve, and F_{friction} are the frictional forces experienced by the bead cluster[84]. The magnitude of the capillary force ($F_{\text{capillary}}$) is derived from the Young-Laplace relation (2.11) for a rectangular capillary microvalve[83], rewritten as forces;

$$F_{\text{capillary}} = -2\gamma_{\text{liquid,IP}}\left(h + w\cos\theta_{\text{liquid,IP}}\right), \tag{2.14}$$

where $\gamma_{\text{liquid,IP}}$ is the interfacial tension of the liquid-immiscible phase interface, h and w are the height and width of the capillary microvalve, respectively, and $\theta_{\text{liquid,IP}}$ is the contact angle of the liquid.

The frictional forces can be divided into two; F_{surf} that is the frictional force between the bead cluster and the chip surface, and F_{drag} that is the drag force on the bead cluster due to movement through liquid:

$$F_{\text{friction}} = F_{\text{surface}} + F_{\text{drag}}. \tag{2.15}$$

If we treat the bead cluster as a solid material and note that the z-component of the magnetic force is balanced out by the normal force (F_{N}) *i.e.* $F_{\mathrm{magnet},z} + F_{\mathrm{N}} = 0$, F_{surface} can be described by

$$F_{\mathrm{surf}} = \mu_{\mathrm{k}} F_{\mathrm{N}} = -\mu_{\mathrm{k}} F_{\mathrm{magnet},z}, \tag{2.16}$$

where μ_{k} is the kinetic friction coefficient. F_{drag} cannot be described readily because the dimensions of the microfluidic channel is not uniform and the shape of the bead cluster changes during its path through the capillary microvalve.

In general, an arbitrary volume of magnetisable material (V_{particle}) in vicinity of a magnet will experience a force, $\mathbf{F}_{\mathrm{magnetic}}$ given by

$$\mathbf{F}_{\mathrm{magnetic}} = \mu_0 \int_{V_{\mathrm{particle}}} (\mathbf{M} \cdot \boldsymbol{\nabla})\mathbf{H} \mathrm{d}V, \tag{2.17}$$

where μ_0 is the permeability of free space, $\mathbf{H}$ is the magnetic field generated by the magnet, and $\mathbf{M}$ is the magnetisation of the particle.

In the system shown in Figure 2.4, $\mathbf{F}_{\mathrm{magnetic}}$ can be approximated by letting the finite volume of the bead cluster be defined as $V_{\text{bead cluster}} = m_{\text{bead cluster}}/\rho_{\text{bead cluster}}$, where m and ρ are the mass and density of the bead cluster, respectively. Assuming a uniform bead cluster, it can be divided into voxels. By calculating $\mathbf{H}$ for each discrete voxel and assuming the $\mathbf{H}$-field is uniform within a voxel, the magnetisation of the bead voxel can be described by $\mathbf{M} = \chi(H)\mathbf{H}$, where $\chi(H)$ is the field-dependent magnetic susceptibility of the bead cluster. Taking all this together yields:

$$\mathbf{F}_{\mathrm{magnetic}} \approx \frac{1}{2}\mu_0 \frac{m_{\text{bead cluster}}}{\rho_{\text{bead cluster}} N_{\mathrm{voxel}}} \sum_{i=1}^{N_{xy}} \left(\sum_{j=1}^{N_z} \chi_{\text{bead cluster}}\left(H_{i,j}\right) \nabla \mathrm{H}_{i,j}^2 \right), \tag{2.18}$$

where $\mathbf{F}_{\mathrm{magnetic}}$ is approximated by summing up each voxel that constitute the bead cluster, as defined by $N_{\mathrm{voxel}} = N_{xy} \times N_z$, where N_{xy} defines a cross-sectional area of the bead cluster and N_z defines each layer. $H_{i,j}$ and $\nabla \mathrm{H}_{i,j}^2$ are the magnetic fields evaluated at the centre of a voxel with index *i,j*. $H_{i,j}$ and $\nabla \mathrm{H}_{i,j}^2$ were estimated by finite element analysis of the magnetic field, as described in chapter 4. Relating back to eq. ((2.13) and eq. ((2.16), only the x and z components are of interest.

Equation ((2.18) is used in the project to derive the force profile of a magnetic bead cluster during extraction, based on the same overall approach employed by den Dulk *et al.*[12].

Chapter 3 Chip manufacturing methods

A central aspect of this dissertation lies within efficient manufacturing of commercially appealing, rapid prototyped chips with mass production in mind. This goes hand in hand with the central goal of the PolyNano project, which is why this chapter is dedicated to the methods chosen for chip manufacturing.

An important thing to note is the lack of use of cleanroom techniques, which deviates from the rest of PolyNano. The reason for this is the nature of the lab-on-a-chip systems devised *i.e.* mobile solid phase extraction of nucleic acids facilitated by immiscible phase filtration using magnetic beads. This technique relies critically on actuation of relatively large clusters of magnetic beads, which take up a certain volume, making it impossible to apply microfluidic channel systems with dimensions < 100 µm, since the beads simply get stuck. In principle such large channel systems could be fabricated in the cleanroom[85], however, other techniques for producing lab-on-a-chip systems are favourable as will become apparent in the following sections.

3.1 Chip design using CAD software

Regardless of the manufacturing method chosen, creating a design is always the first step. Computer-aided design (CAD) was utilised in this project, because it is an efficient method that allows for easy modification of designs – an essential part of rapid prototyping. CAD drawings are widely supported by production software, meaning only a single master file is needed, from which sketches or models can be exported.

3.2 Choice of materials

The main goal of PolyNano is to lower the technology barrier between laboratory developed chip systems and production-ready chip systems. For this reason, the production material must be commercially appealing. Following the discussion in chapter 1, glass and silicon were discarded because they are more difficult to manufacture, more expensive, and there was no need for the mechanical, electrical, or optical properties. Thermosets and elastomers could be applied, but the need for curing each chip limits the throughput, and neither thermosets nor elastomers play well with the large scale production apparatus. Furthermore, PDMS is non-disposable[50]. We are then left with thermoplastics that is already an industrial favourite and well suited for high-volume, low-cost production.

There is an immense, confusing amount of thermoplastics commercially available and finding the perfect grade takes the expertise of a materials specialist that was not present in this project. Rather than exploring in-depth a variety of polymer distributor catalogues, a handful of the most referred polymers in recent reviews was selected for choosing: PMMA, PC, PS, PE, COC, PP and PTFE[55,57]. Limiting the pool of materials also makes sense from an institutional viewpoint, allowing for build-up of

competences and experience for using various types of polymers for different applications. This also means that more optimal choices of materials, other than the one chosen here probably exist that could improve on the system.

The fabrication processes applied in this project were injection moulding, ultrasonic welding, and laser micromachining for reasons stated below. The thermoplastic selected thus had to be compatible with these methods as well as with the application of sample extraction.

In principle, any of the polymers presented in Table 3.1 could be adapted for this project. Usually different thermoplastics are selected for their respective solvent compatibility, optical properties, water absorption, T_g, heat deflection temperature, *etc.*[55,59,64,66], but neither of those are particularly important for the applications in this project, with the exception of resistance to hydrocarbon based solvents (oils for the immiscible phase), where all of these polymers fare poorly (not counting PTFE). Table 3.1 shows a few parameters that influence the performance or fabrication of the chip system.

Table 3.1 Various parameters of the thermoplastics considered for fabrication in this project. Attractive properties have been highlighted in green. [a]Average advancing contact angle measured in the laboratory. [b]Data from www.accudynetest.com/polytable_03.html. Contact angles are given as the mean of all equilibrium and advancing contact angles of the database.

Polymer	Price	Crystallinity	Contact angle
COC	Low	Amorphous	96°[a]
PC	Low	Amorphous	82°[b]
PE	Low	Semi crystalline/Amorphous	96°[b]
PMMA	Low	Amorphous	70°[b]
PP	Low	Semi crystalline/Amorphous	102°[b]
PS	Low	Semi crystalline/Amorphous	87°[b]
PTFE	High	Semi crystalline/Amorphous	109°[b]

For the capillary microvalve to be effective, a high contact angle is preferred, since this results in a higher burst pressure, see equation (2.12)[83]. The crystallinity is not a decisive factor, but semi-crystalline materials are harder to ultrasonically weld than amorphous ones[86]. Price should ideally be kept low for commercial aspects. Of the thermoplastics presented, COC is the most appealing, followed by PE, PP, and PTFE. PTFE is environmentally hazardous and not considered on that account. PP and PE are good candidates and could replace COC. A few experiments with PP have also been conducted, but the grade available at DTU Danchip is almost opaque and thus difficult to experiment on. Note that the contact angles presented in Table 3.1 are representative values and the contact angle of any thermoplastic will vary from grade to grade and depending on the characteristics of the surface.

COC is a newer type polymer that is used increasingly due to its low water absorption (<0.01%), great optical properties (high optical transparency from 300-1200 nm, refractive index of 1.53, and low birefringence), and good solvent resistance. The many grades of COC also allow for a very customisable T_g[87]. COC has a low water vapour permeability (important in *e.g.* packaging), is able to be sterilised and is ISO 10993 standardised (www.iso.org/iso/catalogue_detail.htm?csnumber=44908, accessed

2015-06-11), meaning it is approved for application in the pharma and diagnostics sector. The low hygroscopicity and amorphous character is ideal for ultrasonic welding[86]. COC is a disposable polymer that shows good biocompatibility that is essential for medical and diagnostic disposable LoCs (TOPAS COC product overview, www.topas.com/sites/default/files/files/TOPAS_Brochure_E_2014_06(1).pdf, accessed 2015-06-21).

3.3 Generating moulds for thermoplastic chip fabrication via micromilling

As will be further discussed in chapter 4, the injection moulding setup utilised in this project is based on a mould insert that is fitted in a macro mould[88]. For that reason, the task of creating new designs is greatly simplified, since the overall shape and dimension of the microfluidic chip is pre-defined and only the microfluidic channel lay-out needs to be defined in a $\varnothing = 85$ mm aluminium disc (the mould insert). Using the same macro mould also promotes its use for rapid prototyping, because investment in new moulds is not required[89].

A variety of processes for fabricating moulds for injection moulding exist, reviewed by Giboz *et al.*[90]. The different approaches have their benefits and limitations, depending on the tolerances, aspect ratio, and typical size of the structures in the mould[90]. In this project, the smallest features of the moulds are in the range of 50 µm with large aspect ratios, and for that reason the most applicable manufacturing technologies are EDM and micromilling. Die-sink EDM is the most applied technology of the two in the industry, because construction of the masters by vapour deposition allows for atomic resolution[91]. One drawback of EDM is that the EDM tool is itself a master, which is not ideal for rapid prototyping, since this adds another process step. There are alternate approaches such as µEDM[92], but µEDM is not superior to micromilling, except for the ability to machine very tough materials, not needed in this project. In addition, µEDM is a very slow process compared to *e.g.* micromilling, where a mould insert can be fabricated within a few hours, depending on the tolerance requirements.

Micromilling has received attention in a recent review by Guckenberger *et al.*[61]. The review focuses on micromilling as a tool for direct fabrication of microfluidic systems, but the benefits and limitations discussed also apply when using micromilling to fabricate mould inserts. The primary benefits are that the vast variety of tools allow for creation of full 3D designs over just a few hours. On the down side, micromilling produces more roughness compared to other processes and corners will always carry the internal radius of curvature of the tools used. For the designs used in this project, these characteristics are suitable. When rapid prototyping, the mould insert is only required to last for a few hundred to a few thousand replication cycles. Thus, the mould insert can be fabricated in aluminium instead of more durable materials like steel. In this project, aluminium grade 2017 is used as substrate. The 2017 alloy combines outstanding machinability with high strength, an ideal combination for micromilling and injection moulding (www.aircraftspruce.com/catalog/mepages/aluminfo.php, accessed 2015-06-21).

3.4 Producing chips with injection moulding

Replication manufacturing far outperforms one-step manufacturing methods when talking high-volume production. Having decided on thermoplastics, the choice for chip production is thus limited to; injection

moulding, thermoforming, and hot embossing. The methods differ in different aspects, such as equipment price, through-put, start material requirements, *etc.*[55,61]. A key advantage to injection moulding is the ability to manufacture in full 3D, allowing to introduce fluid interconnects directly[93], which are otherwise introduced by back-end processing. Still, from a rapid prototyping point of view, all of these fabrication processes fulfil the main criteria of using a mould and thermoplastics that are the important components for mass production. At DTU Nanotech there is an injection moulding machine available, which is very fortunate, since this allows for direct-to-pilot scale production.

A thorough description of injection moulding will not be presented here (see *e.g.* [94] for that), but a few terms and technical details will be covered to further understanding and discussion. Figure 3.1 shows a schematic of an injection moulding machine that can be used as reference.

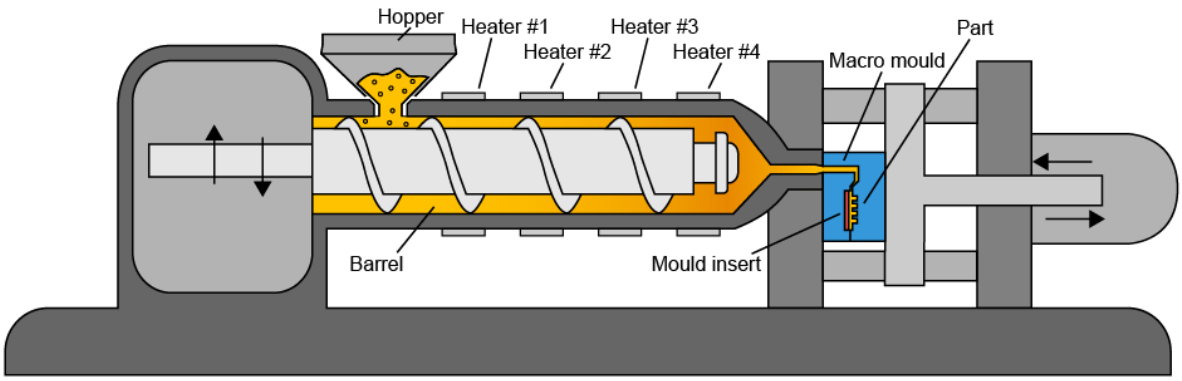

Figure 3.1 Schematic of the injection moulding machine showing the positions of the mould and other components. Figure adapted from Brendan Rockey, University of Alberta Industrial Design, for Injection Molding Wikipedia article.

An injection moulding cycle consists of five phases. After the mould tool is closed it is *filled* with *melt* (molten polymer in the barrel) by injecting it under high pressure. The pressure is held for a short period of time to *pack i.e.* compress the polymer in the mould in order to ensure complete filling. The pressure is then reduced to a *holding* pressure, while the polymer cools down to compensate for polymer shrinkage. Once the *gate* (the point of entry of the melt into the cavity of the mould) has solidified, the pressure is further dropped, since polymer can no longer flow out of the mould and the part is *cooled* until it is solid enough to be *demoulded*. The mould then opens and the part is ejected[94]. Every one of these phases are influenced by a number of parameters, such as mould filling pattern, pressure distribution, thermal mass of mould, *etc.*, and the mould is typically designed specifically to take all these into account. Injection moulding can be run as two types of processes. The variotherm process and the isotherm (classical) process, see Figure 3.2.

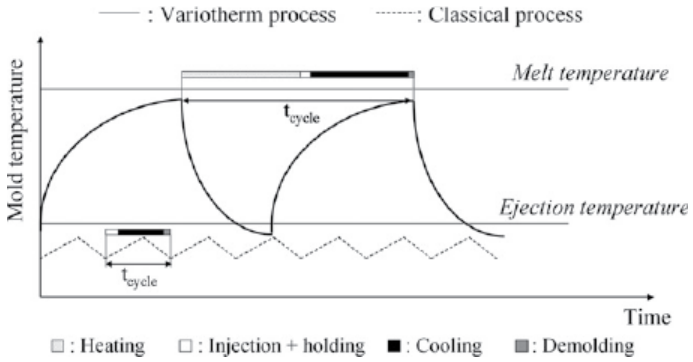

Figure 3.2 A variotherm and classical (isotherm) moulding cycle. The cycle time of variotherm processes are longer than isotherm processes, primarily due to the active heating and cooling of the mould. Figure adapted from Giboz, J[90].

As the name implies, the difference between the two processes is that the isotherm process is kept at a fixed temperature (slight heating is unavoidable during melt introduction), whereas in variotherm, the mould is actively heated and cooled. The variotherm process allows for easier filling of tiny cavities and reduces the residual stress of the moulded parts due to a slower cooling process[90]. On the other hand, variotherm processes are much more time consuming, due to the entire mould has to be heated and cooled. For high-volume production, this is unfavourable. In this project the chip structures are large enough to allow for isothermal production.

3.5 Bonding by ultrasonic welding

Of the bonding methods presented in section 1.5 the most appealing are; transfer adhesives, solvent bonding, and ultrasonic welding, because they provide the fastest back-end processes that are compatible with mass production. Transfer adhesives were incompatible with the capillary microvalves, as they became unstable. Solvent bonding takes up to half an hour for the solvent to evaporate[95], encouraging the use of UW where the fusion happens in milliseconds. Furthermore, UW is an interesting research topic, as it is the most applied fusion process for thermoplastic parts in the industry, yet mostly overlooked in microfluidics.

Ultrasonic welding is not a common method for microfluidics and will thus be explained in some detail. Figure 3.3a shows the schematics of a typical 20 kHz table top press system.

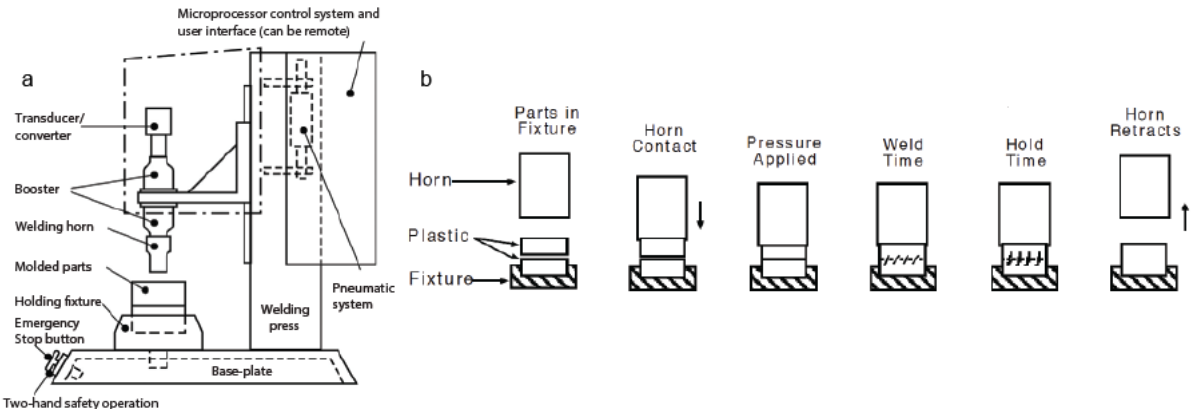

Figure 3.3 (a) Schematics of an ultrasonic welding machine. (b) Steps involved in ultrasonic welding. Briefly, the sonotrode(horn) is pressed onto the plastic parts and high frequency mechanical vibrations are applied. The sonotrode then retracts and the welded parts are removed. Figures adapted from Troughton, MJ[86] and Dukane Corporation[96].

UW functions by producing high frequency, low amplitude mechanical vibrations that it exerts on the parts to-be-fused via an acoustic metal instrument called a sonotrode. The parts are clamped between the sonotrode and a fixture, ensuring a good transfer of energy into the parts. The interface between the parts is heated up by the oscillating sonotrode, causing them to melt together. Figure 3.3b shows the steps involved in fusing two parts using UW. Parts are placed in the fixture under the sonotrode and the welding machine is engaged, moving the sonotrode down onto the parts and applying pressure. The machine then fires a burst of vibrational energy, followed by a short holding time. Finally, the sonotrode retracts allowing for removal of the now fused part. Going from power outlet to part, the core components of an ultrasonic welding machine are:

- A *generator* (not shown in figure), capable of turning the standard 50/60 Hz electrical supply frequency into a kHz range frequency. UW machines are typically in the 15-70 kHz range. The frequency chosen is based on application and practicalities. The lower the frequency, the more power is available, but the machines also grow very noisy and expensive. Two of the most common machines; are the 20 kHz type shown in Figure 3.3 that is good for welding smaller parts, and the 40 kHz type that is usually a hand-held device used for spot welding, staking objects, or other delicate parts[97].
- An electromechanical *transducer*. The transducer is the heart of the ultrasonic welding machine. It consists of a stack of piezoelectric ceramic discs bolted together between two metal blocks. In-between each disc are thin metal sheets that functions as electrodes. The discs expand and contract in response to the sinusoidal signal and depending on the frequency of the input, the mechanical vibrations vary in amplitude (*e.g.* 20 µm for 20 kHz and 9 µm for 40 kHz)[86].
- A *booster*. The amount of energy needed to achieve a good weld is material dependent, but most often the amplitudes produced by the transducer are insufficient to provide melting. Typical values for different thermoplastics can be found in[96]. The booster is an acoustic tool that amplifies the amplitudes of the incoming vibrations by a gain factor.
- A welding horn/*sonotrode*. The primary function of the sonotrode is to transfer the mechanical vibrations to the workpiece, but being an acoustic tool it also has a certain gain. The sonotrode

is shaped to fit the parts that need fusing, and oscillates in the longitudinal direction following the sinusoidal wave. Thus, the amplitude is equal to the peak-to-peak vertical movement of the lower plane of the sonotrode.

- A *fixture*. The fixture provides two basic elements. First, it serves to align the parts together and hold them stationary, allowing for efficient energy transfer from sonotrode to part. Second, the fixture supports the parts to make sure that uniform pressure is exerted on the parts while welding is taking place. See Figure 4.3 for an example of a fixture.
- A pneumatic actuator or *press*. The press is used to provide force on the workpiece, by pressing the transducer-booster-sonotrode assembly onto the parts. It is important that the sonotrode is kept in close contact with the workpiece, so the vibrational energy is transferred directly into the parts and does not dissipate at the sonotrode-part interface.

Ultrasonic welding is a fusion process facilitated by heat generation in the two parts to-be-fused. The exact mechanism behind the heat generation is not known, but the current view is that it should be regarded as a topochemical reaction. Recently, S.S. Volkov has published an analysis that suggests the heating stems from hysteresis during cyclic deformation[98]. The energy, E, deposited during ultrasonic welding is given by

$$E = P_{\text{mech}}\, t, \tag{3.1}$$

where P_{mech} is mechanical power and t is time. It should be noted that this relation only applies in practice when t is short, as heat dissipates quickly from the weld area[97].

By definition[97],

$$P_{\text{mech}} = F\, V_{\text{vibrational}} \cos \phi_{\text{phase}}, \tag{3.2}$$

where F is the force applied to the parts by the pneumatic press and vibrations, $V_{\text{vibrational}}$ is the vibrational velocity, and ϕ_{phase} is the phase angle between force and velocity. Mechanical impedance (Z) relates to $V_{\text{vibrational}}$ by $F/Z = V_{\text{vibrational}}$ and $\cos \phi_{\text{phase}} = R_{\text{visc}}/Z$, where R_{visc} is the viscous resistance of the parts. With this we arrive at

$$P_{\text{mech}} = R_{\text{visc}}\, V_{\text{vibrational}}^2. \tag{3.3}$$

Knowing that

$$V_{\text{vibrational}} = \omega\, D, \tag{3.4}$$

where ω is the vibrational frequency and D is the displacement of the sonotrode *i.e.* the vibrational amplitude, we see that the power delivered to the part is proportional to the viscous resistance of the parts and the amplitude squared. Thus, when operating the ultrasonic welder it is important to keep in mind that changing the weld time and pressure has a proportional effect on the energy deposited, whereas changing the amplitude has a square effect on the power and energy. By tuning the power, but keeping a constant energy, it is possible to vary the local polymer peak temperature.

Perhaps the greatest limitation (and strength) of UW is the need to include special joints in order to localise the vibrations of the sonotrode to the areas where welding is required. By including *energy directors* on one of the parts to-be-fused, the stress induced by the vibrations are focused, causing rapid heating and melting of the energy director, resulting in a very fast fusion process[97]. The energy director can take up many forms, but the simplest design is a simple apex shaped protrusion, see Figure 5.4 for examples. The parameters of the machine are set to provide enough energy to just completely melt the energy director. The benefit of energy directors lie with the fact that these are the only places where the welding takes place, so the rest of the parts are unaffected. This opens up for opportunities like pre-loading of reagents[71], that would otherwise get damaged by pressures, chemicals, or high temperatures used in other bonding methods.

UW is influenced by a number of parameters beyond the ones already mentioned, most importantly the morphology of the thermoplastic. Figure 3.4, illustrates how semi-crystalline thermoplastics are much harder to weld than amorphous ones. Amorphous polymers are characteristic in having the glass transition state, at which point the polymer chains of the material are able to move about, becoming more and more mobile as the temperature rises. Such properties are ideal for UW, since it renders a broad range of temperatures where the welding can be conducted.

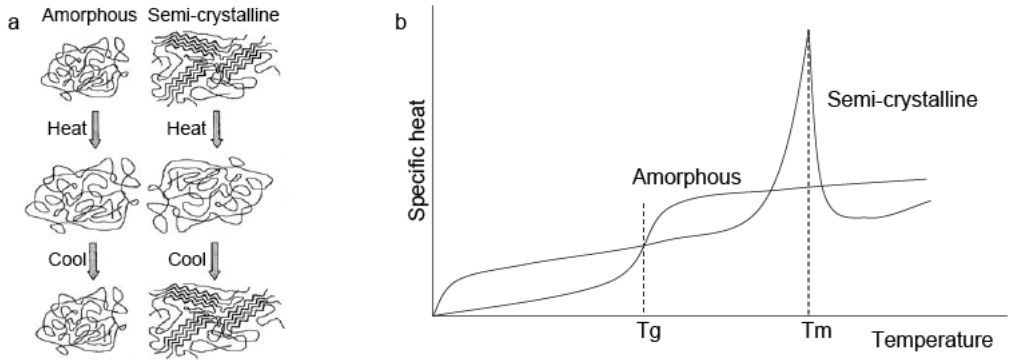

Figure 3.4 (a) Schematics of the morphology of amorphous and semi-crystalline polymers. Amorphous polymers does not change their overall structure when heated and cooled, whereas semi-crystalline polymers loose and regain their structure if heated and cooled, respectively. (b) Specific heat of amorphous and semi-crystalline thermoplastics. Amorphous polymers show a gradual transition from solid to liquid form marked by the glass transition temperature (T_g). Semi-crystalline polymers requires more energy to melt and quickly reforms, because of the stability the crystalline structure induces, evident by the sharp peak at which the polymer melts (T_m). Figures adapted from Malloy, RA[94] and Troughton, MJ[86], respectively.

Semi-crystalline polymers, on the other hand, have relatively defined melting temperatures and require much more heat to melt. The crystalline structure acts like a spring that absorbs the vibrational energy before it can be transmitted to the joint interface, and once melted, the semi-crystalline polymer quickly re-solidifies due to the structural elements. Furthermore, fillers, additives, mould release agents, plastic grade, and moisture affect the welding[86]. COC is an amorphous polymer with very low hygroscopicity (< 0.01%) and no fillers[87].

UW allows for welding of large-aspect ratio structures, since the welding occurs locally and it potentially provides alignment via the energy directors, depending on the design. Be aware of *diaphragming*, when bonding large chambers. Diaphragming is the result of the sheet cracking due to resonance vibration.

This problem can be solved by changing the vibrational amplitude. Depending on the design of the energy director and success of the welding process, there are two unfavourable outcomes of a welding, as can be seen in Figure 3.5.

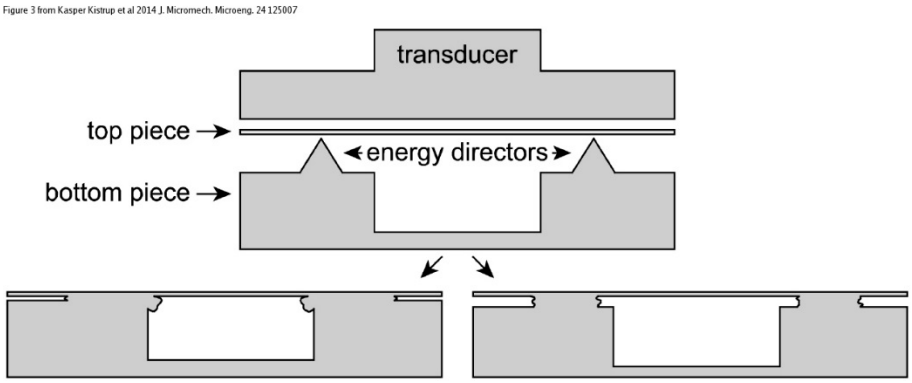

Figure 3.5 Cross-sectional sketch of a microfluidic channel with energy directors on each side, being welded to a sheet. Two cases can be the outcome of the welding. Either flash is generated *i.e.* polymer flowing into the channel, or the welding is incomplete, leaving a tiny gap at the top of the channel. In either case, the welding results in an added height. Figure adapted from Paper 1.

Too much energy will cause polymer to flow into the channels. This phenomena is known as *flash*. Alternately, too little energy will result in incomplete melt, leaving a small gap, changing the dimension of the channel. In both cases, ultrasonic welding will result in added height to the channel for this type of joint design.

A note on terminology: In principle, a butt joint refers to the simplest type of joint used in ultrasonic welding *i.e.* matching raised plateaus of the two parts-to-be-fused. As explained above, all butts are fitted with an energy director, to optimise the weld. In this project, the simplest joint applied is an energy director running around the outer boundary of the channel system on the chip part, which is welded to a sheet part. Here, this is referred to as a *butt joint*, meaning the entire surface of the chip/sheet is the butt.

Chapter 4 Experimental methods

This chapter contains detailed descriptions of all experimental work, which expands on the information already given in the published material as well as covering all other relevant experiments.

4.1 Chip fabrication

All chips consist of two parts: (1) A *chip part* featuring the majority of the structures to be used in a given design, such as the microfluidic channel network and chip-to-world connectivity. (2) A *sheet part* consisting of either an extruded thin polymer sheet or a thin injection moulded part to be fused to the chip part. The energy directors needed to fuse the two parts by ultrasonic welding can be present on either of the parts.

4.1.1 Chip designs

During the project a multitude of chip systems have been produced. This is a principal part of rapid prototyping, but can also give rise to confusion, since more versions of the same general design will exist and some experiments will be conducted on one version and some experiments on another version. Therefore section 4.1.1.2 contains a table for each design that is noteworthy containing its specifications.

All chip designs were drawn in Autodesk Inventor 2014 (www.autodesk.com, accessed 20-05-2015), keeping in mind that the chips are injection moulded, so what is actually drawn is the mould inserts featuring the inverse structures of the final chip.

4.1.1.1 Mould descriptions

Three standard moulds with room for mould inserts are available to use with the injection moulding machine at DTU Danchip: (1) A mould that produces a (75 × 25) mm microscope slide part, where one face of the slide can be altered by a mould insert. (2) A mould producing a ⌀50 mm, max. 3.35 mm thick disc shaped part, where one face of the disc can be altered by a mould insert. (3) A mould identical to (2), except it is fitted with 12 Luer-Slip connections on the opposite face of the mould insert. Moulds two and three have been used in this project and fitted with custom mould inserts. Figure 4.1 shows a detailed schematic of the dimensions of the moulded part.

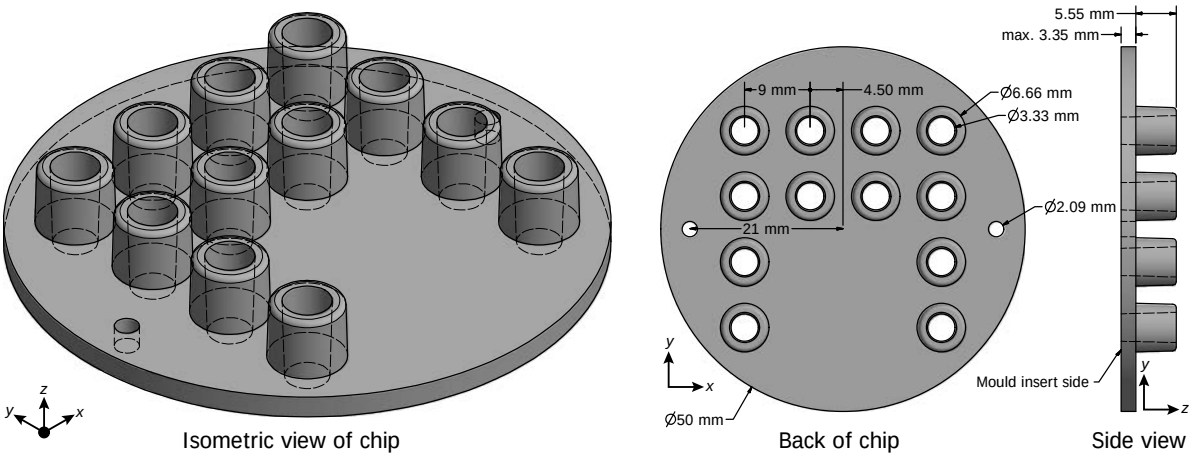

Figure 4.1 Illustration of the chip part with Luer-Slip connectors made with one of the moulds available at DTU Danchip. The chip part can be customised on the "mould insert side" by adding structural features to a custom-made mould insert[88].

The cavity of the mould without mould insert is 3.35 mm, which sets the maximum part thickness. The standard thickness of a master insert at DTU Danchip is 1.35 mm, yielding a part of 2 mm thickness, which is suitable for most applications. The master insert itself is a ⌀85 mm disc with two angled chords cut out for alignment.

4.1.1.2 Produced chips

This section covers the details of the individual chip systems presented via tables. It should serve as look-up tables. The nomenclature of the chips is as follows: XX.YY.MMV, where XX denominates the project, YY the year, MM the month and V the version of a given design. As an example, PN.14.02B is the second version of a chip made in the PolyNano project, February 2014.

Table 4.1 Specifications of the PN.13.03 design.

Description	Chip ID	PN.13.03

This chip was designed to test the burst pressures of a range of capillary microvalves. The chip part features channels with individual inlets laid out in parallel with a range of different dimensioned capillary microvalves, see schematic for the individual width/heights. All the capillary microvalve channels gathered in a common outlet, but had small 25 µm x 25 µm constrictions to ensure no fluid could flow into other channels via the outlet.
Post-processing by FDTS coating of the chip was necessary, since the post-bonding gap was large enough to otherwise cause failure for the capillary microvalves.
CNC micro milled apex shaped (60°) 130 µm high energy directors were placed 500 µm from the channel edges following the entire microfluidic system (not visible in the schematic).

Energy director type	CNC micro milled conventional butt joints
Pre processing	Polished master insert
Back-end processing	FDTS coating
Sheet part	254 µm thick extruded COC sheet

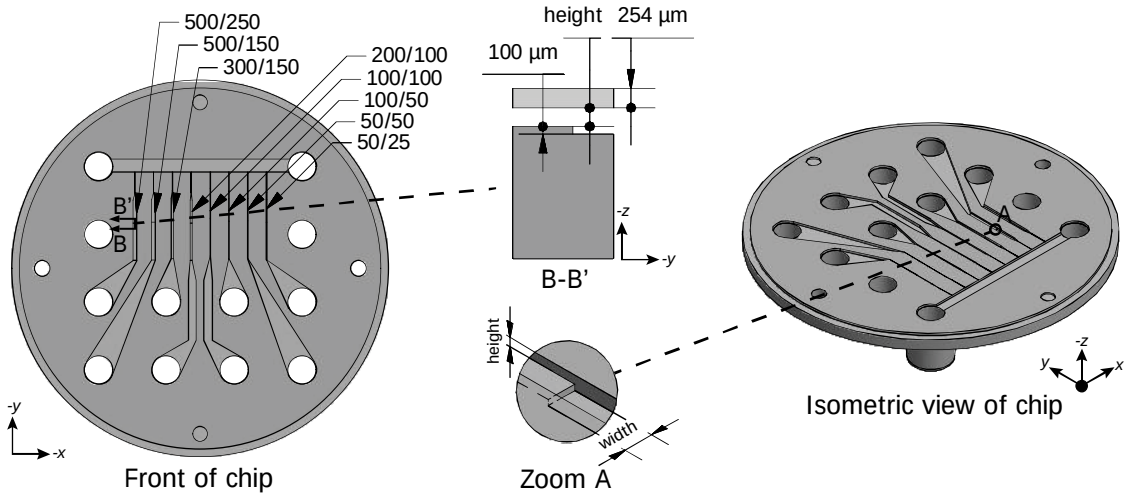

Table 4.2 Specifications of the PN.14.02B design.

Description	Chip ID	PN.14.02B
This chip was the first fully functioning system for nucleic extraction that was bonded using ultrasonic welding. The chip part features three chambers; for sample, immiscible phase filter, and elution. Energy directors were simple butt joints, but they were introduced by laser micromachining. The critical dimension is that of the capillary microvalve, which has the dimensions of 500 µm x 150 µm (w x h). The sheet part was a simple COC sheet of various thickness.		
Energy director type	Laser micromachined conventional butt joint	
Pre processing	Polished master insert, Laser micromachining	
Back-end processing	None	
Sheet part	167 µm, 254 µm, or 500 µm thick extruded COC sheet	

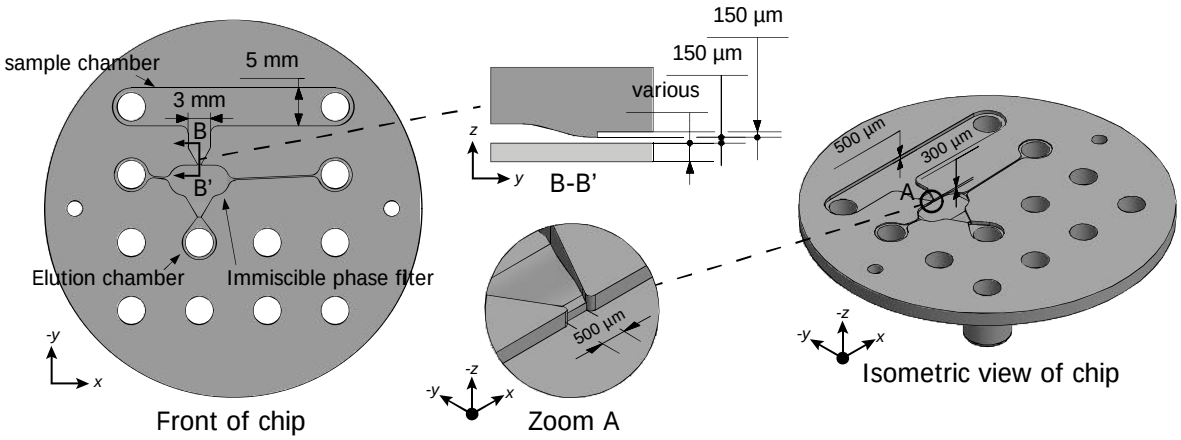

Table 4.3 Specifications of the PN.14.02F design.

Description	Chip ID	PN.14.02F

This design was the second iteration of a chip for nucleic acid extraction and featured tongue-and-groove joints. The chip part has the same basic layout as PN.14.02B, with an added groove around the microfluidic system. The sheet part was designed with tongues to allow for aligning of the foil as well as reducing the post-bonding gap. The first iteration had a capillary microvalve width of 500 µm and is presented in Paper 2 and Paper 3. The second iteration had a width of 750 µm to support more magnetic beads.

Energy director type	CNC micro milled conventional tongue-and-groove joint
Pre processing	None
Back-end processing	None
Sheet part	Injection moulded 500 µm COC sheet with tongues that matches the grooves of the chip part.

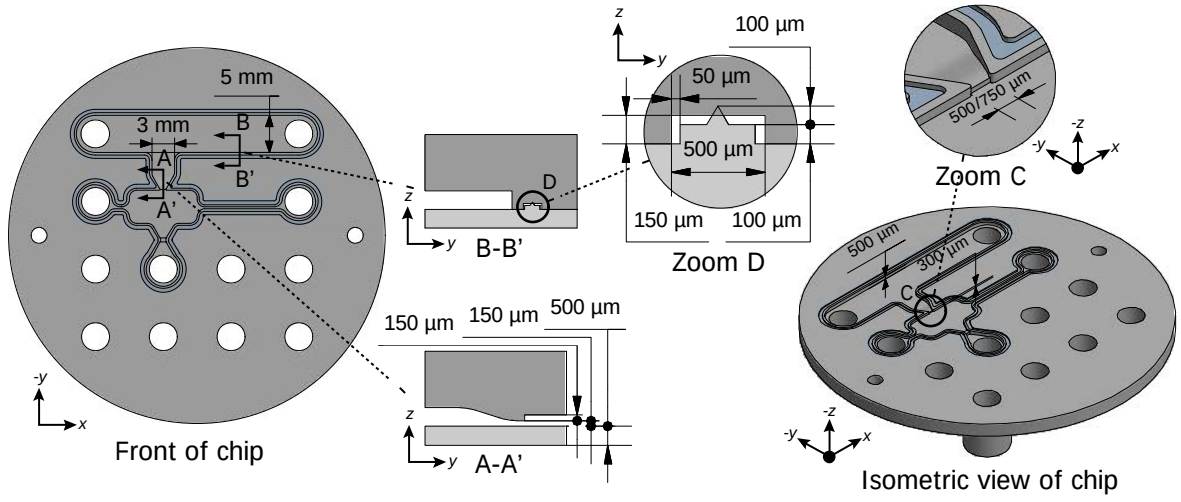

Table 4.4 Specifications of the TF.15.01 design

Description	Chip ID	TF.15.01
This chip was designed to illustrate the ability to ultrasonically weld free-standing high-aspect ratio channels, as well as the ability to add laser micromachined energy directors to a deep cavity master insert that is unreachable by micro milling. The design consisted of a simple 400 µm wide, 2 mm tall channel (red) with a 500 µm wide, 2 mm high channel wrapping around it (blue). The channels had to be sunk slightly into the base of the chip, because of the limitations of the macro mould cavity dimensions. The channel walls were 550 µm wide and carried 200 µm wide cone-like-protrusion (CLP) micropillar laser micromachined energy directors centred on top (not shown in the sketch).		
Energy director type	Laser micromachined micropillar butt joint	
Pre processing	Laser micromachining	
Back-end processing	None	
Sheet part	500 µm extruded COC sheet	

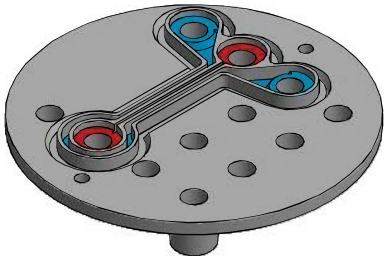

Isometric view of chip

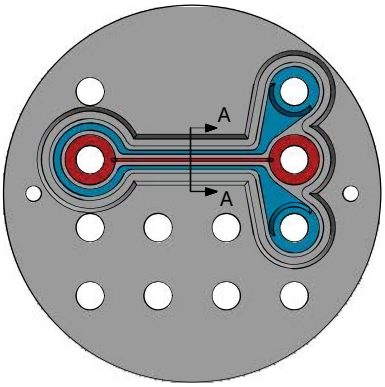

Front of chip

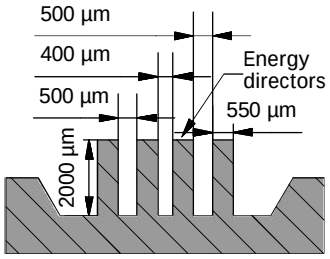

A-A'

Table 4.5 Specifications of the TF.15.03A/B design.

Description	Chip ID	TF.15.03A/B
This chip was designed with the sole purpose of determining the bonding strength of energy directors. Two variants were created, TF.15.03A with conventional CNC micro milled butt joints (115 µm high) and TF.15.03B with CLP micropillar butt joints (ca. 25 µm high). The chip part featured three plateaus laid out in parallel with long energy directors situated on top to allow for easy access with a razor blade from the right hand side. Note the schematics show a conventional micro milled energy director.		
Energy director type	CNC micro milled conventional butt joint Laser micromachined micropillar butt joint	
Pre processing	Laser micromachining	
Back-end processing	None	
Sheet part	167 µm extruded COC sheet	

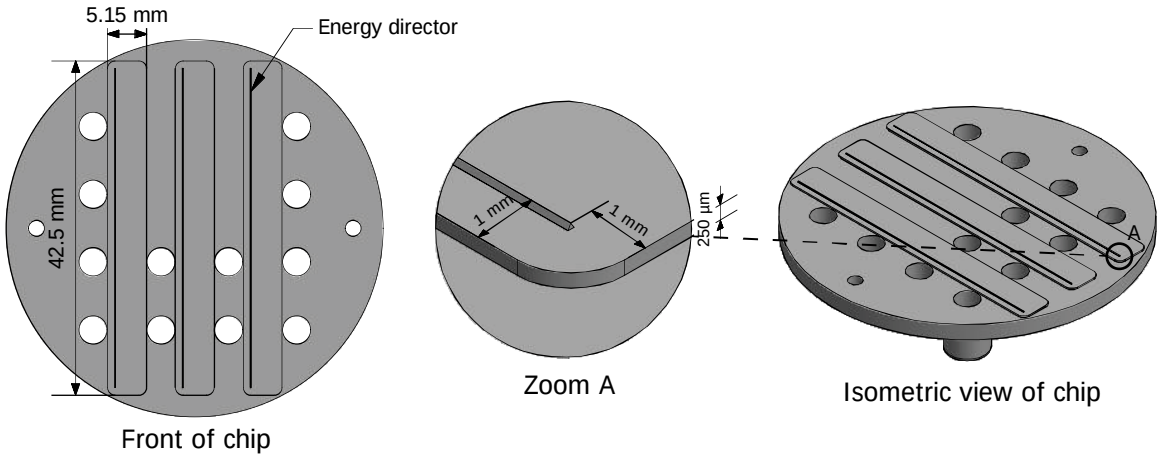

4.1.2 Micromilling of mould inserts

Once a part design was completed it was imported into CimatronE v11 (www.cimatron.com, accessed 2015-05-10). CimatronE allows for Graphical User Interface assisted generation of G-code to use with a CNC machine tool. The milling tools available for the machine tool were loaded into CimatronE, and appropriate tools, workpiece dimensions, toolpaths, and micromilling parameters were selected. The G-code was then exported and loaded into the tool machine CNC software, Artsoft Mach 3 (www.machsupport.com, accessed 2015-05-11).

A three-axis Mini-Mill/3 mill frame fitted with a Nakanishi E3000C spindle and controller (Minitech Machinery, Norcross, Georgia) was used to micro mill the mould inserts. The workpiece, a 100 mm × 100 mm (width × length) cut piece aluminium alloy 2017 from 2 or 3 mm thick "mill finish" rolled sheets (Metalcentret, Glostrup, Denmark) was fitted on the machine tool stage: First, the workpiece was fixed on a same size piece of PMMA using double sided tape to serve as a sacrificial spacer. Next, an aluminium square toroid fixture that also served as reservoir for cutting oil was screwed on top of the workpiece, see Figure 4.2.

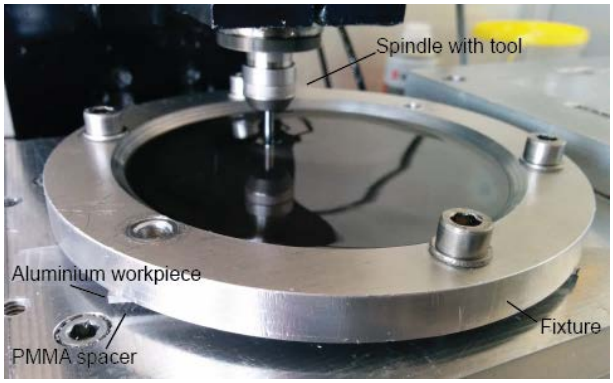

Figure 4.2 Photography of the micromilling setup showing milling of a master insert.

An appropriate tool was then fitted in the spindle and its x,y, and z position calibrated. Cutting oil was added to the reservoir and milling was commenced in Mach 3. Once the milling process was completed, the finished mould insert was released, cleaned, and dried.

If applicable, the mould insert was polished by fixation of the mould insert with tape and then applying Autosol Metal Polish (Autosol, Austin, Texas) with cleanroom wipes before taking it to the injection moulder.

4.1.3 Post-processing by laser modification of mould inserts

Energy directors were applied to some chip designs by means of a laser micromachining post-processing step. All laser post-processing of mould inserts was carried out at DTU Danchip on a microSTRUCT vario (3D-Micromac AG, Chemnitz, Germany) equipped with a FUEGO 1064 nm, 50 W picosecond laser.

In all cases the manual specified by DTU Danchip was followed. In brief, a mould insert was mounted on a frame fitted with Semiconductor wafer tape (SWT20+, Nitto, Japan) and placed on the chuck inside the microSTRUCT vario. A laser micromachining task was created by loading a job file (a CAD drawing) with the pattern to be milled and a parameter file with values found below. Before the actual pattern was micromachined, an alignment step was performed.

Two sets of parameter settings were utilised; one for micromachining of conventional energy directors, and one for generating cone-like-protrusion (CLP) patterns following the pattern of energy directors, see Table 4.6.

Table 4.6 Laser micromachining parameters. Power indicates the percentage of laser power output based on one measured during calibration. Toolpath for the laser was defined by a # of lines spaced by a given pitch offset a given distance from the microfluidic channel system edges. The focus plane was defined as 0 at the mould insert surface. The laser was set to follow the toolpath with a given velocity for a given # of repetitions.

Energy director type	Power (%)	# of lines	Pitch (µm)	Distance from channel edge (µm)	Laser velocity (mm/s)	Focus plane (mm)	# of repetitions
Laser	100	9	20	200	1000	0	20
CLP	50	20	10	Variable	1000	+1.3	20

Power indicates the percentage of laser power output based on a measured calibration value. Toolpath for the laser was defined by a # of lines spaced by a given pitch offset a distance from the microfluidic channel system edges. The focus plane was defined as 0 at the mould insert surface. The laser was set to follow the toolpath with a given velocity for a given # of repetitions.

PN.14.02B was post-processed to yield conventional energy directors and was used in Paper 2 and Paper 3.

CLP energy directors were used for razor blade testing in Paper 4.

4.1.4 Injection moulding of chips

Injection moulding for Paper 1 was conducted primarily by Peter Friis Østergaard (Danish Technological Institute). Throughout the project injection moulding has been partly assisted by Carl Esben Poulsen and Marco Matteucci (both from the Department of Micro- and Nanotechnology, Technical University of Denmark). All Injection moulding was carried out at DTU Danchip on an Engel Victory 80/45 Tech hydraulic injection moulding machine (ENGEL, Schwertberg, Austria) using Cyclic Olefin Copolymer (COC, TOPAS grade 5013L-10) from TOPAS Advanced Polymers GmbH, Frankfurt-Höchst, Germany.

Injection moulding was carried out following the manual specified by DTU Danchip. In brief, COC was loaded into the hopper and the barrel heaters were switched on. The mould insert was then fitted into the macro mould and the mould heaters switched on. After the heaters had reached the desired

temperatures of $T_{Heater\ \#1}$=240 °C, $T_{Heater\ \#2}$=250 °C, $T_{Heater\ \#3}$=260 °C, $T_{Heater\ \#4}$=270 °C, $T_{Mould,front}$=120 °C, $T_{Mould,back}$=120°C, the barrel was cleaned and the machine setup to run an isothermal program. In this project 13 cm^3 COC was injected for main parts (8 cm^3 for sheets) until an injection pressure limit of 2200 bar was reached, after which a holding pressure of 1766 bar was applied for 5 s. The part was then cooled for 30 s, demoulded, and moved to the conveyer belt by a robot. This amounted to a total cycle time of 42 s. A schematic of the injection moulding machine with relevant legend can be found in Figure 3.1. After a process was finished, the sprues were removed from the produced parts and they were packed on SWT20+ tape.

4.1.5 Chip coating

Chip coating with 1H,1H,2H,2H-perfluorodecyltrichlorosilane (FDTS) was performed by Kenneth Brian Haugshøj at the Centre for Microtechnology and Surface Analysis, Danish Technological Institute. The methodology was described thoroughly in Paper 1 and will hence only be briefly summarised here.

Coating of COC sheets and chip parts was performed with a MVD100 (Applied Microsystems, San Jose, California) molecular vapour deposition system prior to bonding. The coating consists of two layers; a silicon oxide adhesion layer and the FDTS layer, both applied using a gas phase multi-step deposition process performed under set pressures at 35 °C. The COC surfaces were activated by oxygen plasma before simultaneous introduction of silicon oxide precursors (silicon tetrachloride and water). The chamber was then pumped down again and purged with nitrogen. Subsequently FDTS and water was introduced simultaneously to form a self-assembled monolayer of FDTS.

4.1.6 Bonding by ultrasonic welding

Ultrasonic welding was carried out manually on a Telsonic USP4700 20 kHz ultrasonic welder (Telsonic, Erlangen, Germany). The machine outputs 50-100% (depending on the settings in the software) of 14 µm vibrations from the transducer that are then increased in amplitude by a booster (Telsonic) by a factor of 2, and further increased by a sonotrode (Telsonic) by 2.1. The sonotrode is square and has an area slightly larger than a microtiterplate. Thus, the vibrational amplitude (A) the machine exerts on the parts can be calculated using $A = 14\ \mu m * \%_{amplitude} * 2 * 2.1$, resulting in vibrational amplitudes between 29.4 µm and 58.5 µm.

First, A chip part was placed in a custom CNC micro milled fixture (see Figure 4.3) with a sheet placed freely on top of the chip part. The ultrasonic welder was then engaged and the chip part and sheet welded together. The total time for welding including mounting of the parts was about 30 s per chip.

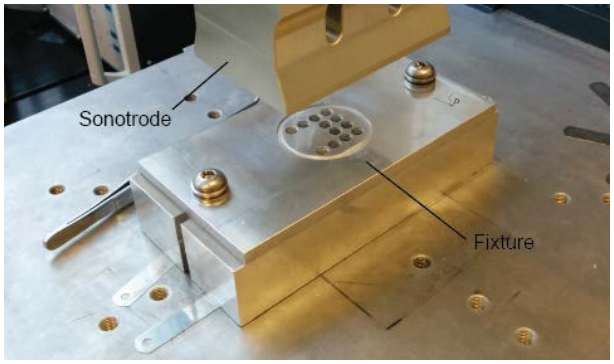

Figure 4.3 Photograph of the fixture for the ultrasonic welder.

The parameters used for ultrasonic welding was optimised for each chip system and has been gathered in Table 4.7 for clarity. For some chip systems it was required to further align the fixture to the sonotrode to ensure that the chip part surface plane and sonotrode plane were parallel.

Table 4.7 Ultrasonic welding parameters. [a] 500 µm width version. [b]700 µm width version.

	Type	Trigger force (N)	Energy (J)	Hold time (s)	Amplitude (%)	Down pressure (bar)	Weld pressure (bar)
PN.14.02B	Laser	400	40	0.35	80	0.2	1
PN.14.02F[a]	CNC	850	85	0.35	80	0.8	1
PN.14.02F[b]	CNC	515	40	0.35	55	0.4	1
TF.15.03A	CNC	360	50	0.35	50	0.1	1
TF.15.03B	CLP	360	50	0.35	50	0.1	1

4.2 Customisable chip mount with magnet actuators

In order to be able to perform precise and consistent chip handling, a custom chip mount was constructed. Figure 4.4 illustrates the setup. Going from top to bottom, the setup exists of:

- A custom milled aluminium chip holder for easy fitting and release of chips.
- A custom milled aluminium magnet casing including a permanent magnet stack consisting of four axially aligned cylindrical magnets (top to bottom): two N48, NdFeB, ⌀3 mm, 1mm high magnets (#S-03-01-N, Supermagnete, Gottmadingen, Germany) and two N45, NdFeB, ⌀6 mm, 3mm high magnets (#S-06-03-N, Supermagnete, Gottmadingen, Germany). The stack was based on the configuration from [13], differing by having two cylindrical large magnets instead of one large cubic magnet.

- A linear z-axis stage (#55-031+#58-290, Edmund Optics, Barrington, New Jersey) fitted with a high precision adjustment screw allowing for 10 µm increment adjustments of the magnet-chip distance.
- A spring-loaded linear y-axis stage (#M-423, Newport, Irvine, California) fitted with a 100 TPI adjustment screw (#AJS100-1, Newport, Irvine, California) for precise y-positioning. The spring loading allows for quick sliding of the magnet stack to the inlet of the chip during loading of magnetic beads.
- A rail based slider platform (#9026-M+#9028-M+#9022NF, Newport, Irvine, California) for rough y-axis positioning.
- A motorised x-axis lateral stage (#LTS150, Thorlabs, Newton, New Jersey) for accurate control of acceleration and velocity of the magnet stack.

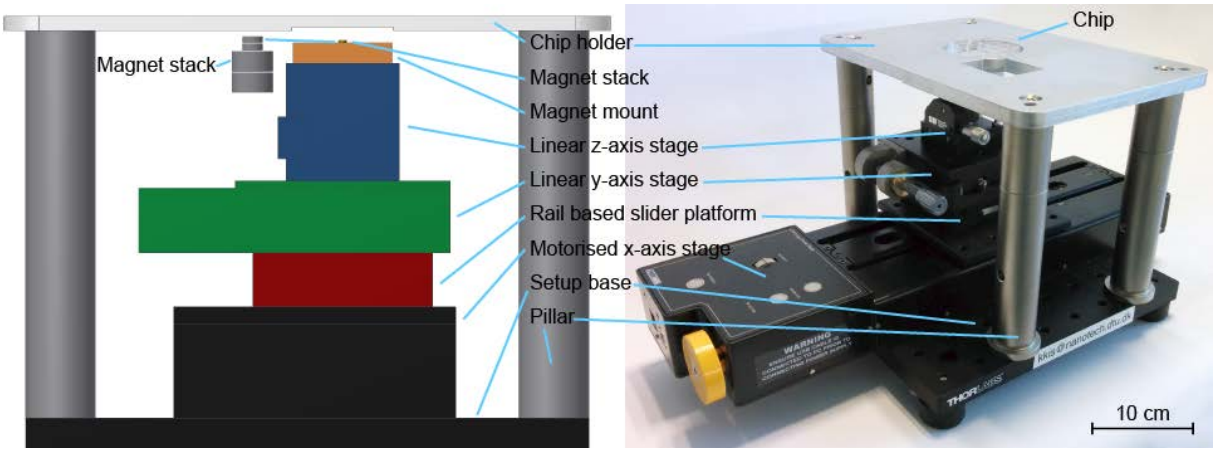

Figure 4.4 Sketch and photograph of the chip mount. The setup allows for easy loading of chips as well as axis-based controlled movements. Once the stages have been set to match a chip design it is easy to perform replicate experiments. Details on the parts that make up the setup are found in the main text.

4.3 Chip structural characterisation

4.3.1 Stress testing and annealing

Injection moulding and ultrasonic welding induces residual stress in moulded parts [99], which may compromise their use with certain solutions, especially those of like chemical composition. The residual stress of PN.14.02B moulded to a 167 µm COC sheet was qualitatively studied, as well as means of removing such stress by annealing to prevent part failure. Experiments were conducted together with Carl Esben Poulsen (Department of Micro- and Nanotechnology, Technical University of Denmark).

The annealing process consisted of a simple heat treatment in an Memmert UFE 400 oven (Memmert GmbH, Schwabach, Germany) for 3 hours at 120 °C after which the oven was switched off and the chips allowed to cool to room temperature while the oven remained shut.

Stress testing was performed on two sets of three chips. One set, where 1-octanol (Sigma-Aldrich, St. Louis, Missouri) with 10 %(V/V) Span 80 (Sigma-Aldritch) was added and one control set without any

fluids added. Each set consisted of an un-annealed chip, a chip that was annealed prior to ultrasonic welding, and a chip that was annealed post-ultrasonic welding. The chips were then analysed qualitatively by detecting cracks in the samples using a Leica FluoCombi III fluorescence stereomicroscope (Leica Microsystems, Wetzlar, Germany) fitted with a Sony DFW-X710 firewire camera (Sony Corporation, Tokyo, Japan). Micrographs were taken immediately, after 41 hours, and again after two weeks.

4.3.2 Roughness and replication quality analysis

Roughness analysis was carried out at the Danish National Metrology Institute in collaboration with Jørgen Garnæs and Morten Hannibal Madsen (both Danish National Metrology Institute).

Roughness and quality of replication conformance of the mould and plastic parts were analysed by investigating the aluminium mould inserts and corresponding COC parts of PN.14.02B (polished) and PN.14.02F (unpolished). The analysis was carried out using a S Neox optical profiler (Sensofar, Spain) set to confocal profiling mode and a Scanning Probe Microscope (SPM) set to tapping mode. For the Sensofar analysis, the entire width (5 mm) of the sample chamber was analysed by stitching together micrographs taken with a 20X/0.45 objective and the profiles averaged over a 637 µm range. The surface roughness analysis was carried out with a 50X/0.8 objective, scanning a single 255 µm × 191 µm area inside the sample chamber. For the SPM analysis, a single 69.4 µm × 90.9 µm area inside the sample chamber of PN.14.02B/F was analysed.

Scanning Probe Image Processor (SPIP) v6.3.1 (www.imagemet.com, accessed 2015-05-17) was used to analyse the data acquired. In all cases raw data was loaded into SPIP and further analysed.

For Sensofar data, noise filtering was achieved by applying a 2 µm or 0.8 µm ISO 16610-21 Gaussian short filter (S-filter) for 20x or 50x micrographs, respectively. Plane correction was carried out by applying the global correction polynomial fit (first order) algorithm. The algorithm subtracts a fitted plane from the raw data based on a linear least mean square fit of the dataset. Where applicable, void pixels and outliers were filled with appropriate values based on the SPIP filtering options. The SPIP manual with details on all functions can be accessed via the SPIP online manual (www.imagemet.com/WebHelp6/Default.htm, accessed 2015-04-28).

For SPM data, the same global correction as above was applied. S-filtering and void pixel/outlier removal was not required.

Roughness was calculated as the root mean square or the roughness average (S_q), which is defined as the root mean square of the arithmetic mean of the magnitude of the deviation from the mean plane of the surface:

$$S_q = \sqrt{\frac{1}{MN}\sum_{k=0}^{M-1}\sum_{l=0}^{N-1}[z(x_k, y_l)]^2} \qquad (4.1)$$

Where M and N defines the dimensions of the plane, and z is the recorded plane at position x_k, y_l. Note that the mean plane value is not subtracted from z when calculating S_q, which is in accordance with ISO 25178-2. Instead this was accommodated by applying the global correction.

4.3.3 Bonding strength assessment

The bonding strength of the ultrasonic welding seams was tested by two means: (1) By subjecting a closed chip system to pressurised air. (2) By utilising the razor blade test[100,101]. Bonding strength testing was carried out together with Carl Esben Poulsen (Department of Micro- and Nanotechnology, Technical University of Denmark).

4.3.3.1 Pressure testing

Pressure testing was conducted by applying pressurised air to PN.14.02B (bonded with a 167 µm sheet) and PN.14.02F (bonded 530 µm sheet), via the inlet after first blocking the remaining Luer-Slip connections. The pressure was then slowly ramped up until failure or a maximum pressure of 8.5 bar was reached. Three experiments were conducted on each chip system.

4.3.3.2 Razor blade testing

Razor blade testing was carried out on TF.15.03A (conventional energy directors) and TF.15.03B (micropillar energy directors), which were designed for the purpose, see Table 4.5 for design. First, the chip under investigation was mounted on the custom fixture (Figure 4.3) and placed under a Leica FluoCombi III fluorescence stereomicroscope (Leica Microsystems, Wetzlar, Germany) fitted with a Sony DFW-X710 firewire camera (Sony Corporation, Tokyo, Japan). A razor blade was then forced by hand in-between the bonded sheet and chip part surface, slowly advancing the blade edge towards the welding seam, while keeping the two parallel to one another. The blade was stopped once a sufficient part of the welding seam had fractured from the main chip part and a photograph was taken. Next, the distance from the fracture line to the face of the blade was measured using ImageJ 1.49k (http://imagej.nih.gov/ij/, accessed 2015-05-14), see Figure 4.5, left for an example of such a distance measurement.

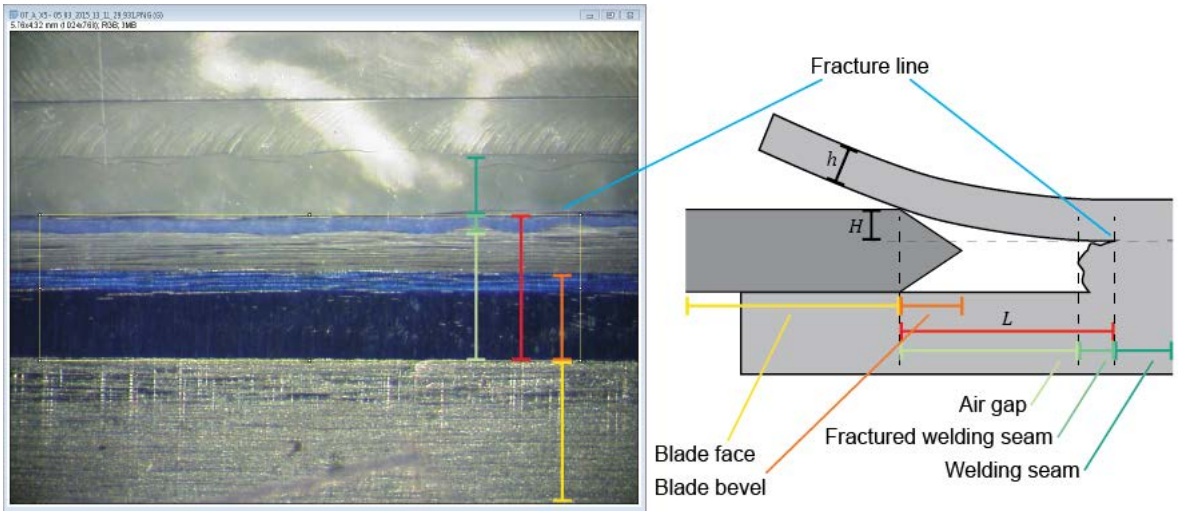

Figure 4.5 Razor blade test data analysis in ImageJ (left). The sketch on the right shows the relevant dimensions.

The surface energy, γ (bonding strength), was calculated in Paper 4 using the following expression based on the equation from Maszara *et al.*, which comes from the equilibrium between the potential energy of a deflected cantilever and the surface energy of the material [100], see Figure 4.5 right:

$$\gamma = \frac{3}{16}\frac{H^2 h^3}{L^4}E, \tag{4.2}$$

where H is the height from the fracture line to the face of the blade *i.e.* the height of the deflection and was calculated by subtracting the added height from the welding seam (15.3 µm and 14.1 µm for the conventional and micropillar energy directors, respectively, determined using SEM) from the thickness of the blade (250 µm). h is the thickness of the sheet (167 µm), L is the distance from the fracture line to the face of the razor blade, and E is the Young's modulus of the sheet, which for TOPAS 5013S-04 is 3.2 GPa (www.topas.com/sites/default/files/TDS_5013S_04_e_1.pdf, accessed 2015-05-20). Note that eq. ((4.2) differs from the one presented in [100] by the fact that $H = 2y$ and that a single sheet is deflected from a rigid chip surface, rather than two silicon wafers that are split apart. This can be taken into account by introducing a mirror plane in-between the two wafers, which effectively doubles γ, because the mirror planes have the same surface energy as the cantilevers. A total of 10 chips were analysed for each type of energy director.

4.4 Chip physical performance

4.4.1 Contact angle and interfacial tension measurements

All measurements were performed on a Krüss DSA10 Contact Angle Measuring System (Krüss GmbH, Hamburg, Germany) with the associated DSA1 v1.9 software.

Advancing contact angles (θ_{adv}) were measured by first placing a piece of substrate on the DSA10 stage and filling one of the dispenser systems with a given solution. The needle of the dispenser system was

then brought to focus using the integrated camera and positioned just above the substrate surface. A small droplet (5 µl) of solution was then deposited and the stage realigned in *x*, *y*, and *z*, so the center of the droplet was below the needle. The software was set to measure "pendant drops" and fit the recorded images using the "tangent method 2", which is based on a rational function selected by Krüss. Before the syringe was set to dispense, lines were positioned on the live feed to help the program detect the surface and needle thickness (for scaling). The "TrackerMan" function was used to record images automatically once the software detected movement of the meniscus. To record a series of measurements, 40 µl of solution was dispensed from the syringe at 60 µl/min velocity. The fitted left and right contact angles of the droplet was then averaged to yield the average advancing contact angle. These measurements were then repeated by retracting the fluid from the surface and re-dispensing it a number of times. This process was repeated for a number of positions on the substrate. A thorough description of the functions used can be found in the manual of the equipment, which is not readily available online, but can be acquired by contacting Krüss (www.kruss.de/contact, accessed 2015-06-17).

For Paper 1, two pieces of 254 µm extruded COC sheet (TOPAS grade 5013S-04, TOPAS Advanced Polymers GmbH, Frankfurt-Höchst, Germany) was used as substrate. One piece was uncoated, and the other piece was coated with FDTS as described previously. Two locations were investigated in triplicate.

4.4.2 Hydrostatic burst pressure measurements

The hydrostatic burst pressure measurements were described in detail in Paper 1 and is thus partly quoted.

Hydrostatic burst pressures of PN.13.03, PN.14.02B, and PN.14.02F were measured using a custom built setup. It consisted of a 50 ml syringe (without piston) used as water column that was connected to a horizontally fixed chip via tubing with luer connectors. The water column could then be raised vertically via a LTS150 motorised lateral stage (Thorlabs, Newton, New Jersey), see Figure 4.6 for a photograph of the setup.

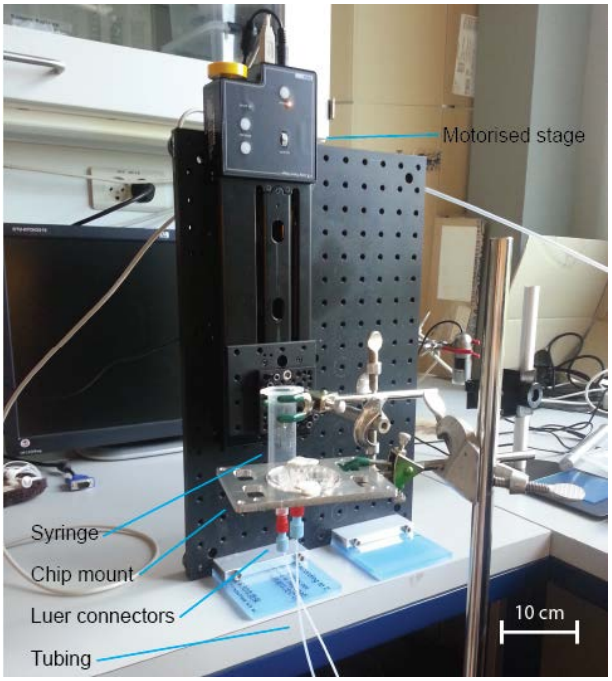

Figure 4.6 The setup used for measuring hydrostatic burst pressures.

Before initiating a measurement, the chip was positioned so the surface vertical position matched that of the water surface. The syringe was then raised at 1 mms^{-1} while the capillary microvalve was carefully monitored. Once the water advanced into the channel leading to the capillary microvalve, the stage was paused and the fluid allowed to pin at the capillary microvalve, after which the stage was re-engaged. When the water burst through the capillary microvalve, the stage was stopped immediately and the height recorded. The syringe vertical position was then reset, and after the meniscus had retracted past the capillary microvalve the process was repeated. A total of three measurements per capillary stop was performed.

For PN.13.03, burst pressures of every capillary microvalve were measured three times. The chips were then rinsed, dried and the experiments repeated on the same chip. This process was repeated on 2–3 chips, resulting in a total of 12–18 measurements per capillary microvalve.

For PN.14.02B, three measurements were conducted on each chip on a total of two chips.

For PN.14.02F, three measurements were conducted on each chip and rinse-repeated for one chip, resulting in a total of four chips.

The burst pressures were calculated using $p = \rho g H$, where p was the calculated pressure, ρ=998 kgm^{-3}, g=9.82ms^{-2}, and H was the measured height.

4.4.3 Surfactant compatibility experiments

In Paper 2, the compatibility of PN.14.02B with various surfactant types and amounts was tested. A chip was considered compatible if the chip could form a stable liquid system during filling and transport 40

µg Dynabeads MyOne SILANE (Life technologies, Carlsbad, CA) MBs without failing. The following surfactants were investigated:

- 0.1 (V/V)% Triton X-100 (Sigma-Aldrich)
- 0.25 (V/V)% Triton X-100
- 0.0625 (V/V)% Sarkosyl (Sigma-Aldrich)
- 0.125 (V/V)% Sarkosyl
- 1 (V/V)% Tween-20 (Sigma-Aldrich)

First, 100 µl of Milli-Q water or Lysis-binding buffer (6M citrate buffered guanidine hydrochloric acid (AppliChem, Darmstadt, Germany), pH 4.5) with surfactant was added to the sample chamber. Then, 100 µl Tris-EDTA buffer (Sigma-Alrich) was added to the elution chamber and the filling was completed by addition of 50 µl 3M fluorinert electronic liquid FC-40 (Walbom A/S, Kastrup, Denmark).

MB transport compatibility was tested by adding 40 µg of MBs from a 1:10 dilution of the stock (40 µg/µl). The MB cluster was then transported from the sample chamber, through the capillary microvalves and immiscible phase chamber, and into the elution chamber using the custom chip mount operated at 1 mm/s.

The hydrostatic pressure exerted by the liquid column in the Luer-Slip inlet was calculated to $p_{\mathrm{hyd}} = \rho g h = 998\,\mathrm{kg/m^3} \times 9.82\,\mathrm{m/s^2} \times 6\,\mathrm{mm} = 59\,\mathrm{Pa}$. The Young–Laplace pressure inside the luer was calculated using $p_{\mathrm{luer}} = -2\gamma_{\mathrm{aq,air}}(\cos\theta_{\mathrm{aq,air}}/r_{\mathrm{luer}})$, where $r_{\mathrm{luer}} = 2\,\mathrm{mm}$.

4.4.4 Liquid carry-over determination

The liquid carry-over of PN.14.02B was investigated in Paper 2, where it was determined for two solutions; Milli-Q water, and a lysis-binding buffer containing 5M citrate buffered guanidine hydrochloric acid (AppliChem, Darmstadt, Germany) pH 4.1 with 0.1 (V/V)% Triton X-100 (Sigma-Aldrich). A range (10-120 µg) of Dynabeads MyOne SILANE (Life technologies) MBs were investigated.

In brief, 200 µl of solution containing 2 mM rhodamine B fluorescent dye (Sigma-Aldrich) was added to the sample chamber, followed by addition of 100 µl solution without dye to the elution chamber. Lastly, 100 µl 3M fluorinert electronic liquid FC-40 (Walbom A/S, Kastrup, Denmark) was added to the immiscible phase chamber to stabilise the system. The desired amount of MBs was then added to the sample chamber from a 1:10 dilution of the stock (40 µg/µl). The MB cluster was transported by magnet actuation as described above. The chip was then removed from the chip mount and 90 µl (including the MBs) was pipetted from the elution chamber and transferred to a microtiter plate, where the MBs were removed using a PickPen (Bio-Nobile, Pargas, Finland). This action was repeated for every relevant combination of solution and MB amount in triplicate.

The liquid carry-over volume was determined by relating the concentration of rhodamine B in the sample chamber to the concentration of rhodamine B in the post-extraction elution chamber by analysing

the dye content of the microtiter plate wells. The microtiter plate was placed in a LaVision BioAnalyzer 4F/4S scanner (LaVision BioTec GmbH, Bielefeld, Germany), where each well was subsequently exposed to 1 ms of Cy3 filtered light. An image of the interior of each well (focused inside the solution) was acquired and exported into ImageJ 1.49k (http://imagej.nih.gov/ij/, accessed 2015-05-14), where the average intensities were quantified. The intensities were then converted into concentrations by relating them to established standard curves generated from 0-5 µM rhodamine B solutions over 11 steps. Finally, the concentrations (c_{outlet}) were converted into volumes using $(c_{outlet}/c_{inlet})V_{outlet}$, where c_{inlet} was the sample chamber dye concentration (corrected for the volume addition of the MB suspension), and V_{outlet} was the volume of the elution chamber.

4.4.5 Magnetic force calculations

The COMSOL simulations, VSM data analysis, and image processing algorithm was conducted and developed by Karen Skotte Jørgensen.

The magnetic field (**H**) from the permanent magnet stack was calculated numerically in COMSOL by finite element analysis, using cylindrical coordinates for an axisymmetric model with the permanent magnet stack centered, *cf.* Figure 2.4 and Figure 4.4. The magnetic susceptibility (χ) of the magnetic beads was measured in a Vibrating Sample Magnetometer (VSM), and the data was fitted with a linear combination of a Langevin function and Fröhlich-Kennelly function, weighted evenly.

In order to estimate the magnetic force, a series of top-view images displaying the position of the magnetic bead cluster relative to the underlying magnet during the extraction was recorded for every experiment conducted. The distance (z_0) between the upper magnet surface and microfluidic channel floor was controlled.

An image processing algorithm able to detect the permanent magnet, the bead cluster, and the capillary microvalve was developed in MATLAB vR2015a (www.mathworks.com, accessed 2015-06-27). For each image, the bead cluster was divided into a number of voxels (N_{voxel}), and the positions of these relative to the center of the magnet and capillary microvalve were recorded. The image length scale was determined by referencing the permanent magnet stack. Under the assumption that the number of beads was constant throughout the extraction and that gravity and buoyancy could be neglected, the bead cluster was divided into a set of layers (N_z), each comprised of a number of pixels (N_{xy}); $N_{\text{voxel}} = N_{xy} \times N_z$. Confocal imaging (data not shown) revealed the bead cluster to have a 150 µm high filleted cylindrical shape regardless of z_0, supporting the model.

The magnetic force ($\boldsymbol{F}_{\text{magnetic}}$) could now be estimated using equation (2.18), knowing $m_{\text{bead cluster}} = 40$ µg and $\rho_{\text{bead cluster}} = 1800\ \text{kg/m}^3$.

The experiments were conducted by subsequently filling the sample chamber, extraction chamber, and immiscible phase filter of PN.14.02B with 225 µl Brilliant Blue R dyed Milli-Q water, 75 µl Milli-Q water, and 35 µl FC-40 oil, respectively. After filling, 40 µg of MyOne SILANE beads were added from a 1:10 diluted stock. The external magnet was then actuated at 0.5 mm/s from the sample chamber and

into the immiscible phase filter. The distance from the top plane of the permanent magnet stack and the floor of the microchannel (z_0) was varied during the experiments. Three experiments were carried out for each distance.

4.5 MRSA sample extraction and quantification

The PN.14.02B chip was tested for application using MRSA culture spiked into whole blood.

Reagents For the extraction experiments phosphate buffered saline containing 0.01%(V/V) Tween-20 and 0.1%(V/V) BSA (Sigma-Aldrich, PBS-T-BSA) was used as buffer. All samples were based on over-night cultured MRSA diluted in PBS-T-BSA if applicable. The sample matrix consisted of citrate treated bovine whole blood (State Serum Institute, Copenhagen, Denmark).

Magnetic bead conjugation Dynabeads MyOne Streptavidin C1 magnetic beads (Life Technologies) were conjugated with biotin labelled monoclonal anti-protein-A antibody (SPA-27) (Sigma-Aldrich). 0.03 µl antibody/µg beads were incubated on an orbital shaker for 30 min, followed by four washing steps in 200 µl PBS-T-BSA. The beads were then blocked by resuspending them in 300 µl 10 mg/ml bovine serum albumin in tris-buffered saline and incubating them for 30 minutes on an orbital shaker. The beads were further incubated over night in the fridge. Finally, the beads were resuspended in PBS-T-BSA to a concentration of 10 µg/µl.

MRSA culture Approximately 1 µl of MRSA (USA300 strain) stock was set to a culture tube along with 5 ml tryptic soy broth media (Sigma-Aldrich). The MRSA stock solutions provided by Julia Skov (DELTA) were kept at -80 °C. The culture tube was then incubated over-night in an incubator with an orbital shaker.

4.5.1 MRSA sample preparation and extraction

Samples consisted of 10X dilution series (10^1-10^5 range, n=4) prepared from over-night MRSA culture diluted in PBS-T-BSA. *Off-chip reference* (n=4) samples were diluted culture directly added to the PCR tubes. *No antibody* (n=4) control was sample extractions based on a 1:10 dilution sample, but using unconjugated beads. *NTC* (n=3) was the no template control based on Milli-Q water added directly to the PCR tubes instead of MRSA culture. *No MRSA* (n=4) control was an on-chip sample extraction with no MRSA added.

On-chip extraction samples were prepared by first mixing 146 µl whole blood with 4 µl conjugated beads and 50 µl diluted MRSA culture sample in a 1.5 ml tube, adjusted to a 0.1%(V/V) Tween-20 concentration and left to bind for 5 min. A PN.14.02B chip placed in the chip mount was then loaded by sequentially adding 200 µl sample to the sample chamber, 75 µl Milli-Q water to the extraction chamber, and 50 µl FC-40 oil to the immiscible phase filter. The bead cluster was transferred to the extraction chamber using the external magnet operated at 0.5 mm/s. Next, the chip was removed from the magnet, the bead cluster resuspended and the entire extraction chamber volume transferred to a 1.5 ml tube. Finally, the volume was vortexed to ensure a uniform distribution of beads in the sample and 2.5 µl was added to the PCR tubes.

4.5.2 MRSA quantification

MRSA was quantified using qPCR on a Chromo4 system (Bio-Rad, Hercules, California). Each 25 µl reaction contained 1X iQ Supermix (Bio-rad), 0.4 µM *mecA* primers (*mecA* F2, 5'-AGTAGCACTCGAATTAGG; *mecA* R2, 5'- AAGGATCTGTACTGGGTTA), 0.32 µM TaqMan probe (*mecA* P2, 5'-FAM-CAGGTTACGGACAAGGTGAAA-BHQ1), 2.5 µl sample, and Milli-Q water to reach the final 25 µl reaction volume. The amplification procedure was: t_1, 94° for 3 min; t_2, 94° for 20 s; t_3, 57° for 20 s; t_4, 72° for 20 s; steps t_2-t_4 repeated 40 times, where the fluorescence signal was quantified after each cycle.

Plating Plating was performed to quantify the efficiency and background of conjugated beads. 40 µl of $1{:}10^5$ diluted MRSA culture in PBS-T-BSA was mixed with 40 µg of magnetic beads and mixed for 5 min by pulse vortexing. The beads were washed twice in PBS-T-BSA and resuspended in 50 µl PBS-T-BSA, before plating the sample on potato dextrose agar plates for over-night culture. Colony forming units were counted the day after. Three sample types were prepared in duplet: A positive control with 50 µl $1{:}10^5$ diluted culture directly plated. One sample using conjugated beads. One sample using un-conjugated beads.

Chapter 5 Results and discussion

The results and discussion section has been divided into three subsections covering: *structural characterisation*, *physical performance*, and *application* of the chips.

The manufacturing philosophy of this project was, as mentioned, to produce prototypes that were as production-ready as possible. To substantiate this claim, all chip experiments performed in this project have been carried out in a single-use manner, unless otherwise stated. Because of the rapid prototyping nature of this project, the results shown have been produced on a range of chip designs (see section 4.1.1.2 for overview) over its course, meaning that different elements of the chip designs have progressed from design to design, *e.g.* the type of energy director varies with chip design.

5.1 Fabrication cycle time and yield

To compete with the production time of PDMS casting it is important to be able to generate chips in a truly rapid fashion.

Given a design, creating a simple PDMS device takes a few steps. First you need to generate a replication master. This can be done by printing the design on a plastic sheet, creating a mask. The mask pattern is then transferred to a silicon wafer covered by photoresist. The uncured photoresist is removed and the mould is ready. Devices are cast in a serial manner by pouring PDMS into the mould and allowing it to cure for about an hour. Some back-end processing then needs to be done such as drilling holes for connections and bonding. Effectively a handful of chips can be fabricated in a day's work, depending on the back-end processes chosen[48].

The strategy applied in this study generates the replication master using CNC micromilling, which takes 3-5 hours, depending on the complexity of the design. Devices are then injection moulded using an isothermal program, having a cycle time of about 45 s per chip. The mould is complete with Luer-Slip connections, so the only back-end processing needed is that of bonding. Ultrasonic welding is performed manually and takes roughly 30 s per chip including mounting of the chip, amounting to a total production time of *ca.* 80 s per chip.

A first prototype can probably be generated faster using the PDMS approach, but keeping in mind each chip requires a curing step of 1 h, it is quickly overtaken by injection moulding. The end-goal of lab-on-a-chip systems is ultimately to be used in a single-use, disposable fashion, so ideally, the sooner one can get to perform single-use experiments, the sooner the robustness of a design can be assessed. The injection moulded/UW approach is well equipped to facilitate this, whereas the slow overall cycle time of PDMS device production is not.

It is noted that the CNC micromilling process of 3-5 h is rather short compared to industrial standards. The short milling time is achieved for two reasons. First, only the master insert disc needs to be micro milled, so only minor amounts of material needs to be removed. The second reason is a question of tolerance. The roughness of the master inserts fabricated in this project analysed in section 5.2.2 is not insignificant, but is endured to allow a shorter time from design to device. If a better surface finish is required, the micromilling process can be optimised to provide a lower surface roughness, however finishing passes are very time consuming.

Another important factor for large-scale production is that of yield. In this project, after all process parameters had been optimised, a high yield was generally observed roughly estimated to be more than 95% (no close investigations of this have been carried out). The aluminium master inserts are more than capable of producing the amount of chips required for rapid prototyping and the injection moulder very rarely produced erroneous chips. The only real contributor to lower the yield was the ultrasonic welding. When bonding thin sheets to parts, there is a risk of hitting resonant frequencies of the sheets, which can cause them to crack. However, as stated, after optimisation of the welding parameters this rarely occurred.

5.2 Chip structural characterisation

This section presents the data obtained when characterising the chips as they were developed. It deals with factors that could affect chip performance such as; the roughness of the replicated part surfaces, the compatibility of the moulded parts with oils to be used in the immiscible phase filtration, and bonding quality/strength.

It is beyond the scope of this text to cover in detail the art of thermoplastics processing and injection moulding (there are plenty of books for that[94,102]), yet, when manufacturing using injection moulding, the process will induce characteristics in the part that will affect its performance. The processes that govern these outcomes will be described in some detail.

5.2.1 Stress and annealing

When injection moulding it is impossible to avoid the build-up of residual stress in the part [99], due to how an injection moulding cycle occurs, see section 3.4 for details. The residual stress arises from the immense shear stress that the viscous molten polymer is subjected to during injection. In this project, the 270 °C COC melt is injected with 2200 bar into the relatively cold 120 °C mould. The filling of a mould with molten polymer is a very complex process, but simply explained, the residual stress occurs due to formation of a *skin layer* of solid polymer at the mould/melt interface, causing the molecules of the outer polymer layer to be locked in a specific orientation. The core of the polymer stream is still very hot and follows a laminar flow profile, meaning that the outer layer is subjected to both viscous heating from the flow and conductive heat loss from the mould (kept at a constant temperature in this study)[94,103]. Depending on the shape of the mould, these flow patterns grow very complex and result in a more or less stressed part, as layer upon layer of polymer solidifies until the part is cooled. The flow patterns depend on the polymer type and the parameters used for moulding. The amount of stress that

can be tolerated is determined by the application of the part and is ideally optimised, since the cooling time in particular takes up the largest fraction of the cycle time during fabrication.

Another source of stress comes from UW. Though UW is referred to as a gentle method, because it does not require *e.g.* bulk heating of the part, it is still quite rough to the material at the energy directors. The ultrasonic welding machine used in this study is set to vibrate the sonotrode with an amplitude of roughly 30 µm at a frequency of 20 kHz, while pushing down on the parts with several hundred N. This high frequency compressive force causes the welding by friction heating and hysteresis[104]. Since the vibrations are only applied for a short period of time, the melting and solidification is rapid, thus inducing residual stress.

As mentioned, thermoplastics are more or less resistant to organic solvents, depending on their chemical composition. Immiscible phase filtration systems require application of oil to the chips, and therefore several oils where tested for their compatibility with COC. UW chips were loaded with dyed water into the sample chamber and elution chamber, followed by addition of either mineral oil (Sigma-Aldrich), olive oil (local supermarket), liquid PDMS (Trimethylsiloxy terminated, 450-550 centistokes), or FC-40 oil (Walbom A/S) to the immiscible phase filter. The chips were carefully sealed to avoid evaporation and left for 24 hours. Inspection of the chips revealed that the mineral oil and olive oil had both formed cracks in the chip and diffused out, causing failure of the chip system. Liquid PDMS and FC-40 were compatible with the chip system, evident by intact fluid systems (data not shown). The results fit well with the chemical resistance table from[87] that states incompatibility of COC with aliphatic and aromatic hydrocarbons. Chill-out Liquid Wax (Bio-Rad) was also tested, but caused the chips to dissolve.

It has been observed during this project that bonded chips sometimes tend to form cracks after a few weeks of storage, probably caused by residual stress in the chips. One way of confirming this is by using a plane polariscope to observe the isochromatics and isoclinics caused by birefringence [105]. Unfortunately, the photoelastic constant of COC is -2×10^{-12} Pa^{-1} to -7×10^{-12} Pa^{-1} (www.topas.com/sites/default/files/files/TOPAS_Brochure_E_2014_06.pdf, accessed 2014-06-02), making it impossible to observe isochromatics and hence the shear stress.

Annealing was performed in attempt to avoid cracking. Annealing is a common method for relieving stress from materials. It is a simple heating procedure, where you heat up the material enough to allow the strained molecule chains to relax, but not enough for the bulk material to reshape[102]. The efficiency of the annealing process was evaluated by adding octanol with 10 %(V/V) Span 80 surfactant to PN.14.02B. Three chips were investigated; one where no annealing was performed, one where annealing was performed post-injection moulding, and one where annealing was performed post-UW. The results can be seen in Figure 5.1.

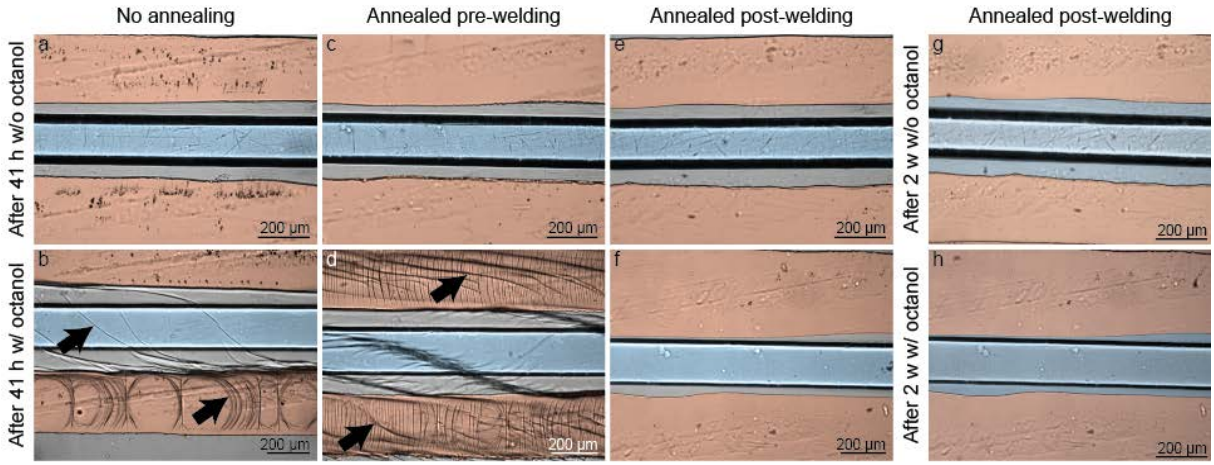

Figure 5.1 Micrographs of bonded chips showing a 200 µm x 150 µm (width x height) channel. The chips were incubated either with or without octanol with 10 %(V/V) Span 80. (a,b) Un-annealed chips without and with solvent after 41 h. (c,d) Chips annealed pre UW, post-injection moulding without and with solvent after 41 h. (e,f) Chips annealed post-UW without and with solvent, respectively after 41 h and again after 2 weeks (g,h). Arrows indicate stress induced cracks. Channels (and gaps) have been coloured blue and welded areas are shown in red for clarity.

It is clear to see from Figure 5.1 that both the injection moulding and UW processes induce stress to such an extent that it causes failure of the system, since chips annealed pre UW also result in failure. However, annealing the chips post-UW makes the chips resistant to octanol w/ Span 80. COC is resistant to octanol, but due to the lipophilic nature of both COC and octanol (plus the added surfactant), the octanol is able to penetrate into microcracks formed by stress and expand these to the point of failure. Another explanation could be that miniscule amounts of octanol are absorbed into the COC, weakening the material and allowing highly stressed areas to fail. Performing annealing post-UW renders the chips immune to such effects, even after two weeks.

The oil that has been used the most in this project is FC-40 oil, composed of a mixture of tertiary amines with perfluoronated carbon chains that is completely inert to COC. The solvents and samples are hydrophilic and for these reasons the chips did not fail, even if visible cracks occurred, reducing the cracks to a cosmetic problem. Since annealing was not required to ensure chip performance with FC-40, annealing was omitted to save time. Chips were usually bonded close to the time of use, to keep cosmetic cracks to a minimum. If at some point annealing becomes a requirement, it is a batch process that can easily process many chips at a time, so it should not affect the overall cycle time too much.

5.2.2 Replication quality and roughness analysis

It is important to investigate the quality of the produced parts when working with replication moulding techniques. Poor replication conformance can be devastating for microfluidic systems, since the microscopic features are easily impacted *e.g.* by incomplete filling of a mould. Surface metrology provides both a controlling and predictive role. Control over the quality of conformance has to do with manufacturing processes and ensuring repeatability. The predictive role deals with the function of the part, also called quality of design *i.e.* how do parameters such as roughness affect the ability of a part to provide its function[106].

Roughness is particularly important for microfluidic systems, because surface forces dominate over volume forces at the microscale. The capillary microvalves of this project depend highly on dimensions[83], and roughness is well known to affect the propagation of liquids[107]. Using an S Neox optical profiler and SPM, the roughness and quality of conformance were assessed for two chip designs of which the mould inserts were either polished or left unpolished.

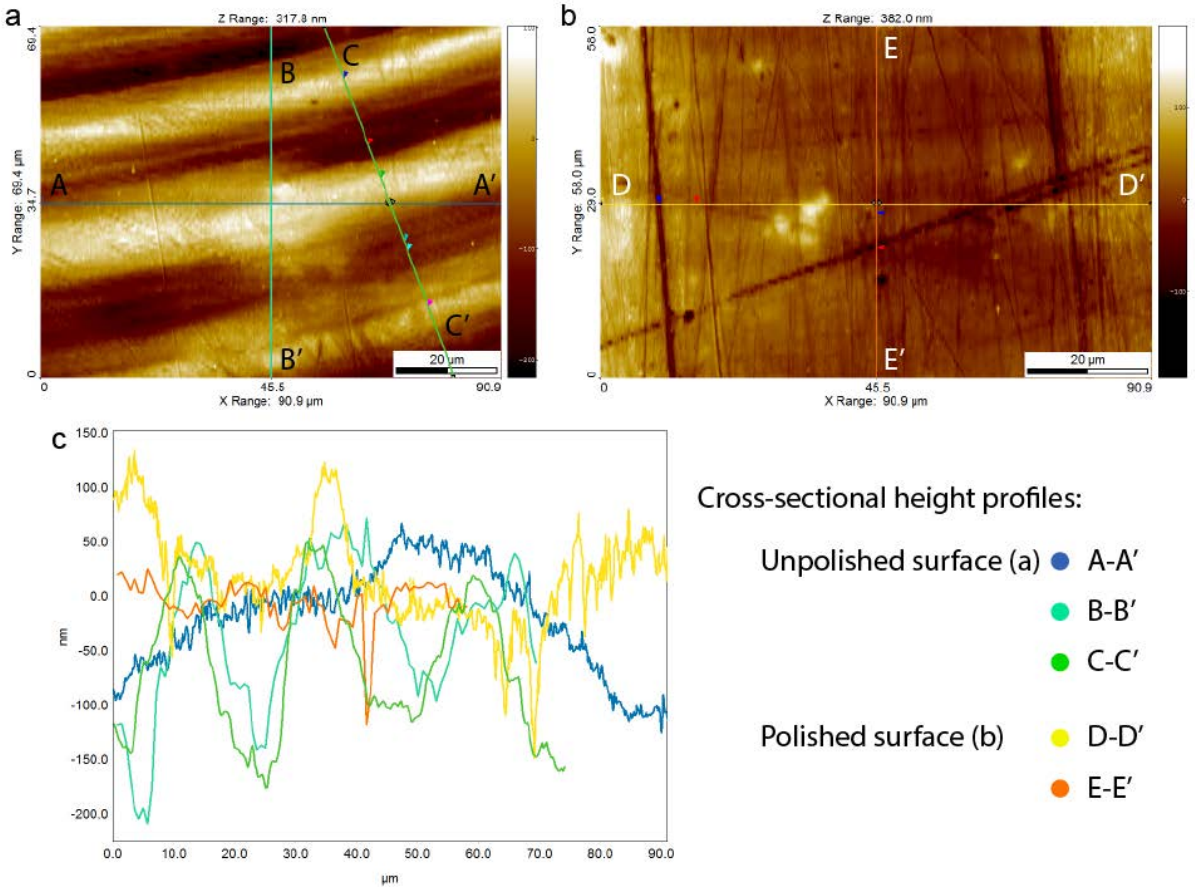

Figure 5.2 shows topographical images of an unpolished (a) and polished (b) mould insert. The micrographs are SPM scans. (c) shows a collection of cross-sectional height profiles from (a) and (b).

Figure 5.2 shows SPM data of the unpolished mould inserts (a), polished mould inserts (b), and interpolated height profiles of the two (c). In (a) the unpolished mould inserts reveal the complex lay pattern of the milling process causing a wavy profile. The polished mould insert presents itself with small scratches, probably caused by particles in the polishing cream. Looking at Figure 5.2(c) it can be seen that the features of the surfaces are about equal in size.

Table 5.1 shows calculated Sq values of the surfaces of Figure 5.2(a,b). A comparable area was analysed using the S Neox optical profiler, where both the mould insert and chip part were investigated.

Table 5.1 Roughness of chip surfaces.

Chip	Analysis tool	S_q (nm)
Unpolished, mould insert	SPM	64
Polished, mould insert	SPM	31
Unpolished, mould insert	Optical profiler	73
Unpolished, chip part	Optical profiler	61

The polished mould insert is about half as rough as the unpolished mould insert, however the roughness in general was satisfactory taking into account the rapid micromilling process. The roughness of the mould insert and the chip part was comparable, indicating that the replication process was of high quality for small structures. This agrees with the data presented by Tanzi and Østergaard *et al.* who used a similar fabrication approach[108].

The replication quality of the parts was further analysed by scanning the entire width of the sample chamber (5 mm) with the S Neox optical profiler using a 20X/0.45 objective. Figure 5.3 shows average profiles of the unpolished mould insert and the produced chip part (light colours), as well as the corresponding polished set (dark colours). Blue indicates mould insert profiles and red indicates chip part profiles.

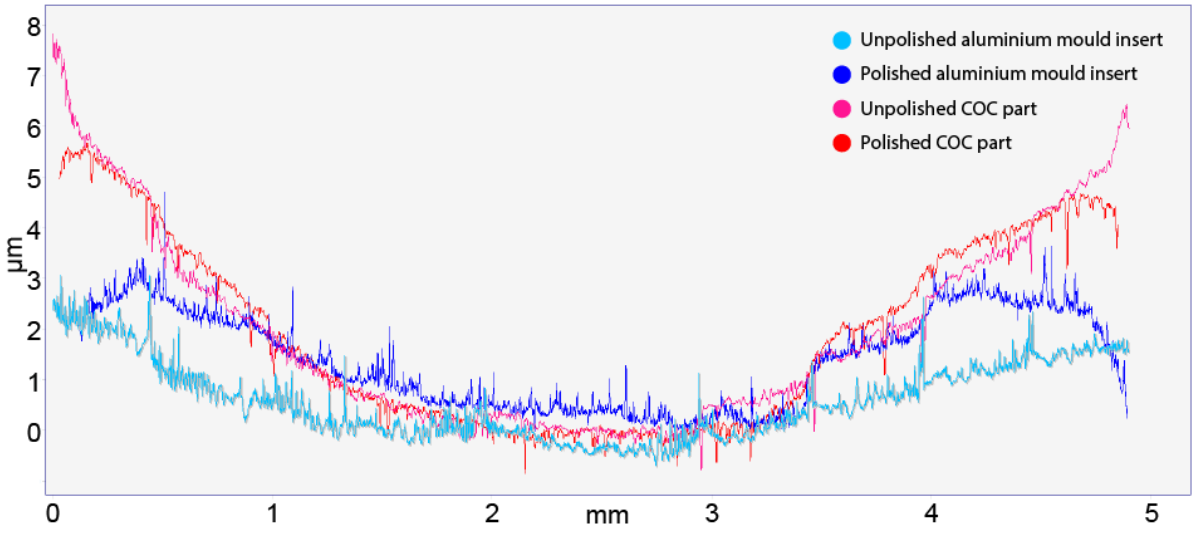

Figure 5.3 Cross-sections of stitched images taken across the entire width of the inlet channel with a 20X objective using the Sensofar optical profiler. Light blue represents the unpolished Al mould insert, while dark blue represents the polished Al mould insert. Pink and red represents the corresponding unpolished and polished injection moulded parts, respectively. The replication as well as flatness of the inlet channel is acceptable with a waviness of about 5 µm over a range of 5000 µm.

There is a good correlation between the mould insert profiles and the chip part profiles, with a slight curvature occurring over the width of the sample chamber. Figure 5.3 shows a waviness of about 5 µm

over a total width of 5000 µm. The mould insert profile data has been flipped to account for the replication process and allow for comparison.

Process validation and hereunder replication quality has been investigated in PolyNano by Matteo Calaon (Department of Mechanical Engineering, Technical University of Denmark) in his PhD Thesis.

The process validation involved quantitative and qualitative evaluation of *finger print* key test structures, consisting of three connected crosses of equal height (62 nm, nominal). The crosses had equal length wings of 10, 2, and 0.5 µm width. The finger print was written with e-beam lithography, followed by conversion of the silicon wafer into a master insert by nickel electroplating. The crosses were placed in the centre of a 22 × 22 μm^2 square master insert and produced in COC (TOPAS 6013, TOPAS Advanced Polymers GmbH). Parts were ejected using side pins to avoid deformation of the finger print. The quality control analysis consisted of channel depth measurements of every cross and covered both the silicon wafer, nickel master insert and polymer part[109].

The results showed that both process parameters (mold temperature, packing time, and packing pressure) and design parameters (channel width and direction with respect to polymer flow) influenced replication fidelity of the finger print, and it was concluded that the width of channels critically affected the vertical replication at sub-µm scale. With a rejection tolerance of ±5% of the norminal dimensions; acceptance rates were 88.9%, 77.8%, and 66.7% for the 10, 2 and 0.5 µm width crosses, respectively[109]. Keeping in mind that the microfluidic chip systems produced in this project are orders of magnitude larger than the largest cross width - and the tendency of the replication fidelity to go up with dimensions, the production quality of the injection moulding process was considered satisfactory and was not further analysed.

Roughness causes contact angle hysteresis and in its most extreme case, local roughness can result in pinning of liquids during their propagation[107]. If the size of the roughness is very small compared to the liquid interface it interacts with, Wenzel's law can be applied to describe the advancing interface. Wenzel's law will not be derived, but was briefly covered in section 2.3 and we can recall from equation (2.8) that it states that $\cos\theta_W = r\cos\theta$, where r is the roughness (defined as the real length of a rough surface, compared to the projected and thus always greater than 1). θ_W is the contact angle on the rough surface and θ is the *true* contact angle on a smooth surface. Wenzel's law implies that roughness will enhance the wetting characteristics of a surface, so if $\theta > 90°$, the roughness will cause an increase in the actual contact angle, θ_W. Since COC is slightly hydrophobic, the roughness was expected to slightly increase the contact angle, which for capillary microvalves is beneficial.

5.2.3 Bonding types, quality and strength

Based on the arguments given in section 3.5 and preliminary bonding experiments with thermal bonding and transfer adhesives, it was concluded that ultrasonic welding was most suited for the manufacturing strategy applied in this PhD project. Choosing ultrasonic welding meant facing a challenge: Ultrasonic machining/welding is applied in a range of markets on a multitude of applications; anything from cutting food, to fusing fabrics, wiring, assembly of small plastic parts, embedding of metal inserts, food

packaging, attaching membranes, *etc*. (see www.telsonic.com/en/application-finder/ for examples, accessed 2015-06-03). However, within the field of microfluidics, the application of ultrasonic welding is limited[73–78]. One issue is that some of the requirements for bonding of microfluidic systems are often stricter than bonding of the examples mentioned above: First, it is required that the welding seam is placed close to the channels to form a tight seal. Second, channel uniformity is often a concern, so the flow patterns of the microfluidic channel system do not change significantly, and may be accurately predicted. Third, the small physical size of microfluidic chips with closely packed channels pose a challenge when designing energy directors. There are guides available to assist with energy director design put out by the companies that supply ultrasonic welding machines, but these guides are aimed at general parts and do not take the above criteria into account (www.emersonindustrial.com/en-US/branson/Products/plastic-joining/Pages/PlasticJoiningLiterature.aspx and www.dukane.com/us/DL_DesignGuides.asp, accessed 2015-06-03).

5.2.3.1 Energy director types

The results of this section were presented in Paper 1 and Paper 3.

Considerable time has been put into optimising energy director design for a microfluidic setting. Starting out with the conventional CNC micro milled butt joints presented in Paper 1, moving onto tongue-and-groove joints presented in Paper 3, laser micromachined butt joints presented in Paper 2 and Paper 3 – and finally laser micromachined micropillar energy directors based on CLPs presented in Paper 4. Sketches of the energy director types are presented in Figure 5.4.

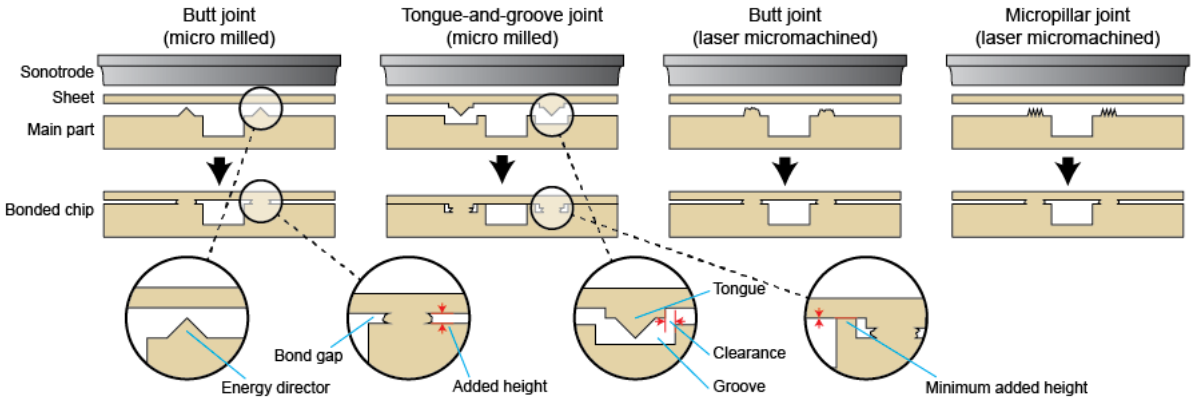

Figure 5.4 Sketches of the different types of energy directors fabricated in this project pre- and post-bonding. From left to right is shown the common butt joint and the tongue-and-groove joint fabricated by CNC micromilling, followed by the butt joint and micropillar type energy directors that were laser micromachined. Sketches are not drawn to scale.

Joints designed for ultrasonic welding can be – and should be – tailored for a given system. Parameters such as part (material, size, structural lay-out), bond strength, hermetic seal, flash, *etc*., all influence the design of an energy director. For this reason a portfolio of joint types exist, but part requirements vary widely and so each part must be treated as unique. There are three key requirements to keep in mind[86]:

1. Parts-to-be-fused must be aligned and laterally constricted so the joint halves do not move during welding (however, they must still be free to vibrate).

2. There must be close uniform contact between the mating surfaces for even energy distribution. Ideally, the surfaces-to-be-fused should be in the same plane and parallel with the sonotrode plane.
3. A small initial contact is required to focus the vibrational energy *i.e.* an energy director. This lowers the amount of energy and time required for melting.

There are two ways to fulfil the third requirement; shear joints and energy directors. Energy directors were chosen for this project, because they are well suited for joining of amorphous polymers like COC. In its simplest form, an energy director is just an apex shaped protrusion, like the one shown in Figure 5.4(left). Since the microfluidic system has no need for alignment, the first design applied in this project simply consisted of an energy director following the boundaries of the channel system, slightly offset. A more advanced form of joint type is the tongue-and-groove joint (Figure 5.4(middle)). By having the energy directors placed on a small plateau called a *tongue* that fits into a *groove*, the tongue-and-groove joint adds the ability to align the two parts-to-be-fused. The groove is basically a smaller corresponding channel system in the other part that can contain the *tongue*. An added benefit of the tongue-and-groove joint is that the *groove* functions as a flash trap preventing the melted polymer to flow into the channel system. Because the critical features of microfluidic systems are much smaller than those of regular parts, the energy directors were made smaller by switching from CNC micro milling to laser micromachining (Figure 5.4(right)).

Figure 5.5 shows SEM micrographs of examples of energy directors of a micro milled butt joint (left), micro milled tongue of the tongue-and-groove joint (middle), and laser micromachined micropillar joint (right). The micro milled energy directors have some roughness to their sides, which is due to the tool path step size and to burrs in the mould insert. The sharpness of the tip of the energy director was limited by the milling tool.

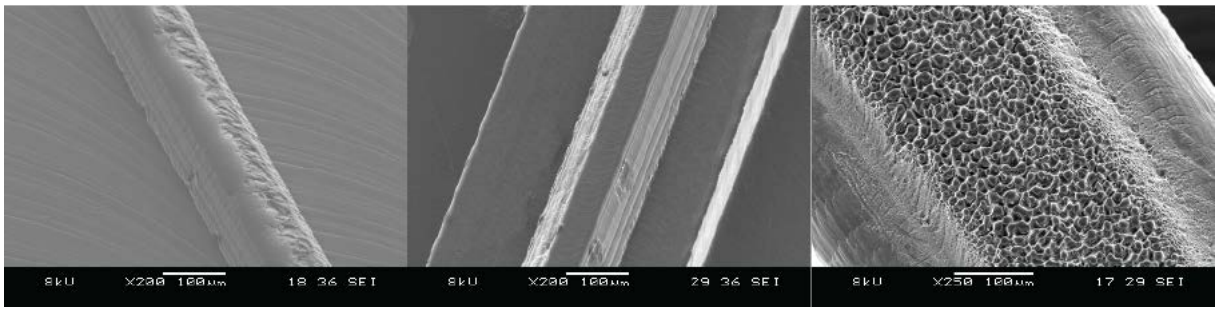

Figure 5.5 SEM micrographs of three types of energy directors as they appear in the COC parts. (left) Micro milled butt joint. (middle) The tongue-part of a micro milled tongue-and-groove joint. (right) Laser micromachined micropillar/CLP energy director. SEM images taken by Carl Esben Poulsen.

The laser micromachined micropillar energy directors have a different morphology than conventional energy directors. They are based on plateaus with variable widths, depending on the chip design. The top of the plateau features a stochaistic pattern of ⌀ = 10 µm pillars spaced approximately 10 µm apart (determined by SEM). The laser micromachined butt joint is not shown, but has the same general morphology as Figure 5.5(right), except the top is not composed of micropillars, but rather of a rough

surface. The overall design resemble the energy directors applied by Lee *et al.* that were 10 µm × 10 µm square protrusions, following the boundary of the channels, fabricated using injection moulding using a mould insert generated via photolithography and nickel electroplating[78].

The main motivation for optimising the energy director design was to address the added height, or more specifically, the bond gaps imposed by energy directors as indicated in Figure 5.4. It is generally expected that ultrasonic welding will introduce an added height of $w/64$, based on a butt joint of width w with an energy director of height $w/8$[110]. This is within tolerance for most normal parts, but as mentioned by Luo *et al.*, the added height becomes proportional with the microstructures when constructing microfluidic devices[75].

Figure 5.6 shows two chips; one with laser micromachined butt joints (a-c, PN.14.02B) and one with micro milled tongue-and-groove joints (d-f, PN.14.02F). The chips were filled with a fluorescent dye to illustrate that fluid was able to flow into the bond gap of the butt joints (a-b), but not into the tongue-and-groove joints (d-e). Further investigation by confocal microscopy revealed a gap between the chip part and sheet part for PN.14.02B (c), whereas no surfaces were found for the tongue-and-groove joint (f), indicating that the tongue-and-groove joint type can be applied to minimise the bond gap.

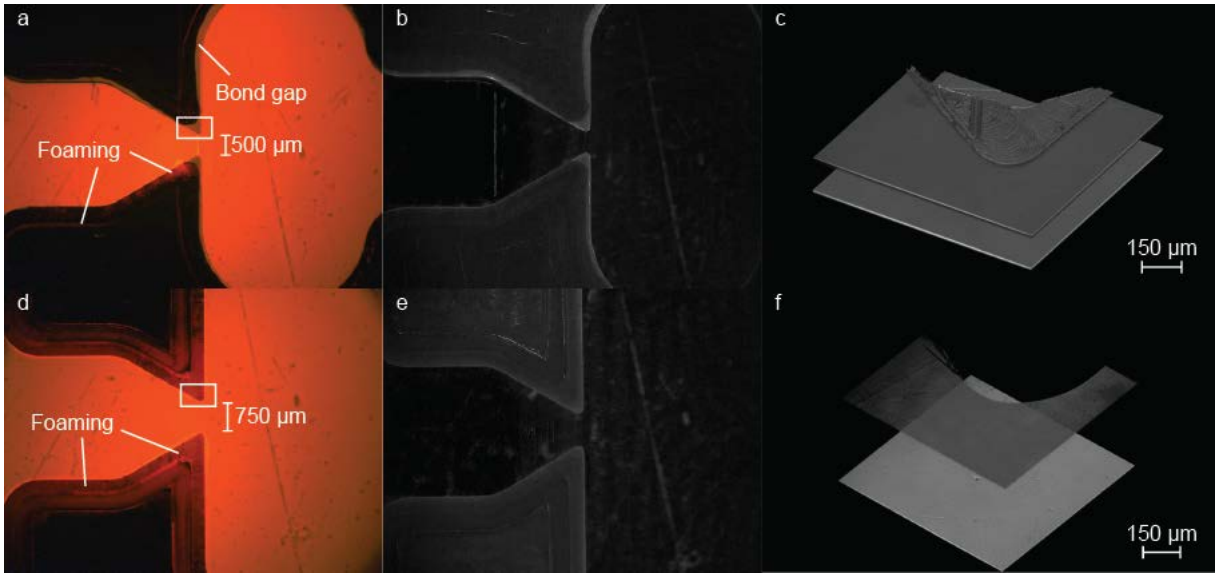

Figure 5.6 Post-ultrasonic welding comparison of laser micromachined butt joint (a-c) and micro milled tongue-and-groove joint (d-f). (a+d) is recorded with fluorescence microscopy. (b+e) recorded with standard bright field microscopy. Note that the foaming, especially present in (d), reflects the light emitted from the rhodamine B solution; however, this is distinctly different from where actual fluid is present around the edges in (a). (c+f) shows a 3D representation of confocal micrographs recorded at the upper corner of the capillary microvalve as marked with the white squares in (a+d) (Zeiss LSM 700 confocal microscope (20x/0.5, z-stack images, 1.590 µm sections). The bottom plane is the outer sheet surface, and the upper plane the inner sheet surface. Note that in (c) the corner of the main chip part is also visible due to the gap, whereas in (f), no such surface exists.

From prototype to prototype, the design of the energy directors has changed, but representative examples of energy director dimensions have been provided in Table 5.2. The micro milled energy directors were always machined with the same 60° apex engraving machine tool, having heights ranging from 100 µm to 150 µm. The laser micromachined energy director plateau widths were specified for each design, but

ranged between widths of 100 µm to 250 µm. The heights varied depending on the laser settings, but were *ca.* 25 µm. The bond gaps were measured to be *ca.* 25 µm for conventional energy directors and *ca.* 10 µm for laser micromachined energy directors. Micropillar energy directors are not presented in Table 5.2, because they followed the result pattern of the laser micromachined butt joints. However, it should be noted that TF.15.01 is different from a design point-of-view in that the energy directors were situated on top of free-standing walls. From figure 4h in Paper 4 it is evident that there was some flash, which argues that micropillar energy directors on free-standing walls have zero to very little bond gap. However, a single SEM image is not conclusive supported by the micrograph in figure 4f (Paper 4) that shows the weld line is not completely uniform.

Table 5.2 Dimensional characteristics of energy directors as measured by confocal microscopy (20x/0.5, z-stack images, 0.942 µm sections) and SEM.

Joint type	Width [µm]	Height [µm]	Bond gap [µm]
Butt joint (micro milled)	250	130	24
Tongue-and-groove joint (micro milled)	145	99	0
Butt joint (laser micromachined)	228	24	9

The lowest recommended size of an energy director is width = 254 µm and height = 127 µm[86], which is similar to the largest energy directors employed in this project. The smaller energy directors means less material to melt and thus a gentler, more controllable welding process. There was a tendency for the lower height energy directors to produce smaller bond gaps, but the effect was without any direct correlation. For the tongue-and-groove joints the bond gap was reduced to zero. The bond gap height varied from chip design to chip design for reasons discussed in the next section. It was tempting to remove the energy directors entirely to reduce the bond gap, but the vibrational heating is then concentrated at the edges of the channels, causing flash. Luo *et al*. presented thermal assisted and solvent assisted ultrasonic welding methods, where they successfully bonded a PMMA chip system without the use of energy directors[75], producing no bond gaps. However, heating and solvents add extra steps to the welding process, undermining the benefits of using ultrasonic welding in the first place.

5.2.3.2 Bond quality

If proper energy director design and structures have been produced, and the right settings applied to the ultrasonic welding machine, it will produce consistent high-strength joints in a rapid fashion – at least in theory. Unfortunately, this is rarely the case. Through-out this project, a number of issues have been encountered while trying to achieve near perfect bonding.

One of the common things to observe is *foaming*. Ideally, ultrasonically welded joints are transparent, because the two parts literally fuse together, leaving no boundary for refraction to occur. If for some reason a joint (or part of a joint) receives too much pressure or energy, small air bubbles will occur causing a foamy appearance. Three different energy directors are shown in Figure 5.7 showing no (a), intermediate (b), or major foaming (c). Though one could expect foamed joints to be of lower strength

than non-foamed joints, this is not the experience in this project, where foaming has generally only caused aesthetically unappealing joints.

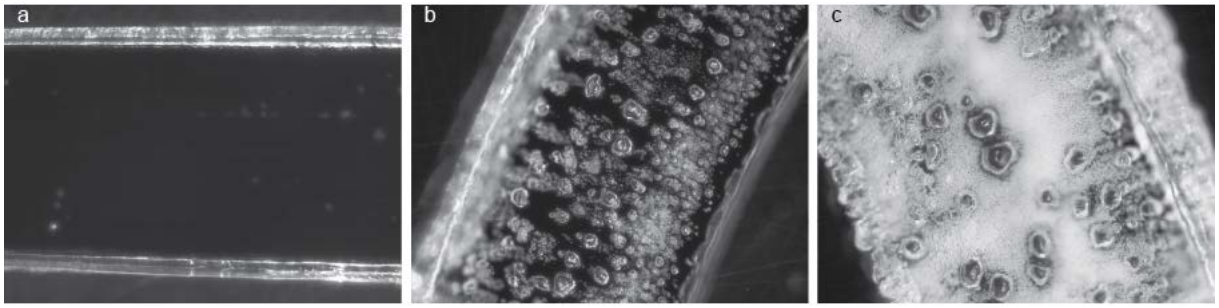

Figure 5.7 Ultrasonically welded energy directors with no foam (a), intermediate foam (b) and lots of foaming (c). Darkfield micrographs were recorded with a Zeiss LSM 700 confocal microscope (10x/0.25). The width of the welded energy directors are all approximately 500 µm wide.

An often met challenge during this project concerns the requirement for uniform contact. The mould inserts fabricated in this project present themselves with some roughness due to relatively low vertical precision when manually changing tools in the milling machine. The moulds are also not fabricated to take polymer shrinkage during the moulding process into account, resulting in slightly warped, uneven parts. The joint types presented thus far are placed directly on top of the main surface of the part, causing the areas that are slightly more elevated due to warpage to be welded first. This has resulted in uneven bonding for some chip designs, and while hermetic joints were always achieved, it did affect bond gaps. Another effect of the warped surfaces was that they sometimes came into contact at the same time as the energy directors, causing some of the energy to go into those contact points (*e.g.* burrs) instead of into the energy director.

As an example, PN.13.03 was prone to foaming near the centre of the chip where the microchannels were laid out in parallel. Because that area contained a local high concentration of energy directors, a large amount of energy had to be deposited into the chip to reduce the bonding gap, causing overwelding at some areas of the chip. This was due to the unsymmetrical nature of the energy director lay-out and uneven part surface. Furthermore, the energy directors were large micro milled energy directors which also meant a large energy requirement.

In Paper 4, a chip design was presented (TF.15.01), where the microfluidic channel system was defined by protruding walls, rather than trenches in a disc. The protruding walls then feature the micropillar energy directors (resembling a macroscopic butt joint). This type of chip provided excellent welds with very little (if any) bond gap, despite not featuring a flash trap. In retrospect, this design type should have been employed much earlier.

5.2.3.3 Bonding strength

The results of this section were presented in Paper 4.

Bonding strength is a critical quality of a bonding technique, and was investigated for the micro milled butt joint and the laser micromachined micropillar joint using the razor blade test[100]. The results are

shown in Table 5.3 along with a comparison with other bonding techniques applied on thermoplastics in the literature.

Table 5.3 Bonding strength expressed in terms of surface energy, γ. [a]Literature surface energies calculated from channel dimensions, Young's modulus, and bursting pressure. See Supplementary Information of Paper 4 for calculations. [b]A two-sample (unpaired) T-test showed no significant difference in the bonding strength between micro milled and laser micromachined micropillar energy directors $t(10)=-1.84$, $p=0.084$.

Bonding method	Material	γ [J/m^2]
UW, micro milled butt joint[Paper 4]	COC TOPAS 5013L-10	[b]100±30
UW, CLP joint[Paper 4]	COC TOPAS 5013L-10	[b]122±23
UV activated thermal bonding[101]	COC TOPSA 5013L-10	61
UV/ozone thermal bonding[111]	COC Zeonor 1020 R	8.1
Solvent bonding (cyclohexane)[112]	COC TOPAS 8007	[a]6.2
Plasma activated thermal bonding[113]	COP ZEONEX	8
Solvent bonding, 75% acetone[114]	PMMA	13.6
Oxygen plasma[115,116]	PDMS	[a]44.4±2
Uncured PDMS as adhesive[115]	PDMS	[a]227

It was found that the two types of energy directors performed equal in regard to bonding strength, *cf.* Table 5.3. Furthermore, when comparing with other bonding strengths found in the literature for thermoplastics, ultrasonic welding provides the strongest fusion. This is likely because all of the other bonding techniques partly rely on chemical modification of the surfaces to cause fusion, whereas ultrasonic welding relies on melting the two parts together.

5.2.3.4 Experiences gathered during energy director development

When setting out to use ultrasonic welding for bonding, very little knowledge was present at the department. Therefore, the general approach recommended by manufacturer guides combined with the limited experience held was followed. This prompted the use of apex shaped engraving tools to micro mill energy directors. It was believed at the time that the parts were so small, that raised plateaus were not needed and little design restriction was put on the lay-out of the energy directors.

With the results obtained from PN.13.03 it was realised that having local concentrations of energy directors complicated welding, since over welding of those areas was often the result. Furthermore, too many energy directors on one chip meant that the welding machine had problems depositing enough energy without causing foaming, and a uniform energy deposition was problematic. The overall product was uneven welds with spot wise foaming and flash. Several initiatives were taken to combat these issues: The total amount of energy directors in a chip design was significantly reduced and the lay-out of energy directors was more spread out over the chip surface. The distance from the energy directors to the channel edge was optimised to reduce flash. Laser micromachining was introduced to provide smaller dimension uniform energy directors. These efforts were reflected in PN.14.02B, which generally bonded satisfactory. Yet, bond gaps were still present and the problem of spot wise bonding over the chip surface remained.

In attempt to remove the bond gap, the concept of tongue-and-groove joints were introduced. Micro milled energy directors were chosen, because their larger size also allowed for easier inclusion of the alignment feature, which was interesting to investigate. PN.14.02F shows the successful implementation of tongue-and-groove joints.

The lower bond gap observed and ease of implementation of laser micromachined energy directors was further investigated and lead to the TF.15.01 design. Here, the spot wise welding was attempted to be solved by raising the microfluidic channel system from the base of the chip to free-standing walls. The results were very promising with arguably no observed bond gap and uniform welds over the whole chip. The free-standing walls also illustrate the flexibility available when introducing energy directors via laser micromachining.

To sum up the experiences gathered, laser micromachining is superior to micro milling for implementation of energy directors to a microfluidic chip-sized device. It is faster to introduce structures and the smaller energy directors yield a more consistent and uniform welding, especially in combination with free-standing walls. The laser micromachining also provide more flexibility in terms of design, while not compromising bonding strength.

5.3 Chip physical performance

The immiscible phase filtration approach relies on the ability of the microfluidic chip to support stable two-phase systems, in this case by use of capillary microvalves – and by the ability to support the movement of magnetic beads, without disrupting the interfaces. Furthermore, many samples have surfactants and lysis agents added to them to aid in accessing the target *e.g.* nucleic acids of bacteria. Surfactants change the surface tension of a solution, which in turn affect the performance of the chip system. These characteristics were investigated before conducting extraction experiments on-chip.

5.3.1 Burst pressures of capillary microvalves

The results of this section were presented in Paper 1.

One way to characterise the ability of the capillary microvalves to stop fluid flow, is to measure their hydrostatic burst pressure. This was done in Paper 1 by using the PN.13.03 chip featuring a range of capillary microvalves (see Table 4.1 for design of chip and dimensions of the capillary microvalves). Section 2.3 covered the theory for capillary microvalves. Briefly, each capillary microvalve is based on a channel that forms a 90° expansion towards the main chip part, causing the liquid to pin at the expansion point, due to the now larger contact angle associated with the triple contact line at this position (see Table 4.1 for a schematic of a capillary microvalve). A setup was constructed to measure the hydrostatic burst pressure of each capillary microvalve. See section 4.4.2 for a description of the procedure. The measured burst pressures were related to burst pressures estimated using (2.12), and burst pressures simulated using COMSOL (simulations were done by C.E. Poulsen). The results are shown in Figure 5.8.

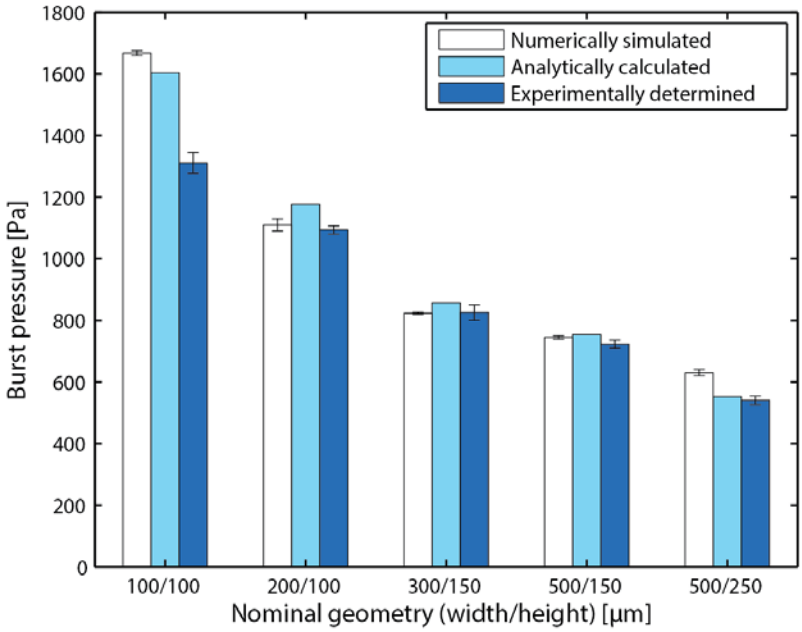

Figure 5.8 Numerically simulated, analytically calculated, and experimentally determined burst pressures of the selected capillary microvalve geometries. Light blue columns represent the burst pressures calculated from the analytical expression equation (2.12). White columns denote the numerically simulated burst pressures, n = 2, 3, 2, 3, and 3 for 100/100, 200/100, 300/150, 500/150, and 500/250 (width/height), respectively. Dark blue columns denote the experimentally determined hydrostatic burst pressures, n=18 for 100/100 and 500/250 and n = 12 for 200/100, 300/150, and 500/150. Error bars represent the sample standard deviation (figure adapted from Paper 1).

Before discussing the results, there are a few things that should be noted about the chip fabrication. At the time, bonding by use of ultrasonic welding had just commenced and the design utilised was CNC micro milled 130 µm high, 250 µm wide, 90° apex shaped energy directors placed 500 µm from the channel edges. This energy director design differs from the standard recommendations *e.g.* from the *Guide to Ultrasonic Plastics Assembly* published by the Dukane Corporation (energy directors should have a 60° angle, be closer to the channels, and the energy director should be wider, see section 5.2.3 for more discussion on this). The more acute angle was chosen to ensure a good quality weld. The conservative placement and size of the energy director was in order to reduce the risk of flash. Unfortunately, ultrasonic welding of the chips left a bonding gap due to incomplete polymer melting, estimated to be 23.9 ± 1.7 µm high around most of the channel, though some flashing also occurred, especially at the small 25 µm × 25 µm channels. The gaps reduced the robustness of the capillary microvalves, since they were no longer completely rectangular in shape and were increased in size. To compensate for this, the chips were coated pre-UW with FDTS using molecular vapour deposition, raising the advancing contact angle of the COC chip surface from 96 ± 3° to 120 ± 2°. Additionally, the micromilling process of the mould insert caused the actual widths and heights of the capillary microvalves to deviate from 1.2-10.7 % from their nominal values (see Paper 1 for values). In Figure 5.8, the actual widths and heights (including added height of bond gap) and measured contact angles were applied in the simulations and calculations of the burst pressures. The structural changes to the channel caused by the bond gaps were not taken into account.

Considering Figure 5.8 there is a good correlation between measured, calculated, and simulated burst pressures, except for the *100/100* capillary microvalve, which has a notably lower experimental burst pressure. The reason for this is thought to be the bond gap. While performing experiments fluid creeped into the gap prior to bursting, effectively lowering the burst pressure. The analytical expression consistently overestimated the measured burst pressures, increasingly, when going from larger (2.2%) to smaller (7%) dimensions (not counting the 100/100 microvalve). The numerically simulated burst pressures deviated 5.2% on average from the experimental values, which is comparable to the 4.5% average deviation of the analytically calculated burst pressures. The numerical simulations have the added benefit that they can be carried out on complex geometries in COMSOL, while the analytical expression is limited to simple geometries. It is believed that the numerical approach presented in Paper 1 can be a valuable tool, when designing complex microfluidic systems featuring capillary microvalves, by allowing for fewer prototype iterations.

It was concluded that injection moulding and ultrasonic welding could be successfully used to fabricate microfluidic chips with robust capillary microvalves that yielded reproducible results. One drawback was the bond gap left by the ultrasonic welding that prompted the inclusion of a FDTS coating, resulting in an additional back-end batch process.

To solve the bond gap problem, the other energy director designs described in section 5.2.3 were implemented in subsequent prototypes. PN.14.02B was fitted with the much smaller laser micromachined butt joints, PN.14.02F featured a CNC micro milled tongue-and-groove joint, and TF.15.01 was fitted with laser micromachined micropillar joints placed on raised walls. The goal was to minimise the post-welding bond gap. For PN.14.02B, the bond gap was measured to be 8 µm high by using confocal microscopy, whereas no bond gap was observable for PN.14.02F. TF.15.01 showed no bond gap, but a tiny amount of flash (see Paper 4, Figure 4). The microvalves of PN.14.02B and F were characterised by measuring their hydrostatic burst pressures as with PN.13.03 and the results can be seen in Table 5.4.

Table 5.4 Analytical and measured burst pressures of PN.14.02B and PN.14.02F. Analytical calculations were based on equation (2.12) with dimensions measured using confocal microscopy. n = 6 for PN.14.02B, n=12 for PN.14.02F, and error is SD.

PN.14.02B		PN.14.02F	
Analytical [Pa]	Measured [Pa]	Analytical [Pa]	Measured [Pa]
590	623±39	706	707±70

PN.14.02B and PN.14.02F showed more variance with an SD of 39 Pa and 70 Pa, respectively, versus an average SD of 19 Pa for PN.13.03. In regard to deviation from the analytical expression, the chips were on par with PN.13.03 with a deviation of 5.6% and 0.1% from the analytical predictions for PN.14.02B and PN.14.02F, respectively. Taking into account that the FDTS back-end process was excluded for these chips and considering the experimental errors, the results are satisfactory.

5.3.1.1 Robustness of performance of chips

Ideally lab-on-a-chip systems should be single-use and disposable to avoid contamination [59,117]. Performing experiments during rapid prototyping in a single-use manner ensures that the chip design is valid as a disposable device. The hydrostatic burst pressure measurements conducted on PN.13.03 provided data for investigating the reproducibility of measurements on the same chip, as well as in-between chips. Table 5.5 shows the acquired data.

Table 5.5 Statistical comparisons of the repeatability of experiments for PN.13.03 on the same chip and in-between multiple chips. Each cell presents the significance (P value) of two sets of triplicate experiments performed on the same chip for each capillary microvalve, as described in section 4.4.2 Bottom row shows comparison in-between chips of experiments performed on a given capillary microvalve. N/A means not acquired. [a]Unpaired two-tailed t test with Welch's correction. [b]Ordinary one-way ANOVA. Cases where there is a significant difference between groups are shown in bold.

Chip #	100/100	200/100	300/150	500/150	500/250
#1	**0.01**[a]	0.16[a]	0.30[a]	0.83[a]	0.20[a]
#2	0.69[a]	N/A	0.13[a]	N/A	0.88[a]
#3	0.74[a]	0.31[a]	N/A	0.07[a]	0.13[a]
#1 vs #2 vs #3	0.283[b]	0.8900[a]	**0.002**[a]	**0.005**[a]	**0.001**[b]

The general reproducibility of experiments was satisfactory with an average CV of 1.7% for measurements performed on one chip; one set of experiments done in triplicate, followed by another set of experiments after washing and drying of the chip (n=6). This type of use mimics that of a lab-on-a-chip system that is re-used, rather than producing a new chip. From Table 5.5 it is evident that only 1 out of 12 sets of experiments showed a significant difference between experiments performed on the same chip before and after the washing/drying step, despite having a low CV. The picture is quite different for the chip-to-chip variation. Here, 3 out of 5 capillary microvalves performed significantly different from chip to chip. These results show that even though a chip performs robustly, there might still be chip-to-chip variation that needs to be taken into account. In plenty of the microfluidic literature, data is produced using a single device, and the demonstrated robustness may be exaggerated. By performing research one chip, one experiment at a time, inter-chip uncertainty is included in the results and accounted for.

5.3.2 Surfactant compatibility

The results of this section were presented in Paper 2.

With a functioning capillary microvalve, the next step is to test its performance with more relevant solvents and magnetic beads. The immiscible phase filtration based devices produced has very versatile applicability due to the magnetic beads, which have a multitude of applications (see [118] for an excellent review by Gijs *et al*). Nucleic acid extraction[10,19], ELISA[14,119], co-immunoprecipitation[23], and cell isolation[22,24] have all been performed using IPF combined with

MBs. All these applications use different solvents, but a common component is surfactants. For this project, surfactants are both important for aiding in lysis of carriers of nucleic acids, like vira or bacteria, and for preventing components of the sample and magnetic beads to adhere to the chip channel surfaces.

Table 5.6 presents the compatibility of PN.14.02B with various surfactants in a common lysis buffer – also presented in Paper 2. A chip was considered compatible if a stable immiscible phase system formed during loading of the chip and a 40 µg magnetic bead cluster could be transported from the sample chamber, through the immiscible phase filter (FC-40 oil), and into the extraction chamber. Three surfactants were tested for compatibility: Triton X-100, Sarkosyl, and Tween-20.

Table 5.6 Compatibility of various surfactants with PN.14.02B including the measured interfacial tensions ($\gamma_{\mathrm{aq,oil}}$ and $\gamma_{\mathrm{aq,air}}$), advancing contact angles on COC in air ($\theta_{\mathrm{aq,COC,air}}$), burst pressures ($p_{\mathrm{burst}}$) calculated using equation (2.12), and $\Delta p = p_{\mathrm{burst}} - p_{\mathrm{hyd}} - p_{\mathrm{luer}}$, where p_{hyd} and p_{luer} were the hydrostatic and capillary pressures of the luer inlet, respectively. A chip was considered compatible if filling of the chip was successful and a 40 µg MB cluster could be transported through the immiscible phase filter without bridge formation. In the case of 0.25% Triton X-100 and 0.125% Sarkosyl, the filling was unsuccessful. All solutions apart from Milli-Q water were prepared from surfactant free lysis-binding buffer.

Solution [(V/V)%]	$\gamma_{aq,oil}$[mN/m]	$\gamma_{aq,air}$[mN/m]	$\Theta_{aq,COC,air}$[°]	p_{burst}[Pa]	Δp[Pa]	Compatibility
Milli-Q water	44.1±0.4	72.0±0.0	96.1±2.6	562	495	YES
0.1% Triton X-100	9.5±0.1	52.8±1.0	63.5±2.6	101	65	YES
0.25% Triton X-100	6.2±0.2	42.8±0.6	50.7±6.5	-4	-36	NO
0.0625% Sarkosyl	7.8±0.2	44.7±1.0	64.0±4.8	89	50	YES
0.125% Sarkosyl	5.3±0.4	39.0±0.6	41.3±5.2	-53	-82	NO
1% Tween-20	8.3±0.2	49.2±0.7	65.6±4.9	111	73	YES

Concentrations up to 0.0625% Sarkosyl and 0.1% Triton X-100 were compatible with the system. Sarkosyl and Triton X-100 are common detergents used for lysis, and ideally larger amounts than the ones compatible with this system are desired for effective lysis buffers. Tween-20 was compatible up to 1%, which is sufficient for these applications. The compatibility was linked to the microvalve burst pressures (p_{burst}) of the system via measured contact angles and interfacial tensions. If the predicted burst pressure was negative, the chip was confirmed to be non-compatible by experiments. Keep in mind that the predictions made here do not take into account the uncertainties introduced by the roughness of the chips, nor the dynamic wetting conditions introduced by surfactants[120,121].

5.3.3 Liquid carry-over determination

The results of this section were presented in Paper 2.

The efficacy of any immiscible phase filtration system relies critically on being able to minimise the amount of liquid that is co-transported with the magnetic bead cluster, since the sample most often contains inhibitors or other components that will interfere with downstream analysis of the sample. The liquid *carry-over* is thus an important parameter to quantify, which was done in Paper 2. The carry-over arises from the complex interplay there is between the sample-oil interface and magnetic bead cluster. Interfacial tension is a complex entity that together with the rest of the system is influenced by a number of parameters. These include, but are not limited to, MBs (size, amount, magnetisation, transport speed, surface chemistry, and morphology); liquid viscosity; dimensions of the capillary microvalve; surface modifications (chemical or physical); magnet geometry; strength of the magnet; magnet to MB cluster distance; any agents altering the intrinsic surface energy of the respective liquids, such as surfactants. When the MBs pass through the sample-oil interface, all of these factors play in and cause a small volume of liquid to be trapped between the beads, and to cover the cluster as a thin film. Figure 5.9 shows single planes of confocal micrographs of a bead cluster placed in a chip that has been filled with rhodamine B containing Milli-Q water, meaning that only the dyed water is visible in the micrographs.

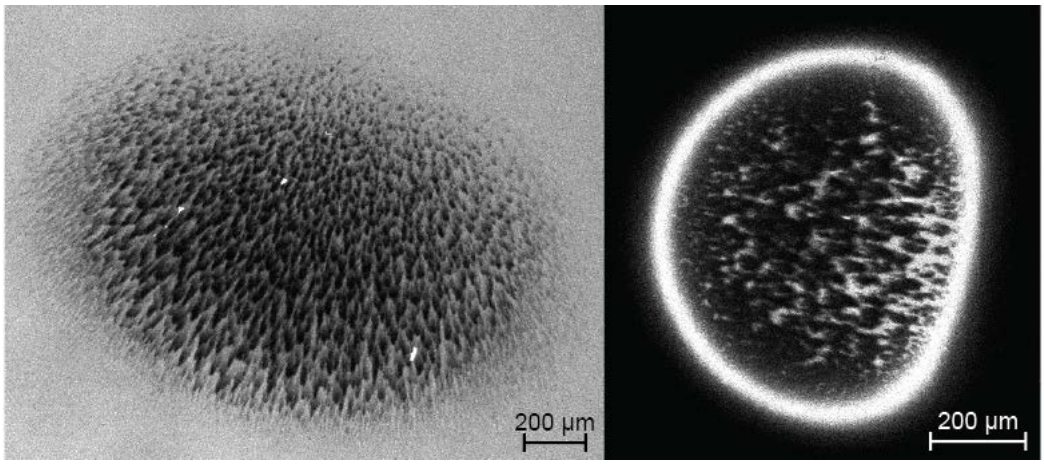

Figure 5.9 Confocal micrographs of a bead cluster in aqueous solution (left) and oil phase (right).

The left part of the figure shows the bead cluster situated in the Milli-Q water, illustrating how the liquid penetrates into the hedgehog-like appearance of the bead cluster. The bead cluster itself is localized on the bottom of the channel, due to the permanent magnet stack situated underneath the chip. The right part of the figure shows the same bead cluster after it was transported into the oil phase, where the carry-over is clearly visible as fluid in-between the beads and as a layer around the cluster.

The amount of target that can be extracted is directly related to the surface area of the MBs and hence the amount of beads supported by the system. Moreover, the size of the bead cluster affects the amount of liquid carry-over. The carry-over was thus quantified *vs.* the amount of MBs, for Milli-Q water and

a lysis binding buffer containing 0.1% Triton X-100 surfactant. Section 4.4.4 provides the details of the quantification procedure.

The results of the liquid carry-over determination are shown in Figure 5.10.

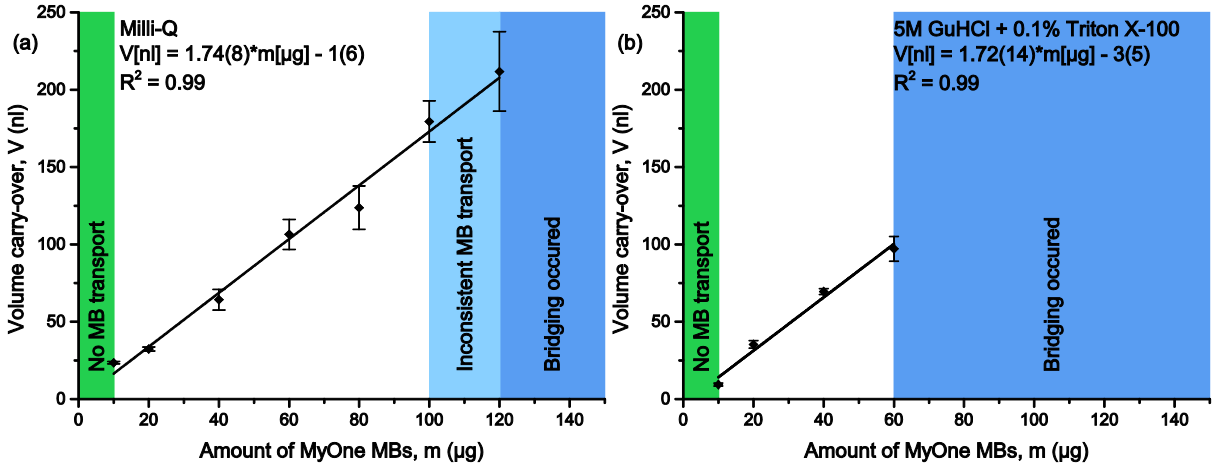

Figure 5.10 The liquid carry-over performed on PN.14.02B of (a) Milli-Q water and (b) 0.1% Triton X-100 in 5M guanidine hydrochloride. The extraction was repeated for different amounts of MyOne SILANE MBs, and the liquid volume carry-over was estimated using fluorescence spectroscopy. The green area sets the lower limit of the system and the dark blue area sets the upper. The light blue area indicates MB amounts where not all MBs could be transferred in one extraction, and the MB extraction therefore had to be done stepwise. n = 3. Figure adapted from Paper 2.

A linear correlation was found between the amount of magnetic beads added and the volume of liquid carry-over, which is in agreement with what was reported by Sur *et al.*[10]. It was not possible to extract magnetic bead clusters lower than 10 µg, because the magnetic force could not overcome the interfacial tension of the sample-oil interface, meaning the beads would get left behind at the capillary microvalve (see Figure 5.10). For Milli-Q water (Figure 5.10a), the bead cluster got partly stuck in the capillary microvalve during extraction of 100 µg or more magnetic beads, however the beads could still be extracted in a sequential manner. Above 120 µg of MBs the oil was unable to close around the magnetic bead cluster, causing a liquid bridge to extend through the immiscible phase filter and into the extraction chamber, resulting in failure of the system. The average volume carry-over was deduced to be 1.74 ± 0.08 nl/µg. For Lysis buffer with 0.1% Triton X-100 (see Figure 5.10b), an average carry-over of 1.72 ± 0.14 nl/µg was found. It was not possible to perform partial extraction for the surfactant containing solution, and liquid bridging occurred already at 60 µg. No statistical difference was found between the carry-over for Milli-Q water and the surfactant containing lysis buffer. The carry-over of the system was compared to other systems reported in the literature in Table 5.7. There seems to be a general tendency in the literature for lower carry-over with larger bead diameters, yet such a conclusion should be made with caution. As mentioned above, the immiscible phase system is influenced by a number of parameters and these systems differ greatly in regard to; MB characteristics, type and dimensions of the capillary microvalve; material of the chip; volumes, and types of the solvents/oils used.

Table 5.7 Summary of liquid carry-over reported for microfluidic chip systems in the literature that use MB-based SPE via IPF. Volume denotes the starting (sample) liquid volume. *Indicates that the values were not stated directly, but had to be estimated. [a]indicates an *open* system with no lid. [b]indicates a *closed* system with lid and walls. [c]indicates a *closed* system with virtual walls.

Study	Volume [µl]	Avg. carry-over [nl/µg]	Bead type	Bead diameter [µm]	Bead mass [µg]	Surfactant	Immiscible phase
Shikida *et al.*[18][a]	50	0.08	Non-commercial	32.7	150-600	None	Silicone oil
Chen *et al.*[119][b]	0.14	0.39	Bangs laboratories	3.18	9*	None	Silicone oil
Berry *et al.*[11][b]	8.5	N/A	Oligo-dT Dynabeads	2.8	6*	1% TX-100	Olive oil
den Dulk *et al.*[12][c]	14	0.86	M-270 COOH Dynabeads	2.8	150	None	Air
Paper 2[b]	200	1.74	MyOne SILANE	1	10-120	None	FC-40 oil
Paper 2[b]	200	1.72	MyOne SILANE	1	10-60	0.1% TX-100	FC-40 oil
Sur *et al.*[10][a]	611	2.02	Ambion MagMax	0.45	40-180	None	Liquid wax

The system presented in this project and the one presented by Sur *et al.* are both able to analyse 150+ µl of sample, which is important because the concentrations of targets in a patient sample may be too low to be detected in small volumes. Berry *et al.* have also recently presented a system capable of handling volumes up to 500 µl. They do not write the mass or size of the MBs (MagAttract Suspension F, Qiagen) they use, but present that they have a 1.7%±0.2% volume carry-over amounting to *ca.* 8.5 µl[16].

The following section is quoted from Paper 2 since no further elaboration was called for. Table 5.6 illustrates well the large impact surfactants have on the burst pressure of capillary microvalves by modifying the interfacial tension between the aqueous solutions and the immiscible phase ($\gamma_{\mathrm{aq,oil}}$). The value of $\gamma_{\mathrm{aq,oil}}$ is important, since it, together with $\gamma_{\mathrm{oil,surface}}$, defines the force the MB cluster must overcome to enter the immiscible phase. Moreover, it sets the energy scale for the interface between the oil and the aqueous phase. The presence of surfactants modify all involved surfaces and interfacial tensions [120,121] and to get a full picture of when bridge formation will occur, the total energy associated with the surfaces, $\Delta E = \Delta A\left(\gamma_{\mathrm{aq,surface}} - \gamma_{\mathrm{oil,surface}} + \gamma_{\mathrm{aq,oil}}\right)$ should be considered. ΔA is the change in the footprint area of the solutions. Berry *et al.*[11] also comments on this equilibrium while discussing liquid bridge formation and points to unexpected results, because some reagents affect multiple parameters, *e.g.* $\gamma_{\mathrm{oil,surface}}$ may change after contact with the surfactant molecules. However, the value of $\gamma_{\mathrm{aq,oil}}$ still hints at whether liquid bridge formation will occur, since a small $\gamma_{\mathrm{aq,oil}}$ will increase the likelihood of a positive ΔE, implying a lower risk of bridge formation. This is consistent with our observation that higher amounts of MBs can be successfully transported through Milli-Q water ($\gamma_{\mathrm{aq,oil}} = 44.1\ \mathrm{mN/m}$ than the 0.1% Triton X-100 containing solution ($\gamma_{\mathrm{aq,oil}} = 9.5\ \mathrm{mN/m}$).

One might expect that a decrease of $\gamma_{\mathrm{aq,oil}}$ would also result in a larger carry-over, since the interface between the liquids will exert less force on the sample solution covering the MB cluster, and a decrease

in $\gamma_{aq,surface}$ would allow for the sample solution to easier wet the COC surface. This is not observed and can possibly be explained by the complex nature of the total energy associated with the surfaces, as stated above. In addition, the capillary microvalve used in this system is geometrical and hence imposes a physical restriction on the movement of the MB cluster, compared to *e.g.* the capillary microvalve employed by den Dulk *et al.*, which consists of two parallel glass plates selectively modified with a hydrophobic coating[12]. This system allows for the MB cluster to expand into the hydrophobic regions, since there is no physical barrier forcing the MB cluster together at the capillary microvalve. When the magnetic beads are exposed to a magnetic field, they align to the field, forming chains. Combining this with the physical compression of the channel wall, a hedgehog like structure of interlocking bead chains is formed. This is thought to be the reason behind the beads getting stuck for clusters of 100 µg or more.

There are ways to increase the burst pressure of a capillary microvalve system. A material with a lower surface tension could be selected (*cf.* Young-Laplace law (2.11)). TOPAS 5013 (the COC grade used in this project) has a contact angle of 96.1° with water, putting it in the higher end of thermoplastics, but it is not enough for *e.g.* a 0.25% Triton X-100 containing solution. It would be an option to use *e.g.* FDTS coating to further increase the contact angle, but this adds another back-end process, which is impracticable from a production viewpoint. Changing material is also an option, but high contact angle fluorinated polymers like polytetrafluoroethylene (PTFE, θ = 109°, www.accudynetest.com/polytable_03.html, accessed 2015-06-06) are expensive, unfriendly to the environment, and most of them opaque (though they are bondable with ultrasonic welding). PP and PE are candidates that could be investigated, though they do not show as high contact angles as the fluorinated polymers. Increasing the contact angle by inducing roughness in the surface by means of laser ablation has been attempted without success. The surfactant containing solutions all have contact angles lower than 90° (*cf.* Table 5.6) with COC and penetrate the cavities of the surface, causing the liquid to go from the cassie-baxter state (2.9) to the wenzel state (2.8), nullifying the contact angle-enhancing effect.

In conclusion, the immiscible phase system relies on open interfaces between the sample, oil, and extraction buffer, and dependents on the total energy ΔE of the system, making it fragile and inherently vulnerable to surfactants – at least when they are constructed in a planar fashion. Sur *et al.* who presented the original immiscible phase system actually used a gravity assisted design, which circumvents this problem[10]. If high levels of surfactants are required for extraction of a given target, one should consider other approaches.

5.3.4 Investigation of the magnetic force applied to the bead clusters during extraction

The results of this section are part of a manuscript currently in preparation together with Karen S. Jørgensen and estimations of the magnetic force based on micrographs was conducted by her. Only some of the results are shown here, but due to the incomplete nature of the manuscript it is not included as appendix.

To further the fundamental understanding of the IPF microfluidic system presented in this project, the magnetic force experienced by the bead cluster was quantified. Sections 2.4 and 4.4.5 provide the details as to how the x-component of the magnetic force ($F_{\text{magnetic},x}$) was estimated.

As stated in equation (2.13), the movement of the bead cluster is a balance between $F_{\text{magnetic},x}$ that is the main driving force of the system and the frictional forces (F_{friction}) acting on the bead cluster plus the energy barrier formed by the capillary microvalve ($F_{\text{capillary}}$).

Figure 5.11 shows the force profile of four series of experiments where the distance from the permanent magnet stack to the bead cluster (z_0) was varied.

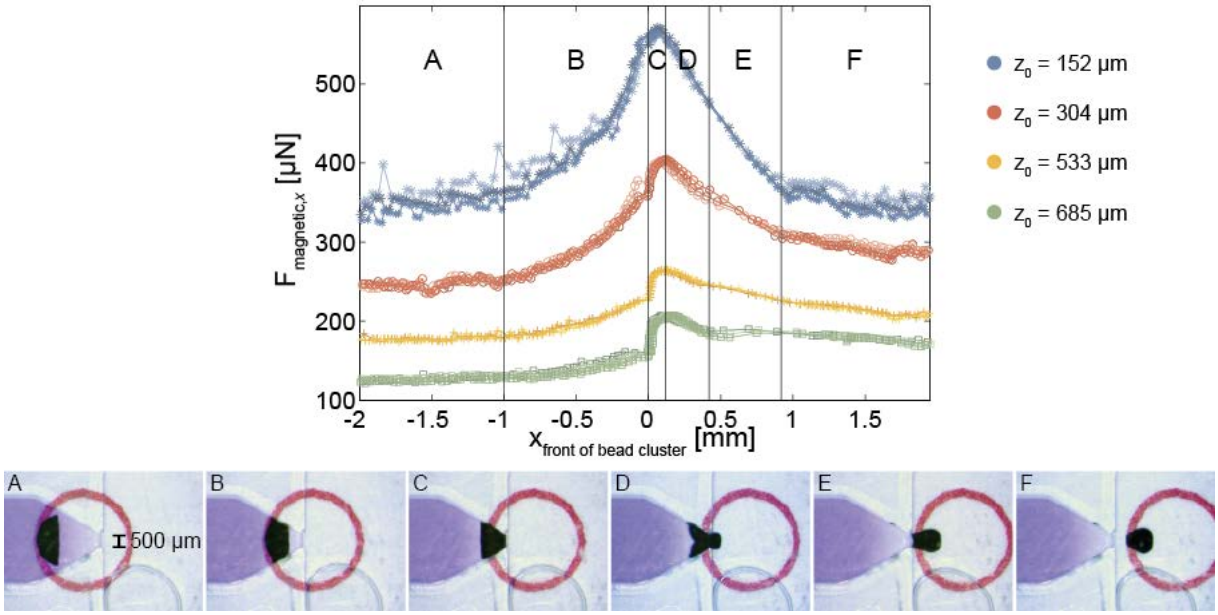

Figure 5.11 Magnetic force calculations *vs.* the position of bead clusters being pulled from the sample chamber (blue dye) and into the immiscible phase filter. The inner diameter of the magenta circle denotes the position of the magnet. Four series of experiments were conducted, where the vertical distance from the top magnet surface to the floor of the micro channel (z_0) was varied, *cf.* Figure 2.4. Blue, red, yellow, and green lines correspond to a 152 µm, 304 µm, 533 µm, and 685 µm distance, respectively. $x_{\text{front of bead cluster}}$ denotes the position of the front of the bead cluster relative to the capillary microvalve. The graph is divided into phases from A-F corresponding to different situations illustrated by the inserts. (A) A bead cluster moving freely in the aqueous phase. (B) The channel walls start to press on the bead cluster. (C) The bead cluster reaches the interface between the aqueous phase and the oil phase. (D) The meniscus bulges into the oil chamber. (E) Pinch-off occurs, where the bead cluster separates from the aqueous phase. (F) Free bead cluster movement in the oil phase.

The inserts A-F provide overview micrographs of the extraction process to better illustrate the force profiles. Following the micrographs: (A) A slight increase in $F_{\text{magnetic},x}$ is observed in response to the decreasing cross-sectional area of the channel, causing F_{drag} to increase. (B) Further constriction of the cross-sectional area, combined with the beads touching the walls of the microchannel causes the frictional forces to have a more prominent effect on the force profile. (C) The bead cluster comes in contact with the liquid/immiscible phase interface, causing $F_{\text{capillary}}$ to exert its effect and a noticeable jump in the force profile. (D) Once the capillary microvalve is traversed, the bead cluster bulges into the immiscible phase filter, causing a drop in $F_{\text{magnetic},x}$. (E) As the bead cluster is pulled free from

geometric constrictions the force profile continually drops until the interface is fully closed behind the bead cluster. (F) $F_{\text{magnetic},x}$ is once again constant since the bead cluster is now moving across the large immiscible phase filter, only affected by the friction of the surface and drag, albeit these forces are slightly higher in the FC-40 oil, than in the water.

The results show good reproducibility, confirming a low inter-chip variation and from the force profiles it is easy to dissect the different phases of extraction. The overall shape of the force profile is similar to the one shown by den Dulk *et al.*[12] in their similar analysis, but the detailed force profiles are different, which can only be expected due to the many differences between the two systems.

From Figure 5.11 it can be seen that the closer the permanent magnet stack is to the bead cluster, the more force is needed to overcome the frictional forces (assuming the capillary force is not influenced by variations of z_0). $\mathbf{F}_{\text{magnetic}}$ increases as the permanent magnet is placed closer to the bead cluster causing it to be pulled more towards the floor of the microchannel and grow more compact and rigid. A lower $\mathbf{F}_{\text{magnetic}}$ yields a looser bead cluster arrangement, allowing it to mould itself to the shape of the channel. There is a delicate balance here. A very rigid bead cluster can clog the capillary microvalve and the increased downward pull of the magnet can cause the bead cluster to stick to the floor of the microchannel. On the other hand, if $F_{\text{magnetic},x}$ is reduced too much it will not be able to overcome the counter-balancing forces at the capillary microvalve, causing the bead cluster to be left behind. For the experiments shown here it was not possible to extract the bead cluster when $z_0 > 533$ µm. The key is to strike a balance where robust extraction can be achieved.

5.4 On-chip MRSA sample extraction and quantification

The work on sample extraction is on-going and regrettably only preliminary data is available to be presented here, as the PCR assay and extraction process are still being optimised. The results presented were achieved in collaboration with Karen Skotte Jørgensen.

To illustrate the functionality of the manufactured IPF chip system, a series of experiments aimed at extracting Methicillin-resistant *Staphylococcus aureus* from a complex biological matrix (bovine whole blood) were performed.

MRSA is a highly relevant pathogen that is a major source of infections world-wide [122]. Many different strains of MRSA exist, but most of them carry the *mecA* gene encoding the low-affinity penicillin-binding protein, yielding it resistant to beta-lactam antibiotics. For this reason, detection by PCR ia an obvious approach to confirm the presence of MRSA for proper diagnosis and treatment of patients[123,124]. Recently, a new *mecA* gene homologue dubbed *mecC* has emerged in MRSA strains. *mecC* is not detected by the conventional laboratory analysis, calling for novel assays[125]. The presence of *mecA* in many coagulase-negative *Staphylococcus spp. e.g.* the non-pathogenic Methicillin-resistant *Staphylococcus epidermidis* (MRSE) further complicates matters, as contamination of patient samples by *S. epidermidis* on the skin can cause false positives[124]. The IPF approach opens up for pre-selection of MRSA from a complex sample matrix containing both MRSA and MRSE, by using

antibody-labelled MBs specific for MRSA[126]. An assay that selectively isolates MRSA from complex biological matrices using the IPF microfluidic chip followed by off-chip multiplex PCR is currently under development in our laboratory.

Figure 5.12 presents preliminary results where $1{:}10^1$-$1{:}10^5$ dilutions of over-night MRSA culture were spiked into whole blood. The MRSA was then isolated with antibody labelled MBs using the PN.14.02B chip and quantified off-chip by qPCR. The performance of PN.14.02B was evaluated by comparing quantification cycles (C_q) of the extracted samples with reference samples where the culture dilutions were directly quantified by qPCR. Three controls were also prepared: One, where unlabelled magnetic beads were used (*no antibody* control) to confirm the specificity of the beads. One, where no MRSA was added to the whole blood to provide a background signal for the extraction. One no template control (NTC), where the PCR was run without MRSA to provide the background of the PCR.

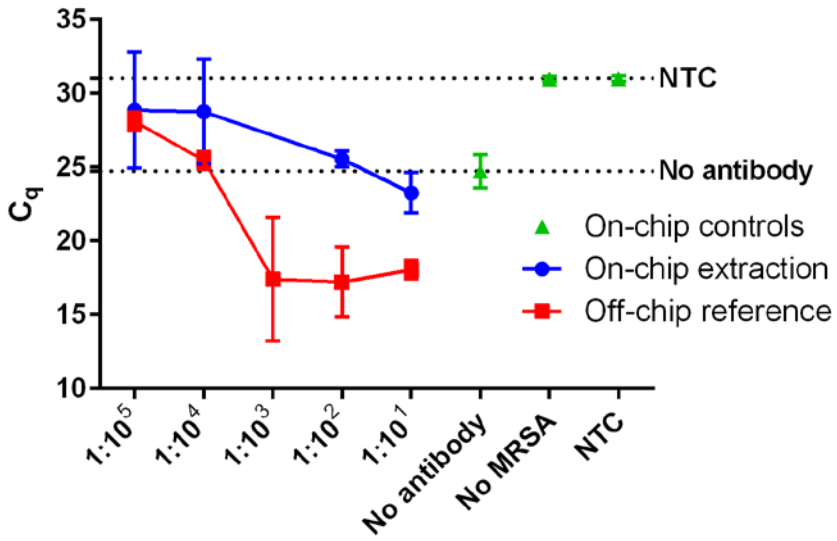

Figure 5.12 qPCR data from the extraction experiments. Blue dots denote the C_q values of the extracted samples, whereas red squares denote the C_q values of the off-chip reference samples. Green triangles denote C_q values of the extraction controls with unlabelled beads, without presence of MRSA, and the no template control. n=4 for all samples, except for the NTC where n=3. Error bars show the standard deviation. Dotted lines indicate the C_q values of the NTC and No antibody controls.

It was possible to detect MRSA in all the extracted samples (blue circles), however, the most diluted samples had a lot of variation. In theory, the C_q values should increase by 3.3 for every 10 fold dilution, resulting in a slope of -3.32 for a linear fit (PCR efficiency $= 10^{(-1/\text{slope})} - 1$). This is not the case here (slope = -1.42, $R^2 = 0.94$), indicating either inefficient MRSA capture from the samples or an inefficient PCR. The three highest concentrations of reference samples (red squares) were associated with the same C_q, but looking at the actual qPCR curves (data not shown), it was evident that the PCRs were inhibited by the very high concentration of MRSA since they did not elicit the characteristic "S" shaped curve of a PCR. For the $1{:}10^4$ and $1{:}10^5$ reference samples the PCR curves looked normal. The control with no MRSA had a C_q comparable to the NTC, which was expected. The *no antibody* control had an average C_q value of 24.7, slightly less than the $1{:}10^5$ diluted reference sample for which the average $C_q = 25.5$.

The efficacy of immunocapture was assessed by counting the colony forming units (CFUs) of samples grown over-night on potato dextrose agar plates (see section 4.5.2 for experimental details). Off-chip immunocapture and extraction from $1{:}10^5$ diluted MRSA culture samples using 40 µg of labelled magnetic beads yielded an average CFU of 68, which was comparable to the positive control (directly plated $1{:}10^5$ diluted MRSA culture samples) that yielded an average CFU of 68. Off-chip immunocapture and extraction using unconjugated beads yielded an average CFU of 12, suggesting unspecific binding of MRSA to the beads.

By comparing the extracted samples with the off-chip references, it is plain to see that the extracted samples were detected at higher C_q values than the reference samples. There are a number of possible explanations for this discrepancy. For the C_q of the extraction sample and reference to be identical, it would require a perfect extraction where every single MRSA cell was captured by the beads and transferred to the PCR tube. In the experiments conducted the outlet chamber contained 75 µl, whereas the reference samples were based on 50 µl volumes, causing the extracted samples to be diluted by a factor of 1.5 amounting to approximately 0.5 C_q. Furthermore, it is known that the MBs will carry along with them approximately 100 nl of liquid per 40 µg of MBs. Whole blood contains PCR inhibitors such as haemoglobin that might also affect the C_q. Morever, it cannot be expected that 100% of the MRSA present in the samples was captured, despite what the plating experiments suggest. Keep in mind that platings were prepared from pure culture, whereas the extractions were performed on whole blood samples, which is a much more complicated matrix.

In the conducted experiments, the antibodies were first conjugated to the magnetic beads followed by incubation with the bacteria. Both the bacteria and MBs are about 1 µm in diameter and thus the interactions between the antibody-bead complex and bacteria are limited by the migration during mixing. A different approach would be to add the antibodies to the sample first, allowing them to diffuse and bind to the bacteria, since this is the weakest bond. However, when conducting many experiments (and for a commercial system) it is more convenient to have the MBs pre-labelled.

The *No antibody* control based on a $1{:}10^1$ dilution was expected to yield a C_q value equivalent to a 1:8000 reference dilution of MRSA, taking into account the contribution from MRSA in the carry-over volume. This fits well with the results shown in Figure 5.12, where the *No antibody* control has a slightly lower C_q than the 1:10000 reference.

The designed chip system will ultimately serve as a means of rapid extraction of biological targets from complex samples. The results presented here provide the first steps, illustrating the basic functionality of the chip.

Chapter 6 Conclusions and outlook

The goal of this PhD project was to explore the potential of using production-ready techniques for rapid prototyping of microfluidic chip systems. Development of an all-polymer device for sample extraction using MB-based SPE via IPF served as case study for the overall methodology. The strategy was to employ injection moulding for part fabrication and ultrasonic welding for fusion of the parts of the microfluidic chip system.

Injection moulding was already an established technology at DTU Nanotech before the beginning of this project. With a macro mould already present, the injection moulding of parts could be commenced quickly by simply fabricating a mould insert. The IPF devices require relatively large channel dimensions, which allowed for using micro milling to fabricate the mould inserts. This was advantageous from a rapid prototyping viewpoint, since clean room fabrication is much more time-consuming and expensive. Once the polymer had been selected and an injection moulding protocol developed, going from design to injection moulded parts could be accomplished within a day.

An ultrasonic welding machine was also present at DTU Nanotech, however, the know-how of the technology was limited and thus integrating ultrasonic welding into the work-flow required more elaborate work. Using ultrasonic welding required implementation of energy directors as a structural element of the parts, meaning they had to be introduced at the design stage. With micro milling and injection moulding it was straight forward to include the energy directors in the fabrication of the part, while the main challenge was choosing a proper design that provided satisfactory bonding. Design guides for energy directors are generally aimed at larger parts, and thus, ideal dimensionality and shape of the energy directors for microfluidic systems had to be uncovered. Moreover, a type of design that could be quickly implemented was preferred. After several attempts, the most successful approach was to implement energy directors by laser micromachining the finished mould inserts, as a back-end process. The short processing time of laser micromachining combined with the capability to generate small structures provided the needed functionality. For the IPF devices, laser micromachined micropillar energy directors were sufficient to create a functional device, though bond gaps had not been completely eliminated. Bond gaps could be further reduced by raising the microfluidic channel system, so the channels themselves were made from protruding walls on which the energy directors were placed. This greatly lowered the contact area between the chip parts and generated the best results with no (or minimal) detectable bond gap.

IPF systems are very dependent on the physical and chemical environment of the device, and even slight changes to samples or buffers can cause the system to fall out of balance. Over the course of the project, several different sample matrices and targets have been investigated, causing a prolonged optimisation process for each system. Looking back, choosing a different case study than IPF devices would probably

have been more productive, and for the same reason, only preliminary results on extraction have been presented in the thesis. On the other hand, the delicate nature of IPF forced the investigation on elimination of bond gaps, catalysing the development of new energy director designs. Furthermore, development of new prototypes require short design-to-experiment cycles, since the optimal design is not known in advance. In the beginning of the project the mould insert fabrication was outsourced to other partners in PolyNano, who were to fabricate the master inserts in the clean room. Unfortunately, the turn-around time from a design was submitted to a master insert was delivered was too long, because of the nature of clean room fabrication. It was concluded that fast prototype iteration was more important than the features the clean room could provide, which prompted the search for alternative master insert fabrication methods.

Working with injection moulding and ultrasonic welding for rapid prototyping has been considered a success. One of the major concerns was if mould inserts of sufficient quality could be generated fast enough to keep up with other rapid prototyping techniques. This was achieved by use of micro milling. The injection moulding itself provided excellent replication conformity down to nanoscale and the relatively large dimensions of the microfluidic system allowed for easy fabrication of parts. The use of ultrasonic welding for bonding was met with some challenges, since the concept of the energy directors had to be reconsidered for the miniature scale of microfluidic systems. In the end, methodology for fast introduction of micropillar energy directors via back-end laser micromachining was developed. This technique provided quality bonding at a much faster pace than related bonding methods. All in all it is concluded that the developed rapid prototyping methodology is well suited for rapid prototyping and provides the benefit of easier technology transfer from academia to commercial applications.

The literature often highlights the high initial cost of injection moulding machines as the primary reason for their limited use. However, the concept of using a macro mould with mould inserts has great potential. The main issue is the lack of standardisation in the microfluidics community. If standard microfluidic formats existed, such master moulds could be purchased as a commodity or kept at injection moulding service providers. The laboratories would thus only need to produce mould inserts that are far easier and cheaper to fabricate with methods generally available. Alternatively, mould insert designs could be evaluated at the laboratories by using hot embossing that only requires a simple thermal press. Initiatives to introduce standardisation are currently underway by the large international networks like the Microfluidics Consortium (www.cfbi.com/microfluidics.htm, accessed 2016-06-29), and hopefully their work will bring a wider implementation of mass-production technologies like injection moulding into the microfluidics community.

Functional IPF devices could be fabricated with a short cycle time, allowing single-use chip research. Disposing chips after each experiment removed the hassle of cleaning chips and verified that the designs were robust. The concept of single-use chip research provides a platform that is much closer to real application and takes one step further away from the unfavourable *chip-in-a-lab* situation by eliminating the concept of a *favourite chip* that is cleaned and re-used over and over by a given researcher.

Further development and optimisation of the IPF chip system is underway and will be continued in a planned postdoc. However, it is stressed that the IPF system in its current form is problematic to develop to some extent, since the fragile balance of the surface energies is influenced by so many parameters. Other design approaches *e.g.* taking advantage of gravity can probably assist in this matter. Take note that these challenges are entirely related to the IPF system and not to the rapid-prototyping strategy.

The methodology applied in this project was not more taxing or time consuming than alternative approaches to rapid prototyping and is highly recommended for rapid prototyping. Especially for systems without components that are as critically dependent on the microenvironment, such as the capillary microvalve.

References

[1] G.M. Whitesides, The origins and the future of microfluidics., Nature. 442 (2006) 368–73. doi:10.1038/nature05058.

[2] E.K. Sackmann, A.L. Fulton, D.J. Beebe, The present and future role of microfluidics in biomedical research, Nature. 507 (2014) 181–189. doi:10.1038/nature13118.

[3] S.C. Terry, J.H. Jerman, J.B. Angell, A gas chromatographic air analyzer fabricated on a silicon wafer, IEEE Trans. Electron Devices. 26 (1979) 1880–1886. doi:10.1109/T-ED.1979.19791.

[4] A.Y. Fu, C. Spence, A. Scherer, F.H. Arnold, S.R. Quake, A microfabricated fluorescence-activated cell sorter, Nat. Biotechnol. 17 (1999) 1109–11. doi:10.1038/15095.

[5] H.-P. Chou, C. Spence, A. Scherer, S. Quake, A microfabricated device for sizing and sorting DNA molecules, Proc. Natl. Acad. Sci. 96 (1999) 11–13. doi:10.1073/pnas.96.1.11.

[6] R. Mariella, Sample preparation: The weak link in microfluidics-based biodetection, Biomed. Microdevices. 10 (2008) 777–784. doi:10.1007/s10544-008-9190-7.

[7] J.M. Ramsey, The burgeoning power of the shrinking laboratory, Nat. Biotechnol. 17 (1999) 1061–1062. doi:10.1038/15044.

[8] S. Berensmeier, Magnetic particles for the separation and purification of nucleic acids, Appl. Microbiol. Biotechnol. 73 (2006) 495–504. doi:10.1007/s00253-006-0675-0.

[9] D. Horák, M. Babic, H. Macková, M.J. Benes, Preparation and properties of magnetic nano- and microsized particles for biological and environmental separations, J. Sep. Sci. 30 (2007) 1751–72. doi:10.1002/jssc.200700088.

[10] K. Sur, S.M. McFall, E.T. Yeh, S.R. Jangam, M.A. Hayden, S.D. Stroupe, et al., Immiscible phase nucleic acid purification eliminates PCR inhibitors with a single pass of paramagnetic particles through a hydrophobic liquid, J. Mol. Diagn. 12 (2010) 620–8. doi:10.2353/jmoldx.2010.090190.

[11] S.M. Berry, E.T. Alarid, D.J. Beebe, One-step purification of nucleic acid for gene expression analysis via Immiscible Filtration Assisted by Surface Tension (IFAST), Lab Chip. 11 (2011) 1747–53. doi:10.1039/c1lc00004g.

[12] R.C. den Dulk, K.A. Schmidt, G. Sabatté, S. Liébana, M.W.J. Prins, Magneto-capillary valve for integrated purification and enrichment of nucleic acids and proteins, Lab Chip. 13 (2013) 106–118. doi:10.1039/C2LC40929A.

[13] O. Strohmeier, A. Emperle, G. Roth, D. Mark, R. Zengerle, F. von Stetten, Centrifugal gas-phase transition magnetophoresis (GTM) - a generic method for automation of magnetic bead based assays on the centrifugal microfluidic platform and application to DNA purification, Lab Chip. 13 (2013) 146–55. doi:10.1039/c2lc40866j.

[14] M. Shikida, K. Takayanagi, H. Honda, H. Ito, K. Sato, Development of an enzymatic reaction device using magnetic bead-cluster handling, J. Micromechanics Microengineering. 16 (2006) 1875–1883. doi:10.1088/0960-1317/16/9/017.

[15] L.N. Strotman, G. Lin, S.M. Berry, E.A. Johnson, D.J. Beebe, Facile and rapid DNA extraction and purification from food matrices using IFAST (immiscible filtration assisted by surface tension), Analyst. 137 (2012) 4023–8. doi:10.1039/c2an35506j.

[16] S.M. Berry, A.J. LaVanway, H.M. Pezzi, D.J. Guckenberger, M.A. Anderson, J.M. Loeb, et al., HIV Viral RNA Extraction in Wax Immiscible Filtration Assisted by Surface Tension (IFAST) Devices, J. Mol. Diagn. 16 (2014) 1–9. doi:10.1016/j.jmoldx.2014.01.004.

[17] H. Bordelon, N.M. Adams, A.S. Klemm, P.K. Russ, J. V Williams, H.K. Talbot, et al., Development of a low-resource RNA extraction cassette based on surface tension valves, ACS Appl. Mater. Interfaces. 3 (2011) 2161–8. doi:10.1021/am2004009.

[18] M. Shikida, K. Takayanagi, K. Inouchi, H. Honda, K. Sato, Using wettability and interfacial tension to handle droplets of magnetic beads in a micro-chemical-analysis system, Sensors Actuators B Chem. 113 (2006) 563–569. doi:10.1016/j.snb.2005.01.029.

[19] J. Pipper, M. Inoue, L.F.-P. Ng, P. Neuzil, Y. Zhang, L. Novak, Catching bird flu in a droplet, Nat. Med. 13 (2007) 1259–63. doi:10.1038/nm1634.

[20] S.M. Berry, L.N. Strotman, J.D. Kueck, E.T. Alarid, D.J. Beebe, Purification of cell subpopulations via immiscible filtration assisted by surface tension (IFAST), Biomed. Microdevices. 13 (2011) 1033–42. doi:10.1007/s10544-011-9573-z.

[21] S.M. Berry, L.J. Maccoux, D.J. Beebe, Streamlining immunoassays with immiscible filtrations assisted by surface tension, Anal. Chem. 84 (2012) 5518–23. doi:10.1021/ac300085m.

[22] A.L. Howard, H.M. Pezzi, D.J. Beebe, S.M. Berry, Exclusion-based capture and enumeration of CD4+ T cells from whole blood for low-resource settings, J. Lab. Autom. 19 (2014) 313–321. doi:10.1177/2211068213509248.

[23] S.M. Berry, E.N. Chin, S.S. Jackson, L.N. Strotman, M. Goel, N.E. Thompson, et al., Weak protein–protein interactions revealed by immiscible filtration assisted by surface tension, Anal. Biochem. 447 (2014) 133–140. doi:10.1016/j.ab.2013.10.038.

[24] B.P. Casavant, D.J. Guckenberger, S.M. Berry, J.T. Tokar, J.M. Lang, D.J. Beebe, The VerIFAST: an integrated method for cell isolation and extracellular/intracellular staining, Lab Chip. 13 (2013) 391–6. doi:10.1039/c2lc41136a.

[25] L. Strotman, R. O'Connell, B.P. Casavant, S.M. Berry, J.M. Sperger, J.M. Lang, et al., Selective nucleic acid removal via exclusion (SNARE): Capturing mRNA and DNA from a single sample, Anal. Chem. 85 (2013) 9764–70. doi:10.1021/ac402162r.

[26] P.C. Thomas, L.N. Strotman, A.B. Theberge, E. Berthier, R. O'Connell, J.M. Loeb, et al., Nucleic acid sample preparation using spontaneous biphasic plug flow, Anal. Chem. 85 (2013) 8641–8646. doi:10.1021/ac4012914.

[27] D.J. Guckenberger, P.C. Thomas, J. Rothbauer, A.J. LaVanway, M. Anderson, D. Gilson, et al., A combined fabrication and instrumentation platform for sample preparation, J. Lab. Autom. 19 (2014) 267–274. doi:10.1177/2211068213518312.

[28] B.P. Casavant, D.J. Guckenberger, D.J. Beebe, S.M. Berry, Efficient sample preparation from complex biological samples using a sliding lid for immobilized droplet extractions, Anal. Chem. 86 (2014) 6355–6362. doi:10.1021/ac500574t.

[29] A. Manz, J.C. Fettinger, E. Verpoorte, H. Lüdi, H.M. Widmer, D.J. Harrison, Micromachining of monocrystalline silicon and glass for chemical analysis systems A look into next century's technology or just a fashionable craze?, Trends Anal. Chem. 10 (1991) 144–149. doi:10.1016/0165-9936(91)85116-9.

[30] A. Manz, N. Graber, H.M. Widmer, Miniaturized total chemical analysis systems: A novel concept for chemical sensing, Sensors Actuators B Chem. 1 (1990) 244–248. doi:10.1016/0925-4005(90)80209-I.

[31] R. Mukhopadhyay, Microfluidics: On the slope of enlightenment, Anal. Chem. 81 (2009) 4169–4173. doi:10.1021/ac900638w.

[32] H. Becker, Hype, hope and hubris: The quest for the killer application in microfluidics, Lab Chip. 9 (2009) 2119–22. doi:10.1039/b911553f.

[33] N. Blow, Microfluidics: The great divide, Nat. Methods. 6 (2009) 683–686. doi:10.1038/nmeth0909-683.

[34] H. Becker, Chips, money, industry, education and the "killer application," Lab Chip. 9 (2009) 1659–60. doi:10.1039/b909379f.

[35] H. Becker, IP or no IP: That is the question, Lab Chip. 9 (2009) 3327–9. doi:10.1039/b920548a.

[36] H. Becker, It's the economy..., Lab Chip. 9 (2009) 2759–62. doi:10.1039/b916505n.

[37] H. Becker, Non scholae sed vitae discimus!, Lab Chip. 10 (2010) 2497–8. doi:10.1039/c005497f.

[38] H. Becker, One size fits all?, Lab Chip. 10 (2010) 1894–7. doi:10.1039/c005380p.

[39] H. Becker, Collective wisdom, Lab Chip. 10 (2010) 1351–4. doi:10.1039/c004239k.

[40] H. Becker, Lost in translation, Lab Chip. 10 (2010) 813–5. doi:10.1039/c002744h.

[41] H. Becker, Mind the gap!, Lab Chip. 10 (2010) 271–3. doi:10.1039/b925993g.

[42] H. Becker, Start me up…, Lab Chip. 10 (2010) 3197–200. doi:10.1039/c0lc90065f.

[43] H. Becker, All I want for christmas…, Lab Chip. 11 (2011) 1571. doi:10.1039/c1lc90025k.

[44] H. Becker, Famous last words..., Lab Chip. 11 (2011) 2133–4. doi:10.1039/c1lc90051j.

[45] H. Becker, Microfluidics: A technology coming of age, Med. Device Technol. 19 (2008) 21–24.

[46] G.D. Aumiller, E.A. Chandross, W.J. Tomlinson, H.P. Weber, Submicrometer resolution replication of relief patterns for integrated optics, J. Appl. Phys. 45 (1974) 4557–4562. doi:10.1063/1.1663087.

[47] A. Kumar, G.M. Whitesides, Features of gold having micrometer to centimeter dimensions can be formed through a combination of stamping with an elastomeric stamp and an alkanethiol “ink” followed by chemical etching, Appl. Phys. Lett. 63 (1993) 2002–2004. doi:10.1063/1.110628.

[48] J.M.K. Ng, I. Gitlin, A.D. Stroock, G.M. Whitesides, Components for integrated poly(dimethylsiloxane) microfluidic systems, Electrophoresis. 23 (2002) 3461–3473. doi:10.1002/1522-2683(200210)23:20<3461::AID-ELPS3461>3.0.CO;2-8.

[49] G. Whitesides, A. Stroock, Flexible methods for microfluidics, Phys. Today. 54 (2001) 42–48. doi:10.1063/1.1387591.

[50] R. Mukhopadhyay, When PDMS isn’t the best, Anal. Chem. 79 (2007) 3248–3253. doi:10.1021/ac071903e.

[51] E. Berthier, E.W.K. Young, D. Beebe, Engineers are from PDMS-land, biologists are from Polystyrenia, Lab Chip. 12 (2012) 1193–1396. doi:10.1039/c2lc20982a.

[52] J.N. Lee, C. Park, G.M. Whitesides, Solvent compatibility of poly(dimethylsiloxane)-based microfluidic devices, Anal. Chem. 75 (2003) 6544–6554. doi:10.1021/ac0346712.

[53] S.H. Yun, L.M. Cabrera, J.W. Song, N. Futai, Y.C. Tung, G.D. Smith, et al., Characterization and resolution of evaporation-mediated osmolality shifts that constrain microfluidic cell culture in poly(dimethylsiloxane) devices, Anal. Chem. 79 (2007) 1126–1134. doi:10.1021/ac061990v.

[54] M.W. Toepke, D.J. Beebe, PDMS absorption of small molecules and consequences in microfluidic applications., Lab Chip. 6 (2006) 1484–1486. doi:10.1039/b612140c.

[55] H. Becker, C. Gärtner, Polymer microfabrication technologies for microfluidic systems., Anal. Bioanal. Chem. 390 (2008) 89–111. doi:10.1007/s00216-007-1692-2.

[56] Y. Xia, G.M. Whitesides, Soft Lithography, Annu. Rev. Mater. Sci. 28 (1998) 153–184. doi:10.1146/annurev.matsci.28.1.153.

[57] A. Waldbaur, H. Rapp, K. Länge, B.E. Rapp, Let there be chip—towards rapid prototyping of microfluidic devices: One-step manufacturing processes, Anal. Methods. 3 (2011) 2681–2716. doi:10.1039/c1ay05253e.

[58] E. Sollier, C. Murray, P. Maoddi, D. Di Carlo, Rapid prototyping polymers for microfluidic devices and high pressure injections, Lab Chip. 11 (2011) 3752–3765. doi:10.1039/c1lc20514e.

[59] H. Becker, L.E. Locascio, Polymer microfluidic devices, Talanta. 56 (2002) 267–287. doi:10.1016/S0039-9140(01)00594-X.

[60] U.M. Attia, S. Marson, J.R. Alcock, Micro-injection moulding of polymer microfluidic devices, Microfluid. Nanofluidics. 7 (2009) 1–28. doi:10.1007/s10404-009-0421-x.

[61] D.J. Guckenberger, T. de Groot, A.M.-D. Wan, D. Beebe, E. Young, Micromilling: A method for ultra-rapid prototyping of plastic microfluidic devices, Lab Chip. 15 (2015) 2364–2378. doi:10.1039/C5LC00234F.

[62] X. Li, D.R. Ballerini, W. Shen, A perspective on paper-based microfluidics: Current status and future trends, Biomicrofluidics. 6 (2012) 011301. doi:10.1063/1.3687398.

[63] E. Verpoorte, N.F. De Rooij, Microfluidics meets MEMS, Proc. IEEE. 91 (2003) 930–953. doi:10.1109/JPROC.2003.813570.

[64] H. Becker, C. Gärtner, Polymer microfabrication methods for microfluidic analytical applications, Electrophoresis. 21 (2000) 12–26. doi:10.1002/(SICI)1522-2683(20000101)21:1<12::AID-ELPS12>3.0.CO;2-7.

[65] F.K. Balagaddé, L. You, C.L. Hansen, F.H. Arnold, S.R. Quake, Long-term monitoring of bacteria undergoing programmed population control in a microchemostat, Science. 309 (2005) 137–140. doi:10.1126/science.1109173.

[66] C.-W. Tsao, D.L. DeVoe, Bonding of thermoplastic polymer microfluidics, Microfluid. Nanofluidics. 6 (2009) 1–16. doi:10.1007/s10404-008-0361-x.

[67] S. Franssila, Bonding, in: Introd. to Microfabr., 2nd ed., John Wiley & Sons, Ltd., West Sussex, 2010: pp. 191–201.

[68] F. Dang, S. Shinohara, O. Tabata, Y. Yamaoka, M. Kurokawa, Y. Shinohara, et al., Replica multichannel polymer chips with a network of sacrificial channels sealed by adhesive printing method, Lab Chip. 5 (2005) 472–478. doi:10.1039/b417398h.

[69] C. Lu, L.J. Lee, Y.J. Juang, Packaging of microfluidic chips via interstitial bonding technique, Electrophoresis. 29 (2008) 1407–1414. doi:10.1002/elps.200700680.

[70] W.W.Y. Chow, K.F. Lei, G. Shi, W.J. Li, Q. Huang, Microfluidic channel fabrication by PDMS-interface bonding, Smart Mater. Struct. 15 (2005) S112–S116. doi:10.1088/0964-1726/15/1/018.

[71] Y. Sun, J. Høgberg, T. Christine, L. Florian, L.G. Monsalve, S. Rodriguez, et al., Pre-storage of gelified reagents in a lab-on-a-foil system for rapid nucleic acid analysis, Lab Chip. 13 (2013) 1509–14. doi:10.1039/c2lc41386h.

[72] D.S. Kim, H.S. Lee, J. Han, S.H. Lee, C.H. Ahn, T.H. Kwon, Collapse-free thermal bonding technique for large area microchambers in plastic lab-on-a-chip applications, Microsyst. Technol. 14 (2007) 179–184. doi:10.1007/s00542-007-0416-z.

[73] R. Truckenmüller, R. Ahrens, Y. Cheng, G. Fischer, V. Saile, An ultrasonic welding based process for building up a new class of inert fluidic microsensors and -actuators from polymers, Sensors Actuators A Phys. 132 (2006) 385–392. doi:10.1016/j.sna.2006.04.040.

[74] R. Truckenmüller, Y. Cheng, R. Ahrens, H. Bahrs, G. Fischer, J. Lehmann, Micro ultrasonic welding: Joining of chemically inert polymer microparts for single material fluidic components and systems, Microsyst. Technol. 12 (2006) 1027–1029. doi:10.1007/s00542-006-0136-9.

[75] Y. Luo, Z. Zhang, X. Wang, Y. Zheng, Ultrasonic bonding for thermoplastic microfluidic devices without energy director, Microelectron. Eng. 87 (2010) 2429–2436. doi:10.1016/j.mee.2010.04.020.

[76] Z. Zhang, Y. Luo, X. Wang, S. He, F. Meng, L. Wang, Bonding of planar poly (methyl methacrylate) (PMMA) nanofluidic channels using thermal assisted ultrasonic bonding method, Microsyst. Technol. 16 (2010) 2043–2048. doi:10.1007/s00542-010-1140-7.

[77] M. Bu, I.R. Perch-Nielsen, Y. Sun, A. Wolff, A microfluidic control system with re-usable micropump/valve actuator and injection moulded disposable polymer lab-on-a-slide, in: 2011 16th Int. Solid-State Sensors, Actuators Microsystems Conf., IEEE, 2011: pp. 1244–1247. doi:10.1109/TRANSDUCERS.2011.5969452.

[78] K.G. Lee, S. Shin, B. Il Kim, N.H. Bae, M.-K. Lee, S.J. Lee, et al., Ultrasonic bonding method for heterogeneous microstructures using self-balancing jig, Lab Chip. 15 (2015) 1412–1416. doi:10.1039/C4LC01473A.

[79] A. Taberham, M. Kraft, M. Mowlem, H. Morgan, The fabrication of lab-on-chip devices from fluoropolymers, J. Micromechanics Microengineering. 18 (2008) 064011. doi:10.1088/0960-1317/18/6/064011.

[80] J.G. Bralla, Design for manufacturability handbook, 2nd ed., McGraw-Hill, Boston, 1999.

[81] H. Bruus, Theoretical Microfluidics, 1st ed., Oxford University Press, Chippenham, UK, 2008.

[82] J. Berthier, Theory of Wetting, in: Micro-Drops Digit. Microfluid., Elsevier, Norwich, NY, 2008: pp. 7–73. doi:10.1016/B978-081551544-9.50005-1.

[83] H. Cho, H.-Y. Kim, J.Y. Kang, T.S. Kim, How the capillary burst microvalve works, J. Colloid Interface Sci. 306 (2007) 379–85. doi:10.1016/j.jcis.2006.10.077.

[84] Z. Long, A.M. Shetty, M.J. Solomon, R.G. Larson, Fundamentals of magnet-actuated droplet manipulation on an open hydrophobic surface, Lab Chip. 9 (2009) 1567–75. doi:10.1039/b819818g.

[85] L. Beccai, S. Roccella, A. Arena, F. Valvo, P. Valdastri, A. Menciassi, et al., Design and fabrication of a hybrid silicon three-axial force sensor for biomechanical applications, Sensors Actuators, A Phys. 120 (2005) 370–382. doi:10.1016/j.sna.2005.01.007.

[86] M.J. Troughton, Ultrasonic Welding, in: Handb. Plast. Join., 2nd ed., Elsevier, Boston, 2009: pp. 15–35. doi:10.1016/B978-0-8155-1581-4.50004-4.

[87] P.S. Nunes, P.D. Ohlsson, O. Ordeig, J.P. Kutter, Cyclic olefin polymers: Emerging materials for lab-on-a-chip applications, Microfluid. Nanofluidics. 9 (2010) 145–161. doi:10.1007/s10404-010-0605-4.

[88] K.Ø. Andresen, M. Hansen, M. Matschuk, S.T. Jepsen, H.S. Sørensen, P. Utko, et al., Injection molded chips with integrated conducting polymer electrodes for electroporation of cells, J. Micromechanics Microengineering. 20 (2010) 055010. doi:10.1088/0960-1317/20/5/055010.

[89] R. Karania, D. Kazmer, Low Volume Plastics Manufacturing Strategies, J. Mech. Des. 129 (2007) 1225–1233. doi:10.1115/1.2790978.

[90] J. Giboz, T. Copponnex, P. Mélé, Microinjection molding of thermoplastic polymers: A review, J. Micromechanics Microengineering. 17 (2007) R96–R109. doi:10.1088/0960-1317/17/6/R02.

[91] H.N. Hansen, R.J. Hocken, G. Tosello, Replication of micro and nano surface geometries, CIRP Ann. - Manuf. Technol. 60 (2011) 695–714. doi:10.1016/j.cirp.2011.05.008.

[92] E. Uhlmann, S. Piltz, U. Doll, Machining of micro/miniature dies and moulds by electrical discharge machining - Recent development, J. Mater. Process. Technol. 167 (2005) 488–493. doi:10.1016/j.jmatprotec.2005.06.013.

[93] U.M. Attia, J.R. Alcock, Integration of functionality into polymer-based microfluidic devices produced by high-volume micro-moulding techniques, Int. J. Adv. Manuf. Technol. 48 (2010) 973–991. doi:10.1007/s00170-009-2345-8.

[94] R.A. Malloy, Plastic Part Design for Injection Molding: An Introduction, Hanser Publishers, Gersthofen, 1994.

[95] I.R.G. Ogilvie, V.J. Sieben, C.F. a Floquet, R. Zmijan, M.C. Mowlem, H. Morgan, Solvent processing of PMMA and COC chips for bonding devices with optical quality surfaces, in: Proc. 14th Int. Conf. Miniaturized Syst. Chem. Life Sci., MicroTAS 2010, 2010: pp. 1244–1246.

[96] Dukane Corporation, Guide to Ultrasonic Plastics Assembly, Dukane Corporation, 2011.

[97] A. Shoh, Welding of thermoplastics by ultrasound, Ultrasonics. 14 (1976) 209–217. doi:10.1016/0041-624X(76)90020-2.

[98] S.S. Volkov, Analysis of the process of heat generation in ultrasonic welding of plastics, Weld. Int. 29 (2015) 321–324. doi:10.1080/09507116.2014.921384.

[99] C.A. Griffiths, G. Tosello, S.S. Dimov, S.G. Scholz, A. Rees, B. Whiteside, Characterisation of demoulding parameters in micro-injection moulding, Microsyst. Technol. 21 (2015) 1677–1690. doi:10.1007/s00542-014-2269-6.

[100] W.P. Maszara, G. Goetz, A. Caviglia, J.B. McKitterick, Bonding of silicon wafers for silicon-on-insulator, J. Appl. Phys. 64 (1988) 4943–4950. doi:10.1063/1.342443.

[101] M. Matteucci, T.L. Christiansen, S. Tanzi, P.F. Østergaard, S.T. Larsen, R. Taboryski, Fabrication and characterization of injection molded multi level nano and microfluidic systems, Microelectron. Eng. 111 (2013) 294–298. doi:10.1016/j.mee.2013.01.060.

[102] A.B. Strong, Plastics: Materials and Processing, Prentice Hall, New Jersey, 2000.

[103] J. Giboz, T. Copponnex, P. Mélé, Microinjection molding of thermoplastic polymers: Morphological comparison with conventional injection molding, J. Micromechanics Microengineering. 19 (2009) 025023. doi:10.1088/0960-1317/19/2/025023.

[104] C. Ageorges, L. Ye, M. Hou, Advances in fusion bonding techniques for joining thermoplastic matrix composites: A review, Compos. Part A Appl. Sci. Manuf. 32 (2001) 839–857. doi:10.1016/S1359-835X(00)00166-4.

[105] F. Brémand, J.-C. Baret, Photoelasticity, in: M. Grédiac, F. Hild, A. Pineau (Eds.), Full-F. Meas. Identif. Solid Mech., John Wiley & Sons, Inc., Hoboken, NJ USA, 2013: p. 476. doi:10.1002/9781118578469.

[106] D. Whitehouse, Surfaces and Their Measurement, in: Surfaces Their Meas., Elsevier, 2002: pp. 48–95. doi:10.1016/B978-190399601-0/50003-7.

[107] J. Berthier, The Physics of Droplets, in: Microdrops Digit. Microfluid., 2md ed., William Andrew Publishing, Norwich, Ny, 2008: pp. 75–160. doi:10.1016/B978-081551544-9.50006-3.

[108] S. Tanzi, P.F. Østergaard, M. Matteucci, T.L. Christiansen, J. Cech, R. Marie, et al., Fabrication of combined-scale nano- and microfluidic polymer systems using a multilevel dry etching, electroplating and molding process, J. Micromechanics Microengineering. 22 (2012) 115008. doi:10.1088/0960-1317/22/11/115008.

[109] M. Calaon, H.N. Hansen, G. Tosello, J. Garnaes, J. Nørregaard, W. Li, Microfluidic chip designs process optimization and dimensional quality control, Microsyst. Technol. 21 (2015) 561–570. doi:10.1007/s00542-013-2025-3.

[110] Branson Ultrasonics Corporation, Part Design for Ultrasonic Welding, Branson Ultrasonics Corporation, 2013.

[111] C.W. Tsao, L. Hromada, J. Liu, P. Kumar, D.L. DeVoe, Low temperature bonding of PMMA and COC microfluidic substrates using UV/ozone surface treatment, Lab Chip. 7 (2007) 499–505. doi:10.1039/b618901f.

[112] D.A. Mair, M. Rolandi, M. Snauko, R. Noroski, F. Svec, J.M.J. Fréchet, Room-temperature bonding for plastic high-pressure microfluidic chips, Anal. Chem. 79 (2007) 5097–5102. doi:10.1021/ac070220w.

[113] J. Mizuno, H. Ishida, S. Farrens, V. Dragoi, H. Shinohara, T. Suzuki, et al., Cyclo-olefin polymer direct bonding using low temperature plasma activation bonding, in: 13th Int. Conf. Solid-State Sensors, Actuators Microsystems, 2005. Dig. Tech. Pap. TRANSDUCERS '05., IEEE, 2005: pp. 1346–1349. doi:10.1109/SENSOR.2005.1497330.

[114] A.M.D. Wan, A. Sadri, E.W.K. Young, Liquid phase solvent bonding of plastic microfluidic devices assisted by retention grooves, Lab Chip. 15 (2015) 3785–3792. doi:10.1039/C5LC00729A.

[115] M.A. Eddings, M.A. Johnson, B.K. Gale, Determining the optimal PDMS–PDMS bonding technique for microfluidic devices, J. Micromechanics Microengineering. 18 (2008) 067001. doi:10.1088/0960-1317/18/6/067001.

[116] S. Bhattacharya, A. Datta, J.M. Berg, S. Gangopadhyay, Studies on surface wettability of poly(dimethyl) siloxane (PDMS) and glass under oxygen-plasma treatment and correlation with bond strength, J. Microelectromechanical Syst. 14 (2005) 590–597. doi:10.1109/JMEMS.2005.844746.

[117] S.R. Quake, A. Scherer, From micro- to nanofabrication with soft materials, Science. 290 (2000) 1536–1540. doi:10.1126/science.290.5496.1536.

[118] M.A.M. Gijs, F. Lacharme, U. Lehmann, Microfluidic applications of magnetic particles for biological analysis and catalysis, Chem. Rev. 110 (2010) 1518–1563. doi:10.1021/cr9001929.

[119] H. Chen, A. Abolmatty, M. Faghri, Microfluidic inverse phase ELISA via manipulation of magnetic beads, Microfluid. Nanofluidics. 10 (2010) 593–605. doi:10.1007/s10404-010-0692-2.

[120] K.S. Lee, N. Ivanova, V.M. Starov, N. Hilal, V. Dutschk, Kinetics of wetting and spreading by aqueous surfactant solutions, Adv. Colloid Interface Sci. 144 (2008) 54–65. doi:10.1016/j.cis.2008.08.005.

[121] V. Dutschk, K.G. Sabbatovskiy, M. Stolz, K. Grundke, V.M. Rudoy, Unusual wetting dynamics of aqueous surfactant solutions on polymer surfaces, J. Colloid Interface Sci. 267 (2003) 456–462. doi:10.1016/S0021-9797(03)00723-9.

[122] M. Otto, MRSA virulence and spread, Cell. Microbiol. 14 (2012) 1513–1521. doi:10.1111/j.1462-5822.2012.01832.x.

[123] B. Shopsin, B.N. Kreiswirth, Molecular epidemiology of methicillin-resistant Staphylococcus aureus, Emerg. Infect. Dis. 7 (2001) 323–326. doi:10.3201/eid0702.700323.

[124] A.R. Larsen, M. Stegger, M. Sørum, Spa typing directly from a mecA, spa and pvl multiplex PCR assay-a cost-effective improvement for methicillin-resistant Staphylococcus aureus surveillance, Clin. Microbiol. Infect. 14 (2008) 611–614. doi:10.1111/j.1469-0691.2008.01995.x.

[125] A.C. Fluit, What to do with MRSA with a novel mec gene?, Lancet Infect. Dis. 11 (2011) 580–581. doi:10.1016/S1473-3099(11)70180-3.

[126] P. Francois, D. Pittet, M. Bento, B. Pepey, P. Vaudaux, D. Lew, et al., Rapid detection of methicillin-resistant Staphylococcus aureus directly from sterile or nonsterile clinical samples by a new molecular assay, J. Clin. Microbiol. 41 (2003) 254–260. doi:10.1128/JCM.41.1.254-260.2003.

Appendices

Appendix 1

Fabrication and modelling of injection moulded all-polymer capillary microvalves for passive microfluidic control

K. Kistrup, C.E. Poulsen, P.F. Østergaard, K.B. Haugshøj, R. Taboryski, A. Wolff, M. F. Hansen

J. Micromechanics Microengineering. **24** (2014) 125007. doi:10.1088/0960-1317/24/12/125007

IOP Publishing Journal of Micromechanics and Microengineering
J. Micromech. Microeng. **24** (2014) 125007 (10pp) doi:10.1088/0960-1317/24/12/125007

Fabrication and modelling of injection moulded all-polymer capillary microvalves for passive microfluidic control

Kasper Kistrup[1,3], Carl Esben Poulsen[1,3], Peter Friis Østergaard[1], Kenneth Brian Haugshøj[2], Rafael Taboryski[1], Anders Wolff[1] and Mikkel Fougt Hansen[1,4]

[1] Department of Micro- and Nanotechnology, Technical University of Denmark, DTU Nanotech, Building 345 East, DK-2800 Kongens Lyngby, Denmark
[2] Centre for Microtechnology and Surface analysis, Danish Technological Institute, Gregersensvej, DK-2630 Taastrup, Denmark

E-mail: mikkel.hansen@nanotech.dtu.dk

Received 15 May 2014, revised 8 August 2014
Accepted for publication 17 September 2014
Published 12 November 2014

Abstract
Rapid prototyping is desirable when developing products. One example of such a product is all-polymer, passive flow controlled lab-on-a-chip systems that are preferential when developing low-cost disposable chips for point-of-care use. In this paper we investigate the following aspects of going from rapid prototyping to pilot (mass) production. (1) Fabrication of an all-polymer microfluidic system using a rapid prototyped master insert for injection moulding and ultrasonic welding, including a systematic experimental characterisation of chip featured geometric capillary microvalve test structures. (2) Numerical modelling of the microvalve burst pressures. Numerical modelling of burst pressures is challenging due to its non-equilibrium nature. We have implemented and tested the level-set method modified with a damped driving term and show that the introduction of the damping term leads to numerically robust results with limited computational demands and a low number of iterations. Numerical and simplified analytical results are validated against the experimental results. We find that injection moulding and ultrasonic welding are effective for chip production and that the experimental burst pressures could be estimated with an average accuracy of 5% using the presented numerical model.

Keywords: injection moulding, capillary stop, polymer microfluidics, microvalve, ultrasonic bonding, finite element analysis

S Online supplementary data available from stacks.iop.org/JMM/24/125007/mmedia

(Some figures may appear in colour only in the online journal)

1. Introduction

Ever since Manz *et al* coined the term 'miniaturized total analysis system' (μTAS), that laid out the fundamental requirements for lab-on-a-chip systems, it has been recognized that microfluidics plays a central role as the mediator linking all the components of a μTAS (Manz *et al* 1990). It is clear that precise control of fluids on-chip is critical for the success of such a microfluidic device. An idealised μTAS is low-cost and easy-to-fabricate, which by today's standards is preferably a single-use all-polymer system, often realised using rapid prototyping (Giboz *et al* 2007, Becker and Gärtner 2008, Waldbaur *et al* 2011). Capillary microvalves are essential components in many lab-on-a-chip systems and are also sensitive to dimensions. They are

[3] These two authors contributed equally to this article.
[4] Author to whom any correspondence should be addressed.

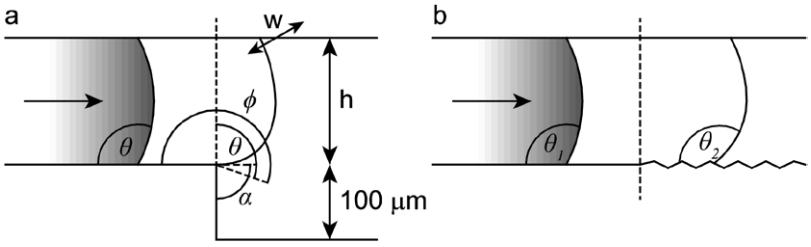

Figure 1. Cross sectional view of capillary microvalve types. (*a*) Geometric capillary microvalve, where pinning is achieved through a sudden change in geometry. θ, α and ϕ denote the channel contact angle, expansion angle and effective contact angle, respectively. w and h denote width and height of the channel. (*b*) Hydrophobic capillary microvalve, where pinning is achieved by abrupt changes in the wetting properties of one or more channel walls. θ_1 and θ_2 denote the contact angles of the smooth and rough channel area, respectively.

therefore chosen to illustrate the applicability of the methods presented here.

An important aspect of lab-on-a-chip systems is the fabrication process itself. When developing a disposable chip for commercial use, it is highly desirable to apply rapid prototyping technologies that are directly compatible with mass production. Lab-on-a-chip systems presented in the scientific literature often consist of different materials that need to be carefully aligned prior to assembly (Begolo *et al* 2011). While this is no hindrance for prototyping, a redesign is needed for implementation into an assembly line or to reduce fabrication costs. Furthermore, the fabrication of a single chip is laborious for silicon chips, glass etched chips and to some extent polydimethylsiloxane (PDMS) chips leading to long production times for each chip.

Injection moulding of thermoplastics is well established as a commercial production technique and serves well to reliably replicate structures down to nanometer size (Attia *et al* 2009, Tanzi *et al* 2012) at turn-around times of ca. 1 min per chip (Matteucci *et al* 2013). Ultrasonic welding is also widely used in production around the world, though its usage for lab-on-a-chip systems is limited (Truckenmüller *et al* 2006a, 2006b). Ultrasonic welding functions without the need of additional adhesives or substrates and only applies a localised friction heating at the welding seam. This is advantageous when working with lab-on-a-chip systems where interactions of chip reagents or sample with the bonding material might dissolve the chip or contaminate the sample.

Passive on-chip fluid management can be realised by utilising the capillarity available due to the large surface-to-volume ratio of microsystems. This approach is known as passive or autonomous flow control. Two examples include capillary pumps and capillary microvalves (Zimmermann *et al* 2008). Active and passive flow control have their benefits and disadvantages. A major drawback of active control is that it adds complexity to the system. Passive components are inexpensive to incorporate, yet they are single-use and most often unidirectional, and are sensitive to surfactants altering the surface and wetting properties. Depending on the desired application one should carefully choose the appropriate components to include in a given μTAS.

Two strategies for creating capillary microvalves exist (figure 1): (a) an abrupt geometry change, and (b) areas of altered wetting properties. A geometric capillary microvalve consists of an abrupt expansion of a micro channel, with expansion angle, α, see figure 1(*a*). From geometric considerations, it is evident that when the interface reaches the edge of the expanded region, the interfacial contact angle to the expanded region, ϕ, is smaller than the expanded region advancing contact angle, θ, and the interface is thus pinned as long as $\phi \leq \theta + \alpha$ (Cho *et al* 2007). A similar pinning effect may be achieved in a hydrophobic capillary microvalve. Here, pinning is achieved by an abrupt change in the wetting properties, increasing the contact angle, see figure 1(*b*). In several studies, this pinning effect have been exploited to create 'virtual walls', guiding the liquid phase (Zhao *et al* 2002, Bouaidat *et al* 2005, den Dulk *et al* 2012).

Passive capillary microvalves have previously been demonstrated in a variety of materials, including, silicon and PDMS (Zimmermann *et al* 2008), PDMS (Duffy *et al* 1999), Polycarbonate (PC)-PDMS (Cho *et al* 2007), and micro machined poly(methyl methacrylate) and pressure adhesive tape (Thio *et al* 2013), for both disc based and conventional planar microfluidic systems. All of these systems are fairly complex in the sense that they are constructed from multiple materials, some require clean room work, and some need careful alignment of the parts during fabrication. They are therefore not applicable for commercial scale chip fabrication.

Since passive flow control is promising for many applications, it is interesting to investigate the relations between analytical expressions and numerical evaluations that predict the rheology of microfluidics, and the performance of on-chip passive flow control components. Previous studies have shown that the finite interface thickness of the volume of fluid (VOF) does not influence the pinning of the interface until the interface width is of comparable to the size of the obstacle, suggesting that this approach may be applicable for estimating the pressure drop on pinned interfaces (Chibbaro *et al* 2009). However, one major disadvantage of VOF is the difficulty to calculate local surface curvatures (Sussman and Puckett 2000) and hence surface tension effects (Gerlach *et al* 2006). Opposed to that, using the level-set (LS) method for the calculation of the surface curvature is simple, but good conservation of mass is lacking (Sussman and Puckett 2000). Therefore, numerical methods combining VOF and LS have been created (Sussman and Puckett 2000, Olsson and Kreiss 2005) and implemented in commercial software.[5]

In this paper we look into two challenges of going from rapid prototyping to pilot (mass) production: (1) fabrication of a

[5] COMSOL v4.3 computer software 2012 (www. comsol.com).

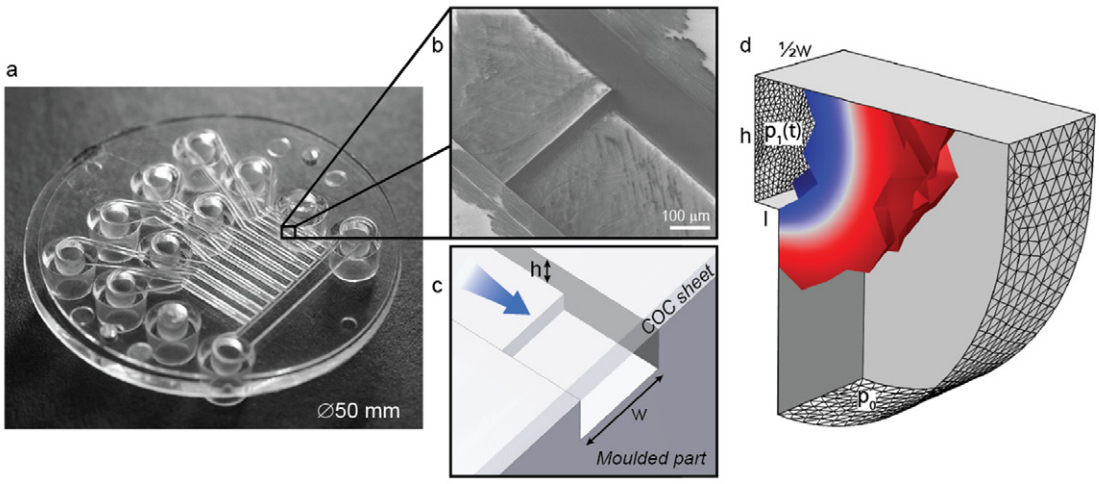

Figure 2. Overview of chip dimensions (*a*) Photograph of the injection moulded main chip part (pre-welding) showing the overall parallel lay-out of the channels containing the capillary stops. The location of a single capillary stop has been marked (box) along with two insets; (*b*) a SEM image showing the actual capillary stop (pre-welding) and (*c*) a 3D representation of the same capillary stop on which dimensions (height and width), flow direction (blue arrow) and a COC sheet has been depicted. (*d*) Geometry used in the COMSOL Multiphysics finite element calculations. The symmetry plane is the transparent face of the figure and an advancing interface is illustrated as filled elements in a blue–white–red gradient going from 75%–50%–25% water content. ½*w*, *h*, p_1 (*t*) and p_0 indicate half width, height, inlet channel length, inlet pressure and outlet pressure, respectively.

microfluidic chip using mass-production techniques from a rapid prototyped master insert; (2) reducing the number iterations by addressing the feasibility of using the LS + VOF method as a numerical tool to predict fluid behaviour in a surface tension controlled all-polymer system. We present a systematic comparison between experimentally measured, numerically estimated and analytically calculated burst pressures of a selection of geometrical capillary microvalves. Our experimental model system is an all-polymer injection moulded chip, made using a rapid prototyped master insert. It consists of two pieces of polymer, which have been thin film coated to increase the hydrophobicity. The chip parts are bonded using ultrasonic welding. All parts of the chip fabrication are directly applicable to mass production and require no careful alignment during assembly.

2. Theory

The theoretical pressure drop required for forcing a liquid through an expanding microfluidic structure such as a capillary microvalve may be estimated analytically for simple geometries. Cho *et al* assumed that the liquid interface will pin to the corner of the expansion forming an angle α (figure 1(*a*)) if the interface angle to the expanded wall, ϕ, is smaller than the expanded region advancing contact angle, θ, leading to the pinning condition (Cho *et al* 2007)

$$\theta \leq \phi \leq \theta + \alpha \tag{1}$$

also known as Gibbs' inequality condition (Gibbs 1906, Dyson 1988).

By geometric considerations, the curvature of the pinned surface can be described and used for calculating the Young–Laplace pressure of the interface (equation (2)) of the capillary microvalve illustrated in figure 1(*a*) (Delamarche *et al* 1998, Huang *et al* 2006, Cho *et al* 2007)

$$\Delta p = -\gamma\left(\frac{2\cos\theta}{w} + \frac{\cos\phi}{h} + \frac{\cos\theta}{h}\right) \tag{2}$$

where γ is the surface tension of the gas–liquid interface, and w and h are the dimensions of the microvalve geometry, see figure 1(*a*). Maximising the pressure drop with regards to ϕ expressed in terms of equation (1) yields the theoretical burst pressure,

$$p_{\text{burst}} = -\gamma\left(\frac{2\cos\theta}{w} + \frac{\cos\left(\min\left\{\theta+\alpha; 180°\right\}\right)}{h} + \frac{\cos\theta}{h}\right). \tag{3}$$

This expression may also be obtained by considering the change in total interfacial energy of the system as a result of the change in volume (Andersson *et al* 2001, Huang *et al* 2006).

3. Experimental

3.1. Chip fabrication and design

The polymer chip consists of two parts: an injection moulded main part of cyclic olefin-copolymer (COC) polymer (TOPAS grade 5013L-10) and a 0.254 mm extruded COC sheet (TOPAS grade 5013S-04) both from TOPAS Advanced Polymers GmbH, Frankfurt–Höchst, Germany. The main part features capillary microvalves laid out in parallel, each with its own luer-fitted inlet, see figure 2(*a*) for an overview photograph of the injection moulded chip part. Injection moulding was conducted on an Engel Victory 80/45 Tech injection moulder (ENGEL, Schwertberg, Austria). It was fitted with a rapid prototyped computer numerical control (CNC) milled aluminium master insert featuring the negative counter-part of the channel layout on one side of the injection moulding tool and a luer-layout counter-part with through-holes (Andresen *et al* 2010) on the other. To complete the chip, the injection

Table 1. Nominal geometries compared to the post fabrication geometries as determined by chip characterisation performed on a single chip. Note that the heights contain the added height of 23.9 μm from the welding process. See figure 2(*c*) for the schematic lay-out of the capillary microvalve.

	w [μm]		h [μm]	
Valve #	Nominal	Actual	Nominal	Actual
100/100	100	92	100	135
200/100	200	202	100	134
300/150	300	286	150	182
500/150	500	486	150	181
500/250	500	447	250	281

moulded part was bonded to the COC sheet using a Telsonic USP4700 ultrasonic welder (Telsonic, Erlangen, Germany).

The channel layout features eight sets of channels with capillary microvalves connecting separate luer fittings to a collective outlet, see figure 2(*a*). Each channel has a unique width and height (see table 1) and a capillary microvalve constructed by a 90° expansion towards the floor of the channel. See figure 2(*b*) for an SEM image of an injection moulded capillary microvalve and figure 2(*c*) for a 3D representation of a capillary microvalve. Energy directors used for the ultrasonic welding were 130 μm wide triangular prism shaped protrusions (apex angle = 60°) centered 500 μm from the channel sidewalls. The chip topography characterization was carried out using a Nova 600 NanoSEM (FEI, Eindhoven, Netherlands) for images and a PLu Neox 3D Optical Profiler (Sensofar-Tech, S.L, Terrassa, Spain) for topographic data.

3.2. Chip coating

To increase the robustness of the system when performing burst pressure measurements, the hydrophobicity of the COC was increased by coating both the injection moulded part and the COC sheet with a hydrophobic 1H,1H,2H, 2H-perfluorodecyltrichlorosilane (FDTS, CAS No 78560-44-8) layer using a gas phase multi-step deposition process, prior to bonding. While FDTS and analogous perfluoroalkylsilanes alone provide a hydrophobic coating on silicon (Mayer *et al* 2000, Ashurst *et al* 2003, Ashurst *et al* 2004), polymers require a metal oxide adhesion layer prior to deposition of FDTS (Kobrin *et al* 2005, Kobrin *et al* 2007). Otherwise, the contact angle with water may be rather low, depending on the substrate. For the present work, silicon dioxide was used as the adhesion layer. The deposition was performed at 35 °C in a MVD100 system from Applied Microstructures (San Jose, California). In brief, the system consists of a deposition chamber, vaporization chambers for the precursors and cylinders housing the different precursors, where the connections between precursor cylinders, vaporization chambers and deposition chamber are controlled by valves. The system is connected to a pump via the deposition chamber. Precursor is vaporized from the cylinders into the vaporization chambers. Once a set pressure in the vaporization chamber is reached, the precursor vapour is introduced into the deposition chamber by means of the pressure difference between vaporization chamber and deposition chamber. During the precursor introduction step and the subsequent reaction, no pumping on the chamber is performed. After the reaction is finished, the reaction chamber is pumped down and purged several times with nitrogen. Prior to the deposition, the sample surface is activated using a remote oxygen plasma generated from a plasma source in the MVD100 system. Subsequently, silicon dioxide and FDTS are deposited at 35 °C in two consecutive process steps. Silicon tetrachloride and water were used as precursors for silicon dioxide. The two precursors are introduced simultaneously and allowed to react for a given time. The simultaneous presence of the two precursors means that the layer thickness obtained in one reaction cycle depends on the partial pressures of the two precursors and the reaction time (Kobrin *et al* 2005). For formation of the FDTS-layer, FDTS and water are introduced simultaneously. The simultaneous action of FDTS and water allows for the deposition of a self-assembled monolayer (SAM) of the perfluoroalkylsilane (Mayer *et al* 2000). The advancing contact angle of water to FDTS-coated COC sheets was measured on a Krüss DSA10 Contact Angle Measuring System (Krüss GmbH, Hamburg) to 120 ± 2°. The advancing contact angle for uncoated COC is 96 ± 3°.

3.3. Bonding by ultrasonic welding

Ultrasonic welding is performed by applying vibrations through a transducer to an energy director that melts and welds two layers together, as illustrated in figure 3. Depending on the success of the welding there are two main outcomes; if too much energy is applied, polymer may flow into cavities, known as flash (figure 3 bottom left). Conversely if too little energy is deposited, the energy directors will not completely melt, leaving small gaps (figure 3 bottom right). In either case, there will be an increase in height due to the presence of the polymer welding seam. This height was estimated by first calculating the cross-sectional area of the triangular shaped energy directors pre-welding and correlating it to the cross-sectional area of the welded energy director, assuming that the volume of the polymer was conserved during welding. Dimensions of the pre- and post-welding energy directors were measured using a PLu Neox 3D Optical Profiler and an optical microscope, respectively. The post-welding height was calculated to be 23.9 ± 1.7 μm, assuming a square cross-sectional area of the welded energy director.

Ultrasonic welding was chosen over thermal bonding because thermal bonding is not applicable with the hydrophobic coating and because ultrasonic welding allows for easy bonding of large area channels. While large area bonding is possible with thermal bonding, e.g. by using a custom pressure plate (Kim *et al* 2007), it requires a custom pressure plate for each design and an aligning step for each chip, which makes this process more complicated.

3.4. Burst pressure measurements

Hydrostatic burst pressures were determined by slowly raising a water column (50 mL syringe without piston) above chip level using a Thorlabs LTS150 motorized stage (Thorlabs, Newton,

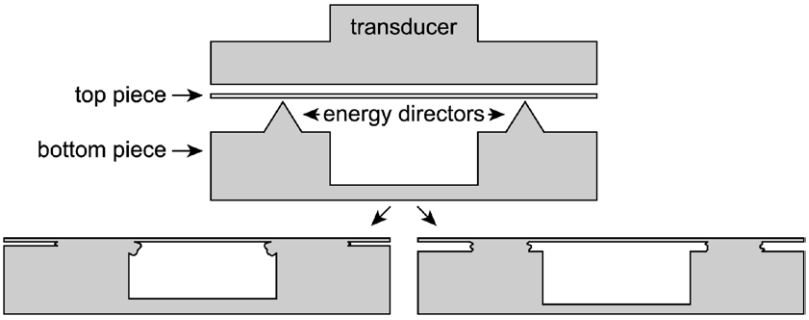

Figure 3. Cross sectional schematic of a channel before (top) and after ultrasonic welding (bottom left and right). The top part of the chip is pressed onto the bottom part with an ultrasonic transducer, which then vibrates to melt the energy directors. Depending on the amount of energy that is deposited via the transducer different outcomes will arise: Too much energy causes flash to form (bottom left) while too little energy causes a gap in the upper part of the channel (bottom right). In both cases, an added height results from the welding process.

NJ, USA). The water column was connected to the chip via tubing with luer fittings, resulting in a stable hydrostatic pressure. Before initiating a measurement, the chip was positioned so the surface vertical position matched that of the water surface. The syringe was then raised at 1 mm s^{-1} while the capillary microvalve was carefully monitored. Once the water advanced into the channel leading to the capillary microvalve, the stage was paused and the fluid allowed to pin at the capillary microvalve after which the stage was re-engaged. When the water burst through the capillary microvalve, the stage was stopped immediately and the height recorded. The syringe vertical position was then reset and after the meniscus had retracted past the capillary microvalve and the process was repeated for a total of three measurements per capillary stop. The chip was then rinsed and dried before another set of measurements was conducted amounting to a total of 6 measurements per chip. For every capillary microvalve, this experiment was repeated on 2–3 chips, resulting in a total of 12–18 measurements per capillary microvalve. An example of a single measurement can be seen in supplementary video 1 (stacks.iop.org/JMM/24/125007/mmedia). The burst pressures were calculated using $p = \rho g H$, where p is the calculated pressure, $\rho = 998\ \mathrm{kg\,m^{-3}}$, $g = 9.82\ \mathrm{m\,s^{-2}}$ and H is the measured height.

3.5. Numerical simulations

3.5.1. Model design. A numerical model for determining the capillary microvalve burst pressures was constructed on the basis of the geometry of the microfluidic chip with a pressure drop applied across the geometry (see figure 2(*d*)). Since steady state models with constant pressure drop was found to have convergence problems when the pressure drop was set to the approximate analytic burst pressure, a different approach had to be taken. The simulation was instead run in time-dependent mode with the initial interface position set at the channel expansion with a pressure drop increasing over time until bursting occurred. Because a capillary microvalve is an abruptly changing system when the valve bursts, a model coupled damping term was included in the expression for the pressure drop. This ensured that the unstable state was approached at a rate that minimized viscous and inertial effects, whilst elucidating the minimum pressure required for bursting (i.e. the burst pressure). Since a higher percentage of the model volume will be occupied with water as the pressure drop increases, the pressure drop dampening term was negatively proportional to the average water content.

The rationale of the model coupling is that the pressure drop increases more slowly when the interface expands; as the burst pressure is reached and the valve starts bursting, the pressure drop is reduced as a result of the increasing volume fraction occupied by water. Yet, regardless of the reduced pressure, the interface will continue to grow due to the smaller pressure required to expand the now larger (and less curved) interface.

3.5.2. Model description. The numerical analysis of the capillary microvalves was conducted using the 'Laminar Two-Phase Flow, Level-Set' package in COMSOL Multiphysics 4.3a (COMSOL A/S, Kgs. Lyngby, Denmark). The governing equations were the Navier–Stokes equation and the reinitialized LS function, $\phi_{\mathrm{ls}}(r)$, used to track the interface and interpolate the material properties (Olsson and Kreiss 2005, COMSOL 2012). The reinitialized LS function operates on an interface of finite thickness with intermediate properties of the two phases. This makes the LS method ideal for calculating curvatures which is crucial for estimating the Young–Laplace pressure, but weak at conserving mass and tracking the meniscus position (e.g. the dynamic contact angle). Properties, such as the density is determined by $\rho = \phi_{\mathrm{ls}}(r)\,\rho_{\mathrm{air}} + \left(1 - \phi_{\mathrm{ls}}(r)\right)\rho_{\mathrm{water}}$, where $\phi_{\mathrm{ls}}(r) = 1$ for 0% water and $\phi_{\mathrm{ls}}(r) = 0$ for 100% water (COMSOL 2012).

The time-dependent pressure drop across the geometry (see figure 2(*d*)) was defined as $p_1(t) = \Delta p(t) + p_0$ where

$$\Delta p(t) = p_{\mathrm{start}} + \alpha t - \beta \overline{\phi_{\mathrm{ls}}}(t) - p_0\,. \tag{4}$$

Here, p_{start} was set larger than the capillary pressure of the inlet channel of the geometry to avoid backwards interface movement. Effectively, $\overline{\phi_{\mathrm{ls}}}(t) = \mathrm{Volume_{water}}(t)\ /\ \mathrm{Volume_{geometry}} = \int_V \phi_{\mathrm{ls}}(r,t)\,\mathrm{d}r \Big/ \int_V \mathrm{d}r$. The pressure drop is thus reduced as more volume is occupied by water, resulting in a dampening of the interface advance. The ambient pressure, p_0, was set to 0, since it cancels out and hence has no contribution to the pressure drop. As shown in the supplementary information (stacks.iop.org/JMM/24/125007/mmedia), appropriate

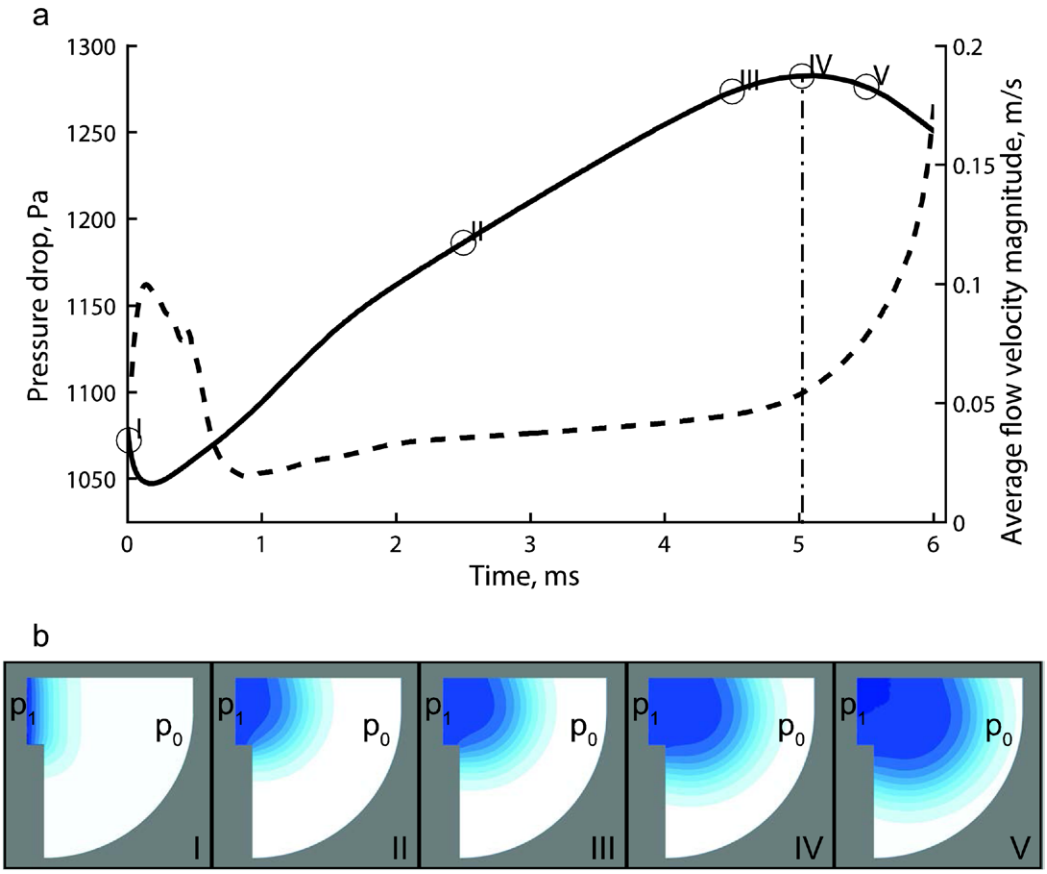

Figure 4. (*a*) Pressure drop, controlled by the model coupling equation (4), and average flow velocity magnitude developing over time. The burst pressure is marked by a vertical dash-dot line. (*b*) (I–V) Contour plots of fraction of water (ϕ_{ls}) spanning [0:1] in steps of 0.1, dark blue being 100% water. (*b*)(I) Initial flat interface with forced contact angle = 90° relaxes rapidly. (*b*)(II) Stabilised and linearly growing interface. (*b*)(III) Interface immediately prior to bursting. (*b*)(IV) Bursting meniscus. Note the concentration of water at the pinning corner is >90%. (*b*)(V) Rapidly expanding meniscus, where the damping term reduces the pressure drop.

values for the pressure ramping rate (α) and the damping range (β) were found to be 50.000 Pa s^{-1} and 200 Pa, respectively. The model was generally found to be robust in terms of these parameters (see table S2 in the supplementary information (stacks.iop.org/JMM/24/125007/mmedia)). However, the simulation time could be significantly prolonged if the α / β ratio was decreased in equation (4). On the other hand, a too high ratio would cause the dampening term to be negligible, complicating the determination of the burst pressure.

To achieve faster convergence, 'transformer oil' ($\rho = 0.879$ g cm^{-3}, $\eta = 20.8$ mPa s) with surface tension equal to that of an air–water interface $(\gamma_{water/air} = 72.89$ mN m$^{-1})$ was used as a substitute for air. This does not take into account the compressibility of air, however, due to the nature of the simulation it is not expected to affect the results. Additionally, the increased density and viscosity of oil will affect the inertial component, however, since the model is already dampened by equation (4) this is not expected to influence the burst pressure. Parameters not listed above used in the COMSOL model are stated in the supplementary information (stacks.iop.org/JMM/24/125007/mmedia), section 1.4.

The inlet channel length, l, was chosen to accommodate the relaxation of the initial (flat) interface (see figure 2(*d*)). Likewise, the outlet chamber was made sufficiently large for the meniscus to burst without interacting with the outlet boundary. The central symmetry plane was exploited to minimise computational demands, see figure 2(*d*).

4. Results and discussion

First a validation of the numerical model including the *modus operandi* of determining the burst pressure is presented. Then, the fabrication process is evaluated and finally the experimental burst pressures are presented and compared to the numerically simulated and analytically calculated results.

4.1. Numerical model analysis

To elucidate that the model coupled dampening term, equation (4), used to control the pressure drop in the simulation, functioned as intended, the pressure drop developing over time is plotted in figure 4(*a*). As evident, the two opposing terms in equation (4) result in three stages: interface relaxation (figure 4(*a*)(I)), linear pressure rise (figure 4(*a*)(II + III)) and bursting (figure 4(*a*)(IV)). To study the behaviour of the virtual interface during the simulation and its interaction with the model geometry, contour plots of fraction-of-water on the symmetry

plane (see figure 2(*d*)) are plotted for the selected times in figure 4(*b*). The readily recognisable peak in figure 4(*a*) and the on-going bursting illustrated figure 4(*b*)(V) confirm that the constructed model coupling works as intended and does not prevent continued bursting of the valve.

The fact that the interface has a finite width that spans to both sides of the pinning corner at all times may seem counter intuitive from an experimentalists point of view, but this is intrinsic for the LS method . In most analytical expressions, the temporal meniscus position defines the burst pressure, whereas in simulations using the LS method, the exact meniscus position is not available (figures 2(*d*) and 4(*b*)). Therefore a different approach for determining the burst pressure has to be taken. In this study, the maximum pressure drop that can be applied without causing a rapid expansion of the interface defines the burst pressure (full line in figure 4(*a*)). To further illustrate the interface dynamics, the average flow velocity magnitude is plotted versus time (dashed line in figure 4(*a*)). It is evident that the interface has rapid movements during the initial interface relaxation and again when bursting occurs. These steep changes in flow velocity within a single ms support the assumption that the added inertia of the transformer oil does not influence the simulation. To stress the importance of the dampening term, an identical simulation was run with no dampening ($\beta = 0$). From the data (figure S1 (stacks.iop.org/JMM/24/125007/mmedia)) it is clear that no burst pressure can be determined either from $p(t)$ or from the average flow velocity magnitude. Without dampening, the burst pressure could not be estimated in a reproducible manner. We propose that this approach may generally assist when determining critical variables in abruptly changing systems.

To validate the numerical model, a set of simple axial symmetrical geometries was analysed. Contrary to the complex rectangular geometries, the burst pressures of the cylindrical geometries have a closed-form analytical solution, see supplementary information (stacks.iop.org/JMM/24/125007/mmedia). From supplementary figure S3 (stacks.iop.org/JMM/24/125007/mmedia) it is evident that the numerical simulations consistently underestimate the analytically calculated burst pressures by 6.7%. As discussed by Olsson and Kreiss, the diffusive representation of the interface results in an attraction between the interface and the walls when the distance is close to the interface thickness (Olsson and Kreiss 2005). This effect may be the cause of the consistent burst pressure undershooting of the LS based model. Obviously, this effect depends in part on the geometry and the impact on the numerical burst pressure varies accordingly. In light of the intrinsic limitations of the LS method, such as the diffuse interface definition and the poor conservation of mass which may destabilise the pinned interface, the consistent underestimation of the burst pressure by 6.7% is acceptable for most applications.

Figure 5 shows numerical simulations as well as analytical calculations (equation (3)) of the burst pressure in structures illustrated in figures 1(*a*) and 2(*c*) for $50\,\mu\text{m} \le w \le 500\,\mu\text{m}$ and $25\,\mu\text{m} \le h \le 281\,\mu\text{m}$ (details given in the supplementary information (stacks.iop.org/JMM/24/125007/mmedia)). Again, a consistent underestimation of the numerical burst pressure is observed compared to the analytically calculated result,

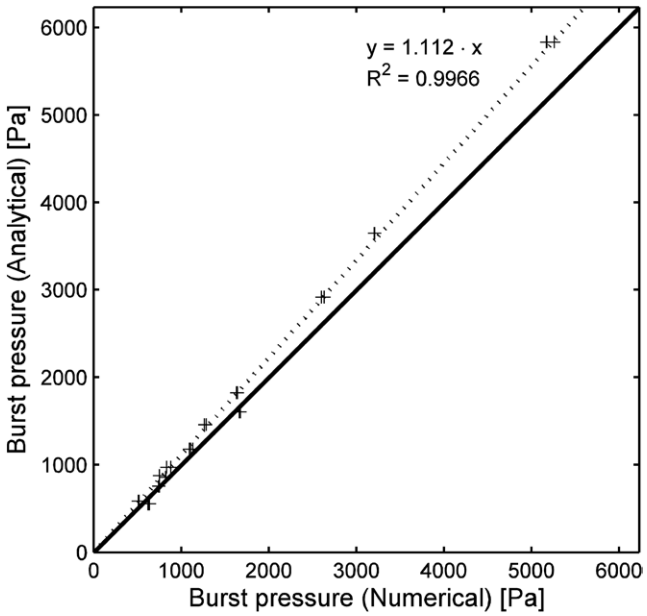

Figure 5. Analytically calculated burst pressures of all nominal and measured geometries plotted versus numerically determined burst pressures (+) of the same geometries (see supplementary information (stacks.iop.org/JMM/24/125007/mmedia), for a complete list of geometries and results). The solid line represents $y = x$ and the dashed line is a linear fit to the data points.

except that the difference is larger (11.2%). This behaviour can be explained by the more complex geometry, which is more taxing for the numerical simulations and also causes the analytical predictions to be less accurate, since a complete solution does not exist. As stated above, we believe that this is an acceptable error for most applications, such as modelling burst pressures of complex microfluidic systems prior to fabrication.

The *R*-squared values (>0.995) for the linear fits of the correlations between the numerically modelled and analytically calculated burst pressures (see figures 5 and S3 (stacks.iop.org/JMM/24/125007/mmedia)) suggest that the model is robust and precise for a wide range of geometries. Furthermore, the similarity in underestimating between the cylindrical and rectangular geometries shows that the model performs equally well with simple and complex problems.

4.2. Geometrical characterisation of chips

A total of eight capillary microvalve geometries (nominal width/nominal height in μm) were chosen for investigation; 50/25, 50/50, 100/50, 100/100, 200/100, 300/150, 500/150 and 500/250, see figure 2(*b*) for an SEM image and figure 2(*c*) for the schematic lay-out of a single capillary microvalve. It was not possible to conduct experiments on the smallest geometries (50/25, 50/50 and 100/50) due to polymer blocking the channels after ultrasonic welding.

The micro milling and injection moulding added some error to the nominal geometries chosen, but for clarity the labels for the different capillary stops have been kept in the 'nominal width/nominal height' format. The actual widths

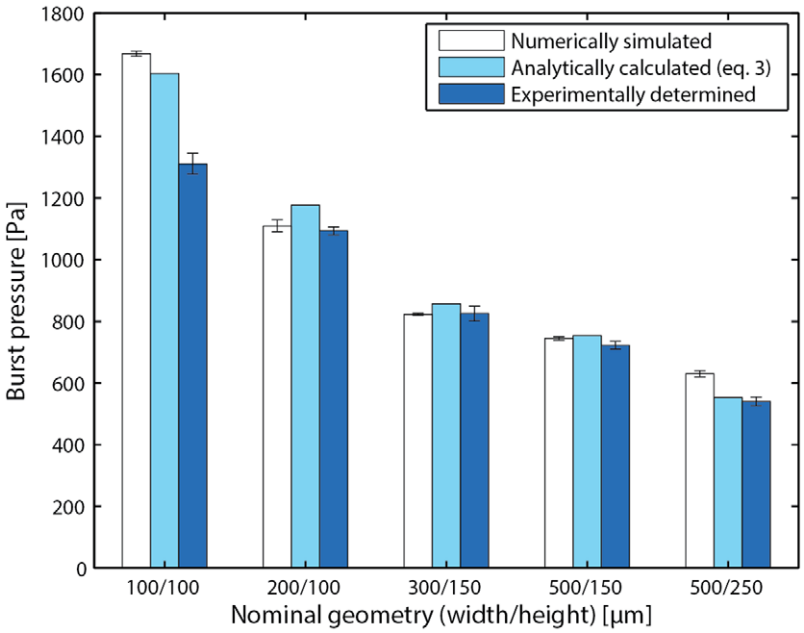

Figure 6. Numerically simulated, analytically calculated, and experimentally determined burst pressures of the selected capillary microvalve geometries. Light blue columns represent the burst pressures calculated from the analytical expression (equation (3)). White columns denote the numerically simulated burst pressures, n = 2, 3, 2, 3 and 3 for 100/100, 200/100, 300/150, 500/150 and 500/250, respectively. Dark blue columns denotes the experimentally determined hydrostatic burst pressures, n=18 for 100/100 and 500/250 and n = 12 for 200/100, 300/150 and 500/150. Error bars represent the sample standard deviation.

and heights deviate 1.2–10.7% from their nominal values as determined by the chip characterisation (see table 1 for geometries). The majority of the error comes from the milling process, which was confirmed by confocal microscopy measurements of the master insert. The master insert dimensions differed on average less than 1 μm from the dimensions measured on the moulded chip. The polymer filling/shrinkage associated with injection moulding of 5013L-10 is negligible (Tanzi *et al* 2012), which is also evident from the SEM image in figure 2(*b*). The average arithmetic mean roughness (Sa) of the chip bottom part surface was measured to 0.6 μm.

The actual widths and heights have been used as input in the analytical expressions as well as the numerical simulations when comparing with the experimentally determined burst pressures.

4.3. Fabrication process

The fabrication process can be split in two. First there is the rapid prototyping, which takes 3–4 h of CNC milling on average per design. Then there is the two-step manufacturing of the chip itself, which consists of injection moulding and ultrasonic welding. The injection moulder has an isothermal cycle time of about 50 s per chip and the (manual) ultrasonic welding takes 30 s on average per chip. The welding itself takes about 5 s, the rest is mounting, removal of protective films and release of the chip. This amounts to 80 s for a standard chip fabricated using this process. For the chip presented in this paper a coating of the COC parts was needed, to be able to get robust measurements. This is a batch process that takes about 60 min. The MVD holds 48 chips at a time amounting to 85 s/chip. The total average fabrication time for the chip presented in this study is thus about 155 s per chip. We typically fabricated about 100 chips per run.

Injection moulding is very fast compared to many other published systems, where each chip is often custom CNC milled or cast in PDMS, which takes up to 4 h, and on par with other micro moulding techniques such as thermoforming and hot embossing. Ultrasonic welding is rapid compared to, e.g. thermal bonding and more durable and less prone to decay than, e.g. bonding using adhesive layers. As the bulk of the chip is not heated, pre-loading of dried or jellified reagents is possible, which is of high relevance to Point-of-Care devices (Sun *et al* 2013). The local heating is applied for ~0.1 s leading to turn-over times of ca. 5 s per welding (excluding mounting and release), which is considerably shorter than other common bonding processes such as thermal bonding and plasma assisted bonding (Bu *et al* 2013). This makes ultrasonic welding very desirable for μTAS rapid prototyping and mass production. The added height imposed by the ultrasonic welding and milling process may be of concern; however, this undesired addition can be avoided by optimising the milling process and energy director design and welding process. Since ultrasonic welding does not have the same cross material compatibility as, e.g. adhesive bonding, the most common practise is to weld together like materials. It does, however, allow for bonding through thin-film layers (e.g. Teflon coatings as demonstrated in this study) or thin sheets of other polymer types (Truckenmüller *et al* 2006a, Bu *et al* 2011).

4.4. Experimental burst pressures

Figure 6 shows the average determined hydrostatic burst pressures for each microvalve geometry compared to the

analytically calculated and numerically simulated values. In general, the experimentally determined burst pressures are lower than the analytically calculated results with larger relative deviations for larger burst pressures, ranging from 2.2% to 18%. There is good reproducibility of the experimental data with regards to repetitions on the same chip and repetitions in-between chips, with a mean coefficient of variation of 2.2%. The large deviation from the analytical and numerical values for the 100/100 capillary microvalve can be explained by incomplete polymer melting during ultrasonic welding: The small gaps left by ultrasonic welding (see figure 3 bottom right) were observed to have lower capillary pressure than the actual capillary microvalve. This led to a premature bursting of the microvalve and hence a lower than expected capillary burst pressure (see figure 6). Disregarding the 100/100 microvalve, a good correlation between the experimentally determined and analytically calculated burst pressures is observed with an average deviation of 4.5%.

Although the analytically calculated results deviate slightly from the experimentally determined burst pressures, they do show that over the investigated aspect ratios and dimensions, equation (3) can on average predict the experimentally determined burst pressures with an accuracy of 4.5%. The small standard deviations on the experimental results demonstrate that injection moulded and ultrasonically welded chips provide excellent reproducibility and stable results. For the smallest geometries it was not possible to produce functional channels due to polymer blocking the channels after bonding by ultrasonic welding (figure 3 bottom left). However, as mentioned it is expected that this can be avoided by optimising the chip design, master insert quality, the energy director geometry and bonding parameters. The chip design used in this study had a high local density of energy directors, which complicates the ultrasonic welding. Micromilling is also not ideal for producing small (~50 μm) structures, because it is difficult to maintain precise alignment upon tool switching with the machines used in the present work.

4.5. Numerically simulated burst pressures

As previously described, the numerical simulations were carried out for both nominal- and actual (measured) chip dimensions using starting pressures (p_{start}) lying in-between the analytically calculated capillary pressure of the inlet channel and the analytically calculated capillary burst pressure. For each of the geometries, two additional control simulations were conducted by using starting pressures of approximately 90% and 70% of the predicted burst pressure of the preceding simulation.

As can be observed in figure 6, the numerical estimates fit well with the experimental values, except for the 100/100 geometry. The numerical model does, however, show good agreement with the analytical estimate for this geometry. When comparing figures 5 and 6, there is a general trend of the numerical simulations to deviate more from the analytically calculated results for large burst pressures, while for small burst pressures there is a better correlation. From the linear fit in figure 5 it can be seen that the numerical model is a good alternative to the analytical expression. It is also evident that the width/height aspect ratio does not influence the results for the investigated range of geometries.

In summary, the numerical model overestimated the experimental burst pressures by 5.2% on average, which, together with the demonstrated robustness of our numerical model indicates that the LS method is promising for burst pressure predictions of more complicated geometries. However, further studies need to be undertaken to confirm this.

5. Concluding remarks

In this work, two aspects of going from rapid prototyping to pilot (mass) production were investigated:

(1) We have presented an all-polymer chip system fabricated using a rapid prototyped master insert for injection moulding and ultrasonic welding, which can be directly implemented in mass production. The chip has a short production time of 80 s per chip (155 s including coating assuming a batch of 48 chips).
(2) A numerical tool was developed to aid in rapid prototyping by predicting geometries required to achieve capillary microvalves with a desired burst pressure.

The fabrication process and numerical tool were validated via investigations of geometrical capillary microvalves. In both cases the numerically simulated and analytically calculated burst pressures were found to be within 5.2% and 4.5% of the experimentally determined burst pressures, respectively. The numerical model was further validated, by modelling a more simple geometry for which a complete analytical expression exists. The LS approach was found to be precise and robust with regards to geometry and model parameters and The included dampening term may also be beneficial to others when simulating unstable or abruptly changing systems. The data presented in this study supports the idea of using numerical simulations as a tool in rapid prototyping to predict burst pressures of complex geometries before physically crafting the prototypes, ideally reducing the number of iterations needed from idea to functioning prototype to final product.

The ability to tailor and mass-produce capillary microvalves with a quantitatively predictable behaviour in all-polymer microfluidic systems is important and beneficial for many medical, biological and chemical applications.

Acknowledgments

This work is supported by the Danish Council for Strategic Research through the Strategic Research Center PolyNano (Grant No. 10-092322/DSF).
We would like to acknowledge Minqiang Bu, Department of Photonics Engineering, Technical University of Denmark, and Ivan R Perch-Nielsen, DELTA, Hørsholm, Denmark, for sharing experience in micro-fabrication and ultrasonic welding, and Fridolin Okkels, Department of Micro- and Nanotechnology for discussions on COMSOL related topics.

References

Abhari F, Jaafar H and Yunus N A 2012 A comprehensive study of micropumps technologies *Int. J. Electrochem. Sci.* **7** 9765–80

Andersson H *et al* 2001 Hydrophobic valves of plasma deposited octafluorocyclobutane in DRIE channels *Sensors Actuators* B **75** 136–41

Andresen K Ø *et al* 2010 Injection molded chips with integrated conducting polymer electrodes for electroporation of cells *J. Micromech. Microeng.* **20** 055010

Ashurst R W *et al* 2004 Improved vapor-phase deposition technique for anti-stiction monolayers *Proc. SPIE* **5342** 204–11

Ashurst W R, Carraro C and Maboudian R 2003 Vapor phase anti-stiction coatings for MEMS *IEEE Trans. Device Mater. Reliab.* **3** 173–8

Attia U M, Marson S and Alcock J R 2009 Micro-injection moulding of polymer microfluidic devices *Microfluid Nanofluidics* **7** 1–28

Becker H and Gärtner C 2008 Polymer microfabrication technologies for microfluidic systems. *Anal. Bioanal. Chem.* **390** 89–111

Begolo S, Colas G, Viovy J-L and Malaquin L 2011 New family of fluorinated polymer chips for droplet and organic solvent microfluidics *Lab Chip* **11** 508–12

Bouaidat S *et al* 2005 Surface-directed capillary system; theory, experiments and applications *Lab Chip* **5** 827–36

Bu M *et al* 2013 A temperature control method for shortening thermal cycling time to achieve rapid polymerase chain reaction (PCR) in a disposable polymer microfluidic device *J. Micromech. Microeng.* **23** 074002

Bu M, Perch-Nielsen I R, Sun Y and Wolff A 2011 A microfluidic control system with re-usable micropump/valve actuator and injection moulded disposable polymer lab-on-a-slide *Proc. 16th Int. Solid-State Sensors, Actuators Microsystems Conf. IEEE (Beijing, Jun. 2011)* pp 1244–7

Chibbaro S *et al* 2009 Capillary filling in microchannels with wall corrugations: a comparative study of the Concus–Finn criterion by continuum, kinetic, and atomistic approaches *Langmuir* **25** 12653–60

Cho H, Kim H-Y, Kang J Y and Kim T S 2007 How the capillary burst microvalve works *J. Colloid. Interface Sci.* **306** 379–85

Delamarche E *et al* 1998 Microfluidic networks for chemical patterning of substrates: design and application to bioassays *J. Am. Chem. Soc.* **120** 500–8

den Dulk R C *et al* 2012 Magneto-capillary valve for integrated purification and enrichment of nucleic acids and proteins *Lab Chip* **13** 106–18

Duffy D C *et al* 1999 Microfabricated centrifugal microfluidic systems: characterization and multiple enzymatic assays *Anal. Chem.* **71** 4669–78

Dyson D C 1988 Contact line stability at edges: comments on Gibbs's inequalities *Phys. Fluids* **31** 229

Gerlach D, Tomar G, Biswas G and Durst F 2006 Comparison of volume-of-fluid methods for surface tension-dominant two-phase flows *Int. J. Heat Mass Transf.* **49** 740–54

Gibbs J W 1906 *Scientific Papers of J. Willard Gibbs...: Thermodynamics* (Longmans, Green and Company)

Giboz J, Copponnex T and Mélé P 2007 Microinjection molding of thermoplastic polymers: a review *J. Micromech. Microeng.* **17** R96–109

Huang W, Liu Q and Li Y 2006 Capillary filling flows inside patterned-surface *Microchannels. Chem. Eng. Technol.* **29** 716–23

Kim D S *et al* 2007 Collapse-free thermal bonding technique for large area microchambers in plastic lab-on-a-chip applications *Microsyst. Technol.* **14** 179–84

Kobrin B, Dangaria N and Chinn J 2007 Low temperature nanolayers of metal oxides by MVD^{TM} *Tech. Proc. 2007 NSTI Nanotechnol. Conf. Trade Show* vol **4** pp 575–7

Kobrin B, Nowak R, Yi R C and Chinn J 2005 Controlled deposition of silicon-containing coatings adhered by an oxide layer *US Patent* US20050271809 A1

Manz A, Graber N and Widmer H M 1990 Miniaturized total chemical analysis systems: a novel concept for chemical sensing *Sensors Actuators* B **1** 244–8

Matteucci M *et al* 2013 Fabrication and characterization of injection molded multi level nano and microfluidic systems *Microelectron. Eng.* **111** 294–8

Mayer T M *et al* 2000 Chemical vapor deposition of fluoroalkylsilane monolayer films for adhesion control in microelectromechanical systems *J. Vac. Sci. Technol. B Microelectron. Nanom. Struct.* **18** 2433

Oh K W and Ahn C H 2006 A review of microvalves *J. Micromech. Microeng.* **16** R13–39

Olsson E and Kreiss G 2005 A conservative level set method for two phase flow *J. Comput. Phys.* **210** 225–46

Sun Y *et al* 2013 Pre-storage of gelified reagents in a lab-on-a-foil system for rapid nucleic acid analysis *Lab Chip* **13** 1509–14

Sussman M and Puckett E G 2000 A coupled level set and volume-of-fluid method for computing 3D and axisymmetric incompressible two-phase flows *J. Comput. Phys.* **162** 301–37

Tanzi S *et al* 2012 Fabrication of combined-scale nano- and microfluidic polymer systems using a multilevel dry etching, electroplating and molding process *J. Micromech. Microeng.* **22** 115008

Thio T H G *et al* 2013 Theoretical development and critical analysis of burst frequency equations for passive valves on centrifugal microfluidic platforms *Med. Biol. Eng. Comput.* **51** 525–35

Truckenmüller R *et al* 2006a An ultrasonic welding based process for building up a new class of inert fluidic microsensors and -actuators from polymers *Sensors Actuators* A **132** 385–92

Truckenmüller R *et al* 2006b Micro ultrasonic welding: joining of chemically inert polymer microparts for single material fluidic components and systems *Microsyst. Technol.* **12** 1027–9

Waldbaur A, Rapp H, Länge K and Rapp B E 2011 Let there be chip—towards rapid prototyping of microfluidic devices: one-step manufacturing processes *Anal. Methods* **3** 2681

Zhao B, Moore J S and Beebe D J 2002 Principles of surface-directed liquid flow in microfluidic channels *Anal. Chem.* **74** 4259–68

Zimmermann M, Hunziker P and Delamarche E 2008 Valves for autonomous capillary systems *Microfluid Nanofluidics* **5** 395–402

Fabrication and Modelling of Injection Moulded All-Polymer Capillary Microvalves for Passive Microfluidic; Journal of Micromechanics and Microengineering; K. Kistrup, C.E. Poulsen, P.F. Østergaard, K. B. Haugshøj, R. Taboryski, A. Wolff and M. F. Hansen, Department of Micro- and Nanotechnology, Technical University of Denmark, mikkel.hansen@nanotech.dtu.dk

1 Supplementary information

1.1 Dimensions of simulated geometries

Table S1 contains a list of all capillary microvalve geometries simulated using the constructed COMSOL model, the starting pressures, the simulated burst pressures and the analytically calculated burst pressures.

Table S1 Geometries used for numerical calculations. Note that both nominal geometries and post fabrication geometries are included. The configurations are sorted by the analytically calculated burst pressure.

Width [µm]	Height [µm]	Starting pressure [Pa]	Numerical burst pressure [Pa]	Analytical burst pressure [Pa]
447	281	300,0	620,0	552,8
447	281	400,0	640,0	552,8
447	281	400,0	630,0	552,8
500	250	400,0	508,9	583,2
500	250	450,0	518,2	583,2
500	250	300,0	508,1	583,2
486	181	400,0	748,0	753,9
486	181	500,0	738,0	753,9
486	181	400,0	748,0	753,9
286	182	500,0	820,0	857,0
286	182	600,0	825,0	857,0
500	150	600,0	748,0	874,8
500	150	600,0	748,0	874,8
500	150	500,0	748,0	874,8
300	150	800,0	831,1	972,0
300	150	700,0	878,0	972,0
202	134	1000,0	1130,0	1176,8
202	134	900,0	1108,0	1176,8
202	134	800,0	1091,0	1176,8
200	100	1050,0	1265,8	1458,0
200	100	1100,0	1282,7	1458,0
92	135	1400,0	1673,7	1603,9
92	135	1200,0	1662,0	1603,9
100	100	1600,0	1630,2	1822,5
100	100	1500,0	1630,3	1822,5
100	100	1650,0	1643,3	1822,5
100	50	2200,0	2601,7	2916,0
100	50	2200,0	2631,8	2916,0
50	50	2850,0	3205,3	3645,0
50	50	2800,0	3210,0	3645,0
50	25	4700,0	5177,0	5832,0
50	25	4500,0	5172,0	5832,0
50	25	4700,0	5258,0	5832,0

1.2 Undampened model simulation

To elucidate the importance of the dampening term an identical simulation to the one run in Fig. 4a was conducted, where $\beta = 0$ *i.e.* without the dampening term (Fig. S1). It is evident that there is no correlation between the bursting pressure and the average flow velocity magnitude (*cf.* Fig. 4a). The burst pressure could not be determined from Fig. S1 in a reproducible fashion.

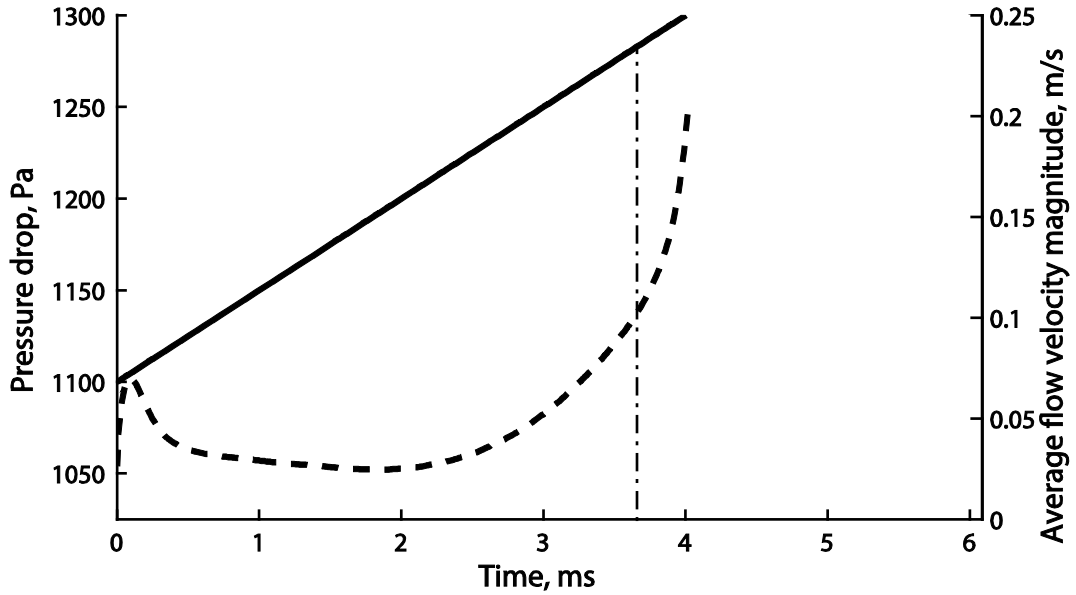

Fig. S1 Pressure drop, controlled by the model coupling Equation (3.1) with $\beta = 0$, and average flow velocity magnitude developing over time. The bursting pressure estimated with dampening is marked by a vertical dashed-dot line in the figure.

1.3 Model validation using an axial symmetrical geometry

To validate the developed COMSOL model and the applicability of the Level-Set method for burst pressure determination, simulations were conducted on geometries having axial symmetry. The two major differences between the rectangular capillary microvalves characterised in this study and these cylindrical geometries are the lack of corners on the pinning edge and the fact that an exact analytical expression can be constructed for the cylindrical microvalves. The analytical burst pressures, $p_{burst,cyl}$, can by geometric considerations be expressed using the Young-Laplace equation as

$$p_{burst,cyl} = -4\gamma \frac{\cos(\min\{\theta + \alpha; 180°\})}{D}. \qquad \textbf{(1.1)}$$

where D is the diameter of the capillary. Similarly to the rectangular capillary microvalves characterised in this paper, the expansion angle, α, was kept constant at 90°and the contact angle, θ, was set to 120°. Fig. S2 shows the axial symmetrical COMSOL model. The inlet and outlet are denoted by wireframes, walls are shown in grey and the isosurface represents 50% water content ($\phi_{ls} = 0.5$).

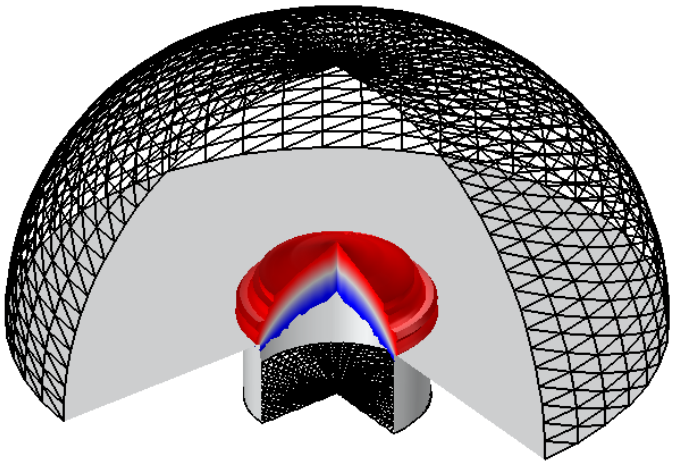

Fig. S2 Cylindrical capillary microvalve. Fine and coarse wireframes are inlet and outlet, respectively, grey surfaces are walls with contact angle θ and the volume filling denotes elements with $\phi_{ls} = [0.25, 0.75]$ where the blue colour denotes higher water content.

Simulation data for 24 geometries of diameter 30 µm to 260 µm is plotted in Fig. S3.

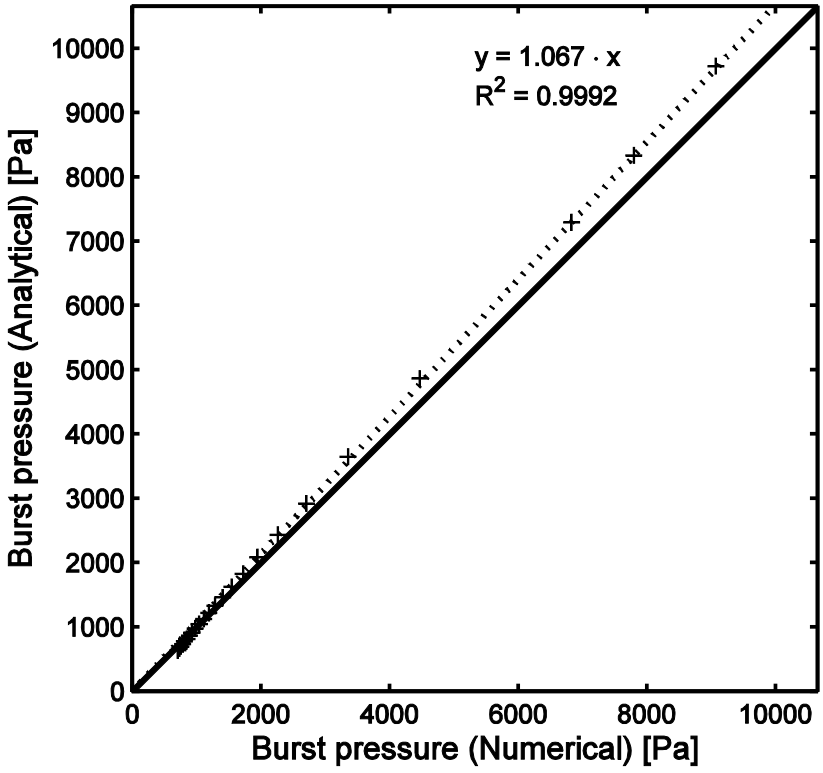

Fig. S3 Analytically calculated burst pressures of cylindrical geometries plotted versus numerically determined burst pressures (+) of the same geometries. The solid line represents $x = y$ and the dashed line is a linear fit of the data points.

It is evident that the trend of underestimating at higher burst pressures is similar to that observed for the rectangular geometries, see Fig. S3 and Fig. 5.

The R-squared value of 0.9992 for the linear fit of the correlation between the numerically modelled and analytically calculated burst pressures suggests that the model is robust and precise for a wide range of geometries. Furthermore, the similarity in underestimating between the cylindrical and rectangular geometries shows that the model performs equally with simple and complex problems. As mentioned in Section 4.1, the diffusive representation of the interface results in an attraction between the interface and the walls when the distance is close to the interface thickness (Olsson and Kreiss 2005).

1.4 Additional model parameters

To avoid interactions between the pinned interface and the outlet of the model, the circular section, centered on the pinning corner (see Fig. 2d), was set to be larger than$2.2 \times h$ (diameter for cylindrical model). Similarly, the inlet capillary length, l, was set to 25 µm. The interface thickness parameter was set to half of the maximum element size (default setting in COMSOL), resulting in an interface thickness of 15.65 µm. Memory consumption and computational demands were minimised by using a minimum mesh element size of 7.83 µm and applying stop condition to terminate the simulation as soon as the average water content on the outlet boundary exceeded 50%, $\overline{\phi_{ls,outlet}} \geq 0.5$. The time dependent solver was set to extract data every 10 µs and was allowed to run for a total of 50 ms. In this time span, bursting always occurred, and the model was hence terminated by the stop condition.

As mentioned in the main text, the values used for the pressure ramping rate (α) and the damping range (β) were 50.000 Pa/s and 200 Pa, respectively. Examples simulations with other values for these two parameters are listed in Table S2.

Table S2 Twin simulations of the rectangular geometry using alternative values for α and β and the resulting numerical pressure.

α [Pa/s]	β [Pa]	Numerical burst pressure [Pa]	Analytical burst pressure [Pa]
50000	300	831.1	728.9
75000	300	878.0	728.9
25000	200	1586.8	1457.8
50000	200	1604.2	1457.8
50000	100	3205.3	2915.6
75000	100	3210.0	2915.6

Appendix 2

Liquid carry-over in an injection moulded all-polymer chip system for immiscible phase magnetic bead-based solid-phase extraction

K. Kistrup, K. Skotte Sørensen, A. Wolff, M. Fougt Hansen

J. Magn. Magn. Mater. **100** (2014) 1–6. doi:10.1016/j.jmmm.2014.10.020

Journal of Magnetism and Magnetic Materials 380 (2015) 191–196

Contents lists available at ScienceDirect

Journal of Magnetism and Magnetic Materials

journal homepage: www.elsevier.com/locate/jmmm

Liquid carry-over in an injection moulded all-polymer chip system for immiscible phase magnetic bead-based solid-phase extraction

Kasper Kistrup [a], Karen Skotte Sørensen [a,b], Anders Wolff [a], Mikkel Fougt Hansen [a,*]

[a] Department of Micro- and Nanotechnology, Technical University of Denmark, DTU Nanotech, Building 345 East, DK-2800 Kongens Lyngby, Denmark
[b] Center for Integrated Point of Care Technologies (CiPoC), DELTA, Venlighedsvej 4, DK-2870 Hørsholm, Denmark

ARTICLE INFO

Article history:
Received 30 June 2014
Received in revised form
30 September 2014
Accepted 4 October 2014
Available online 13 October 2014

Keywords:
Polymer microfluidics
Magnetic beads
injection moulding
Ultrasonic welding
Immiscible phase filtration
Capillary stop
Mobile solid-phase extraction

ABSTRACT

We present an all-polymer, single-use microfluidic chip system produced by injection moulding and bonded by ultrasonic welding. Both techniques are compatible with low-cost industrial mass-production. The chip is produced for magnetic bead-based solid-phase extraction facilitated by immiscible phase filtration and features passive liquid filling and magnetic bead manipulation using an external magnet. In this work, we determine the system compatibility with various surfactants. Moreover, we quantify the volume of liquid co-transported with magnetic bead clusters from Milli-Q water or a lysis-binding buffer for nucleic acid extraction (0.1 (v/v)% Triton X-100 in 5 M guanidine hydrochloride). A linear relationship was found between the liquid carry-over and mass of magnetic beads used. Interestingly, similar average carry-overs of 1.74(8) nL/μg and 1.72(14) nL/μg were found for Milli-Q water and lysis-binding buffer, respectively.

1. Introduction

Paramagnetic particles or magnetic beads (MBs) are increasingly being applied within different fields of science as sensors, labels, carriers/separators *etc.*, [1]. In particular, the use of MBs as the solid-phase matrix for solid-phase extraction (SPE) has become popular and spawned a number of commercial kits and functionalised particle solutions [2,3].

Within the last ten years a variant of MB-based SPE has emerged, where an immiscible phase is used as a filtering step to circumvent the washing steps otherwise needed to perform a successful extraction. This is done by transporting the target–MB cluster through an immiscible phase, such as oil [4–6], wax [4,7,8], or air [8], often using an external permanent magnet. Such systems have been demonstrated for a number of applications including enzyme linked immunosorbent assays [6,9,10], nucleic acid extraction [4,7,8,11–14], protein extraction [8], and cell extraction [15,16].

The efficacy of these immiscible phase filtration systems relies heavily on the ability to limit the amount of co-transported liquid with the MB cluster. They are mostly "open" systems, often connected by capillary microvalves that rely on surface tension forces to function. Interface tension is, however, a complex entity that together with the rest of the system is influenced by a number of parameters. These include, but are not limited to MBs (size, amount, magnetisation, transport speed and morphology); liquid viscosity; dimensions of the capillary microvalve; surface modifications (chemical or physical); magnet geometry; strength of the magnet; magnet to MB cluster distance; any agents altering the intrinsic surface energy of the respective liquids, such as surfactants. The amount of co-transported liquid is thus an important benchmark and has been reported for a number of different published systems. However, all of these systems vary in respect to the parameters stated above, so a direct comparison should be done with caution. The carry-over, that is, the amount of co-transported liquid per mass of MBs, does, however, provide a simple number for the efficacy of the system.

Shikida et al. determined an average carry-over of 0.08 nL/μg using 150–600 μg of 32.7 μm MBs in a 10% KCl solution [5]. Chen et al. reported 3.62 nL carry-over of water using 5×10^5 MBs having a diameter of 3.12 μm amounting to approximately 0.37 nL/μg [6]. Sur et al. used 40–180 μg of 450 nm MBs to estimate the carry-over of Tris buffer in their system amounting to 2.02 nL/μg. They also tested guanidinium isothiocyanate (GuSCN) and ethanol carry-over using 85 μg MBs [7]. Berry et al. did not report details of their carry-over; however, they claim to be able to successfully extract 5.95 μg MBs in a 1% Triton X-100 (TX-100) PBS solution [4]. den Dulk et al. reported an average

* Corresponding author.
E-mail addresses: kkis@nanotech.dtu.dk (K. Kistrup), karen@nanotech.dtu.dk (K. Skotte Sørensen), anders.wolff@nanotech.dtu.dk (A. Wolff), mikkel.hansen@nanotech.dtu.dk (M. Fougt Hansen).

http://dx.doi.org/10.1016/j.jmmm.2014.10.020
0304-8853/

Table 1
Summary of liquid carry-over reported for immiscible phase magnetic bead-based SPE systems in the literature. Volume denotes the starting liquid volume.

Study	*Volume* (μL)	*Avg. carry-over* (nL/μg)	*Bead type*	*Bead diameter* (μm)	*Bead mass* (μg)	*Surfactant*	*Immiscible phase*
Shikida et al. [5]	50	0.08*	Non-commercial	32.7	150–600	None	Silicone oil
Chen et al. [6]	0.14	0.39*	Bangs laboratories	3.18	9*	None	Silicone oil
Sur et al. [7]	50	2.02	Ambion MagMax	0.45	40–180	None	Liquid wax
Berry et al. [4]	8.5	N/A	Oligo-dT Dynabeads	2.8	6*	1% TX-100	Olive oil
den Dulk et al. [8]	14	0.86	M-270 COOH Dynabeads	2.8	150	None	Air
This work	200	1.74	MyOne SILANE	1.0	10–120	None	FC40 oil
This work	200	1.72	MyOne SILANE	1.0	10–60	0.1% TX-100	FC40 oil

* Indicates that the values were not stated directly and had to be estimated.

water carry-over of 0.86 nL/μg using 150 μg of 2.8 μm MBs [8]. An overview of the reported characteristics is given in Table 1.

A common feature of microfluidic chip systems is that they are rapid prototyped, meaning that they are produced by hand in small volumes, since the fabrication methods are most often not applicable in an industrial setting [17]. In this study, we present a planar chip system that has been fabricated using industrially relevant machinery. The main chip part containing the channels and Luer inlets and outlets is injection moulded in COC and sealed with a COC foil lid using ultrasonic welding – both techniques can readily be applied in mass production. This approach provides a substantial number of single-use chips for research and circumvents the need for re-thinking the design and materials for a production scale-up. The chip is fitted with geometric capillary microvalves for MB-based SPE using immiscible phase filtration and is capable of handling sample volumes up to 200 μL.

We first determine the basic parameters needed to investigate the influence of surfactants on the liquid handling compatibility of the system. Next, we systematically investigate the volume of co-transported liquid for the system as function of the amount of magnetic beads suspended in milli-Q water and in a lysis-binding buffer containing detergent, which is typically used for SPE extraction of nucleic acids using the Boom method [18].

2. Experimental section

2.1. Chip fabrication

The polymer chip consists of two parts: an injection moulded main part of Cyclic Olefin Copolymer (COC) (TOPAS grade 5013L-10) and a 0.152 mm thick extruded COC foil (TOPAS grade 5013S-04), both from TOPAS Advanced Polymers GmbH, Frankfurt-Höchst, Germany. Injection moulding was conducted on an Engel Victory 80/45 Tech injection moulder (ENGEL, Schwertberg, Austria) fitted with a custom computer numerical control milled aluminium mould insert, featuring the negative counter-part of the microfluidic layout on one side of the injection moulding tool, and a Luer-Slip layout counter-part with through-holes on the other, see [19] for details. To complete the chip, the injection moulded part was bonded to the COC foil using a Telsonic USP4700 ultrasonic welder (Telsonic, Erlangen, Germany).

2.2. Chip design

The assembled chip is disc shaped (⌀=50 mm) and built for immiscible phase filtration SPE using MBs. It features a Luer-Slip layout with an inlet channel connected to an oil-containing parallel "filter" channel via a geometric capillary microvalve. The filtration channel is further connected to an outlet chamber *via* another capillary microvalve. Energy director welding seams (height=10–18 μm) are located all around the channel lay-out and enable bonding by ultrasonic welding. Fig. 1(a,b) shows the design and a photograph of the chip system. The red arrow denotes the motion path of the permanent magnet stack and thus the path of the MB cluster during extraction. The blue arrows indicate the welding seams and the white arrows show the positions of the geometric capillary microvalves. A zoom-in of the first capillary microvalve with the relevant dimensions can be seen in Fig. 1(c). The width and height of the capillary microvalve are $w=500$ μm and $h=150$ μm, respectively. The channel heights outside the capillary microvalve region are 500 and 300 μm in the inlet/outlet and filter channels, respectively.

2.3. Magnetic bead transportation setup

MB transportation was conducted in a custom built setup consisting of a chip mount set above a Thorlabs LTS150 lateral motorised stage (Thorlabs, Newton, NJ, USA). The stage was fitted with a permanent magnet stack consisting of four axially aligned cylindrical magnets (top to bottom): two N48, NdFeB, ⌀3 mm, 1 mm high magnets (#S-03-01-N, Supermagnete, Germany) and two N45, NdFeB, ⌀6 mm, 3 mm high magnets (#S-06-03-N, Supermagnete, Germany). The magnet stack was positioned so it could be moved around just below the chip.

2.4. Reagents

Solutions used were Milli-Q water, TE buffer and lysis-binding buffer (citrate buffered guanidine hydrochloric acid (GuHCl) (AppliChem, Germany)). For the contact angle and liquid carry-over experiments a 5M GuHCl, pH 4.1 lysis-binding buffer was used and for the surfactant compatibility experiments a 6 M GuHCl, pH 4.5 lysis buffer was used. Surfactants used were Triton X-100 (Sigma-Aldrich, MO, USA), Sarkosyl (Sigma-Aldrich, MO, USA) and Tween-20 (Sigma-Aldrich, MO, USA). Rhodamine B (#R6626, Sigma-Aldrich) was used as fluorophore. 3M fluorinert electronic liquid FC40 oil (Walbom A/S, Kastrup, Denmark) was used as the immiscible phase. Dynabeads MyOne SILANE (Life technologies, CA, USA) were used as MBs. They were 1 μm in diameter (CV < 5%), coated with silanol groups and delivered in a 40 mg/mL stock.

2.5. Contact angle and interfacial tension measurements

Contact angles and interfacial tensions are basic parameters for wetting and passive filling and give insight into the liquid spreading. They are also needed for burst pressure calculations.

The average advancing contact angles ($\theta_{aq,air}$) and interfacial tensions ($\gamma_{aq,oil}$ and $\gamma_{aq,air}$) were measured using a Krüss DSA10 Contact Angle Measuring System (Krüss GmbH, Hamburg).

For the advancing contact angles, a droplet of water, lysis-binding buffer alone, or lysis-binding buffer with either Triton X-100, Sarkosyl, or Tween-20 (the amounts of surfactant indicated in Table 2) was deposited on an injection moulded flat COC (TOPAS 5013L-10) disc using a syringe. The advancing contact angle was

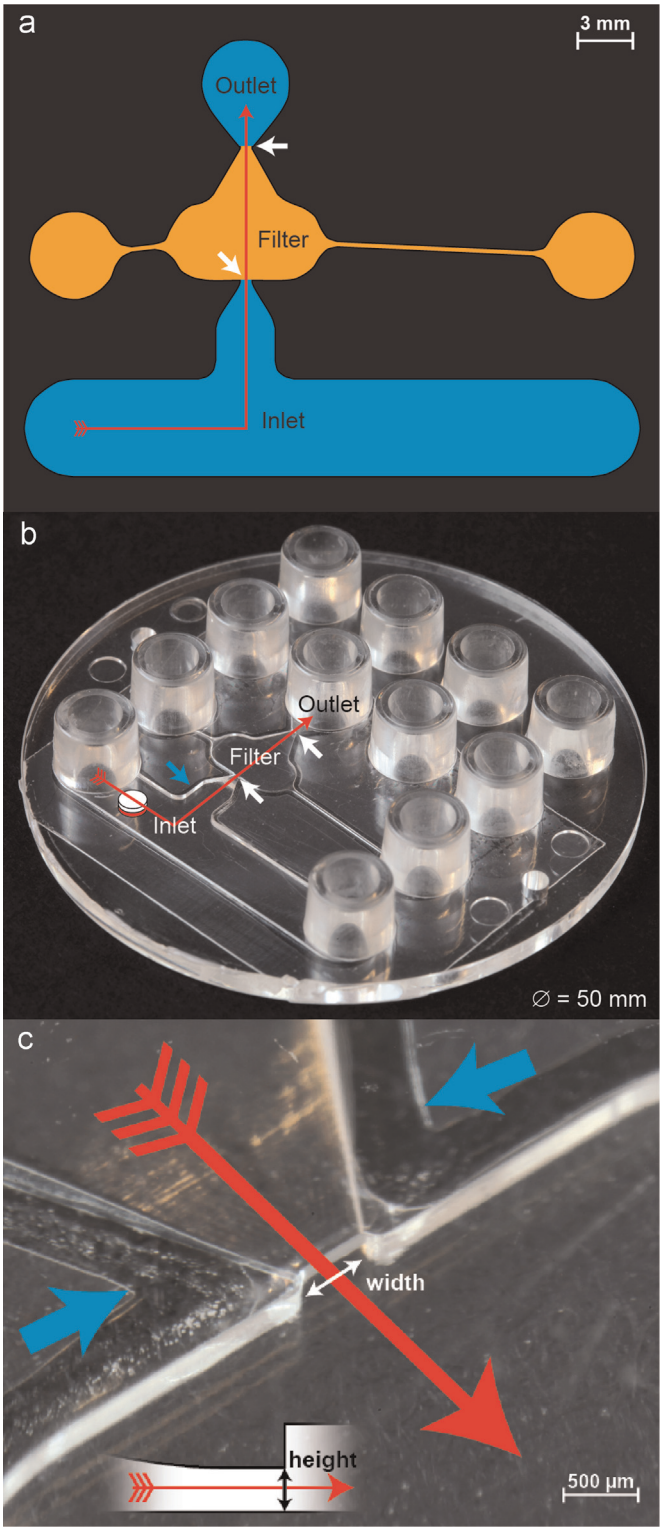

Fig. 1. The chip system. (a) Sketch of the chip design. Blue areas denote aqueous phases, orange area denotes immiscible phase. The red arrow indicates the magnet path from inlet to outlet. White arrows indicate the positions of the capillary microvalves. (b) An overview photograph of the whole chip. The ultrasonic welding seams are located at the blue arrows (c) A zoom-in photograph of the first capillary microvalve. Width $w=500\ \mu m$ and height $h=150\ \mu m$, as sketched in side-view (inset). Note, that the lower image is rotated 90° around the plane of the chip to provide a better view of the capillary microvalve. (For interpretation of the references to colour in this figure legend, the reader is referred to the web version of this article.)

then recorded while the meniscus propagated forward during a continuous increase of the droplet. The chip was then rinsed with Milli-Q water, ethanol, and dried before the process was repeated.

The interfacial tensions were measured using the pendant drop method [20]. For the measurements of $\gamma_{aq,oil}$, FC40 oil was dripped into the various surfactant-containing lysis-binding buffers, since FC40 oil has the highest density (1855 kg/m^3).

2.6. Burst pressure calculations

The burst pressure is used to predict whether or not the solution meniscus will propagate through a capillary microvalve, and is hence an important reference parameter for designing geometric capillary microvalves.

Capillary microvalve burst pressures for the filling of aqueous solutions were estimated using the Young–Laplace equation modified for a rectangular capillary microvalve derived by Cho et al. [21]:

$$p_{burst} = -\gamma\left(\frac{2\cos\theta}{w} + \frac{\cos(\min\{\theta+\alpha, 180°\})}{h} + \frac{\cos\theta}{h}\right), \quad (1)$$

where $\alpha=90°$, $h=500\ \mu m$, $w=150\ \mu m$, $\theta=\theta_{aq,air,}$ and $\gamma=\gamma_{aq,air}$ for the solution under investigation. The hydrostatic pressure exerted by the liquid column in the Luer-Slip inlet was calculated to $p_{hyd}=\rho gh=998\ kg/m^3\times 9.82\ m/s^2\times 6\ mm=59\ Pa$. The Young–Laplace pressure inside the luer was calculated using $p_{luer}=-2\gamma_{aq,air}(\cos\theta_{aq,air}/r_{luer})$, where $r_{luer}=2\ mm$.

2.7. Surfactant compatibility with chip

Compatibility was defined as the ability to form a stable liquid system during filling, and to transport the MB cluster without forming a liquid bridge through the oil phase connecting the two chambers. If this was achieved, the system was considered compatible with MB-based SPE.

For the compatibility experiments, the following liquids were added sequentially to the respective Luer reservoirs (*cf.* Fig. 1): (1) 100 µL of lysis-binding buffer (inlet), (2) 100 µL TE buffer (outlet), and (3) 50 µL FC40 oil (filter). Subsequently, 40 µg of MyOne SILANE MBs was added to the inlet and transferred to the outlet by moving the external permanent magnet at 1 mm/s using the motorised stage.

2.8. Liquid carry-over determination

The liquid carry-over was estimated by relating the concentration of rhodamine B in the starting solution, to the concentration of rhodamine B post-extraction in the outlet chamber.

The chip was mounted in the setup with the magnet situated under the inlet Luer. 200 µL of 2 mM rhodamine B containing solution was pipetted into the inlet channel and 100 µL solution without dye was pipetted into the outlet chamber. 100 µL FC40 oil was added to the middle filter channel to complete the loading. Various volumes of the MB suspension corresponding to MB masses between 10 and 140 µg were then added to the inlet from a 1:10 diluted stock. MBs were then transferred from the inlet to the outlet by moving the magnet at 1 mm/s. After removing the magnet from the outlet chamber, the MBs were resuspended and 90 µL of the outlet solution was transferred to a microtiter plate. The MBs were then removed using a PickPen (Bio-Nobile, Pargas, Finland).

The liquid carry-over volume was estimated from analysis of the dye content of the microtiter plate well. The microtiter plate was placed in a LaVision BioAnalyzer 4F/4S Scanner (LaVision Biotech Germany) and exposed to 1 ms of light through a Cy3 filter. The concentration of rhodamine B in the outlet was

Table 2
Compatibility of various surfactants with the chip system including the measured interfacial tensions ($\gamma_{aq,oil}$ and $\gamma_{aq,air}$), advancing contact angles ($\theta_{aq,air}$), burst pressures (p_{burst}) calculated using Eq. (1), and $\Delta p = p_{burst} - p_{hyd} - p_{luer}$, where p_{hyd} and p_{luer} are the hydrostatic and capillary pressures of the luer inlet, respectively. A chip was considered compatible if filling of the chip was successful and a 40 μg MB cluster could be transported across the immiscible phase without bridge formation. In the case of 0.25% Triton X-100 and 0.125% Sarkosyl, the filling was unsuccessful. All solutions apart from Milli-Q water were prepared from surfactant free lysis-binding buffer.

Solution ((v/v)%)	$\gamma_{aq,oil}$ **(mN/m)**	$\gamma_{aq,air}$ **(mN/m)**	$\theta_{aq,air}$ **(deg)**	p_{burst} **(Pa)**	Δp (Pa)	***Compatibility***
Milli-Q water	44.1 ± 0.4	72.0 ± 0.0	96.1 ± 2.6	562	495	YES
0.1% Triton X-100	9.5 ± 0.1	52.8 ± 1.0	63.5 ± 2.6	101	65	YES
0.25% Triton X-100	6.2 ± 0.2	42.8 ± 0.6	50.7 ± 6.5	−4	−36	NO
0.0625% Sarkosyl	7.8 ± 0.2	44.7 ± 1.0	64.0 ± 4.8	89	50	YES
0.125% Sarkosyl	5.3 ± 0.4	39.0 ± 0.6	41.3 ± 5.2	-53	-82	NO
1% Tween-20	8.3 ± 0.2	49.2 ± 0.7	65.6 ± 4.9	111	73	YES

estimated using a standard curve generated from reference concentrations (0–5 μM) of rhodamine B over 11 steps. The obtained outlet concentration c_{outlet} was converted to a volume using $(c_{outlet}/c_{inlet})V_{outlet}$, where c_{inlet} is the inlet dye concentration (corrected for the addition of the magnetic bead suspension) and V_{outlet} is the outlet volume.

Two series of data were recorded; one with Milli-Q water, and one with lysis-binding buffer containing 0.1 (v/v)% Triton X-100. All experiments were performed in triplicate.

3. Results and discussion

The chip presented in this study is designed for MB-based SPE, a process where the starting material is often a complex biological matrix that has to be disrupted in order to gain access to the target of interest, *e.g.* using a combined lysis-binding buffer for nucleic acid extraction. To facilitate this, surfactants are often added to extraction buffers, and it is hence of interest to map the compatibility of the extraction system with common surfactant types and concentrations. Because surfactants alter biological systems they may also interfere with downstream processes relying on proteins. For this reason, knowing the contamination level of surfactant post SPE is important.

3.1. Fabrication process

To fabricate chips we first created a mould insert. This was done through rapid prototyping by CNC micromachining of an aluminium sheet and took 3–5 h. The mould insert was then placed in the injection moulder for chip production. The cycle time of the injection moulder is ~45 s per chip and the ultrasonic welding process takes ~30 s including mounting and release, which allows for an average production time of less than 1.5 min/chip. Ultrasonic welding is fast compared to other common bonding types, such as thermal bonding and has the added feature that it avoids elevated temperatures. The rapid and robust production allows for all experiments to be conducted on new chips, ensuring that the system is indeed single-use compatible.

3.2. Surfactant compatibility

We investigated the compatibility of the different solutions with our system *via* (1) calculation of the burst pressure, and (2) by experimental investigations of the filling and magnetic bead transportation.

Table 2 shows the measurements of the interfacial tensions between the aqueous solutions and the FC40 oil ($\gamma_{aq,oil}$), the interfacial tensions between the aqueous solutions and air ($\gamma_{aq,air}$), and the advancing contact angles of the solutions on COC ($\theta_{aq,air}$).

The Young–Laplace pressures required for the aqueous solutions to burst through the capillary microvalves (p_{burst}) were calculated using Eq. (1). Other important parameters are the hydrostatic pressure exerted by the inlet (p_{hyd}) and the Young–Laplace pressure of the inlet (p_{luer}), see Section 2.6. The success of the filling could then be quantified by the difference $\Delta p = p_{burst} - p_{hyd} - p_{luer}$. A negative difference indicates incompatibility of the system, *i.e.*, that the capillary microvalve will burst. From Table 2 it is evident that the burst pressures of the non-compatible solutions are negative and are hence expected to burst. For the rest of the solutions, Δp is positive indicating that the capillary microvalve should be compatible with these solutions. Ideally, the microvalve should burst if the total pressure becomes negative. However, we note that measurement uncertainties together with the unavoidable surface roughness introduced by the CNC milled master insert may cause deviations from Eq. (1). In addition, Eq. (1) is only valid for systems in equilibrium and it is known that adding surfactants to solutions also affects the wetting kinetics and result in a time-dependant contact angle [22,23].

The experimental evaluation was done through a qualitative study of the compatibility of the range of common surfactants with the chip system. A surfactant was deemed compatible if filling and transport of 40 μg of MBs could be completed without problems. As can be seen in Table 2, concentrations of Triton X-100 and Sarkosyl (two common detergents used in lysis) above 0.1% and 0.0625%, respectively, were not compatible with the present system. Tween-20 was compatible up to concentrations of 1%, which is sufficient for most applications. For this reason, higher concentrations of Tween-20 were not investigated. These observed results correlate well with the calculated Δp-values in Table 2.

Compatibility of concentrations of Triton X-100 and Sarkosyl up to 1% is preferred, because this amount of surfactant is sometimes needed to perform a successful lysis (depending on the starting material). Berry et al. [4] claim that their system is compatible with such a level of surfactant, but show no quantitative results. The system presented here has a relatively low intrinsic contact angle of about 90° to water, which is not ideal for working with surfactants. It is expected that the surfactant compatibility could be improved by either switching to a more hydrophobic polymer, such as polypropylene, or by coating the chip with a highly hydrophobic compound, such as perfluoro-decyl-trichloro-silane (FDTS). Both of these approaches are compatible with ultrasonic welding [24].

3.3. Liquid carry-over

When the MB cluster is pulled through the immiscible phase, a small amount of the inlet volume will always be carried along, since it is trapped between the magnetic beads and to a certain extent covers the beads as a thin film. As stated in the introduction, the amount of co-transported liquid is an important benchmark for a MB-based SPE system and it was thus quantified. The amount of target (*e.g.* DNA) that can be extracted depends on

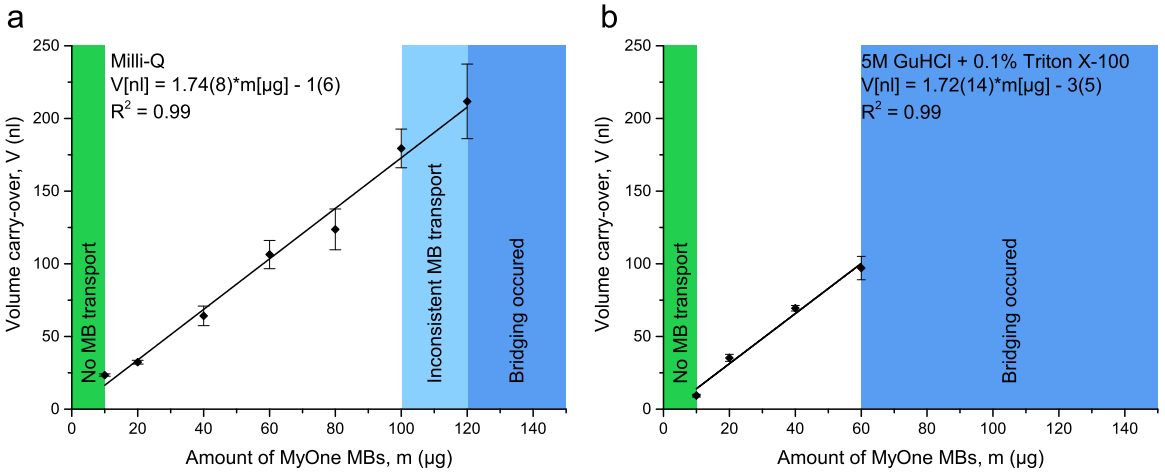

Fig. 2. The liquid carry-over of (a) Milli-Q water and (b) 0.1% Triton X-100 in 5 M guanidine hydrochloride. The extraction was repeated for different amounts of MyOne Silane MBs, and the liquid volume carry-over was estimated using fluorescence. The green area sets the lower limit of the system and the dark blue area sets the upper. The light blue area indicates MB amounts where not all MBs could be transferred in one extraction, and the MB extraction therefore had to be done stepwise. $n=3$. (For interpretation of the references to colour in this figure legend, the reader is referred to the web version of this article.)

the available MB surface area which is determined by the amount of MBs used. Moreover, the ability to perform the MB transportation through the interface separating the two phases also depends on the amount of beads. For this reason, we chose to quantify the liquid carry-over *vs.* the amount of MBs used. We chose to investigate the carry-over of rhodamine B dye dissolved in Milli-Q water and in lysis-binding buffer with 0.1% Triton X-100 as this surfactant is commonly used. To our knowledge, this is the first time liquid carry-over of a surfactant containing solution has been quantified in the literature for this type of system.

Fig. 2a shows the liquid carry-over of Milli-Q water as a function of MB mass and Table 1 shows the data needed to compare these results with already published work. As also reported by Sur et al. [7], a linear correlation was found with a liquid carry-over of 1.74(8) nL/µg. MB extraction was not possible for less than 10 µg of MBs, because the magnetic force that could be applied to the MB cluster was insufficient to overcome the interfacial tension between the sample solution and the FC40 oil. Above 100 µg, the MB extraction also became problematic, as the MB clusters tended to get stuck in the geometric capillary microvalve and hence broke up. Still, MB extraction could be completed by sequential extraction of several MB clusters. For more than 120 µg of MBs, liquid bridges formed through the FC40 oil. Thus, this set the upper amount of MBs compatible with the present system for Milli-Q water.

Fig. 2b shows the results obtained for 0.1% Triton X-100 in lysis-binding buffer. Interestingly, the found liquid carry-over of 1.72 (14) nL/µg was within the uncertainty identical to that obtained for Milli-Q water. However, the upper compatibility limit decreased to 60 µg. 1.72–1.74 nL/µg fits with the general tendency of a smaller carry-over for larger bead diameters, *cf.* Table 1. There are, however, notable differences between the systems in regard to materials, fabrication and magnetic bead properties, as noted in the introduction, so comparing the systems directly should be done with caution.

Table 2 also presents the measured values of $\gamma_{aq,oil}$. The value of $\gamma_{aq,oil}$ is important, since it together with $\gamma_{oil.surface}$ defines the force the MB cluster must overcome to enter the immiscible phase. Moreover, it sets the energy scale for the interface between the oil and the aqueous phase. The presence of surfactants modify all involved surfaces and interfacial tensions [22,23] and to get a full picture of when bridge formation will occur, the total energy associated with the surfaces, $\Delta E = \Delta A(\gamma_{aq,surface} - \gamma_{oil,surface} + \gamma_{aq,oil})$ should be considered. ΔA is the change in the footprint area of the solutions. Berry et al. [4] also comments on this equilibrium while discussing liquid bridge forming and points to unexpected results, because some reagents affect multiple parameters, *e.g.*, $\gamma_{oil,surface}$ may change after contact with the surfactant molecules. However, the value of $\gamma_{aq,oil}$ still hints at whether liquid bridge formation will occur, since a small $\gamma_{aq,oil}$ will increase the likelihood of a positive ΔE, implying a lower risk of bridge formation. This is consistent with our observation that higher amounts of MBs can be successfully transported through Milli-Q water ($\gamma_{aq,oil}$ =44.1 mN/m) than the 0.1% Triton X-100 containing solution ($\gamma_{aq,oil}$=9.5 mN/m).

One might expect that a decrease of $\gamma_{aq,oil}$ would also result in a larger carry-over, since the interface between the liquids will exert less force on the sample solution covering the MB cluster and a decrease in $\gamma_{aq,surface}$ would allow for the sample solution to easier wet the COC surface. This is not observed and can possibly be explained by the complex nature of the total energy associated with the surfaces, as stated above. In addition, the capillary microvalve used in this system is geometrical and hence imposes a physical restriction on the movement of the MB cluster, compared to, *e.g.*, the capillary microvalve employed by den Dulk et al., which consists of two parallel glass plates selectively modified with a hydrophobic coating [8]. In the system employed by den Dulk et al. [8], the MB cluster can expand into the hydrophobic regions, since there is no physical barrier forcing the MB cluster together at the capillary microvalve. If geometrical capillary microvalves impose a normalisation effect on the carry-over of different solution types it would be beneficial to systems, where such a variation in carry-over is undesirable.

The system presented here is compatible with volumes up to 200 µL, which is larger than any of the systems presented in Table 1. However, Berry et al. have later presented a system compatible with liquid volumes up to 500 µL [13]. This is important, since a sample volume of several hundred microlitres is often needed when extracting targets from patient samples, since the concentrations of targets are too low to be quantified from small volumes.

4. Conclusion

We have presented an injection moulded all polymer chip system, capable of forming a stable immiscible phase system. It is a

passive microfluidic system and the fabrication process, which at present takes 1.5 min per chip, is compatible with mass production technologies to provide low-cost and single-use polymer chips. The chip is designed for MB-based SPE, is compatible with various surfactants in low concentrations, and elicits a liquid carry-over of 1.74(8) nL/μg and 1.72(14) nL/μg for Milli-Q water and lysis-binding buffer with 0.1% Triton X-100, respectively. The chip can process a 10–100 μg MB load for Milli-Q water and 10–60 μg for a lysis buffer with surfactant.

Future work will focus on chip applications, including nucleic acid extraction from large volume biological samples.

Acknowledgements

This work is funded by the Danish Council for Strategic Research through the Strategic Research Centre PolyNano (Grant no. 10-092322/DSF) and supported by the Centre for integrated Point of Care technologies (CiPoC), DELTA, Hørsholm, Denmark.

References

[1] M. a M. Gijs, F. Lacharme, U. Lehmann, Microfluidic applications of magnetic particles for biological analysis and catalysis, Chem. Rev. 110 (2010) 1518–1563. http://dx.doi.org/10.1021/cr9001929.

[2] S. Berensmeier, Magnetic particles for the separation and purification of nucleic acids, Appl. Microbiol. Biotechnol. 73 (2006) 495–504. http://dx.doi.org/10.1007/s00253-006-0675-0.

[3] D. Horák, M. Babic, H. Macková, M.J. Benes, Preparation and properties of magnetic nano- and microsized particles for biological and environmental separations, J. Sep. Sci. 30 (2007) 1751–1772. http://dx.doi.org/10.1002/jssc.200700088.

[4] S.M. Berry, E.T. Alarid, D.J. Beebe, One-step purification of nucleic acid for gene expression analysis via Immiscible Filtration Assisted by Surface Tension (IFAST), Lab Chip. 11 (2011) 1747–1753. http://dx.doi.org/10.1039/c1lc00004g.

[5] M. Shikida, K. Takayanagi, k. Inouchi, H. Honda, K. Sato, Using wettability and interfacial tension to handle droplets of magnetic beads in a micro-chemical-analysis system, Sens. Actuators B: Chem. 113 (2006) 563–569. http://dx.doi.org/10.1016/j.snb.2005.01.029.

[6] H. Chen, A. Abolmatty, M. Faghri, Microfluidic inverse phase ELISA via manipulation of magnetic beads, Microfluid. Nanofluid. 10 (2010) 593–605. http://dx.doi.org/10.1007/s10404-010-0692-2.

[7] K. Sur, , S.M. McFall, E.T. Yeh, S.R. Jangam, M.A. Hayden, S.D Stroupe, Immiscible phase nucleic acid purification eliminates PCR inhibitors with a single pass of paramagnetic particles through a hydrophobic liquid, J. Mol. Diagn. 12 (2010) 620–628. http://dx.doi.org/10.2353/jmoldx.2010.090190.

[8] R.C. den Dulk, K. a Schmidt, G. Sabatté, S. Liébana, M.W.J. Prins, Magneto-capillary valve for integrated purification and enrichment of nucleic acids and proteins, Lab Chip. (2012) 106–118. http://dx.doi.org/10.1039/c2lc40929a.

[9] M. Shikida, K. Takayanagi, H. Honda, H. Ito, K. Sato, Development of an enzymatic reaction device using magnetic bead-cluster handling, J. Micromech. Microeng. 16 (2006) 1875–1883. http://dx.doi.org/10.1088/0960-1317/16/9/017.

[10] S.M. Berry, L.J. Maccoux, D.J. Beebe, Streamlining immunoassays with immiscible filtrations assisted by surface tension, Anal. Chem. 84 (2012) 5518–5523. http://dx.doi.org/10.1021/ac300085m.

[11] L.N. Strotman, G. Lin, S.M. Berry, E. a Johnson, D.J. Beebe, Facile and rapid DNA extraction and purification from food matrices using IFAST (immiscible filtration assisted by surface tension), Analyst 137 (2012) 4023–4028. http://dx.doi.org/10.1039/c2an35506j.

[12] L. Strotman, R. O'Connell, B.P. Casavant, S.M. Berry, J.M. Sperger, J.M. Lang, et al., Selective nucleic acid removal via exclusion (SNARE): capturing mRNA and DNA from a single sample, Anal. Chem. 85 (2013) 9764–9770. http://dx.doi.org/10.1021/ac402162r.

[13] S.M. Berry, A.J. Lavanway, H.M. Pezzi, D.J. Guckenberger, M.A. Anderson, J. M. Loeb, HIV viral RNA extraction in wax immiscible filtration assisted by surface tension (IFAST) devices, J. Mol. Diagn. 16 (2014) 1–9. http://dx.doi.org/10.1016/j.jmoldx.2014.01.004.

[14] O. Strohmeier, A. Emperle, G. Roth, D. Mark, R. Zengerle, F. von Stetten, Centrifugal gas-phase transition magnetophoresis (GTM) – a generic method for automation of magnetic bead based assays on the centrifugal microfluidic platform and application to DNA purification, Lab Chip 13 (2013) 146–155. http://dx.doi.org/10.1039/c2lc40866j.

[15] S.M. Berry, L.N. Strotman, J.D. Kueck, E.T. Alarid, D.J. Beebe, Purification of cell subpopulations via immiscible filtration assisted by surface tension (IFAST), Biomed. Microdevices 13 (2011) 1033–1042. http://dx.doi.org/10.1007/s10544-011-9573-z.

[16] B.P. Casavant, D.J. Guckenberger, S.M. Berry, J.T. Tokar, J.M. Lang, D.J. Beebe, The VerIFAST: an integrated method for cell isolation and extracellular/intracellular staining, Lab Chip 13 (2013) 391–396. http://dx.doi.org/10.1039/c2lc41136a.

[17] H. Becker, C. Gärtner, Polymer microfabrication technologies for microfluidic systems, Anal. Bioanal. Chem. 390 (2008) 89–111. http://dx.doi.org/10.1007/s00216-007-1692-2.

[18] R. Boom, C.J. Sol, M.M. Salimans, C.L. Jansen, P.M. Wertheim-van Dillen, J. van der Noordaa, Rapid and simple method for purification of nucleic acids, J. Clin. Microbiol. 28 (1990) 495–503.

[19] K.Ø. Andresen, M. Hansen, M. Matschuk, S.T. Jepsen, H.S. Sørensen, P. Utko, et al., Injection molded chips with integrated conducting polymer electrodes for electroporation of cells, J. Micromech. Microeng. 20 (2010) 055010. http://dx.doi.org/10.1088/0960-1317/20/5/055010.

[20] J. Berthier, K.A. Brakke, Theory of wetting, in: Microdrops Digit. Microfluid., William Andrew Publishing, Norwich, NY (2008) 7–73. http://dx.doi.org/10.1016/B978-081551544-9.50005-1.

[21] H. Cho, H.-Y Kim, J.Y. Kang, T.S. Kim, How the capillary burst microvalve works, J. Colloid Interface Sci. 306 (2007) 379–385. http://dx.doi.org/10.1016/j.jcis.2006.10.077.

[22] V. Dutschk, K.G. Sabbatovskiy, M. Stolz, K. Grundke, V.M. Rudoy, Unusual wetting dynamics of aqueous surfactant solutions on polymer surfaces, J. Colloid Interface Sci. 267 (2003) 456–462. http://dx.doi.org/10.1016/S0021-9797(03)00723-9.

[23] K.S. Lee, N. Ivanova, V.M. Starov, N. Hilal, V. Dutschk, Kinetics of wetting and spreading by aqueous surfactant solutions, Adv. Colloid Interface Sci. 144 (2008) 54–65. http://dx.doi.org/10.1016/j.cis.2008.08.005.

[24] M. Bu, I.R. Perch-Nielsen, Y. Sun, A. Wolff, A microfluidic control system with re-usable micropump/valve actuator and injection moulded disposable polymer lab-on-a-slide, in: Proceedings of the 16th IEEE International Solid-State Sensors, Actuators Microsystems Conference, pp. 1244–1247, 2011. doi:10.1109/TRANSDUCERS.2011.5969452.

Appendix 3

Ultrasonic welding for fast bonding of self-aligned structures in lab-on-a-chip systems

K. Kistrup, C.E. Poulsen, M. Hansen, A. Wolff

Lab Chip. **15** (2015) 1998-2001. doi:10.1039/C5LC00174A

Lab on a Chip

TECHNICAL INNOVATION

View Article Online
View Journal | View Issue

Cite this: *Lab Chip*, 2015, **15**, 1998

Ultrasonic welding for fast bonding of self-aligned structures in lab-on-a-chip systems†

K. Kistrup, C. E. Poulsen, M. F. Hansen and A. Wolff*

Received 12th February 2015,
Accepted 10th March 2015

DOI: 10.1039/c5lc00174a

www.rsc.org/loc

Ultrasonic welding is a rapid, promising bonding method for the bonding of polymer chips; yet its use is still limited. We present two lab-on-a-chip applications where ultrasonic welding can be preferably applied: (1) self-aligned gapless bonding of a two-part chip with a tolerance of 50 μm; (2) bonding of a large area shallow chamber (1.8 cm^2 × 150 μm). Using injection moulding combined with ultrasonic welding we achieved a total production and bonding time of 60 s per chip, and a batch of chips could be produced within a day going from design to finished chips. We believe that the technical solutions offered here can significantly help bridge the gap between academia and industry, where the differences in production methods and materials pose a challenge when transferring technology.

Introduction

In industry, ultrasonic welding is one of the leading fusion processes for thermoplastics and is ubiquitously used, historically moving from commodities, to the automotive industry, to medical devices.[1,2] Ultrasonic welding has had great impact on the plastics industry, because it is fast (rapid welding process, no curing or solvent that needs to dry), requires no soldering materials and is easy to automate. Moreover, it can be used for a range of applications, including welding of wires in electronics, embedding metal objects in plastics and fusion of virtually any thermoplastic with some cross-material compatibility.[1] A general rule of thumb is that materials of similar molecular structures and melting temperatures are compatible.[3–6]

As noted by Tsao *et al.*,[5] thermoplastics are well suited for microfluidic systems. However, bonding remains a critical and non-trivial step. The use of ultrasonic welding within the lab-on-a-chip research field is very limited,[7–12] perhaps, because the technique is thought to have a low depth resolution and requires special chip designs with energy directors to enable reproducible ultrasonic welding.[5,13] We believe that ultrasonic welding will be a key technology, also in the lab-on-a-chip field for the following reasons: (1) it is rapid and well suited for all-polymer rapid prototyping, (2) it generates high-strength hermetic bonds, (3) the ultrasonic energy is focused on the contact points between the parts allowing the energy director to penetrate thin films[14] or membranes,[11] and it prevents heating and destruction of pre-loaded reagents.[15] Moreover, combining ultrasonic welding with other mass production techniques such as injection moulding or embossing in the research phase on a lab-on-a-chip system substantially eases the transfer to commercial production of chip systems. An additional advantage is that a large number of truly single use chips can be made available in the research phase while maintaining a short time from design to prototype.

In this work, we show that ultrasonic welding can efficiently be applied to microfluidic systems and that energy directors can easily be incorporated in prototypes with parts fabricated using injection moulding.[14,16] Specifically, we demonstrate two novel aspects, where ultrasonic welding can be taken advantage of in microfluidic systems: (1) self-aligned gapless bonding of a two-part chip, and (2) sealing of low aspect ratio, large area chambers.

Ultrasonic welding of polymer chips

Ultrasonic welding is a simple thermal fusion process, where two parts are melted together by inducing vibrational friction heating at their interface. Using energy director structures the welding is localized to predefined areas of the part. Fig. 1a and b show two types of energy directors that both rely on an apex to focus the applied energy. Briefly, an ultrasonic welding machine consists of five core components: (1) a kHz range power supply, (2) a piezoelectric transducer that converts the signal to mechanical vibrations, (3) a booster horn that helps amplify and shape the vibrations, (4) a welding horn (sonotrode) that provides pressure and a contact point to pass the vibrations onto the parts to be fused, (5) a fixture that prevent the parts from moving during

Department of Micro- and Nanotechnology, Technical University of Denmark, DTU Nanotech, Building 345 East, DK-2800 Kongens Lyngby, Denmark.
E-mail: Anders.Wolff@nanotech.dtu.dk

† Electronic supplementary information (ESI) available: Additional micrographs of ultrasonic welded parts and droplet PCR protocol. See DOI: 10.1039/c5lc00174a

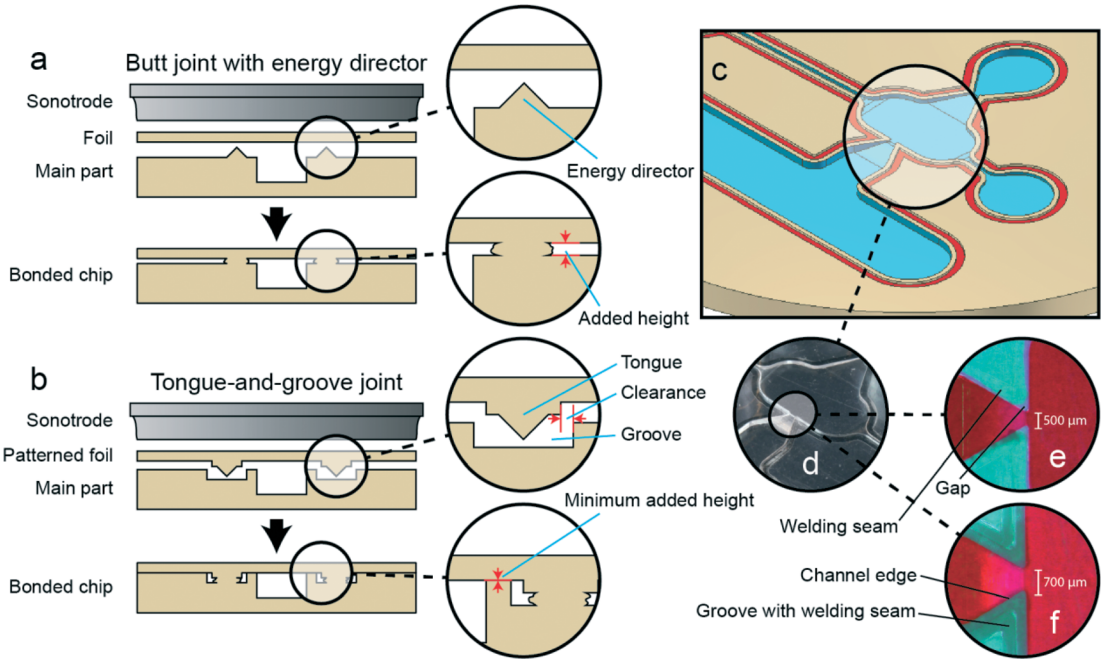

Fig. 1 Sketches of two joint types for ultrasonic welding and presentation of chip systems with like joints. (a) Sketch of butt joint energy director pre and post welding. The energy director material results in an added channel height. (b) Sketch of a tongue-and-groove joint pre and post welding. The energy director material is contained within the groove resulting in no added height. (c) Sketch of the microfluidic main part of Design A2 showing the channel system (blue) and the groove (red). (d) Photograph of ultrasonically welded chip with the same channel system featuring a butt joint. The width of the capillary microvalve is 500 μm. Parts (e) and (f) show micrographs of Design A1 and A2 capillary microvalves, respectively, filled with a 1.3% (V/V) sarkosyl Rhodamine B fluorescent dye solution. For the butt joint, the liquid extends outside the channel because of the added height between the chip and foil (panel (e)), whereas no liquid is observed outside the channel for the tongue-and-groove joint (panel (f)). Contrast and colour was adjusted for clarity. The darker tint of turquoise is a welding phenomenon known as flash that changes the refractive properties of the polymer. Supporting micrographs are provided in the ESI† Fig. S3.

welding. The most important parameters influencing the process are: polymer type, transducer amplitude, welding pressure and welding time/energy. Welding time is typically less than 1 second, and production rates of 20 to 60 parts per minute are routinely achievable.[1]

Fabrication of polymer chips

Three chip designs (Design A1, A2, and B) are presented in this work. They are all disc shaped (∅ = 50 mm), fitted with 12 Luer-Slip connectors,[17] and are made by fusing an injection moulded main part (featuring the fluidic system) with a foil part.

Designs A1 and A2 were designed for magnetic bead-based solid phase extraction of biological targets using immiscible phase filtration as described in ref. 16. They have the general design shown in Fig. 1c where a critical capillary microvalve structure is highlighted. Designs A1 and A2 differ by having different capillary microvalve dimensions (width = 500 and 700 μm, respectively) and by their energy director design and bonding process. Design A1 was fused *via* a butt joint to a flat 152 μm thick extruded foil by ultrasonic welding, see Fig. 1a. Design A2 was fused *via* a tongue-and-groove joint to a custom made 530 μm thick injection moulded foil, see Fig. 1b. Prior to welding, the chip parts were put together manually by visual alignment of the tongue-and-groove structures and by applying a small pressure until the two parts "clicked" together.

Design B was designed for imaging, incubation and thermal cycling of droplets and is shown in Fig. 2a. It features a

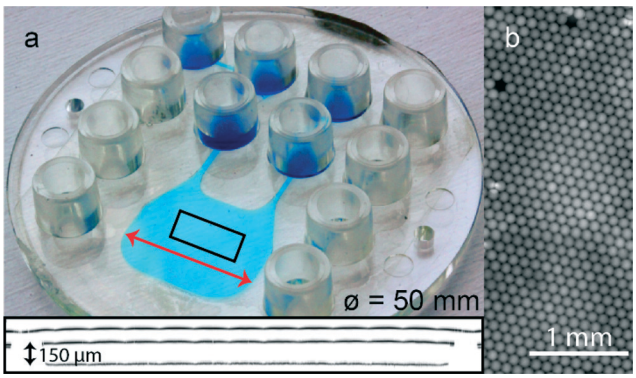

Fig. 2 (a) photograph of an ultrasonic welded polymer chip with a large area, low aspect ratio chamber for ddPCR. Inset: chamber cross section (red arrow) imaged using confocal microscopy. The three lines (top to bottom) show the outer foil surface, the inner foil surface (broken where welding has occurred), and the chip main part surface. The black double arrow denotes the channel height of 150 μm. (b) Fluorescence image of droplets for size statistics and PCR read-out.

critical large (15 mm × 11.8 mm × 0.15 mm) chamber. It was fused *via* a butt joint to the 152 μm thick extruded foil.

Custom mould inserts for the injection moulder were CNC micro machined from Al sheets (grade 2017, MetalCentret, Denmark). The milling process took approx. 3–5 hours per mould insert, depending on the complexity of the design. Dimensions of the tongue-and-groove joint of Design A2 are illustrated in Fig. S1 in the ESI.†

All the main chip parts and the foil for Design A2 were injection moulded in cyclic olefin copolymer (COC, TOPAS 5013L-10) as described in ref. 14 with a cycle time of 40–50 s per part. The 152 μm thick extruded COC foil was of grade TOPAS 5013S-04.

Ultrasonic welding was manually performed on a Telsonic USP4700 20 kHz ultrasonic welder (Telsonic, Erlangen, Germany). The chips were mounted in a custom fixture with the foil placed on top. Design A1 was welded using a 850 N trigger force with a 0.35 s hold time. 85 J was deposited during the welding running at 80% vibrational amplitude. Design A2/B settings differed at the following parameters: Trigger force = 515/500 N; energy = 40/60 J; amplitude = 55/100%, respectively. The average welding time per chip was 30 s including mounting of chip and foil. Once the processes were optimised, the yield of the entire process was higher than 95%. Most failures pertained to the welding process where cracking of the foils occurred due to resonances in the chip.

The bonding strength was assessed by applying pressurised air to Design A1 and A2. Design A1 failed at 3.5 bar where the 152 μm thick foil burst, see Fig. S2 in the ESI.† Design A2 remained intact after exposure to 8.5 bar, which was the highest pressure available for testing.

Design A: Gapless ultrasonic welding with possibility for self-aligning using energy directors

Two joint types are presented to highlight the versatility of ultrasonic welding.

Design A1 features a simple butt joint, which is the most common joint type (illustrated in Fig. 1a (schematic) and Fig. 1e (a post-welding photograph)). Butt joints are simple to integrate and require only a peripheral pattern of small energy directors to be included in the chip main part design (Fig. 1b). Moreover, no alignment is needed. However, the material from the molten energy director inevitably results in an added height to the channel. We have previously published systems featuring this type of energy director.[14,16]

Design A2 features a tongue-and-groove joint. Such joints are common for macroscale objects but have until now not been implemented on microscale in lab-on-a-chip systems. Here, the energy director is situated on the foil (the tongue) and a matching peripheral groove is introduced on the chip main part, see Fig. 1b (schematic) and Fig. 1c (schematic with groove in red). The tongue-and-groove joint makes it possible to self-align the foil to the chip main part by "clicking" the two parts together prior to welding. This allows for inclusion of other features requiring alignment such as local coatings, spotted biomaterial or reagents, electrodes, and channel structures. The groove clearance of 50 μm sets the alignment tolerance of Design A2. The added channel height is eliminated, because the groove underneath the tongue contains the molten polymer from the energy director (Fig. 1b). Tongue-and-groove joints limit the choice of foils, since they have to be custom designed with appropriate structural features. However, these can be fabricated with embossing/moulding techniques, such as injection moulding, as is the case in this work.

To illustrate the performance difference of the two joint types, Designs A1 and A2 were filled with a 1.3 (V/V)% detergent (*N*-lauroylsarcosine, #L7414, Sigma-Aldrich, MO, USA) containing Rhodamine B (#R6626, Sigma-Aldrich, MO, USA) solution and micrographs were taken using a Leica ZMFL III microscope. Detergent was added to ensure filling of the device, since COC is hydrophobic. Fig. 1e shows the solution flowing into the small gap of Design A1 resulting from the added height of the butt joint. In contrast, the welding seam of Design A2 perfectly follows the edge of the channel because, in addition to the welding at the tongue-and-groove welding seam, the foil and channel edge are in contact and have fused together (Fig. 1f). To further characterise the added height, the chips were investigated using a confocal microscope, see ESI† Fig. S3 for details. For Design A1, an added height of 15 μm was found. Depending on the tolerance of the microfluidic system and its application, this added height can modify the behaviour compared to a system with no added height and may compromise the function of the system. No added height was detectable for Design A2.

Design B: bonding of large area, low aspect ratio chambers

Large area, low aspect ratio (height/width) chambers have numerous uses, *e.g.*, for cell culturing and parallelised droplet interrogation by wide field imaging.[18] Because ultrasonic welding relies on localised forces and energy deposition, it is useful for sealing large area shallow chambers, *i.e.*, chambers with low aspect ratio geometries. Such chambers are not easily bonded thermally due to the risk of collapse of the chamber and special precautions have to be taken, for example, by selectively applying bonding pressure using a custom made bonding tool.[19] Moreover, since no new materials, such as glues or adhesives, are introduced, the temperature working range of the microfluidic system is not limited by differences in thermal expansion. To demonstrate these capabilities in a microfluidic setting, we present an all-polymer ultrasonic welded microfluidic chip featuring a single 15 mm × 11.8 mm × 0.15 mm chamber for Droplet Digital™ PCR (ddPCR), see Fig. 2a. The chamber allows for droplet packing into a single monolayer, imaged by fluorescence microscopy (Fig. 2b).

Using a single chip, 13 438 droplets were simultaneously analysed, and a target concentration of 7.2 fM was determined with 28% underestimation. More details on this application of ultrasonic welding are found in the ESI.†

Discussion and conclusion

Bonding is still a recurring challenge and unsolved issue in microfluidics, where most systems are based on two or more parts that need to be fused together or interfaced with other components. This work encourages the use of ultrasonic welding for bonding of lab-on-a-chip systems, where applicable. Ultrasonic welding provides a strong fusion with foils over a range of thicknesses (at least 100 μm to 2 mm, data not shown) and needs no special pre-treatment. It is also devoid of chemicals that may interfere with the chip application or change chip properties over time. As demonstrated in this paper, tongue-and-groove joints add a simple alignment step to the fusion process. In addition ultrasonic welding can be utilized for bonding of large area shallow chambers, expanding the applications of ultrasonic welding within microfluidics.

In spite of these advantages, ultrasonic welding has not yet gained wide academic popularity, which may be ascribed to the fact that energy directors are required and ultrasonic welding is not compatible with thermosetting polymers such as polydimethylsiloxane (PDMS). From an industrial viewpoint, thermosetting polymers are far less attractive than thermoplastics, and it is recommended that prototypes are designed with manufacturability kept in mind for the easy implementation of larger scale testing and for future potential commercial production.[20,21] Most research in the field of microfluidics is, after all, application driven, and commercialization is often highlighted as the objective.

The chip fabrication process described here is rapid and allows for fast design iterations using commercially relevant fabrication techniques. It is possible to go from design to a 'bag of chips' within a day for Designs A1 and B; 3–5 hours micro machining, 1–2 hours injection moulding, and 1–2 hours of back-end ultrasonic welding can easily yield up to 50 ready-to-use chips. For Design A2 a second milling and injection moulding step must be included.

The bonding strength of Design A1 and A2 was assessed by applying air pressure to the chips. Design A2 was able to withstand pressures up to 8.5 bar (maximum tested), whereas Design A1 burst at 3.5 bar. As can be seen in Fig. S2† the mode of failure pertained to the bursting of the 152 μm thick foil over the channel and not the welding seam, which remained intact. This correlates well with the observation of no failure for the 500 μm thick foil of Design A2.

Design A2 has a clearance of 50 μm, see Fig. 1b and S1,† which limits the alignment precision. We remark that an alignment precision of 50 μm may be sufficient for most microfluidic applications and note that no optimization was performed to minimize the clearance. If needed, this clearance can likely be further reduced.

Acknowledgements

The authors of this work would like to acknowledge Professor Dang Duong Bang for supplying PCR reagents and template DNA for the ddPCR and Marco Matteucci for help with injection moulding. This work is funded by the Danish Council for Strategic Research through the Strategic Research Centre Poly-Nano (grant no. 10-092322/DSF) and The Danish Council for Independent Research (grant no. 09066477).

References

1 J. Rotheiser, *Joining of plastics*, 2004.
2 R. S. Soloff and S. G. Linsley, Sonic method of welding thermoplastic parts, *US Pat.*, US 3224916 A, 1965.
3 M. J. Troughton, in *Handbook of Plastics Joining - A Practical Guide*, William Andrew Publishing, Boston, 2009, 2nd edn., pp. 1535.
4 A. Weber, *Assembly*, 2007.
5 C.-W. Tsao and D. L. DeVoe, *Microfluid. Nanofluid.*, 2008, **6**, 1–16.
6 C. Ageorges, L. Ye and M. Hou, *Composites, Part A*, 2001, **32**, 839–857.
7 R. Truckenmüller, Y. Cheng, R. Ahrens, H. Bahrs, G. Fischer and J. Lehmann, *Microsyst. Technol.*, 2006, **12**, 1027–1029.
8 R. Truckenmüller, R. Ahrens, Y. Cheng, G. Fischer and V. Saile, *Sens. Actuators, A*, 2006, **132**, 385–392.
9 Y. Luo, Z. Zhang, X. Wang and Y. Zheng, *Microelectron. Eng.*, 2010, **87**, 2429–2436.
10 Z. Zhang, Y. Luo, X. Wang, S. He, F. Meng and L. Wang, *Microsyst. Technol.*, 2010, **16**, 2043–2048.
11 M. Bu, I. R. Perch-Nielsen, Y. Sun and A. Wolff, in *2011 16th International Solid-State Sensors, Actuators and Microsystems Conference, IEEE*, 2011, pp. 1244–1247.
12 K. G. Lee, S. Shin, B. Il Kim, N. H. Bae, M.-K. Lee, S. J. Lee and T. J. Lee, *Lab Chip*, 2015, **15**, 1412–1416.
13 H. Becker and C. Gärtner, *Anal. Bioanal. Chem.*, 2008, **390**, 89–111.
14 K. Kistrup, C. E. Poulsen, P. F. Østergaard, K. B. Haugshøj, R. Taboryski, A. Wolff and M. F. Hansen, *J. Micromech. Microeng.*, 2014, **24**, 125007.
15 Y. Sun, J. Høgberg, T. Christine, L. Florian, L. G. Monsalve, S. Rodriguez, C. Cao, A. Wolff, J. M. Ruano-Lopez and D. D. Bang, *Lab Chip*, 2013, **13**, 1509–1514.
16 K. Kistrup, K. Skotte Sørensen, A. Wolff and M. Fougt Hansen, *J. Magn. Magn. Mater.*, 2014, **100**, 1–6.
17 K. Ø. Andresen, M. Hansen, M. Matschuk, S. T. Jepsen, H. S. Sørensen, P. Utko, D. Selmeczi, T. S. Hansen, N. B. Larsen, N. Rozlosnik and R. Taboryski, *J. Micromech. Microeng.*, 2010, **20**, 055010.
18 A. C. Hatch, J. S. Fisher, A. R. Tovar, A. T. Hsieh, R. Lin, S. L. Pentoney, D. L. Yang and A. P. Lee, *Lab Chip*, 2011, **11**, 3838–3845.
19 D. S. Kim, H. S. Lee, J. Han, S. H. Lee, C. H. Ahn and T. H. Kwon, *Microsyst. Technol.*, 2007, **14**, 179–184.
20 E. K. Sackmann, A. L. Fulton and D. J. Beebe, *Nature*, 2014, **507**, 181–189.
21 H. Becker, *Lab Chip*, 2010, **10**, 271–273.

Electronic Supplementary Material (ESI) for Lab on a Chip.

Ultrasonic welding for fast bonding of self-aligned structures in lab-on-a-chip systems

K. Kistrup C.E. Poulsen M.F. Hansen and A. Wolff

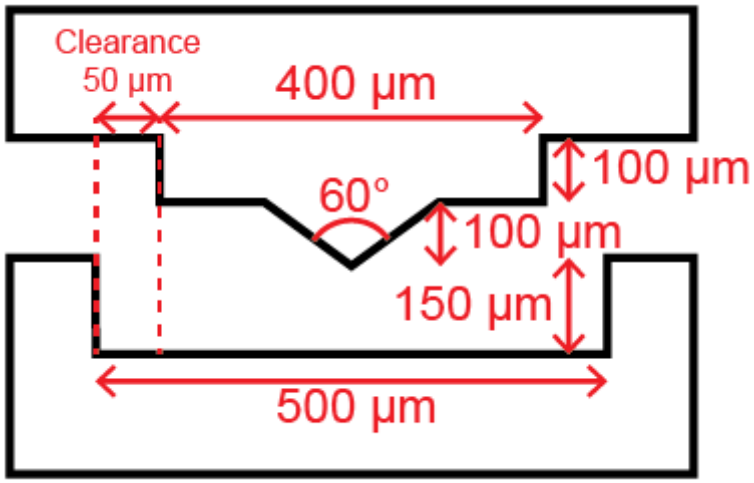

Fig. S1 Technical drawing of the tongue-and-groove joint used in Design A2. The overall design was based on the guides made available by Dukane's "Guide to Ultrasonic Plastics Assembly" (http://www.dukane.com/us/DL_DesignGuides.asp, accessed March 03, 2015). The features themselves were generated by CNC micromachining in aluminium.

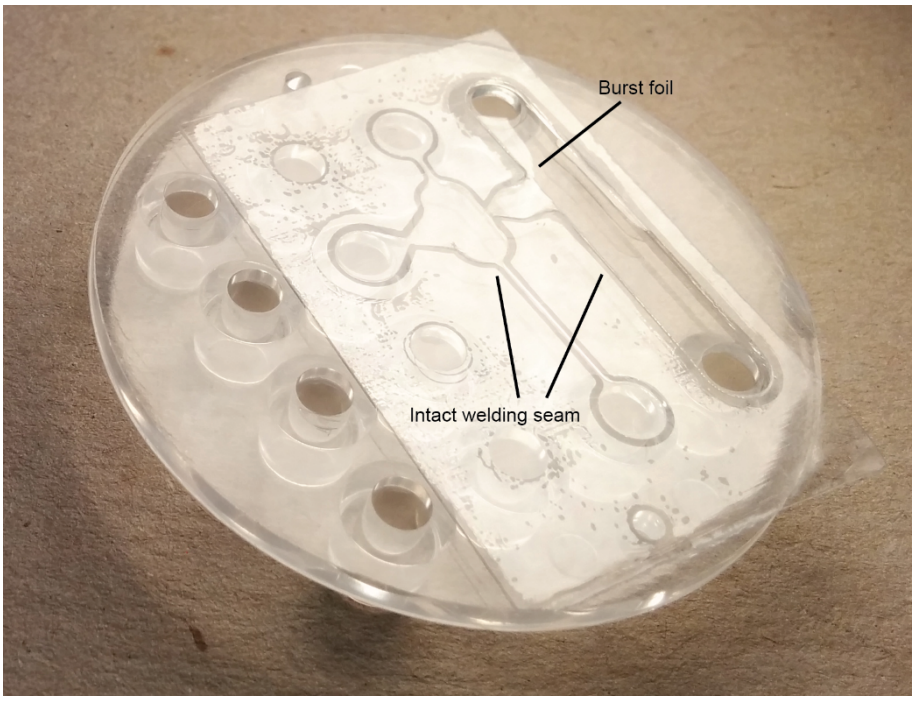

Fig. S2 Chip failure during pressure testing. To investigate the bonding strength of the welding seams pressurised air was applied to the chip inlet, while the other connectors were blocked. Design A1 failed after applying 3.5 bar (see photograph). The mode of failure was bursting of the 152 µm thick foil. Note that the welding seam is intact, as is visible by the darker surface. Design A2 with the 500 µm thick foil did not fail within the testing limits, which was up to 8.5 bar.

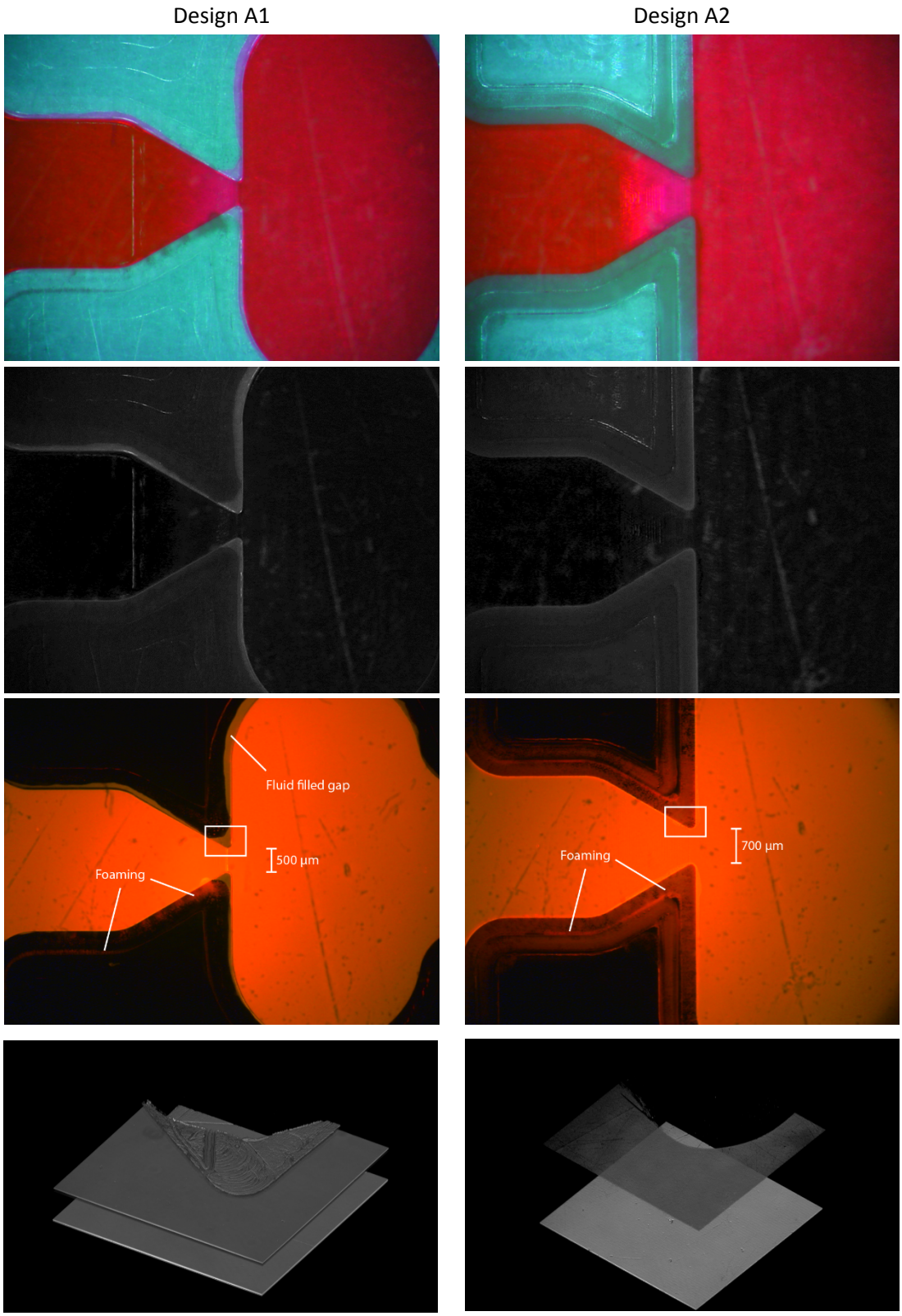

Fig. S3 Various micrographs of the capillary microvalve of Design A1 and A2. First two rows are standard bright field images, with the contrast and colour adjusted for clarity. Third row is taken with fluorescence microscopy. Note that the foaming, especially present in Design A2, reflects the light emitted from the rhodamine B solution; however, this is distinctly different from where actual fluid is present around the edges of Design A1. Row four shows a 3D representation of confocal micrographs taken at the upper corner of the capillary microvalve as marked with the white squares in row three (Zeiss LSM 700 confocal microscope (20x/0.5, z-stack images, 1.590 µm sections). The bottom plane shows the outer foil surface and the upper plane the inner foil surface. Note that for Design A1 the corner of the main chip part is also visible due to the gap, whereas for Design A2, no such surface exists.

Droplet PCR

Droplets were produced off-chip using a Droplet Junction Chip (#3000301, Dolomite, UK) using 2 % (V/V) Pico-Surf™ 1 (Dolomite, UK) in 3M FC40 oil (Walbom A/S, Denmark) as the continuous phase. The dispersed phase consisted of PCR master mixture for detection of *Campylobacter* species using universal Campylobacter primers targeting a 300 bp of 16sRNA gene described previously[1]. 1 pm/µl TaqMan probe labelled with 5´6-FAM and 3' BBQ (DNA Technology, Denmark) was added to the PCR mixture to detect DNA amplification. 10 µM Sulphorhodamine 101 (Cat 80101, Biotium, VWR, Denmark) was also added for improved droplet detection and size statistics. Target DNA samples were 7.2 fM chromosomal DNA isolated from *Campylobacter jejuni*, strain NCTC-11284, using QIAamp DNA mini kit (Qiagen, Germany)[1]. Thermo-cycling was performed on a Bio-Rad DNA Engine PTC-200 flat-bed PCR thermo-cycler with the COC lid contacting the hot-plate, see Fig. S1. Temperature steps used were as described previously[1].In brief, 5 minute hot start of 96 °C followed by 40 cycles consisting of a melting step at 94 °C for 15 seconds, an annealing step a 54 °C for 15 seconds and extension step at 72 °C for 8 seconds. The final extension was run for 60 seconds.

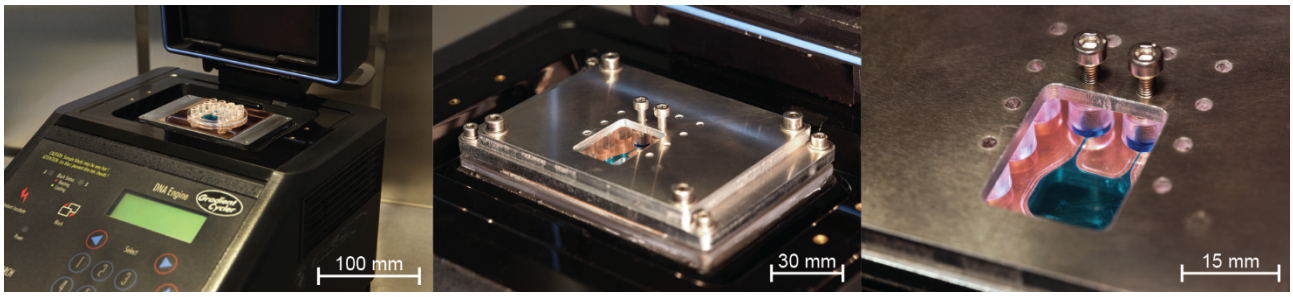

Fig. S4 Mounting of chip B on flat-bed PCR thermo-cycler.

Using circular Hough transformation, 13438 droplets were analysed in a single chip to have a diameter of 98.7 ± 6.0 µm which fits well with the observed monolayer. After thermal cycling, 79% of the droplets were observed to fluoresce from the TaqMan probe (FAM/FITC channel), which corresponds to a concentration of 5.2 fM, estimated using the *Poisson* distribution. As discussed in other ddPCR studies, this underestimation of 28% may be ascribed to the sensitivity of the PCR reaction and sample loss in the upstream microfluidic system[2–4].

1 Y. Sun, J. Høgberg, T. Christine, L. Florian, L. G. Monsalve, S. Rodriguez, C. Cao, A. Wolff, J. M. Ruano-Lopez and D. D. Bang, *Lab Chip*, 2013, **13**, 1509–14.

2 M. M. Kiss, L. Ortoleva-Donnelly, N. R. Beer, J. Warner, C. G. Bailey, B. W. Colston, J. M. Rothberg, D. R. Link and J. H. Leamon, *Anal. Chem.*, 2008, **80**, 8975–81.

3 L. Mazutis, A. F. Araghi, O. J. Miller, J.-C. Baret, L. Frenz, A. Janoshazi, V. Taly, B. J. Miller, J. B. Hutchison, D. Link, A. D. Griffiths and M. Ryckelynck, *Anal. Chem.*, 2009, **81**, 4813–21.

4 G. Jenkins, H. Zhang, Y. Zou, X. Leng, W. Zhang and C. Yang, *rsc.org*, 2011, 945–947.

Appendix 4

Laser ablated micropillar energy directors for ultrasonic welding of microfluidic systems

C.E. Poulsen, **K. Kistrup**, N. K. Andersen, M. F. Hansen, R. Taboryski, A. Wolff

Submitted manuscript

Laser ablated micropillar energy directors for ultrasonic welding of microfluidic systems†

Carl Esben Poulsen[a], Kasper Kistrup[a], Nis Korsgaard Andersen[a], Rafael Taboryski[a], Mikkel Fougt Hansen[a] and Anders Wolff[a]*

[a] Department of Micro- and Nanotechnology, Technical University of Denmark, DTU Nanotech, Building 345 East, DK-2800 Kongens Lyngby, Denmark.

† Electronic Supplementary Information (ESI) available: See DOI: ########

* E-mail: anders.wolff@nanotech.dtu.dk

Abstract

We present a new type of energy director (ED) for ultrasonic welding of microfluidic systems. These micropillar EDs are based on replication of cone like protrusion (CLP) structures introduced using a pico-second laser and may therefore be added to any mould surface accessible to a pico-second laser beam. The technology is demonstrated on an injection moulded microfluidic device featuring high-aspect ratio ($w \times h$ = 2000 µm × 550 µm), free standing channel walls, where bonding is achieved with no detectable channel deformation. Bonding strength is similar to conventional EDs and the fabricated system can withstand pressures of over 9.5 bar.

Keywords: Ultrasonic welding, polymer fusion, Microfluidics, Injection moulding.

(Some figures may appear in colour only in the online journal)

Introduction

In academia, soft imprint lithography with polydimethylsiloxane (PDMS), sealed by plasma activated bonding is by far the most used route for rapid prototyping of microfluidic systems [1]. The high elasticity of PDMS allows for fabrication of advanced valves and gates, and its good solvent compatibility enables the use of multiphase liquids systems [2]. For commercial production, however, hot embossing or injection moulding (IM) combined with ultrasonic welding (UW) are more common for high throughput fabrication of low-cost disposable devices [3]. Since physical and chemical properties of thermoplastics differ significantly from those of PDMS, technology transfer from academia to industrial production may prove unfeasible or require a completely redesigned fabrication process [3]. Moreover, PDMS has fabrication limitations compared to thermoplastics [4]. For example, the high elasticity and self-adhesion of PDMS may induce collapse of high-[5] and low- [6] aspect ratio channels and structures via self-adhesion. Thermoplastics, on the other hand, are generally stiffer and less self-adhering. Recently, we presented ultrasonically welded, injection moulded, large area, low aspect ratio cyclic olefin copolymer (COC) devices [7,8], where fabrication in PDMS of similar devices has traditionally relied on embedded glass slides to achieve sufficient rigidity [9]. Similarly, high-aspect ratio features in PDMS devices can only be realised by use of sacrificial moulding methods [10], where these features have to be structurally supported by a solid bulk part [11]. Many techniques for bonding of thermoplastic devices require elevated temperatures and/or high pressures [12–15], which may cause structural deformation, and bonding of high-aspect ratio structures is therefore not easily realized. UW, on the other hand, is the fastest back-end bonding process, and may be conducted at relatively low pressures and at room temperature. However, it requires the addition of energy director (ED) structures protruding on top of the channel walls. For device fabrication based on replication techniques (e.g. hot embossing and injection moulding), the replication tool has the inverse structure and the ED structures thus have to be realized as depressions in the bottom of the cavity structure used to define the channel wall. ED structures can be realized, e.g., by micro milling, which is a rapid mould tool fabrication process, though the size of the milling tool limits the ED

dimensions that can be realized. Milling tools are made as small as 10-50 µm, yet it is often not feasible to make EDs on high-aspect ratio wall structures by milling, since the drill aspect ratio is often limited to 1:3, and the micro mills are short and mounted on large shanks. (Fig. 1a).

In this paper, we present a new type of micropillar EDs for UW of microfluidic systems. These EDs are formed by introducing cone like protrusion structures [16] as a back-end process in replication moulds using a picosecond laser. They have the substantial advantage over traditional EDs that they can be defined on any surface accessible to a high energy pico-second laser beam (Fig. 1b). Moreover, these EDs can be introduced in designated areas on the tool, and the width of these areas can be chosen independently from the heights of the EDs contrary to traditional EDs, where larger widths are accompanied by higher structures. The CLPs are formed stochastically within the designated area, so only ablation of the general ED shape is required, not the individual CLPs. We demonstrate the technology in an aluminium mould, but also verify the CLP formation in tool steel used for industrial mould. To characterise the performance of this new type of EDs, we compare CLP EDs to micromilled EDs with respect to (1) welding strength, (2) structural deformation of a free-standing high-aspect structure, and (3) formation of particles during welding (any formed particles may interfere with the function of the microfluidic device [17]). Results on particle forming are presented in the Supplementary Information.

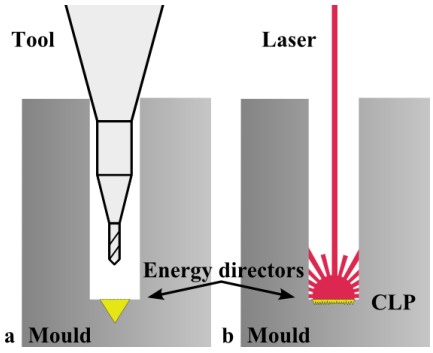

Figure 1. Schematics of methods for introducing ED forming grooves in moulds. (a) Conventional EDs introduced by micro milling (or electric discharge machining). (b) Laser ablated CLPs. Removed material is highlighted in yellow.

Materials and methods

1.1. Chip fabrication

Injection moulding was carried out using a custom-made moulding tool comprising a 50 mm diameter disk cavity with 12 luer inlets [12]. The tool could be combined with mould inserts with structures machined in aluminium 2017 (al2017) [18]. Prior to injection moulding, two types of ED structures were introduced: (1) Traditional EDs introduced by micro milling using a 60° helical engraving tool (#7025, DIXI Polytool, Le Locle, Switzerland). An apex depth of 100 µm was used (width=115 µm). (2) Microstructured CLP-EDs written using a FUEGO 1064 nm, 50 W picosecond laser (Time Bandwidth, 3D-Micromac AG, Chemnitz, Germany) mounted in a microSTRUCT vario (3D-Micromac AG). CLPs were introduced by scanning the designated areas with parallel lines (10 µm spacing), repeated 20 times at 50% power and 1000 mm/s with the focus plane 1.3 mm above the surface. The writing time was 200 seconds/cm^2. These settings were similar to the work by Brüning *et al*. (2014) [16], but tuning was conducted *towards higher* roughness.

To confirm the commercial relevance of the technology, we also demonstrated writing of CLPs in high performance tool steel Orvar2343 (MetalCentret, Glostrup, Denmark). Al2017 was preferred for mould making in this low-volume academic setting study due to its ease of machining.

The injection moulding was carried out on a Victory 80/45 Tech hydraulic injection moulding machine (Engel, Schwertberg, Austria) using COC grade 5013L-10 (TOPAS Advanced Polymers GmbH, Frankfurt-Höchst, Germany) with injection and mould temperatures of 270 °C and 120 °C, respectively. Injection pressure was 1766 bar.

Fabricated chips were bonded to a 500 µm thick foil of COC grade 5013S-04 (TOPAS Advanced Polymers GmbH) by ultrasonic welding. UW was performed at ambient temperature using a Telsonic-USP4700 ultrasonic welder (Telsonic, Erlangen, Germany), depositing 25 J with 75% vibrational amplitude, a trigger force of 400 N and 0.5 bar welding pressure. With the fitted 2× booster and sonotrode, the vibrational amplitudes at the sample surface were approximately 44 µm.

1.2. Bonding strength

The bonding strength was assessed using the *razor-blade test* based on fracture propagation developed by Maszara *et al*. [19], and employed by Matteucci *et al*. [13] to assess the bonding strength of thermal bonding in similar chips. To perform the test, two mould inserts with a milled 5.15×42.5×0.25 mm^3 cavity were fabricated by micro milling. In this cavity, the first insert further featured a 40.5 mm long conventional ED made by conventional milling and the second insert featured a laser micromachined ED with CLPs on an area of 40.5×0.2 mm^2.

The injection moulded structures were bonded to a COC foil as described above. Details of the razor-blade testing as well as results on all chips are given in the Supplementary Material.

1.3. High-aspect ratio microfluidic system

Ultrasonic welding of free-standing structures was demonstrated on an intertwining microfluidic system consisting of two 400 µm wide channels. These channels are separated by 2000 µm high, 550 µm wide, freestanding walls with a 200 µm wide band of micropillar EDs on top (Fig. 2). Note that these EDs cannot be fabricated by conventional methods due to the smaller size of the structures and the large aspect ratio. The microfluidic system spanned a 36.3×25.8 mm^2 rectangle. Note that the 200 µm wide ED structure in expanding regions was separated into two bundles of 10 lines, keeping a constant wall-to-edge distance of 180 µm (Fig. 2c).

Channel deformation was characterised along four cross sections using confocal microscopy using a Zeiss LSM 700 with voxel sizes of X×Y×Z=0.313×0.313×5.387 µm^3. The location of the cross sections and the bonded chip are shown in Fig. 2a and Fig 2b, respectively.

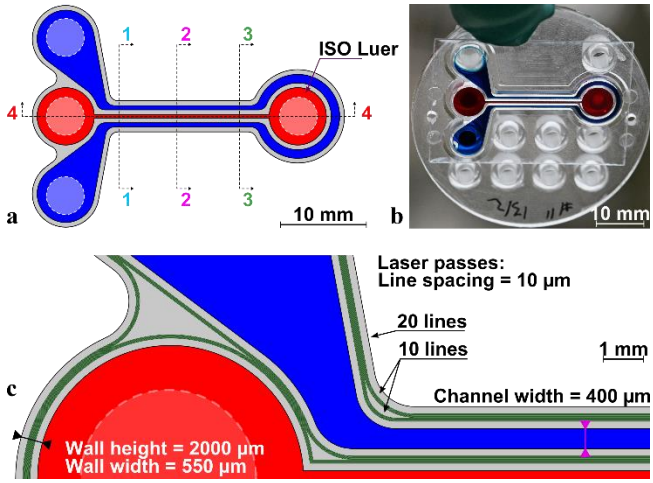

Figure 2. (a) Schematic drawing of high aspect ratio chip. Blue: Outer channel. Red: Inner channel. Gray: Walls. Cross sections 1-4 for confocal imaging are indicated. (b) Image of bonded chip loaded with fruit dye for highlighting channels. Note that the sealing lid only contacts the walls. (c) Chip with laser patterning lines added (green). Note that the 20 lines are separated into two bundles at the corners, to keep a constant edge distance (180 µm).

Results and discussion

1.4. CLP and ED structures

Figures 3a,b show scanning electron microscopy (SEM) images of the CLPs written in the al2017 mould. It is noteworthy that although the laser scanning is conducted in bundles of parallel lines, the formed CLPs are stochastically formed within the laser ablated area. This may be ascribed to the fact that the microphase explosions causing the CLPs are caused by a combination of metal impurities (alloy) picking up the energy, the pulsing nature of the laser beam and non-uniformity of the laser fluence distribution [20]. The CLPs have a typical height and spacing of 10 µm and 10 µm, respectively. On average, the CPL area protrudes 47 µm from the plane of the tool (Fig. 4g). Note that the CLPs are locally convex depressions in the mould that hence facilitate easy demoulding during replication. Fig. 3c shows a SEM image of a COC replica of the mould. The replicated structures are observed to have rounded tops due to imperfect filling during replication. We found that operating at conditions yielding higher fidelity replication resulted in more difficult demoulding due to stronger adhesion between the mould and its replica. This rounding did not affect the performance of the EDs. Fig. 3d shows tool steel Orvar2343 ablated to produce CLPs similar to those demonstrated in al2017.

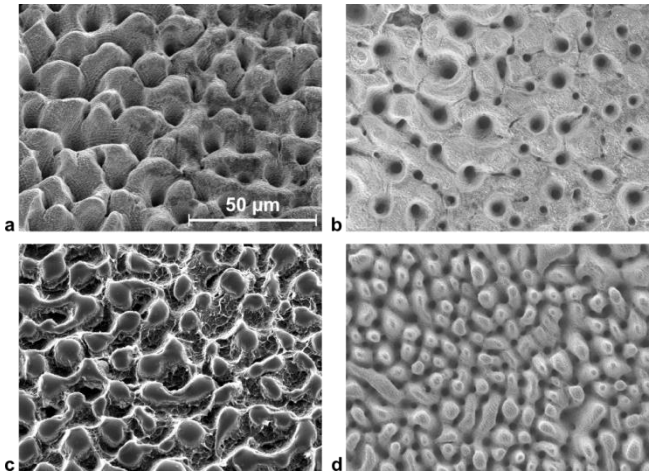

Figure 3. (a)-(b) SEM images of CLPs in al2017 moulds (30° and 0° tilt, respectively) and (c) replicated COC (30° tilt). (d) Industrial mould making steel Orvar2343 modified using the presented technology (0° tilt).

Figures 4a,b show SEM images of the CLP-EDs in the al2017 mould for fabrication of the high-aspect ratio microfluidic system. The images clearly show the feasibility of writing CLP-ED structures at the bottom of the trenches in the mould. Note that the separation and joining of bundles of laser lines do not alter the pattern and formation of CLPs. Thus, CLP-EDs can be formed in any pattern or geometry. Corresponding SEM images of the injection moulded COC replica (Figs. 4c,d) clearly show that micropillar structures are well reproduced on the top of the high-aspect ratio wall.

Figures 4e,f show optical micrographs of the same structures pre and post UW. Due to the structure of the CLPs, the final micropillar CLP-EDs of the polymer chip are opaque (Fig. 4e). However, like conventional

butt joint EDs [8], the joints are transparent post welding (Fig. 4f). It is noteworthy that no signs of trapped or compressed air are observed in structures surrounded by CLP-EDs, such as the pocket in the corner of the structure (Fig. 4e) where little or no gap is observed post UW in Fig. 4f. This indicates that the micropillar structure facilitates the escape of air during UW. SEM images 4g,h highlight the position of CLP-ED polymer pre and post welding.

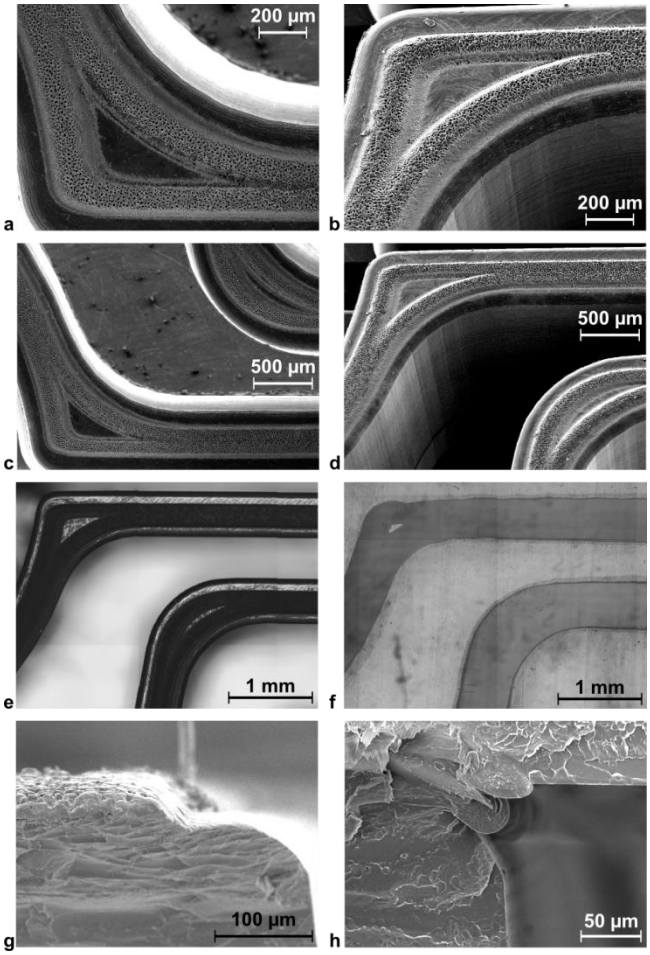

Figure 4. (a),(c) SEM images of modified mould on indicated length scales. (b),(d) SEM images of injection moulded piece, 30 degrees tilt. (e) Micrograph of unbonded micro pillar EDs and (f) bonded. Note the transparent welding seam. (g) Cross-sectional SEM images of unbonded and (h) bonded chips. Note the solidified polymer from the welding process in (h).

1.5. Bonding strength

Bonding strengths in terms of the surface energy, γ, calculated from razor-blade tests are listed in Table 1. Bonding strengths for other materials and bonding methods commonly used in microfluidics are also listed. These were calculated from channel dimensions and channel burst pressures. The full table of bonding strength measurements and calculations are given in the Supplementary Information.

Table 1. Bonding strength results expressed in terms of surface energy, γ. [a]These Literature surface energies are calculated from channel dimensions, Young's modulus and bursting pressure. See Supplementary Information for calculations. [b]A two-sample (unpaired) T-test showed no significant difference in the bonding strength between conventional and CLP-EDs: t(10)=-1.84, p=0.084.

Bonding method	Material	γ [J/m^2]
UW, conventional EDs (this study)	COC Topas 5013L-10	[b]100±30
UW, CLP-EDs (this study)	COC Topas 5013L-10	[b]122±23
UV activated thermal bonding[13]	COC Topas 5013L-10	61
UV/ozone thermal bonding[14]	COC Zeonor 1020 R	8.1
Solvent bonding, cyclohexane[21]	COC Topas 8007	[a]6.2
Plasma + thermal bonding[15]	COP ZEONEX	8
Solvent bonding, 75% acetone[22]	PMMA	13.6
Oxygen plasma[23,24]	PDMS	[a]44.4±2
Uncured PDMS as adhesive[23]	PDMS	[a]227

Table 1 clearly shows that the bonding strength for thermoplastics is largest for structures bonded using ultrasonic welding. No significant difference is observed between conventional EDs and micropillar EDs. Ultrasonic welding likely provides the strongest bonding because the substrate is not chemically altered (e.g. bond breakage by UV radiation or plasma activation for thermal bonding), and the bonding strength is thus limited by the bulk strength of the substrate. In high-pressure applications, it is important to note that the upper limit pressure (burst pressure) of a device is determined by two additional factors: geometry and Young's modulus [25]. A softer material will flex more and result in larger forces in junctions (cracks) [25]. This explains why most PDMS devices burst at pressures lower than 6 bar [23,24], even when covalent bonding methods are used [23].

1.6. High-aspect ratio microfluidic system

The performance of CLP-ED structures were tested in the described high-aspect ratio microfluidic system. First, we verified that the microfluidic channels were leak-tight (cf. Fig. 2b). Further, pressure testing with gas applied to the outer channel while leaving the inner channel at ambient pressure showed that the devices (three tested) could sustain pressure up to at least 9.5 bar (maximum pressure available in our laboratory).

Fig. 5 shows confocal images of the free-standing wall structures of the device along the cross sections 1-4 (cf. Fig. 2a). The images are overlaid with the corresponding CAD file used for the mould fabrication. From the confocal images, we find that the channel height of the welded structure matches that of the design (2000 µm) with a tolerance of ±4.2 µm. This value is smaller than the confocal image voxel height and we conclude that any height difference is below our detection limit.

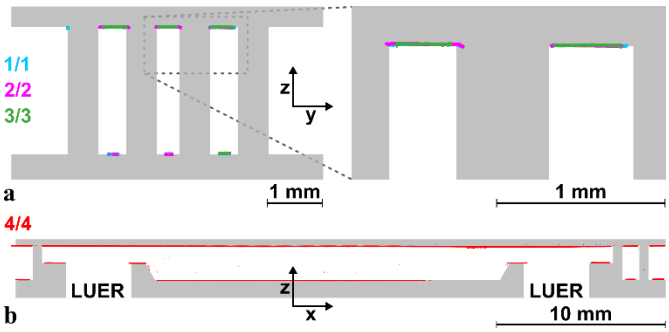

Figure 5. 2D cross-sections 1-4 of bonded chips. Cross sections are denoted by label and colour identical to Fig. 2. These 2D images are generated from the confocal image stacks by averaging 100 cross-sections along the x-axis (top figures) or y-axis (bottom figure). This corresponds to averaging over a length of 31.3 µm. The data is overlaid the chip CAD file (grey). Dashed box: zoom-in on the data.

Conclusion

We presented a new type of ED for ultrasonic welding of microfluidic systems based on micropillar EDs. These are based on replication of CLPs in aluminium, formed using a picosecond laser, and can be added to any mould surface accessible to a high power pico-second laser. We have demonstrated the technology by injection moulding microfluidic devices featuring high-aspect ratio structures and shown that ultrasonic welding of the devices is possible with no detectable channel deformation. This would be impossible by using conventional bonding methods that involve high pressures and temperatures. We have characterised the performance of the CLP-EDs and found that bonding strength is similar to conventional EDs, with no particle formation. The bonded devices could withstand 9.5 bar of hydraulic pressure without fracturing.

Most importantly, the technology has been demonstrated to work in high endurance tool steel used for making high performance injection moulding tools, which is a necessity for commercial applications. Also, with a modification rate of 200 seconds/cm^2 and full 3D capabilities, the technology is fast and allows for addition of CLP-EDs in existing moulds regardless of their origin, be it electric discharge machining, micro milling or cleanroom fabrication (electroforming).

Acknowledgements

This work is funded by DTU Nanotech and the Danish Council for Strategic Research through the Strategic Research Centre PolyNano (Grant no. 10-092322/DSF).

References

[1] Waldbaur A, Rapp H, Länge K and Rapp B E 2011 Let there be chip—towards rapid prototyping of microfluidic devices: one-step manufacturing processes *Anal. Methods* **3** 2681

[2] Sia S K and Whitesides G M 2003 Microfluidic devices fabricated in poly(dimethylsiloxane) for biological studies *Electrophoresis* **24** 3563–76

[3] Becker H 2010 Mind the gap! *Lab Chip* **10** 271–3

[4] Mukhopadhyay R 2007 When PDMS isn't the best *Anal. Chem.* **79** 3248–53

[5] Roca-Cusachs P, Rico F, Martínez E, Toset J, Farré R and Navajas D 2005 Stability of microfabricated high aspect ratio structures in poly(dimethylsiloxane) *Langmuir* **21** 5542–8

[6] Huang Y Y, Zhou W, Hsia K J, Menard E, Park J U, Rogers J a. and Alleyne A G 2005 Stamp collapse in soft lithography *Langmuir* **21** 8058–68

[7] Kistrup K, Poulsen C E, Hansen M and Wolff A 2015 Ultrasonic welding for fast bonding of self-aligned structures in lab-on-a-chip systems *Lab Chip* **15** 1998–2001

[8] Poulsen C E, Wootton R C R, Wolff A, DeMello A J and Elvira K S 2015 A Microfluidic Platform for the Rapid Determination of Distribution Coefficients by Gravity-Assisted Droplet-Based Liquid–Liquid Extraction *Anal. Chem.* **87** 6265–70

[9] Hatch A C, Fisher J S, Tovar A R, Hsieh A T, Lin R, Pentoney S L, Yang D L and Lee A P 2011 1-Million droplet array with wide-field fluorescence imaging for digital PCR *Lab Chip* **11** 3838–45

[10] Kung Y-C, Huang K-W, Fan Y-J and Chiou P-Y 2015 Fabrication of 3D high aspect ratio PDMS microfluidic networks with a hybrid stamp *Lab Chip* **15** 1861–8

[11] Natarajan S, Chang-Yen D a and Gale B K 2008 Large-area, high-aspect-ratio SU-8 molds for the fabrication of PDMS microfluidic devices *J. Micromechanics Microengineering* **18** 045021

[12] Andresen K Ø, Hansen M, Matschuk M, Jepsen S T, Sørensen H S, Utko P, Selmeczi D, Hansen T S, Larsen N B, Rozlosnik N and Taboryski R 2010 Injection molded chips with integrated

conducting polymer electrodes for electroporation of cells *J. Micromechanics Microengineering* **20** 055010

[13] Matteucci M, Christiansen T L, Tanzi S, Ostergaard P F, Larsen S T and Taboryski R 2013 Fabrication and characterization of injection molded multi level nano and microfluidic systems *Microelectron. Eng.* **111** 294–8

[14] Tsao C W, Hromada L, Liu J, Kumar P and DeVoe D L 2007 Low temperature bonding of PMMA and COC microfluidic substrates using UV/ozone surface treatment *Lab Chip* **7** 499–505

[15] Mizuno J, Ishida H, Farrens S, Dragoi V, Shinohara H, Suzuki T, Ishizuka M, Glinsner T, Lindner F P and Shoji S 2005 Cyclo-olefin polymer direct bonding using low temperature plasma activation bonding *13th Int. Conf. Solid-State Sensors, Actuators Microsystems, 2005. Dig. Tech. Pap. TRANSDUCERS '05.* **2** 1346–9

[16] Brüning S, Jenke G, Du K and Gillner A 2014 High Precision Laser Processing of Steel Surfaces with Sub-ns-lasers *Phys. Procedia* **56** 919–26

[17] Branson 1975 Part Design for Ultrasonic Welding *Technical Information PW-3* vol 1 (Branson Ultrasonics)

[18] Kistrup K, Poulsen C E, Østergaard P F, Haugshøj K B, Taboryski R, Wolff A and Hansen M F 2014 Fabrication and modelling of injection moulded all-polymer capillary microvalves for passive microfluidic control *J. Micromechanics Microengineering* **24** 125007

[19] Maszara W P, Goetz G, Caviglia A and McKitterick J B 1988 Bonding of silicon wafers for silicon-on-insulator *J. Appl. Phys.* **64** 4943–50

[20] Wu B, Zhou M, Li J, Ye X, Li G and Cai L 2009 Superhydrophobic surfaces fabricated by microstructuring of stainless steel using a femtosecond laser *Appl. Surf. Sci.* **256** 61–6

[21] Mair D a., Rolandi M, Snauko M, Noroski R, Svec F and Fréchet J M J 2007 Room-temperature bonding for plastic high-pressure microfluidic chips *Anal. Chem.* **79** 5097–102

[22] Wan A M D, Sadri A and Young E W K 2015 Liquid phase solvent bonding of plastic microfluidic devices assisted by retention grooves *Lab Chip* **15** 3785–92

[23] Eddings M a, Johnson M a and Gale B K 2008 Determining the optimal PDMS–PDMS bonding technique for microfluidic devices *J. Micromechanics Microengineering* **18** 067001

[24] Bhattacharya S, Datta A, Berg J M and Gangopadhyay S 2005 Studies on surface wettability of poly(dimethyl) siloxane (PDMS) and glass under oxygen-plasma treatment and correlation with bond strength *J. Microelectromechanical Syst.* **14** 590–7

[25] Anderson T L 2005 *Fracture Mechanics: Fundamentals and Applications, Third Edition* (Taylor & Francis)

SUPPLEMENTARY INFORMATION

Laser ablated micropillar energy directors for ultrasonic welding of microfluidic systems

Carl Esben Poulsen[a], Kasper Kistrup[a], Nis Korsgaard Andersen[a], Rafael Taboryski[a], Mikkel Fougt Hansen[a] and Anders Wolff[a]*

[a] Department of Micro- and Nanotechnology, Technical University of Denmark, DTU Nanotech, Building 345 East, DK-2800 Kongens Lyngby, Denmark

S1. Bonding strength assessment by razor-blade test

Welding strength was assessed using the razor-blade test based on fracture propagation developed by Maszara *et al.* [19], and employed by Matteucci *et al.* [13], which uses the equation $\gamma = 3\mathrm{H}^2h^3E/(16L^4)$. Here, γ [J/m^2] is the surface energy required for fracturing the welding, creating new surfaces, H is the deflection height, h is the foil thickness, L is the equilibrium crack length and E is Young's modulus which for COC 5013S-04 is 3.2 GPa (suppliers datasheet), see Fig. S1 for annotations. H was the blade thickness (250 µm, 20 mm × 39.5 mm, Millarco) minus the ultrasonic welding gap [18]. The welding gap was measured by scanning electron microscopy (SEM) to be 15.3 µm and 14.1 µm for conventional and CLP-EDs, respectively. It is important to note that in this context, the surface energy, γ, includes irreversible bond breakages, and must not be confused with surface tension. In this test, shear effects of the foil are neglected which is reasonable when $L > 3h/2$ as is the case in the presented data [19]. The razor blade test was repeated on ten devices for each ED type. Cross-sectional SEM images similar to the those presented in Figs 4g,h were used for determining the bonding gap height.

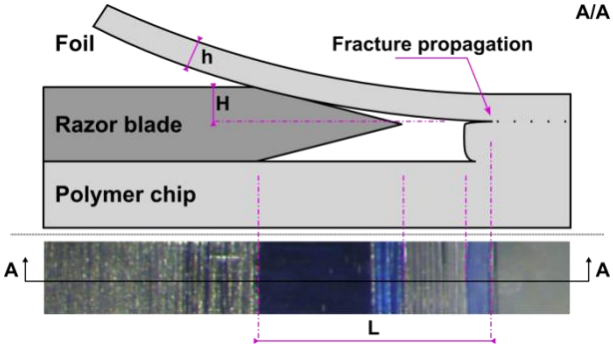

Fig. S1 A/A: Schematic cross-section of the razor blade test for determination of bonding strength (not to scale). Bottom insert: image of experiment with cross-section A/A highlighted.

S2. Bonding strength data

Table S1. Bonding strength data comparing the two types of energy directors. For all samples, blade thickness is 250 µm, *h* is 167 µm, Young's modulus is 3.2 GPa, and the Poisson ratio is 0.37. *H* is 235 µm and 236 µm for the conventional- and micropillar EDs, respectively.

Conventional ED			**CLP-ED**		
Sample#	*L* [mm]	Surface energy [J/m^2]	Sample#	*L* [mm]	Surface energy [J/m^2]
1	1.17	95	1	1.13	111
2	1.26	71	2	1.13	111
3	1.06	142	3	1.02	165
4	1.04	155	4	1.05	151
5	1.13	109	5	1.14	107
6	1.18	93	6	1.16	99
7	1.34	55	7	1.17	95
8	1.23	19	8	1.08	130
9	1.15	101	9	1.08	130
10	1.16	99	10	1.11	120
Avg	1.17	100	Avg	1.11	122
SD	0.09	30	SD	0.05	23
CV%	7.67	30	CV%	4.43	19

S3. Bonding strength calculations from device bursting pressure

The bonding strength in terms of surface energy, γ [$\mathrm{J/m^2}$], can be estimated from the minimum pressure causing the device to fail. This is done by assuming that the applied pressure results in tensile stress normal to the surface, while taking into account the geometry and flexibility of the device [25]. For a circular chamber (for example, an inlet), we solve the equation describing the minimum tensile stress required to cause an infinite sized object harvesting a penny shaped crack to fail [25]. This leads to the equation $\gamma = P_{\mathrm{max}}^2 2(1-\nu^2)a/(\pi E)$, where P_{max} is the minimum failing pressure, ν is the poisson ratio, a is the radius of the chamber, and E is Young's modulus. Similarly, for a rectangular channel, we solve the equation for a rectangular void, leading to the equation $\gamma = P_{\mathrm{max}}^2 \pi a/(2E)$. Here $2a$ is the smallest dimension of the channel.

Table S2. Bonding strength values calculated from literature data on channel dimensions and burst pressure.

Reference	Bonding type	Material	Shape	$2a$ [mm]	ν	E [MPa]	P_{max} [bar]	γ [$\mathrm{J/m^2}$]
Eddings *et al.* (2008)[23]	Oxygen plasma	PDMS to PDMS	Circular	5.0	0.5	2.5	3.0	43.0
Bhattacharya *et al.* (2005)[24]	Oxygen plasma	PDMS to PDMS	Circular	3.0	0.5	2.5	4.0	45.8
Eddings *et al.* (2008)[23]	Uncured PDMS as adhesive	PDMS to PDMS	Circular	5.0	0.5	2.5	6.9	227
Mair *et al.* (2007)[21]	Solvent, cyclohexane	Topas 8007	Rectangular	0.082	0.37	3200	173	6.16

S4. Particle formation

Particle formation is often presumed to be a problem in connection with UW. To quantify whether particles were formed during the vibrations of ultrasonic welding, devices featuring a circular ⌀=6 mm, 300 µm deep chamber were fabricated and bonded using either conventional EDs or CLP-EDs.

Quantification was done by bright field imaging the chamber using a Zeiss Axio Imager.M2 microscope with 10× magnification yielding a pixel width of 0.645 µm. To eliminate background dust and/or mould voids, particle counting was performed pre and post welding.

Testing revealed that UW using either type of EDs in our laboratory did not cause any detectable particle formation. Details are given in Table S3. However, we noted that samples, which had been discarded due to the occurrence of skating during welding (pre-meld, lateral movement of the ED), were the only ones containing particles (on the order of 10 particles/device). The fact that skating generates particles is not surprising when considering that the two polymer surfaces are scrubbing while under high pressure and 20 kHz vibrations.

Table S3. Particle and void count of welded foil before and after ultrasonic welding. As can be seen, the observed number of voids and particles are *fewer* after welding, suggesting little or no particle formation during ultrasonic welding.

	Particles+voids
Unbonded foil	7.5±3.4
Foil bonded using conventional EDs	7.0±2.4
Foil bonded using micropillar EDs	2.5±0.5

S5. References

References used in this supplementary information are numbered according to the bibliography of the main text:

[13] Matteucci M, Christiansen T L, Tanzi S, Ostergaard P F, Larsen S T and Taboryski R 2013 Fabrication and characterization of injection molded multi level nano and microfluidic systems *Microelectron. Eng.* **111** 294–8.

[18] Kistrup K, Poulsen C E, Østergaard P F, Haugshøj K B, Taboryski R, Wolff A and Hansen M F 2014 Fabrication and modelling of injection moulded all-polymer capillary microvalves for passive microfluidic control *J. Micromechanics Microengineering* **24** 125007.

[19] Maszara W P, Goetz G, Caviglia A and McKitterick J B 1988 Bonding of silicon wafers for silicon-on-insulator *J. Appl. Phys.* **64** 4943–50.

[21] Mair D a., Rolandi M, Snauko M, Noroski R, Svec F and Fréchet J M J 2007 Room-temperature bonding for plastic high-pressure microfluidic chips *Anal. Chem.* **79** 5097–102.

[23] Eddings M a, Johnson M a and Gale B K 2008 Determining the optimal PDMS–PDMS bonding technique for microfluidic devices *J. Micromechanics Microengineering* **18** 067001.

[24] Bhattacharya S, Datta A, Berg J M and Gangopadhyay S 2005 Studies on surface wettability of poly(dimethyl) siloxane (PDMS) and glass under oxygen-plasma treatment and correlation with bond strength *J. Microelectromechanical Syst.* **14** 590–7.

[25] Anderson T L 2005 *Fracture Mechanics: Fundamentals and Applications, Third Edition* (Taylor & Francis)

Published by:
DTU Nanotech
Department of Micro- and Nanotechnology
Technical University of Denmark
Ørsteds Plads, building 345B
DK-2800 Kgs. Lyngby